University of Bialystok
Faculty of Biology and Chemistry

Mariana Kozlowska

Noncovalent interactions in the process of carbon nanotubes functionalization with diisocyanates and polyethylene glycol molecules

PhD dissertation

Supervisor: Dr. Habil. Pawel Rodziewicz

Bialystok 2017

Acknowledgements

I would like to express my enormous gratitude to everybody who gave me the possibility to conduct research within my PhD thesis carried out at the Faculty of Biology and Chemistry of the University of Bialystok. Foremost, I would like to acknowledge and thank my scientific supervisor Dr. Habil. Pawel Rodziewicz, who has shown me a good academic practice and great patience with the simultaneous teaching of the *lege artis* research work. I would like to thank Dr. Habil. Pawel Rodziewicz for his motivation, enthusiasm, immense knowledge and hard working, therefore, for the infusing of all these features to me as for the young scientist. It was a great respect to be guided for such a good person and an excellent leader.

It is a great pleassure to thank also Prof. Tadeusz Krogulec for his willing to be my tutor in the specified period of time with the sophisticated deep thinking and serenity during decision-making.

Additionally, I would like to thank people from the Interdisciplinary Centre for Mathematical and Computational Modelling (ICM) at Warsaw University for the permission to perform theoretical calculations and simulations with the usage of their computer resources, which were available within the grants number G55-1, G57-23 and G63-0.

I would like to acknowledge also people who supported me and helped me financially to participate in different national and international conferences, where the results obtained within the PhD thesis were presented. Therefore, great thanks to Prof. Krzysztof Winkler, Prof. Iwona Ciereszko, the PhD Students Council of the University of Bialystok and Podlaskie Voivodeship, which enabled me to be a beneficiary of the project "Scholarship for PhD students of Podlaskie Voivodeship", which was co-financed by European Social Fund, Polish Government and Podlaskie Voivodeship.

I would like to thank Foundation for Polish Science for giving me the possibility to go abroad for the internship at Friedrich-Alexander-Universitaet (FAU) Erlangen-Nuernberg and to experince real scientific life and huge possibilities coming from interdisciplinary collaboration and partnership, which were able due to the Skills-Praxis grant.

Finally, I would like to express the greatest thanks to my parents and friends for their huge support, help and motivation during the whole time of my PhD studies and writing of my PhD thesis. The greatest thanks are expressed to my husband Wojtek and my son Aleksy, who have supported me, believed in all my new ideas and research interests and understood my scientific passion.

Last but not least, I would like to thank all people engaged in the FameLab Poland competition for scientists, who have changed my lifestyle and the way of scientific communication.

Abstract

The conditions of our life have been improved significantly comparing to those, characteristic, for our previous generations. The largest increase in the development of industrial technologies and science took place in the XX century and, until now, it is still rising but with lower growth. On the one hand, fast technology development has influenced on the level and style of our life, but, at the same time, has caused additional problems, such as the excess of garbage, plastics and contaminations in the environment. Current generation of scientists wants to find the "golden mean" between benefits of the technology development and conditions of our environment. The level of the development of state of the art and computer technologies nowadays, enables the usage of theoretical algorythms to explain real phenomena and processes performing computer calculations. Therefore, nowadays a lot of scientists use such theoretical approaches to fulfil their scietific research. In the present PhD thesis, the modern quantum chemistry approaches are used to explain and describe fundamental intermolecular and intramolecular interactions, which take place in the carbon materials synthesized and play an important role in the definition of their properties.

Carbon nanotubes, which belong to the systems analyzed in the present PhD thesis, are widely known nanomaterials since 80.-90. of the previous century, when their unique electrical, mechanical, thermal etc. properties caught the attention of scientists. Together with fullerenes, later also with graphene, carbon nanotubes represent a significant part of nanotechnology, which has developed, in the highest extend, with the development of experimental methods able to investigate objects in nanometric scale. Later, carbon nanotubes were reported not to be used effectively in technology or medicine in the non-modified state, because of their low dispersity in material. Carbon nanotubes exist as bundles, so it is a hard task to disperse them in the solvents during chemical synthesis, e.g. hybrid polymers, thus, their unique properties can not be successfully transferred to the polymer material. The achievement of the satisfactory dispersion of carbon nanotubes, without detailed description of interactions in material, is hard and time–consuming task. As a result, their practical usage is still limited. There are plenty of research concerning different modifications of carbon materials: covalent, noncovalent, endo- or exohedral, but the description of chemical processes during these types of functionalization and the prediction of the final result can not be made with experimental studies only. The usage of theoretical calculations, which are able to mimic and to predict the behavior of molecules in the chemical reactions and physical processes, can be helpful.

The addition of carbon nanotubes to polymers induces positive changes of the polymer material, e.g. they can be more durable or elastic, can adsorb different hazardous sustances more effectively or can be better conductors. It can cause wider or entirely new applications of such modified materials, called hybrid composites. Novel hybrid composites, based on polyurethane and carbon nanotubes, have paid attention of plenty of scientists and polymer

industry, since they were discovered to possess better properties than the pure polymers. Due to their superb properties, such composites are the prior candidates for the usage as shape memory and interference shielding materials, in tissue engineering scaffolds with nanostructured surface topography or in biomedical devices.

The present PhD thesis focuses on the description of intermolecular and intramolecular noncovalent interactions during two, the most widely used, types of functionalization of carbon nanotubes, namely, noncovalent and covalent, which take place during the synthesis of the composites based on polyurethanes and carbon nanotubes. Both types of polyurethane monomers: aromatic diisocyanates and polyethylene glycol molecules, are used to estimate the nature of the noncovalent interactions with the surface of single-walled carbon nanotubes. Different types of the surface of carbon nanotube, i.e. pristine and defective, are used to estimate the influence of the surface modifications of carbon material on the structural properties of the molecules attached and the electronic properties characteristic to the pristine carbon nanotubes.

In general, composites belong to the huge molecular systems due to long polymer chains with molecular weight even 100 kDa. Therefore, the best approach used in their theoretical investigation is the classical molecular dynamics methods. On the one hand, classical approach enables to treat such huge molecular systems as composites, but on the other hand, this approach is based on the parametrized, specially designed, force fields, which can not be effectively used to analyze such weak noncovalent interactions as van der Waals interactions or hydrogen bonds, taking into account their breaking and formation. It can be fulfilled with the usage of the quantum-chemistry-based approaches. The analysis of such huge systems as composites, using quantum chemistry approaches, is very complicated task, which requires high computational resources and simplified models with the specified number of atoms in the system analyzed. To solve the problem of the noncovalent interactions during different types of functionalization of carbon nanotubes, the theoretical approach, based on quantum chemistry calculations, is used in the present PhD thesis. Among the calculations made, both static and dynamical predictions were performed. The static calculations were made with the usage of density functional theory approach, whereas molecular dynamics simulations were performed according to the Car–Parrinello scheme. The usage of quantum based methods, in order to understand the nature of noncovalent interactions in the systems, limits the molecular systems analyzed to c.a. 200–300 atoms. As a result, several models of the covalent and noncovalent functionalization of carbon nanotubes with diisocyanates and polyethylene glycol, formed on the basis of the experimental results reported, were used and analyzed in detail.

Noncovalent interactions are relatively weak type of interactions, but they influence on the functionalization of carbon nanotubes and their dispersion in the polymer. Among the systems, analyzed in the present PhD thesis, are fragments of single-walled carbon nanotubes (defect-free and defective), covalently and noncovalently modified with diisocyanates: MDI (1,1'-methylenebis(4-isocyanatobenzene), and TDI (2,4-diisocyanato-1-methylbenzene), and polyethylene glycol – PEG. The MDI and TDI molecules were chosen, because they are the most frequently used in the polyurethane synthesis, while polyethylene glycol was considered due to the fact that it is a popular polyol with high biocompatibility.

To accomplish the aims of the studies, formulated after the deep analysis of the existing literature data, density functional theory calculations and Car–Parrinello molecular dynamics simulations at finite temperature are utilized either to estimate the conformational space and structural properties of the isolated molecules (MDI, TDI and PEG), which serve as monomers for polyurethane production, or understand their inter- and intramolecular interactions with the carbon nanotubes during their covalent and noncovalent attachment to the surface.

Different noncovalent interactions were obtained in the present research. Among them are hydrogen bonds of various strength and nature, i.e. strong O-H$\cdots$O and weak C-H$\cdots$O, C-H$\cdots\pi$; $\pi-\pi$ interactions, differing in their strength as a result of the additional substituent effects in the aromatic rings; van der Waals interactions, mainly of the weak dispersion nature, i.e. London dispersion interactions; and others. They were investigated with the usage of the additional tools, based on the analysis of the electron density and its derivatives, i.e. Quantum Theory of Atoms in Molecules and noncovalent interaction index (NCI index).

The results obtained confirmed the importance of the noncovalent interactions during the process of covalent and noncovalent functionalization of carbon nanotubes, especially by the aromatic diisocyanates, which are very reactive chemical species with the high physisorption on the surface of the carbon nanotubes. The influence of noncovalent interactions is clearly seen from the comparative studies of the covalent attachment of diisocyanates to different types of the carbon nanotube surface, where the additional interactions with the defective regions impact the structural properties of the TDI-, MDI-modified surface.

Streszczenie

"Oddziaływania niekowalencyjne w procesie funkcjonalizacji nanorurek węglowych cząsteczkami diizocyjanianów i poli(tlenku etylenu)"

Warunki naszego życia zostały znacząco ulepszone w stosunku do tych, które panowały stulecie temu. Największy wzrost rozwoju przemysłu i nauki nastąpił właśnie w XX stuleciu i jest w mniejszym stopniu kontynuowany do dziś. Z jednej strony, taki szybki rozwój technologiczny pozytywnie wpłynął na poziom i styl naszego życia, ale, jednocześnie, spowodował dodatkowe problemy w postaci nadmiaru śmieci, plastiku, zwiększenia zanieczyszczeń w środowisku. Teraźniejsze pokolenie naukowców pragnie znaleźć "złoty środek" pomiędzy korzyściami, które płyną z rozwoju technologicznego, a stanem naszego środowiska. W związku z szybkim rozwojem stanu wiedzy teoretycznej i technologii komputerowych w ostatnich dekadach, coraz częściej naukowcy korzystają z teorii i algorytmów chemii teoretycznej i obliczeniowej w celu uzupełnienia ich badań naukowych i wyjaśnienia rzeczywistych zjawisk i procesów, wykonując obliczenia i symulacje komputerowe. W niniejszej pracy doktorskiej nowoczesne narzędzia chemii kwantowej są wykorzystywane w celu wyjaśnienia i dokonania opisu podstawowych oddziaływań międzycząsteczkowych oraz wewnątrzcząsteczkowych, które istnieją w syntezowanych materiałach węglowych i odgrywają ogromną rolę w definiowaniu ich właściwości.

Nanorurki węglowe, które należą do badanych obiektów w pracy doktorskiej, znane są od lat 80.-90.tych poprzedniego stulecia, kiedy zwróciły uwagę naukowców dzięki swoim unikalnym właściwościom elektrycznym, mechanicznym, termicznym i wielu innym. Razem z fulerenami, a później i grafenem, nanorurki stanowią znaczącą część dziedziny nanotechnologii, która rozwinęła się, w największym stopniu, wraz z rozwojem nowych metod badawczych, pozwalających na badania obiektów w skali nanometrycznej. Kilka lat później okazało się, że nanorurki węglowe nie mogą być efektywnie stosowane w technice czy medycynie bez wstępnej modyfikacji, umożliwiającej maksymalną ich dyspergowalność w materiale. Nanorurki węglowe istnieją w postaci zbitych kłębków: ciężko jest rozproszyć (dyspergować) je w rozpuszczalnikach podczas syntezy, np. polimerów hybrydowych, a zatem ich unikalne właściwości nie mogą być skutecznie przeniesione do materiału polimerowego. W związku z tym, ich praktyczne zastosowanie jest wciąż ograniczone. Powstało wiele prac na temat różnych modyfikacji materiałow węglowych: kowalencyjna, niekowalencyjna, endo- czy egzohedralna, ale osiągnięcie zadowalającej dyspergowalności nanorurek węglowych metodami eksperymentalnymi, bez szczegółowego opisu oddziaływań w materiale, jest trudnym i czasochłonnym zadaniem. Nie zawsze procesy, zachodzące podczas takich funkcjonalizacji, lub wynik reakcji chemicznej, można opisać wyłącznie za pomocą badań eksperymentalnych. Pomocą mogą służyć obliczenia teoretyczne, dzięki którym można z pewną dokładnością przewidzieć zachowanie się cząsteczek w reakcjach chemicznych i procesach fizycznych.

Dodatek nanorurek węglowych do różnych polimerów powoduje zmianę ich właściwości, na przykład, są bardziej wytrzymałe lub elastyczne, mogą więcej adsorbować substancji niebezpiecznych lub lepiej przewodzić prąd. Dlatego nanorurki węglowe są szeroko stosowane w syntezie materiałów na bazie żywic epoksydowych, polipropylenu, polipirolu, polistyrenu i polianiliny. Takie modyfikowane kompozyty są interesującym materiałem dla współczesnego przemysłu, ponieważ posiadają niską gęstość, wysoką odporność na korozję oraz są łatwiejsze w obróbce. Wśród materiałów, które są modyfikowane nanorurkami węglowymi, są polimery poliuretanowe, które mają szeroką gamę zastosowań w zależności od tego, z jakich surowców i w jakich ich proporcjach są syntezowane. Kompozyty polimerowe na bazie polimerów poliuretanowych i nanorurek węglowych mogą być stosowane jako materiały z pamięcią kształtu lub do ekranowania zakłóceń elektromagnetycznych, a także w inżynierii tkankowej i w urządzeniach biomedycznych.

Niniejsza praca badawcza, wykonywana w ramach rozprawy doktorskiej, skupia się na opisie niekowalencyjnych oddziaływań międzycząsteczkowych oraz wewnątrzcząsteczkowych podczas dwóch, najczęściej wykorzystywanych, typów funkcjonalizacji nanorurek węglowych, a mianowicie, niekowalencyjnej i kowalencyjnej, które zachodzą podczas syntezy kompozytów na bazie poliuretanów i nanorurek węglowych. Oba rodzaje monomerów, stosowanych w syntezie polimerów poliuretanowych: aromatyczne diizocyjaniany i poli(tlenek etylenu), są wykorzystywane w pracy doktorskiej w celu oszacowania natury oddziaływań niekowalencyjnych na powierzchni jednościennych nanorurek węglowych. Różne rodzaje powierzchni nanorurek węglowych, w tym surowa (*z ang. "pristine"*) i zdefektowane, są wykorzystywane do oszacowania wpływu modyfikacji powierzchniowych w materiale węglowym na właściwości strukturalne dołączonych cząsteczek oraz na właściwości elektroniczne wyjściowych nanorurek węglowych.

Kompozyty są dużymi układami badawczymi, zawierającymi długie łańcuchy polimerów, których masa cząsteczkowa wynosi nawet 100 kDa. Zatem, najlepszą metodą ich badania teoretycznego jest klasyczna dynamika molekularna. Z jednej strony, podejście klasyczne umożliwia analizę takich dużych systemów molekularnych, ale z drugiej strony, podejście te korzysta z wielu uproszczeń i sparametryzowanych, specjalnie stworzonych, pól siłowych, które nie mogą być efektywnie wykorzystane do analizy słabych oddziaływań niekowalencyjnych, takich jak oddziaływania van der Waalsa czy wiązania wodorowe, z jednoczesnym wyznaczeniem czasu życia wiązań, analizy ich powstawania i zrywania, a także właściwości elektrycznych badanych układów. Fundamentalne oddziaływania niekowalencyjne można przeanalizować poprzez wykonanie symulacji kwantową dynamiką molekularną. Dynamika ta pozwala na symulacje układów, składających się z dziesiątek atomów. Efektywnym odpowiednikiem takiej dynamiki molekularnej jest dynamika molekularna według Car i Parrinello. Dzięki zastosowaniu takiej dynamiki molekularnej, z wykorzystaniem periodycznych warunków brzegowych i fal płaskich, jako funkcji bazy, obliczenia te potrafią opisać niekowalencyjne oddziaływania wewnątrzcząsteczkowe i międzycząsteczkowe w rzeczywistym czasie życia cząsteczek. Takie podejście umożliwia prawidłowy opis właściwości nanorurek węglowych, pochodzących z ich natury periodycznej, oraz może służyć do wstępnej analizy oddziaływań między matrycą polimerową a jednościennymi nanorurkami węglowymi w celu ich późniejszej modyfikacji.

Badanie takich układów, jak kompozyty polimerowe, metodami chemii kwantowej jest bardzo skomplikowane i wymaga dużej mocy obliczeniowej komputera i zasobów czasowych, oraz uproszczonych modeli teoretycznych z odpowiednią ilością atomów w analizowanym układzie. W celu rozwiązania problemu oddziaływań niekowalencyjnych podczas funkcjonalizacji nanorurek węglowych, zostały wykonane obliczenia statyczne w oparciu o teorię funkcjonału gęstości. Dodatkowo, dynamika molekularna wedlug Car i Parrinello została użyta do symulacji układów w realnym czasie życia cząsteczek i w określonej temperaturze. Wyko-

rzystanie danych metod chemii kwantowych ogranicza wielkość badanego układu do ilości atomów ok. 200-300, zatem, w niniejszej pracy doktorskiej, zostały zbadane kilka modeli kowalencyjnej i niekowalencyjnej funkcjonalizacji nanorurek węglowych za pomocą diizocyjanianów i poli(tlenku etylenu), stworzonych na podstawie wyników eksperymentalnych.

Oddziaływania niekowalencyjne należą do stosunkowo słabych, ale mają wpływ na funkcjonalizację nanorurek węglowych i ich dyspergowalność w matrycy polimerowej. Wśród układów badanych w niniejszej pracy doktorskiej, są fragmenty jednościennych nanorurek węglowych, które zostały zmodyfikowane kowalencyjnie i niekowalencyjnie diizocyjanianami (MDI, metylenodifenylo-4,4'-diizocyjanian, i TDI, 2,4-toluilenodiizocyjanian) oraz poli(tlenkiem etylenu) – PEG, które są wykorzystywane do syntezy polimerów poliuretanowych. Cząsteczki MDI i TDI są badane ze względu na ich najczęstsze wykorzystanie w syntezie polimerów poliuretanowych. Poli(tlenek etylenu) został wybrany w związku z jego udowodnionymi właściwościami biokompatybilnymi, wykorzystywanymi w syntezie polimerów do zastosowania w medycynie.

W celu systematycznego opisu oddziaływań niekowalencyjnych pomiędzy nanorurkami węglowymi a monomerami poliuretanów zostały wykonane obliczenia, dotyczące pojedynczych cząsteczek MDI, TDI i PEG oraz zaadsorbowanych na powierzchni materiału węglowego, jak i kowalencyjnie dołączonych do powierzchni nanorurek węglowych z defektami i bez defektów powierzchniowych. Zostały zbadane różne oddziaływania niekowalencyjne: wiązania wodorowe o różnej sile i pochodzeniu, w tym silne O-H$\cdots$O i słabe C-H$\cdots$O i C-H$\cdots\pi$; oddziaływania poprzez $\pi-\pi$ nakładanie, różniące się siłą w zależności od wpływu podstawnika w pierścieniu aromatycznym; oddziaływania van der Waalsa, bazujące się w większości na słabych oddziaływaniach dyspersyjnych; i inne. Dokładna analiza oddziaływań niekowalencyjnych została przeprowadzona za pomocą metody Bader'a pt. "Atomów w Cząsteczce" (Quantum Theory of Atoms in Molecules) oraz indeksu oddziaływań niekowalencyjnych (NCI index), które opierają się na analizie gęstości elektronowej i jej pochodnych.

Otrzymane wyniki badań potwierdziły znaczenie oddziaływań niekowalencyjnych podczas kowalencyjnej i niekowalencyjnej funkcjonalizacji nanorurek węglowych, a szczególnie podczas modyfikacji aromatycznymi diizocyjanianami, które są bardzo reaktywne i posiadają możliwość adsorpcji fizycznej na powierzchni badanych nanorurek. Wpływ oddziaływań niekowalencyjnych jest dobrze widoczny w wyniku analizy porównawczej kowalencyjnego dołączania cząsteczek diizocyjanianów do różnych powierzchni nanorurek węglowych, gdzie dodatkowe oddziaływania z powierzchnią defektu wpływają na właściwości strukturalne powierzchni modyfikowanej cząsteczkami TDI i MDI.

The results published

Parts of this thesis have been published in the following journal articles:

1. J. Goclon, **M. Kozlowska**, P. Rodziewicz, Noncovalent functionalization of single-walled carbon nanotubes by aromatic diisocyanate molecules: A computational study, *Chemical Physics Letters*, **2014**, 598, 10–16.
2. J. Goclon, **M. Kozlowska**, P. Rodziewicz, Covalent functionalization of single-walled carbon nanotubes through attachment of aromatic diisocyanate molecules from first principles, *Chemical Physics Letters*, **2015**, 619, 103–108.
3. J. Goclon, **M. Kozlowska**, P. Rodziewicz, Structural, vibrational and electronic properties of defective single-walled carbon nanotubes functionalised with carboxyl groups. Theoretical studies, *ChemPhysChem*, **2015**, 16(13), 2775–2782.
4. **M. Kozlowska**, J. Goclon, P. Rodziewicz, Impact of vacancy defects in single-walled carbon nanotube on the structural properties of covalently attached aromatic diisocyanates, *Applied Surface Science*, **2016**, 362, 1–10.
5. **M. Kozlowska**, J. Goclon, P. Rodziewicz, Intramolecular hydrogen bonds in low molecular weight polyethylene glycol, *ChemPhysChem*, **2016**, 17, 1143–1153.

Other journal articles published during the PhD studies:

1. **M. Kozlowska**, J. Goclon, P. Rodziewicz, A computational study of intramolecular hydrogen bonds breaking/formation: impact on the structural flexibility of ranitidine molecule, *Journal of Molecular Modeling*, **2015**, 21, 94–105.
2. M. Malinowska, **M. Kozlowska**, A. Hryniewicka, S. Witkowski, J. W. Morzycki, New indenylidene-type metathesis catalysts bearing unsymmetrical N-heterocyclic ligands with mesityl and nitrobenzyl substituents, *Monatshefte für Chemie*, **2016**, 147, 1091–1100.
3. **M. Kozlowska**, P. Rodziewicz, A. Kaczmarek-Kedziera, Structural stability of diclofenac vs. inhibition activity from *ab initio* molecular dynamics simulations. Comparative study with ibuprofen and ketoprofen, *Structural Chemistry*, **2017**, DOI 10.1007/s11224-016-0893-8.

The results presented

The results obtained in the present PhD thesis were presented on several national and international conferences (*only self-presented items are given*):

– international conferences:

- 80th Annual Meeting of the DPG (80. Jahrestagung der DPG und DPG-Frühjahrstagung), 06.03.2016 – 11.03.2016, Regensburg (Germany):
  1) **M. Kozlowska**, "Covalent functionalisation of pristine and vacancy defective single-walled carbon nanotubes with diisocyanates" (*oral talk*)
  2) **M. Kozlowska**, P. Rodziewicz, "*Ab initio* molecular dynamics simulations of intramolecular hydrogen bonds in low molecular weight polyethylene glycol" (*poster*)
- 79th Annual Meeting of the DPG (79. Jahrestagung der DPG und DPG-Frühjahrstagung), 15.03.2015 – 20.03.2015, Berlin (Germany):
  1) **M. Kozlowska**, J. Goclon, P. Rodziewicz, "Structural changes of diisocyanates covalently attached to the semiconducting carbon nanotube" (*oral talk*)
  2) J. Goclon, **M. Kozlowska**, P. Rodziewicz, "First principles study of covalent and noncovalent functionalization of single-walled carbon nanotubes with diisocyanates" (*poster*)
- Polish Scietific Networks, 18.06.2015 – 20.06.2015, Warsaw (Poland):
  M. Kozlowska, P. Rodziewicz, "Theoretical predictions in materials science" (*poster*)
- Jülich CECAM School on Computational Trends in Solvation and Transport in Liquids, 23.03.2015 – 27.03.2015, Jülich Supercomputer Centre, Jülich (Germany):
  M. Kozlowska, P. Rodziewicz, "First principles studies of noncovalent functionalization of single-walled carbon nanotubes with small polyethylene glycol molecules" (*poster*)
- 16th JCF-Frühjahrssymposium 2014, 26.03.2014 – 29.03.2014, Jena (Germany):
  M. Kozlowska, "First principles studies of noncovalent functionalization of single-walled carbon nanotubes with 4,4'-methylene diphenyl diisocyanate" (*poster*)

– national conferences:

- 58.Zjazd PTChem i SITPChem "Chemia w mieście wolności", 21.09.2015 – 25.09.2015, Gdansk:
  M. Kozlowska, J. Goclon, P. Rodziewicz, "Theoretical studies of covalent attachment of defected semiconducting single-walled carbon nanotube by diisocyanates" (*oral talk*)
- III Ogólnopolskie Studenckie Mikrosympozjum Chemików "Chemia – przyszłość zaczyna się dziś", 12.03.2015 – 15.03.2015, Bialystok:

M. Kozlowska, "Correlation between the length of poly(ethylene glycol) chain and its structural stability" (*oral talk*)

- 57.Zjazd PTChem "Chemia – nadzieje i marzenia", 04.09.2014 – 18.09.2014, Częstochowa:
  M. Kozlowska, J. Goclon, P. Rodziewicz, "Car–Parrinello molecular dynamics simulations of covalent functionalization of carbon nanotubes with diisocyanates" (*oral talk*)
- I Środowiskowa Konferencja Doktorantów, 08.05.2014, Bialystok:
  M. Kozlowska, "Badania adsorpcji izocyjanianów na powierzchni jednościennych nanorurek węglowych z pierwszych zasad" (*oral talk*)

List of Abbreviations

AFM	Atomic Force Microscopy
AI	*Ab initio*
BCP	Bond Critical Point
BLYP	Becke–Lee–Yang–Parr
BO	Born–Oppenheimer
BO–MD	Born–Oppenheimer molecular dynamics
CCSD(T)	Coupled–Cluster with single and double and perturbative triple excitations
CF	Covalent Functionalization
CNT	Carbon nanotube
CP	Car–Parrinello
CP–MD	Car–Parrinello molecular dynamics
CPU	Computer Processing Unit
CVD	Chemical Vapour Deposition
DCACP	Dispersion-Corrected Atom-Centered Potential
DFT	Density Functional Theory
DOS	Density of states
DWCNT	Double-walled carbon nanotube
ELF	Electron Localization Function
GGA	Generalized Gradient Approximation
H-bond	Hydrogen bond
Hal-bond	Halogen bond
HRTEM	High-resolution Transmission Electron Microscopy
ICM	Interdisciplinary Centre for Mathematical and Computational Modelling
IR	InfraRed
LDA	Local Density Approximation
LDS	Local Spin Density
MD	Molecular dynamics
MDI	1,1′-methylenebis(4-isocyanatobenzene)
MM	Molecular mechanics
MP2	second-order Møller–Plesset perturbation theory
MWCNT	Multi-walled carbon nanotube
NCI	Noncovalent interaction
NM	Noncovalent Modification
ONIOM	our own n-layered integrated molecular orbital and molecular mechanics

PBC	Periodic Boundary Conditions
PBE	Perdew–Burke–Ernzerhof
PEG	Polyethylene glycol
PM6	parameterized model 6 method
PP	Pseudopotential
PU	Polyurethane
PW	Plane waves
QM	Quantum mechanics
QTAIM	Quantum Theory of Atoms in Molecules
RBM	Radial Breathing Mode
SAPT	Symmetry–Adapted Perturbation Technique
STM	Scanning Tunelling Microscopy
STS	Scanning Tunelling Spectroscopy
SW	Stone–Wales
SWCNT	Single-walled carbon nanotube
TDI	2,4-diisocyanato-1-methylbenzene
TEM	Transmission Electron Microscopy
TM	Trouiller–Martins
USPP	Ultrasoft Pseudopotential
vdW	van der Waals

List of Figures

List of Tables

Contents

Chapter 1

Problem definition. Aims of research

Carbon nanotubes possess low dispersity in polyurethane matrix during the synthesis of hybrid composites. As a result, their unique properties are not successfully transferred to the polymer material. The achievement of the satisfactory dispersion of carbon nanotubes, without detailed description of interactions in material, is a hard and time–consuming task. The present PhD thesis is mainly focused on the detailed desciption of noncovalent interactions, such as hydrogen bonds, $\pi - \pi$ stacking and van der Waals interactions, during the process of functionalization of single-walled carbon nanotubes with diisocyanates and polyethylene glycol molecules, used in the polyurethane synthesis.

The main objective of the PhD thesis is to get fundamental understanding of:

- intramolecular interactions in two types of monomers used in polyurethane synthesis: diisocyanates and polyols,
- structural rearrangements of diisocyanate and polyethylene glycol molecules at finite temperature,
- nature of intermolecular interactions between diisocyanates and single-walled carbon nanotubes during covalent and noncovalent functionalization of carbon nanotubes,
- influence of covalent attachment of the monomers on the electronic properties of carbon nanotubes,
- nature of the different adsorption of the diisocyanate molecules on the carbon nanotubes,
- affinity of low molecular polyethylene glycol molecules to the carbon nanotube surface,
- conformational changes of diisocyanates and polyethylene glycol molecules on single-walled carbon nanotubes and their dynamically averaged structures at finite temperature,
- reactivity of the defective regions on the surface of carbon nanotube and its influence on the most preferable functionalization site,
- influence of defective regions on the surface of carbon nanotube and its functionalization type on structural properties of adsorbed species,
- qualitative and quantitative analysis of noncovalent interactions, such as hydrogen bonds, $\pi - \pi$ stacking and van der Waals interactions.

Chapter 2

Introduction

Materials are characterized with their individual features, properties and possible applications. Nature enriched our world not only in pure materials, but also in their different mixtures, which constitute our world in what it is. Such materials, where two or more different materials are mixed together in a new one, are known as composite or hybrid materials. Composite has the properties of the initial ingredients, which still possess their properties in a mix. Hybrid materials are known to possess new properties on the basis of a combination of the initial ones. The definition of a composite/hybrid material depends on the nature of initial ingredients and the way of their mixing together. Since this PhD thesis is not a lexicological one and is not focused on the detailed mechanism of the origin of material properties, these two terms are used in the text as similar ones.

Among the variety of possible synthesized composite materials are hybrid materials, based on polymers and carbon allotropes such as fullerenes, amorphous carbon, carbon nanotubes or graphene. Such materials are widely investigated due to the efficient reinforcement effect of the polymer matrix and its better properties in comparison with the pure polymer itself [1, 2, 3, 4, 5]. The new materials can be more elastic or resistant, lighter or more convenient in use; they can be conducting even if polymer matrix was an insulator. As a result, there is a lot of different suggestions for novel usage of such new materials, e.g. as coatings, sealants, sensors, transdermal patches, catheters, high performance elastomers, artificial-heart blood vessels [6, 7, 8] etc.

Carbon nanotubes (CNTs) are the carbon-based nanomaterials, which are extensively studied for various purposes, because they possess unique electrical, mechanical, thermal and optical properties [9, 10, 11, 12, 13]. The popularity of CNTs in the last years can be seen from Figure 2.1, where the number of publications in the period of time since 1990 until 2017 (data collected on February 27, 2017) are shown.

It is clearly seen that after 2001 investigations on carbon nanotubes started to grow rapidly and the high popularity of these materials is still kept. Carbon nanotubes are promissing materials for the usage as energy conversion materials [14], sensors [15, 16], hydrogen storage materials [17], molecular electronic devices [18] etc. They have been also reported to be an excellent filler and reinforcing agent [8, 19] in polymer matrices, where they enhance the mechanical strength and decrease the density of such composites. It was reported that the addition of small amounts of CNTs to polymers (1–2 wt %, sometimes even at the level of 0.01–0.3 % [20, 19, 21]) can improve mechanical [20, 21, 22, 23, 24], electrical [25, 26, 27], thermal [28], and optical properties [29, 30] of such hybrid materials. Moreover, composites based on CNTs are attractive owing to their corrosion resistance, flexibility, higher conductivity, and different processing advantages [31], which depend on the amount and type of carbon nanotubes in the matrix. Therefore, carbon nanotubes have been extensively used in

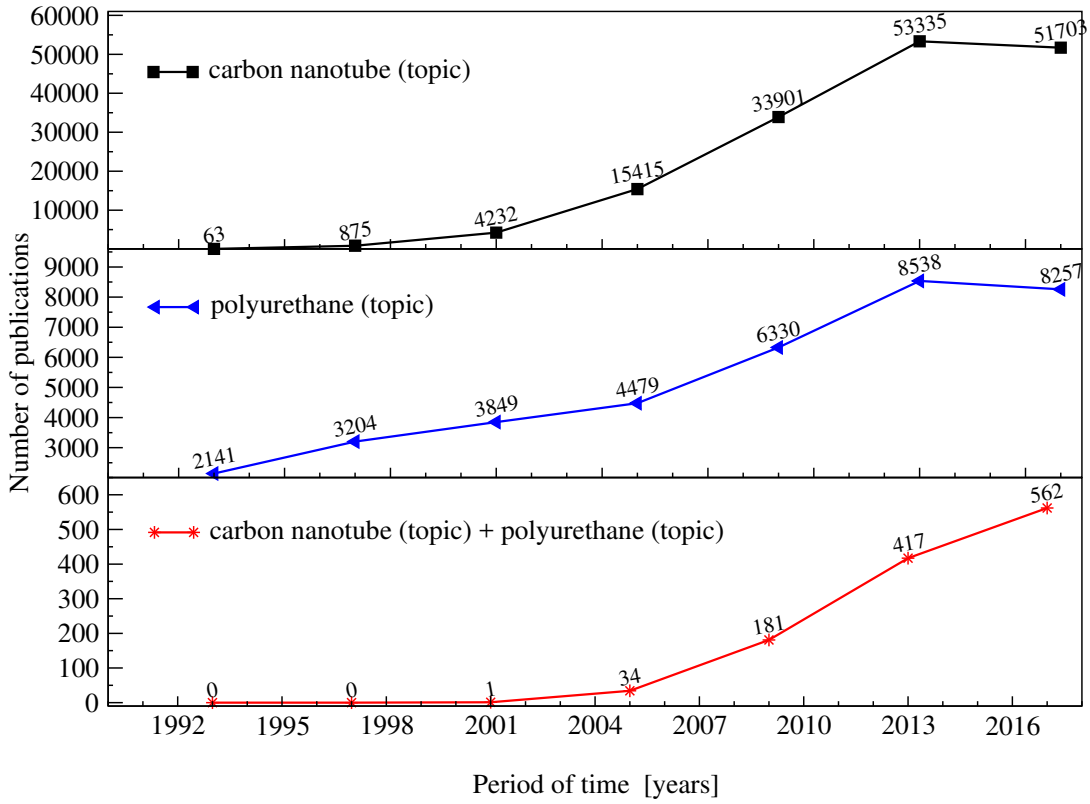

Figure 2.1: Number of publications from the Journal Citation Report list in the corresponding period of time for the keywords "carbon nanotube" in topic (upper chart), "polyurethane" in topic (middle chart), both "carbon nanotube" and "polyurethane" in topic (lower chart). Data collected on February 27, 2017 from ISI Web of Knowledge.

the synthesis of epoxy [32], polypropylene [33] polypyrrole [34], polystyrene, polyaniline [35] etc.

The unique properties of carbon nanotubes can be acquired when they exist in the nanometric form, so when they are maximally dispersed in the polymer or solvent. Since CNTs have very low reactivity and, due to van der Waals interactions among them have a tendency to agglomerate and to exist as the ropes and bundles, it is a real challenge to use them in composite synthesis with effective transfer of their superior properties to the matrix. Moreover, CNTs possess poor interfacial adhesion between their surface and the polymer matrix, which results to an increase of the free volume as the result of weak packing of the polymer chain. The formation of the polymer-CNT interface is suppressed. Therefore, their practical applications have been limited. The applications of CNTs became possible only after the discovery of the effective ways of their functionalization. The type of CNTs functionalization impact on their properties, thus determines their practical usage and large-scale fabrication of new nanomaterials based on them. There are two main approaches for nanotube functionalization: covalent and noncovalent one. Covalent functionalization is easier to handle, but the covalent attachment of molecules to the CNT surface deforms the local structure and directly influences their properties [31, 36]. Contrary to it, noncovalent functionalization has only a small influence on the electric properties of nanotubes [37] due to the weak van der Waals interactions between the CNT and the adsorbate, but it is based on much more subtle effects that are hard to control. Functionalization of CNTs allows to tune their chemical and physical properies. Due to the attachment of different functional groups, such as COOH, OH, COH, NH_2, to the surface of single-walled carbon nanotubes, their dispersion significantly increases. In addition, the adsorption of organic molecules on the surface of carbon

nanotubes opens new opportunities for their applications in nanotechnology, medicine and electronic devices. Even if there are variety of different ways to functionalize CNTs, the large-scale production of separated and monodispersed single-walled carbon nanotubes according to diameter, length and chirality is still a challenge.

Among different types of polymer matrices reinforced with CNTs are also polyurethanes (PUs), which play a crucial role in the global chemical industry [38]. They can be used in a wide range of applications as sealants, coatings, adhesives, thermoplastic elastomers, transdermal patches, catheters [38]. Thermoplastic PUs are often used in underwater applications [8], while segmented PU elastomers are used in various biomedical devices [39] and in tissue engineering scaffolds with nanostructured surface topography [6]. Polyurethane become an interesting polymer material since the discovery of its synthesis in 1937 by Otto Bayer and his coworkers. The discovered methodology was officially published ten years later, in 1947 [40]. Polyurethanes were produced commercially in 1950's by Bayer–Farbenfabriken (Germany) and B. F. Goodrich (The United States) [41], but only from 1970's, the PUs industry started to develop rapidly.

PUs are segmented polymers which are usually produced in the polyaddition process of diisocyanates and polyols [42]. The exemplary chemical reaction with the formation of carbamate (urethane) bonds during the synthesis of polyurethanes is shown in Figure 2.2. Polyurethane polymers consist of hard (diisocyanate) and soft (polyol) blocks that can form

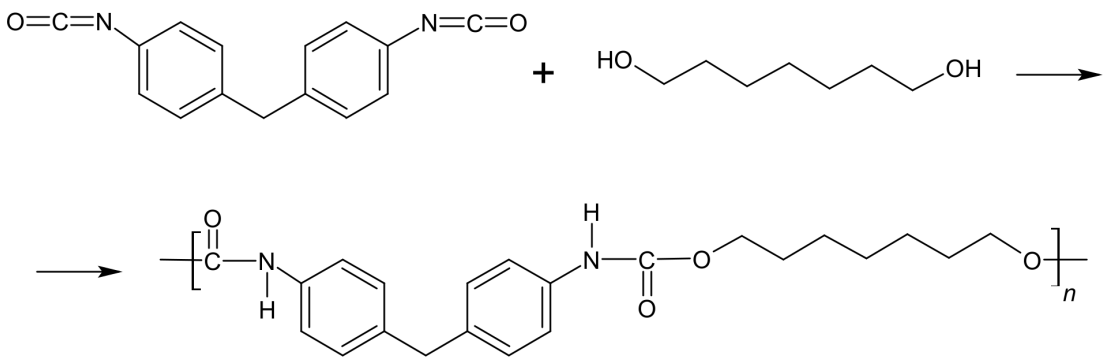

Figure 2.2: Polyaddition process during the synthesis of polyurethane polymer using 1,1'-methylenebis(4-isocyanatobenzene) (MDI) and 1,7-heptanediol.

hard and soft domains within the polymer matrix under the appropriate conditions [43]. Hard PU segments are binded through hydrogen bonds, dipole-dipole and van der Waals interactions. They play the role of a physical crosslinking point and in some way keeps the original material shape after the deformation. At the same time, soft PU segments are flexible and elastic, so they absorb external stress during deformation and define the phase-transition temperature [44]. Apart from the mentioned method for PU synthesis, which is widely used in industry, polyurethanes can be produced on the basis of carbonate derivatives [45, 46] without involving toxic monomers.

Polyurethanes belong to the unique class of polymers, because a large variety of different types of PUs can be synthesized with widely varying physical and chemical properties. This is due to the fact that polyurethanes can be synthesized using different types of monomers with various properties. As a result, PUs can be used in different forms ranging from flexible or rigid lightweight foams to stiff and strong elastomers. The development of techniques for PU modification and synthesis are the most developing among other polymer materials. Figure 2.1 demonstrates the increase of the scientific papers concerning new methods for PU synthesis and modification. It should be mentioned that until 1970 there were only

360 published papers on polyurethanes; at the period of time of 1971–1980 and 1981–1989 this amount increased three times (1083 publications) and c.a. six times (2035 publications), respectively. Polyurethane market increases every year too. The last report made by Grand View Research significantly shows the high demand for PU materials nowadays. As they have reported, PU market size in 2010 was above 33 billion USD, while in 2015 it increased to 53.94 billion USD with the potential to grow by 7 % from 2016 to 2025 [47].

Apart from the numerous advantages of PUs, they have lower resistance comparing to metals and ceramics. Moreover, they suffer from low electrical conductivity. These properties can be tuned due to the addition of polymer fillers, e.g. natural or synthetic fibers, powders, other micro- and nanoparticles. The addition of small amounts of CNTs to the PU matrix can provide electrical conductivity and mechanical reinforcement to these polymers [48, 49, 50, 51]. It was found that CNTs-based polyurethane composites were more resistant to wear than the pure PUs [52]. The incorporation of COOH-modified CNTs to PUs increases the thermal stability of the material with increasing the degradation temperature [44]. Moreover, SWCNT/PU composites are much more functional than basic PUs [5, 53] and have a plenty of possible applications as shape memory [12, 44, 54], or interference shielding materials [4]. New shape memory materials have the ability to deform at a transistory shape until receiving a special stimulus. Therefore, such hybrid composites can be used, for example, for stimulating cell growth and bone tissue regeneration in electrically conductive scaffold [55]. Additionally, electroactive shape memory materials based on PU/CNT have potential usage in actuators and artificial muscles [44]. Polyurethane composites with the addition of multiwalled carbon nanotubes were reported to have promising piezoresistive and large strain sensing capabilities [56, 57, 58].

There are four basic ways to produce a polymer based on polyurethanes and CNTs [19]:

- bulk mixing,
- melt mixing,
- solution processing,
- in situ polymerization.

The last two methods provides composites with better carbon nanotubes distribution in the polymer matrix. During the solution processing carbon nanotubes are dispersed in a solvent, polymer is dissoluted in the same solvent; material is made after mixing of the polymer with CNT proceeded with solvent evaporation. In situ polymerization is based on the reaction of the monomers or prepolymer in the presence of dispersed CNT. A standard procedure for PU/CNT synthesis using in situ polymerization is as follows [59]: CNTs are dispersed in polyol at room temperature with stirring for 1 h, then diisocyanates are added to the suspension and reacted with such modified nanotubes at 40° for 1 h. The procedure of PU synthesis depends on the polyurethane type and the scale of production [8, 53, 60, 61]. Some methods are more preferable for elastic PU, other for thermoplastic.

In contrast to the promising advantages of CNT-based composites, their applications are limited because of the lack of the interfacial adhesion between nanomaterial and polymer matrix. It prevents the efficient transfer of the CNT superb properties to the matrix [43]. Therefore, there are a lot of experimental investigations aimed to modify composite ingredients for the better enhance of the properties. Among them are different modifications of carbon-based filler, e.g. introducing functional groups or defects, which impact positively on the properties of the material. At the same time, there are no detailed descriptions of interactions and processes occuring in such modified composites; these data might help to solve the problem with low CNT dispersity. Thus, **the main challenge is to understand molecule-molecule in-**

teractions in the composite and to discover the effective way for the dispersion of carbon nanotubes in the polymer matrix without CNTs agglomeration [19].

Investigation of interactions between ingredients in the composite, using experimental techniques, is very complicated task. Additional analysis involving theoretical models is needed. Taking into account the size of the composite system used for theoretical calculations, the most commonly performed analysis is based on the classical molecular dynamics. Among the subjects of such studies were CNT/polymer composites based on epoxy polymer chains [62] poly(methyl methacrylate), poly(m-phenylene-vinylene)-co-[(2,5-dioctoxy-p-phenylene) vinylene] [63, 64], polystyrene [35, 65, 66] and poly(phenylacetylene) [35]. Classical molecular dynamics (MD) is complex method requiring parametrization techniques and approximations, but it gives a possibility to simulate the large fragments of the material, such as long large-diameter tubules or nanotube bundles [67]. Such calculations are based on the Newton equation and classical force fields, which do not include the electronic structure effects and bond breaking/formation. Therefore, this approach can not be used to analyze fundamental molecule-molecule interactions and specific bonding formation in the composite. However, classical MD was used to analyze the content (weight percent) of carbon nanotubes in the PU/CNT composite to achieve optimal increase in the elastic moduli of the composite [2]. MD simulations, described in the work of Zhao et al. [66], determined that the diffusion coefficient of polystyrene in CNTs decreases as the polymer chain length increases; moreover, this coefficient shows anisotropy with different CNT distances. Frankland et al. [68] investigated stress-strain curves of single-walled CNTs reinforced polyethylene matrix composites, while Han et al. [63] reported that, using CNTs there is a possibility for efficient mechanical reinforcement of polymer matrices by increasing the low strain elastic modulus, but in the tube longitudinal direction.

The theoretical approach capable to describe interactions in the modeled systems is based on the quantum mechanical calculations. This method is more expensive and implicate the application of more simplified models. For example, most static quantum calculations consider the non-defective carbon nanotubes with no pollution from amorphic carbon material or catalysts. As the result, it is necessary to accurately study various possible models of the materials taking into account the aims of research and the available computational resources. In the present PhD thesis, the advanced computational approach, which is Car–Parrinello molecular dynamics (CP–MD) simulations, is used. CP–MD have been proven to be in a good comparison with Born–Oppenheimer molecular dynamics [69, 70], which applies quantum-chemical methods to calculate energies and forces acting on atoms. Car–Parrinello MD simulations can be effectively used to provide the theoretical description of different types of interactions in the analyzed system. The limitation of this approach is the size of the modeled molecular system, which can not be larger than several hundreds of atoms. The detailed explanation of this limitation is described in Section 6.3.

The research made in this PhD thesis is based on model systems consisted of either monomers for polyurethane synthesis or single-walled carbon nanotubes. They are used to study non-covalent interations during CNT functionalization. Among PU monomers MDI and TDI diisocyanates are used, because they are known to be frequently used in the PU production industry [71] as the result of their higher reactivity in comparison to the aliphatic diisocyanates [42]. Polyethylene glycol (PEG) is used as a model of polyol. It is very hydrophilic and biocompatible polyol with the property to increase water permeability both in bulk and surface and to make polymer material more sensitive to degradation with non-toxic degradation products [72, 73]. Polyurethanes based on TDI and PEG were synthesised to be used as controlled drug delivery systems [74], while MDI and PEG based PUs as new shape memory materials [75].

The present PhD thesis consists of 12 chapters divided according the specific topic of the

research conducted. In the beginning (Chapter 1–6), the introduction to the topic of research, the description of the systems analyzed and methods used are given. The bases of the noncovalent interactions, their strength and impact on the properties of molecules, with the main focus on the hydrogen bonds and $\pi - \pi$ interactions are described in Chapter 3. The nature of the carbon nanotubes, their types, properties and modifications are presented in Chapter 4, where also the theoretical approaches used to treat CNT systems are explained. In the next chapter (Chapter 5), the chemical characteristics and the usage of two types of PU monomers: diisocyanates and polyols, are described. The last chapter of the theory part of the thesis (Chapter 6) focuses on the detailed description of theoretical approaches applied to accomplish the aims of the research undertaken within the framework of the present doctoral thesis.

The chapters, concerning the results and discussion of the research made, is proceeded by Chapter 7, where the computational parameters used and test calculations performed are explained. The research part of the thesis (Chapter 8–12) is divided into 10 sections and 19 subsections, where the results obtained are fully described, clarified and discussed. The chapters, sections and subsections mentioned are divided taking into account different research problems studied. In Chapter 8 the results of the gas-phase calculations, both static and dynamic, for diisocyanate molecules and polyethylene glycol are presented. Noncovalent and covalent functionalizations of the single-walled carbon nanotubes by the PU monomers are described in Chapter 9 and 10, respectively, with the detailed analysis of the noncovalent interactions, which are involved in these processes. The influence of the defective regions on the surface of carbon nanotubes on their electronic properties and the structural rearrangement of the molecules attached is presented in Chapter 11, where the carboxylation of the defective carbon nanotubes is also shown. Finally, in the Chapter 12, the conclusions of the research made are given.

Information about scientific articles published, which refer to the part of results described in the present dissertation, and participation in the conferences, where the results obtained were presented, is given in the preface sections.

Chapter 3

Noncovalent interactions

"There are [...] Agents in Nature able to make the particles of Bodies stick together by very strong Attractions."

Sir Isaac Newton, 1718

Atoms are linked together in a molecule due to common known bonds, namely covalent bonds. During the formation of such chemical bonds the *sharing* of electrons is taking place and the properties of the molecule formed can be significantly changed in comparison to the initial ingredients. One of the modification of the covalent bond is ionic bond, which is based on electrostatic attraction between oppositely charged ions, therefore, electrostatic attractions, but still there is a slight covalent character in ionic bonding, because there is no purely "ionic" compounds when one atom "gives" its electron to the other one. Due to the facts that ionic bonds are characterized with more ionic (polar) character than covalent one and ionic compounds have distinct properties that covalent ones, these two types of chemical bonds are classified as different types of bonding. Moreover, ionic bonds are often classified as noncovalent bonding (interaction). They are the strongest noncovalent interactions, which lie in the basis of milions of crystalline ionic compounds. Due to covalent and ionic bonds the *classical* molecules are formed, but molecular clusters and 3D structures of biomolecules, polymers etc. are made as the result of the interactions, which are far from covalent nature, but still the *sharing* of the electron density is taking place, but on extremely weaker level.

Noncovalent interactions are of great importance, what will be described later in the text, but most of them are very weak (several kJ/mol), so it is very hard to analyze them experimentally. They can be investigated with the usage of high level *ab initio* calculations, but there are still limitations based on the size of the molecular system analyzed and the computational cost of such calculations. One is definitely known is that there is a huge necessity to study these interactions, which are of great interest during the last decades.

3.1 What are they?

Noncovalent interactions (NCI) are specific type of interactions that are based on **electrostatic attractions**. Among them are interactions that can be either stronger than the covalent bonds (i.e. ionic bonds) or weaker than the dipole-dipole interactions (i.e. London dispersion interactions). The classification of noncovalent interactions is shown in Figure 3.1. P. Kollman wrote that "noncovalent interactions are those, in which *i)* electrons stay paired in reactants and products and *ii)* there is no change in the type of chemical bonding in reactants and products" [76]. Taking into account this definition, ionic bonds are not classified to these interactions. As the result, under the term ***noncovalent interactions*** the most important NCI, with the exception of ionic bonds, will be discussed in the present PhD thesis.

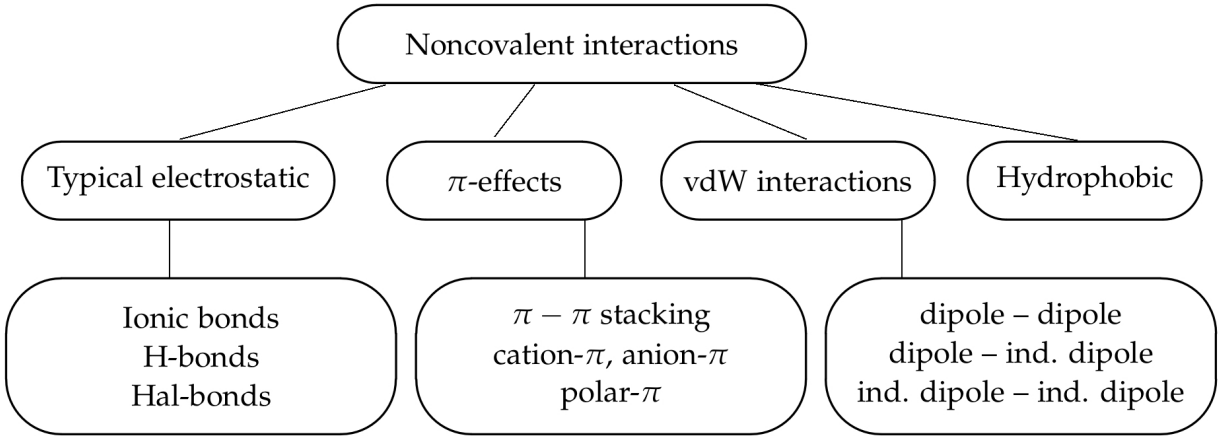

Figure 3.1: Classification of noncovalent interactions.

On the one hand, NCI do not influence the chemical bonding in the system, but on the other hand, they significantly influence the properties of the chemical compounds, e.g. boiling and melting points, vapour preassure etc. A good example of the system, which can be "changed" due to noncovalent interactions is free iodine: when it is dissolved in water, alcohol or other electron-pair donor solvents, the color of the solution is brown, but in the solvents with lower basicity (e.g. tetrachloride or benzene) – I_2 solution is violet or red-violet [77, 78]. The described feature of iodine is the result of the existence of NCI interactions between iodine and the solvent.

NCI are several times weaker than covalent bonds, but they are involved in the specific binding of ligands to proteins, formation of the 3D structures of biomolecules, self-assembly of molecules, synthesis of many organic molecules etc. They play a cruicial role in most of the chemical reactions known for human. In Figure 3.2 some examples of noncovalent interactions (listed in Figure 3.1), are depicted. The stabilization energy of NCI is based on electrostatic, induction, charge-transfer and dispersion contributions. The participation of these forces differs in different types of NCI. In general, the energy of NCI under ambient conditions is comparable to the average thermal energy of the kinetic motion of molecules, which means that even a comparatively strong noncovalent bond can be broken [79]. The strength of the NCI can be presented as follows:
***London dispersion interactions** < $\pi - \pi$ **stacking** < **dipole–dipole interactions** < **hydrogen bonding = halogen bonding** < **ionic forces**.*

Apart from the ionic bonds, which are the strongest noncovalent interactions, **hydrogen bondings (H-bondings/H-bonds)** are the second strongest NCI with the interaction energy in the range of 2–160 kJ/mol. H-bondings play an important role in the definition of characteristic properties of molecular systems. They are essential in the most chemical and biochemical processes, which take place in nature, for example the formation of the DNA (see Figure 3.2: b) or the properties of water, which is the most important solvent all over the world. Moreover, hydrogen bonding play a crucial role in the stabilization of the molecular system [80, 81, 82]. H-bond **X-H**$\cdots$**Y-Z** consists of a X-H hydrogen bond donor and Y-Z hydrogen bond acceptor. Different types of X and Y are involved into the hydrogen bond formation. More detailed description of H-bonding is presented in Section 3.2.

Among donor–acceptor interactions, which are similar to the hydrogen bonds, are **halogen bonds (Hal-bonds)**, **R-X**$\cdots$**Y**. They exist between electron-pair donor molecules R-X, where X is any halogen atom with electrophilic (electron-poor) region, and electron-rich halogen bond acceptor Y (Y = O, S, Se, N, π-system etc.), linked together by linear, halogen molecule

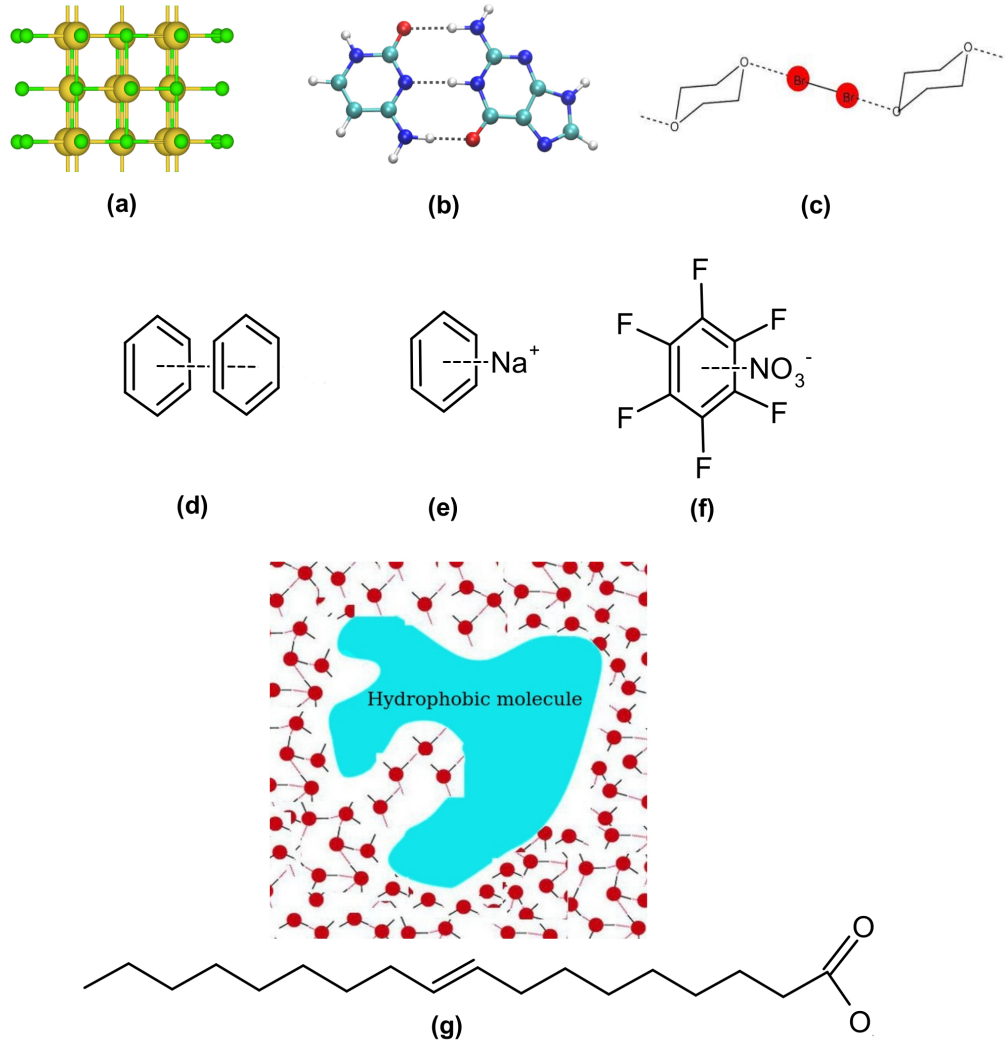

Figure 3.2: Different types of noncovalent interactions: (a) ionic bonds (sodium chloride), (b) hydrogen bonds (guanine cytosine base pair), (c) halogen bonds (bromine + 1,4-dioxane), (d) $\pi - \pi$ interactions (benzene molecules), (e) cation-π interactions, (f) anion-π interactions, (g) hydrophobic interactions (examplary molecule: oleic acid in water).

bridge [78]. R is a group covalently bonded to the halogen atom; it can be presented also by the halogen atom or another atom. List of the most common halogen bond donors and acceptors were published by IUPAC in 2013 [83]. Hal-bonds were discovered in 1954 by O. Hassel and J. Hvoslef [84] between molecular bromine and 1,4-dioxane (see Figure 3.2: c). Using X-ray diffraction technique they had noticed that O$\cdots$Br distance in crystal is 2.71 Å instead of 3.35 Å (the sum of the vdW radii of O and Br atoms). At the same time, the distance between two bromine atoms in Br_2 was slightly longer comparing to the gas-phase Br–Br distance (2.31 Å instead of 2.28 Å). They also reported that each bromine molecule interacts with two dioxane molecules via two O$\cdots$Br interactions, called as halogen bond since 1978 [85]. Halogen bonds have similar structural features as hydrogen bonds: they are specific and directional [83]. Moreover, the strength of Hal-bonds is similar to H-bonds – it varies in the range of 5–180 kJ/mol. Halogen bonds are formed mainly due to electrostatic forces, but polarization, charge transfer and dispersion are also involved [83]. Halogen bonds are of great importance, e.g. in liquid crystal formation, porous inclusion complexes and biological macromolecules, where they involved in the formation of specific structural motifs, protein-ligand interactions, molecular recognition and folding [86, 87, 88].

$\pi - \pi$ **interactions** or $\pi - \pi$ stacking [89] are a type of NCI that are characteristic for the molecular systems consisted with the aromatic rings, which contain π-bonds (see Figure 3.2: d–f). $\pi - \pi$ stacking interactions belong to the weak interactions, for example the interaction energy for benzene dimer is 8–19 kJ/mol [90]. It is very hard to analyze such weak type of interactions experimentally, but the preferred sites of the interaction between molecules that contain phenyl rings, are clearly seen from X-ray crystal structures [91, 92]. Among π interactions two types of more stronger interactions are known, i.e. cation–π and anion–π interactions. Their strength is comparable to the hydrogen bonding, e.g. *ab initio* calculations have shown that the interaction energy in Na^+–π system (see Figure 3.2: e) is c.a. 113.0 kJ/-mol [93]. All π-based NCI are important in many biological systems [94, 95] (e.g. DNA and RNA molecules, molecular recognition, drug design), as also in the organic synthesis and materials science [96, 97]. Due to the fact that some types of $\pi - \pi$ stacking interactions will be analyzed in the PhD thesis, they are discussed in Section 3.3.

van der Waals (vdW) interactions are among the weakest noncovalent interactions, which significantly depend on the distance between molecules and atoms: at the close distances (c.a. 0.2 nm) molecules (or atoms) repulse strongly, whereas at the distance c.a. 10 nm, the vdW attractive interactions completely disappear [98]. They are divided into several types depending on the nature of the interacting molecules: *i)* dipole – dipole interactions, *ii)* dipole – dipole induced interactions, *iii)* induced dipole – induced dipole interactions (London dispersion interactions). vdW interactions consist of repulsive and attractive contributions, as also of polarization and dispersion. Polarization is a key ability of molecules to form temporary dipoles; it is a base of Debye forces (i.e. dipole – dipole induced interactions). London dispersion interactions, of the strength of several kJ/mol, but they are present in all atoms and molecules [98] (they are also present in the examplary systems depicted in Figure 3.2). They are important especially for non-polar systems, see Section 3.3. London dispersion interactions can be explained as, e.g., follows: during the collision of two molecules, the "electron cloud" of the first molecule repulses the "electron cloud" of the second molecule, which causes the displacement of the electron density and the formation of some local differences of the distribution of the electron density away from the nucleus. This change induces small dipole moments in these molecules, which are responsible for the weak dispersion interactions.

The last type of noncovalent interactions are **hydrophobic interactions**. They exist between nonpolar molecules (like Figure 3.2: g) during their mutual aggregation in the polar environment, e.g. in aqueous solutions of low-molecular organic substances. They are the driving forces for the specific association of nonpolar molecules or groups (for example hydrocarbon groups) in polar solvents, therefore, they prevent the dissolution of nonpolar molecules in water. The association process of nonpolar groups is based on entropy effects. The energy of the hydrophobic interactions is directly connected to the length of the carbon chain of hydrocarbons and structure of liquid water [79].

Several types of noncovalent interactions will be investigated in the present PhD thesis, as a result, more detailed description of them is given in the next sections.

3.2 Hydrogen bonding

The first definition of the hydrogen bond was presented by Linus Pauling in 1931, who stated that *"...under certain conditions an atom of hydrogen is attracted by rather strong forces to two atoms, instead of only one, so that it may be considered to be acting as a bond between them"* [99, 100]. Since then, the enormous amount of investigations concerning H-bonds was made and several corrections to the mentioned definition were presented [101, 102, 103, 104, 105, 106, 107, 108]. According to the Pauling definition, some types of H-bonds should not exist, for example

C-H$\cdots$O or weak interactions, where hydrogen bond donor consists of C-H, P-H or As-H groups or hydrogen bond acceptor is associated with the π-electrons. Instead of it, the mentioned hydrogen bonds exist and were confirmed both experimentally [109, 110, 111, 112] and theoretically [113, 114, 115, 116, 117]. To unify the general understanding of the hydrogen bonding, International Union of Pure and Applied Chemistry (IUPAC) reported its new definition in 2011:
"*the hydrogen bond* is an attractive interaction between a hydrogen atom from a molecule or a molecular fragment X-H, in which X is more electronegative than H, and an atom or a group of atoms in the same or a different molecule, in which there is evidence of bond formation" [118].
Taking into account this definition, hydrogen bonds X-H$\cdots$Y-Z can exist between either several molecules or in one molecule. The first mentioned hydrogen bonds are known as intermolecular H-bonds, while the second ones are classified as intramolecular H-bonds.

IUPAC definition of the hydrogen bond [118] is also supported by the list of the required criteria, which should be filfilled to classify the considered system to the hydrogen bonded one. The criteria list starts from the origin of the forces in the hydrogen bonds, which may be classified as electrostatics, charge transfer or dispersion. Other criteria refer to their structural and spectroscopic properties. Among the most important structural parameters of the H-bond are *(i)* the distance (H$\cdots$Y) between the H atom and the H-bond acceptor, *(ii)* change of the distance (X-H) of the H-bond donor and *(iii)* the valence angle (X-H-Y) between hydrogen bond donor X-H and an acceptor Y-Z, which are shown in Figure 3.3. Figure 3.3 contains also different types of hydrogen bond donors and acceptors that participate in the formation H-bonding.

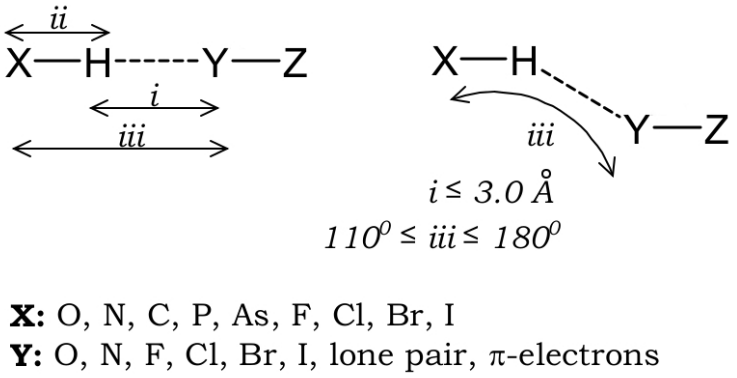

Figure 3.3: Typical model of hydrogen bonding. The explanation of *i, ii iii* is given in the text.

The appropriate H-bond distance can be obtained experimentally using the neutron diffraction experiment, which belongs to the expensive experimental techniques that can be made only in several laboratories worldwide. Therefore, one of the best tools to estimate the the interatomic distances for H-bonds nowadays are *ab initio* calculations. Quantum chemistry calculations enable not only the precise measurement of the structural properties of molecular systems, but also can show changes of the interatomic distances in the molecule of the H-bond donor and acceptor after the H-bond formation. Moreover, with the usage of *ab initio* molecular dynamics the H-bond breaking/formation and a lifetime of certain hydrogen bond can be estimated. Such information is hardly accessible by the experimental techniques, so the usage of the theoretical methods is extremely important. In general, H$\cdots$Y distance should be less that 3.0 Å to classify the interaction as the H-bond.

As it was mentioned in the definition of the hydrogen bond, it is the noncovalent interaction

(X-H$\cdots$Y-Z) originated from the approach of a hydrogen bond donor X-H toward an acceptor Y-Z. The role of the acceptor of H-bond can play an atom, an anion or a fragment of the molecule, which is an electron rich region. Depending on the H-bond donor and acceptor, the elongation [105, 104] or shortening [119, 120, 121] of the covalent donating X-H bond are possible, which are connected (respectively) with red or blue shift of the stretching vibration of the proton donor. As the result, we distinguish red-shifted and blue-shifting hydrogen bonds. The strongest hydrogen bond, the highest is the change of the hydrogen bond donor X-H length. Due to this change of the X-H length, the spectroscopic methods, e.g vibrational spectroscopy, can be used to estimate the strenght of the H-bond.

Sometimes H$\cdots$Y distance between the hydrogen atom and a H-bond acceptor is in the range of a typical hydrogen bond (1.8–3.0 Å), but the X-H-Y valence angle between hydrogen bond donor X-H and an acceptor Y-Z is too low to classify the interaction to H-bonding. This means that there is no directionality of such an interation, which should be fulfilled to enable the H-bond formation. Accordind to IUPAC definition [118], the X-H-Y valence angle of the hydrogen bond should be in the range of 110–180°, while the strongest types of H-bonds are characterized with the high directionality (close to 180°).

All mentioned structural criteria of the H-bonding are correlated with both inter- and intramolecular hydrogen bonds [122, 123]. They also influence the strength of the intermolecular hydrogen bonds [124], which can be estimated also with the usage experimental (e.g. vibrational spectroscopy [125, 126, 127], UV-UV and IR-UV double-resonance spectroscopy [128], terahertz laser spectroscopy [129], nuclear magnetic resonance [130]) and theoretical methods (e.g. post-HF method and density functional theory [114, 131, 132, 133]). The strength of the hydrogen bonds varies from very weak H-bonds [134, 135, 136], which are of the strength of van der Waals interactions, to very strong ones, known as resonance-assisted H-bonds [104, 106, 105, 117, 137]. The total strength of hydrogen bonds can be higher that the contribution of each H-bond in the system. This specific phenomenon of hydrogen bonds is known as cooperativity, which leads to extreme changes in the macroscopic properties of various molecular system, e.g. water.

3.3 π-effects

Noncovalent interactions based on π-effects are characteristic for the systems which possess aromatic ring with π-electrons. Among such types of NCI are $\pi-\pi$ interactions, cation-π and anion-π systems (see Figure 3.2: d–f). Taking into account maximum overlap of two aromatic rings, therefore, maximum dispersion interactions, it was believed that sandwich structure of benzene dimer (see Figure 3.4: a) is the most stable one. In 1990 the first model of $\pi-\pi$ interactions was reported by C. Hunter and J. Sanders during the detailed analysis of the porphyrin systems [91]. They stated that "$\pi-\pi$ interactions are not due to an attractive electronic interaction between the two π-systems but occur when the attractive interactions between π-electrons and the σ-framework outweigh unfavorable contributions such as π-electron repulsion". As a result, C. Hunter and J. Sanders proposed a model of $\pi-\pi$ interactions as positively charged σ-framework sandwiched between the two negatively charged π-electron cloud. They explained that π-electron system, e.g. in benzene dimer, is influenced by the quadrupole–quadrupole and London dispersion interactions. Quadrupole–quadrupole interactions makes the distribution of the charges in the benzene ring in the way that positive charge is localized on the carbon atoms in the ring, while negative charge is smeared on the electron cloud above and below the aromatic ring. Therefore, the structure of benzene dimer, when two benzene rings are located in parallel position with respect to each other (sandwich structure, see Figure 3.4: a), is not the most stable one, because in such orientation the negative charges, located on the electron cloud of

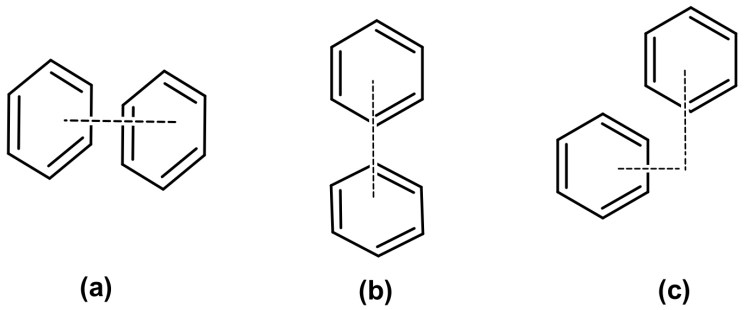

Figure 3.4: Selected configurations of benzene dimer: (a) sandwich (S), T–shaped (T), parallel-displaced (PD).

benzene molecules, repulse destabilizing the system. The parallel displaced and T-shaped structures of benzene dimer (Figure 3.4: b, c) were proven to be the most stable ones, because they enable the most effective energy gain on the basis of quadrupole–quadrupole and London dispersion interactions. The existence of the parallel displaced and T-shaped structures of benzene dimer was shown during molecular beam electric resonance [138], rotational spectroscopy [139] and X-ray diffration analyses [92]. High-accuracy quantum mechanics studies (CCSD(T)/CBS) of benzene dimer confirm the isoenergetic character of parallel displaced and T-shaped structures [90] with the interaction energy varing in the range of 8–19 kJ/mol, depending on the level of theory and basis set used.

Taking into account the existence of negatively charged electron cloud on the benzene ring, interactions with positively charged atoms or parts of molecules can be possible. The common known example of such type of cation–π interactions is presented by the sodium cation complex with benzene (see Figure 3.2: e). The strength of such NCI are comparable to the hydrogen bonded systems, e.g. *ab initio* calculations have shown that the interaction energy in Na^+–π system is c.a. 113.0 kJ/mol [93]. This NCI strongly depends on the cation type and the nature of substituents of the phenyl ring. Smaller cations with larger charge density and electron donating substituents of the phenyl ring increase the interation energy, whereas cations with larger ionic radius and electron withdrawing groups make the interaction weaker. Interactions between transition metals and π-systems are not classified to NCI, because they involve sharing of electron density with π-systems, as the result they are more covalent in their nature. Interactions in anion–π systems are possible due to the change of the quadrupole moment located on the phenyl ring as the result of the introducing electron withdrawing substituents into the π system of the benzene ring, e.g. fluorine groups (hexafluorobenzene), Figure 3.2: f. The detailed description of the substituent effects on the NCI interactions of π-system was reported in Ref. [90, 140]. It should be noted that systems with anion-π interactions are not widespread in nature, but they can be successfully synthesized and used, for example in chemical sensing [141].

$\pi - \pi$ interactions play a significant role in defining the structure and properties of different molecular structures, but theoretical calculations presented by S. Grimme in 2008 [89] have shown that the interaction energies in aromatic and saturated dimers are similar, what indicates the slight role of known "$\pi - \pi$ interactions". He also mentioned that real $\pi - \pi$ interactions exist in the aromatic dimers with more that 10–15 carbon atoms in the monomer. Therefore, S. Grimme suggested "not to overestimate the effect of the π system", especially in the process of stacking nucleobases. Additionally, P. Hobza et al. [79] stated that effects of H-bonds in the stabilization of the structure of nucleobases in DNA is higher than the $\pi - \pi$ stacking. Investigations concerning π-interactions are still performed and, due to the development of novel computational algorithms, they are precisely analyzed.

3.4 Theoretical investigation of noncovalent interactions

Noncovalent interactions can be analyzed using different quantum chemistry methods, but the greatest problem of such calculations is the treatment of London dispersion interactions. As it was mentioned, dispersion interactions are in all particles and they are caused by instantaneous multipole/induced multipole charge fluctuations [90], therefore, Hartree–Fock method, which calculate the motion of electrons in their average field of other electrons, are not able to treat temporary fluctuations. Pure density functional theory (DFT) calculations have the same problem, but due to additional dispersion corrections (Grimme D2 [142], Grimme D3 [143], Tkatchenko–Scheffler [144] etc.) or specially designed pseudopotentials (e.g. Dispersion-Corrected Atom-Centered Potentials, DCACP [145, 146]) this problem have been partially solved [147, 148]. Additionally, second-order Møller–Plesset perturbation theory (MP2), which is known to take into account dispersion interactions, was shown to overestimate the binding energy of NCI [149].

The most accurate method for dispersion interactions is coupled-cluster with single and double and perturbative triple excitations, known as *"a golden standard"* in quantum chemistry, CCSD(T). Unfortunately, CCSD(T) can not be used for systems consisted of more than 50 atoms [150], because such calculations are very expensive computationally and need a lot of time. K. Riley and P. Hobza [150] reported that NCI interactions, especially in larger biomolecules, can be analyzed using symmetry-adapted perturbation technique (SAPT)[151], together with the combination with DFT (DFT–SAPT), and semiempirical quantum chemical parameterized model 6 method, known as PM6, with empirical parts for dispersion and hydrogen bonding energies. In the research conducted in the present thesis dispersion-corrected DFT method (see Section 6.2) will be used to obtain noncovalent interactions during the functionalization of carbon nanotubes.

Apart from the computational methods, used to calculate such properties of molecular systems as energy and geometry, are additional approaches used to analyze qualitatively and quantitatively specific noncovalent interactions, for example hydrogen bonds, on the basis of the electron density analysis. Among such approaches are Electron Localization Function (ELF), Quantum Theory of Atoms in Molecules (QTAIM) and Noncovalent Interaction Index (NCI index).

3.4.1 Quantum Theory of Atoms in Molecules

Quantum Theory of Atoms in Molecules (QTAIM) was proposed by R. Bader in 1990 [152]. It is often used to investigate different intra- and intermolecular interactions. According to the Bader theory, a bond or interaction between two atoms can be characterized by the properties of the electron density in a special point known as the bond critical point (BCP). BCP means a saddle point in the electron density surface between these interacting atoms. Therefore, using the value of the electron density or Laplacian of the electron density, located at the bond critical point, the interaction can be defined. Different systems can be analyzed used QTAIM, e.g., molecules, ions, ionic pairs, complex systems, biomolecules and crystals [153, 154]. In most cases, QTAIM is used to analyze hydrogen bonded systems [114, 123, 153, 155, 156, 157, 158].

In general, electron density ρ can be considered as multivariable function of three space coordinates, (x, y, z), which gives the probability distribution of the average electron charge in the real space. If the value of the electron density is more than the established "minimum", the specific bond (interaction) between atoms is formed. These specific bonds are known as critical points, where the electron density is measured. According to the criteria of U. Koch and P. Popelier [159], the hydrogen bond exists if the value of the electron density in BCP is in the range of 0.002 to 0.034 a.u. Higher values of the electron density correspond to

covalent bonds formation. It should be noted that critical points might describe saddle points or the local minima; they are distinguished using the second derivatives of the electron density [153]. Laplacian of the electron density:

$$\nabla^2\rho(r) = \frac{\partial^2\rho}{dx'^2} + \frac{\partial^2\rho}{dy'^2} + \frac{\partial^2\rho}{dz'^2} = \lambda_1 + \lambda_2 + \lambda_3 \tag{3.1}$$

is obtained after the diagonalization of the Hessian matrix, which consists of nine second derivatives of the electron density, via unitary transformation. x', y', z' correspond to new coordinates, because the unitary transformation of the Hessian matrix can be understood as the rotation of the previously suggested coordinate system [153].

Together with the value of the electron density at the bond critical point, Laplacian of the electron density is used to analyze quantitatively hydrogen bonds: Laplacian of the electron density should be in the range of 0.024–0.139 a.u. [159]. Laplacian possesses negative values when covalent and polarized bonds are formed. Therefore, even the sign of the Laplacian indicates the type of the interaction in the system. Additionally, the formation of the ring critical points, corresponding to the situation when "valley between mountains as the place situated at the lowest height" [153], are possible.

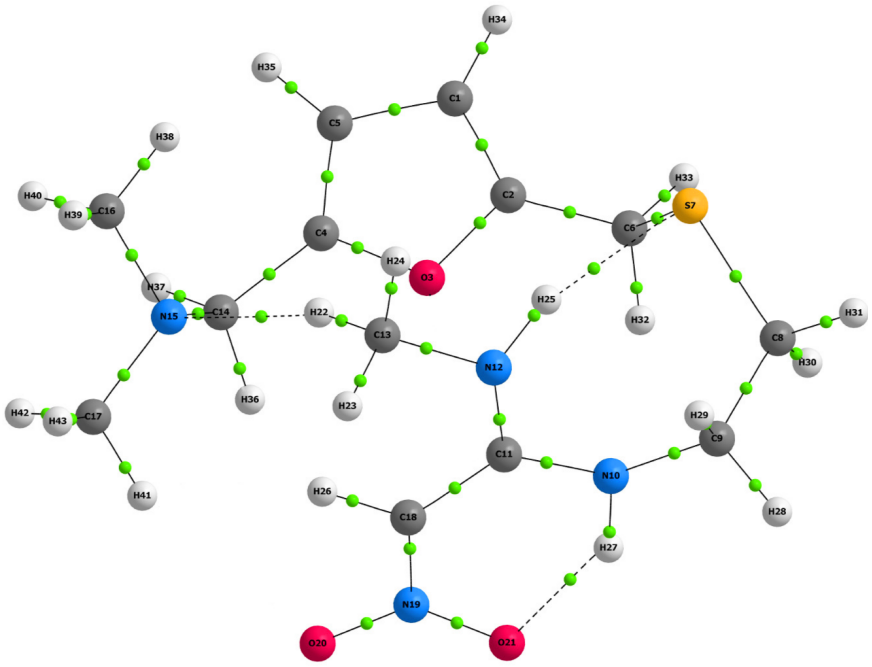

Figure 3.5: The structure of the ranitidine molecule with the bond critical points obtained using the Quantum Theory of Atoms in Molecules [160]. Carbon atoms are marked in grey, hydrogen atoms are white, oxygen atoms are red, nitrogen atoms are blue, sulfur atom is orange. Bond critical points are marked as green balls. Hydrogen bonds are marked with dashed lines.

The examplary analysis of the hydrogen bonds using QTAIM is depicted in Figure 3.5, where the structure of the local minimum of the ranitidine molecule, with corresponding BCPs of hydrogen and covalent bonds, is shown. The values of the electron density and its Laplacian in the H-bonds BCPs are listed in Ref. [158].

3.4.2 Noncovalent Interaction Index

Additional approach, created to detect noncovalent interactions in real space, is Noncovalent Interaction index (NCI index) [161, 162]. NCI index is able to analyze different types

of noncovalent interactions, including attractive forces, like hydrogen bonds or vdW interactions, and repulsive interactions [163]. For this purpose NCI index uses electron density and its derivatives, as it was described for the QTAIM method (Section 3.4.1), but this tool provides also three–dimensional regions around bond critical points. Similarly as for QTAIM, electron density is obtained using quantum-mechanical calculations, e.g. using density functional theory calculations, later the electon density of the whole system is analyzed using specially designed program NCIPLOT [162].

It was reported that a fundamental dimensionless quantity, used to analyze the changes of the electron density in density functional theory, is reduced density gradient s [161], which is originated from the electron density and its first derivative:

$$s = \frac{1}{2(3\pi^2)^{1/3}} \cdot \frac{|\nabla\rho|}{\rho^{4/3}} \tag{3.2}$$

The reduced density gradient has very large positive values, when the electron density is decaying (e.g. regions far away from the molecule). If the electron density is very high (e.g. near nuclei), the reduced gradient is going to zero. The detailed dependencies between ρ and s were reported in Ref. [161]. NCI index uses the values of the reduced density gradient s as a function of the sign of the second eigenvalue (λ_2, see equation 3.1) of the electron-density Hessian, which is the second derivative of ρ. This dependency is shown in Figure 3.6. In

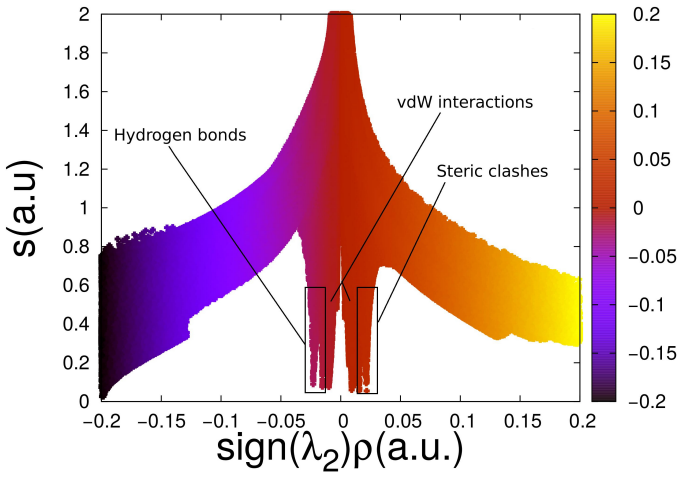

Figure 3.6: Analysis of noncovalent interactions using NCI index implemented in NCIPLOT program [162]: plot of the electron density and its reduced gradient for diclofenac global minimum, reported in Ref. [164].

general, the sign of the Laplacian of the electron density (Equation 3.1) is used to analyze the concentration ($\nabla^2\rho < 0$) or depletion ($\nabla^2\rho > 0$) of ρ at the point, e.g. BCP, but it is impossible to estimate the contribution of different noncovalent interactions basing on $\nabla^2\rho$, because of the greatest contribution coming from covalent bonds. That is why, λ_2, which sign depends on the interaction type, was chosen to characterize the type of NCI in the system analyzed. Negative sign of λ_2 indicates the attractive interactions (violet/red areas in Figure 3.6), whereas positive sign is characteristic for the repulsive forces (orange areas in Figure 3.6).

The signatures of the NCI interactions in the NCI plots are spikes in the low-density, low-gradient regions (see Figure 3.6). The strength of the particular type of NCI can be estimated using the NCI parameters in these spikes. Firstly, if the value of s is closer to zero, the density is higher at this point. Secondly, the values of the electron density (see X–axis in Figure 3.6) in the range of $0.005 < \rho < 0.05$ a.u. indicate strong noncovalent interactions. This

means that strong attractive interactions, such as H-bonds, will have negative values of λ_2 (ρ > -0.05 a.u.), while repulsion forces, steric clashes, will be signed with posivive λ_2, e.g. ρ < 0.05 a.u. NCI surfaces with very low density values (ρ < 0.005 a.u.) show the existence of weak vdW, including dispersion interactions.

As a conclusion, it should be noted that noncovalent interactions are characterized with low electron density and reduced gradient values on the gradient isosurfaces of NCI index. The type of NCI interaction is indicated by the sign of λ_2, while the density value, ρ, divides the NCI interactions onto strong or weak ones. NCI approach can be successfully used to analyze different molecules, including larger biomolecules, which makes it a valuable tool in modern computational chemistry.

Chapter 4

Carbon nanotubes

Japanese electron microscopist Sumio Iijima is known to be the first to report a new fullerence-related structures, consisted of tiny cylinders of graphite closed at each end by caps containing six pentagonal rings, in 1991 [165]. He mentioned these structures as "these molecular carbon fibres", which were noticed at the cathode during electric arc experiments to produce fullerenes. Now these carbon structures are known as carbon nanotubes (CNTs), because their structure reminds the tube or cylinder shape. The mentioned Iijima's report concerned multi-walled carbon nanotubes, which are described in Subsection 4.1. After their *discovery*, there was reported a fact that carbon nanotubes where observed at early 1953, when Davis et al. [166] described very similar thread-like structures from the reaction of carbon monoxide and Fe_3O_4 at 450° on the surface of firebricks. A letter in Nature in October 1992 [167], on the one hand, confirmed that nanotubes could have been observed at early 1953 [166] with words "as fullerenes are now known to be produced in sooting flames, it is not unreasonable to think that the structures produced by Davis et al. might have been nanotubes", but, on the other hand, said that the photos published in 1953 can not confirm unambiguously this fact. Later, the structures shown by Gibson were reported to be quite different ones comparing with carbon nanotubes [168, 169], because they were mostly bent or coiled instead of straight and hollow.

Another controversial fact of the *discovery* of carbon nanotubes was discussed by H. P. Boehm in 1997 [170] and M. Monthioux and V. L. Kuznetsov in 2006 [171]. They noted that the first electron micrographs, which show tubular carbon filaments, were reported by L. V. Radushkevich and V. M. Lukyanovich in 1952 [172], therefore, they should be considered as **the first discoverers of carbon nanotubes**. M. Monthioux and V. L. Kuznetsov gave a special focus on the fact that the paper published in 1952 was in Russian, published in Russian journal and during the Cold War, so their work was not noticed. In their *historical* paper L. V. Radushkevich and V. M. Lukyanovich described new carbon structures found in soot during the decomposition of carbon monoxide at 600° on iron surface [172]. They also presented other possible metal catalysts, which can be used to obtain these strange "vermicular" structures, proposed possible mechanism of their formation and introduced methods for their purification. The reported method of synthesis of these tubular carbon structures reminds chemical vapor deposition, which is among methods of CNT synthesis used nowadays.

Since 1952 till 1991 there were several reports published suggesting the formation of the carbon tubular structures during arc discharge [173, 174]. But only better sample preparation by Iijima (more perfect carbon structures without catalyst contamination) allowed the fact of CNT existence was finally confirmed. The *problem* with the real explorer of CNTs, namely multi-walled CNTs, impact the fact that no Noble Prize was given for their discovery, albeit Iijima's work is the most known in the literature.

Investigations concerning the usage of carbon nanotubes developed rapidly and still CNTs remain to be popular and interesting topic for various purposes worldwide. It can be clearly seen in Figure 2.1 from Introduction section. Their high popularity is caused by their extraordinary properties originated from the specific structure. In this chapter the description of the structural features of carbon nanotubes and an overview of their electronic, mechanical, optical and thermal properties are given. The most common types of CNT functionalization are presented with the explanation of possible theoretical approaches used for CNT calculations and simulations.

4.1 Structure and properties

Carbon is an extraordinary type of atom: it is interconnecting with other carbon atoms with different covalent bonds revealing to specific structures with significantly various properties. Among widely known carbon allotropes abundant in nature are amorphous carbon, graphite and diamond. The last one is known as the hardest substance, the one before last is one of the softest substance, whereas the first one is a non-crystalline form of carbon. Several decades ago the group of carbon allotropes was expanded to new forms of this chemical element, namely carbyne [175], fullerenes [176], carbon nanotubes (CNTs), carbon nanofoam [177] and glassy carbon [178]. All these new structures of carbon opened a new "era" in carbon-based materials with wide range of possible applications.

Carbon nanotubes, which are the subject of the present PhD thesis, consist of sp^2 hybridized carbon atoms organized in the benzene-type hexagonal network, which form one-atom-thick sheets of carbon (known as graphene), rolled into a tubule form with end seamless caps. The structure of the sidewall surface of carbon nanotubes is of cylindrical shape, what can be seen in Figure 4.1. Atomically-perfect *ideal* carbon nanotubes are known to possess the unique

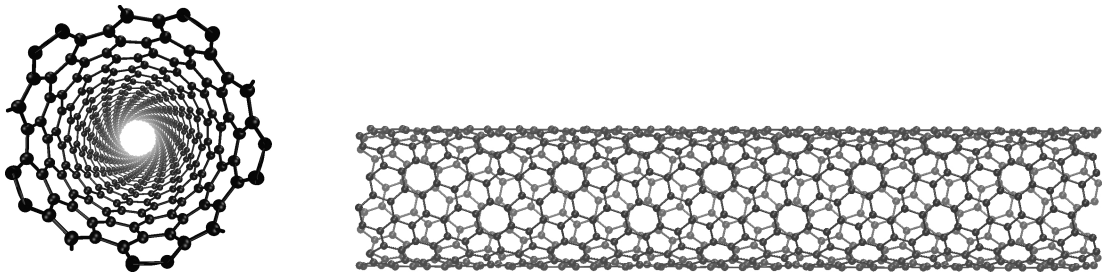

Figure 4.1: The cylindrical structure of single-walled carbon nanotube: (a) top view (perspective mode), (b) side view (orthographic mode).

properties: electronic, mechanical, thermal, optical etc., which come from the high ratio of the CNT length-to-diameter. The length of the carbon nanotube can reach even several micrometers, while its diameter is in the range of 1–50 nm [179], depending on the carbon nanotube type and synthesis. The length-to-diameter ratio for carbon nanotubes normally exceed 10 000, while in the case of ultralong CNTs the ratio is even 132 000 000 [180]. The second reason of characteristic CNT properties is their chirality, which is described in detail in Subsection 4.1.1.

4.1.1 Structure

Carbon nanotubes are cylindrical structures, which can exist as one layer, i.e. single-walled, or several layers, i.e. multi-walled, nanotubes. Figure 4.1 and Figure 4.2 represent models of single-walled carbon nanotube (SWCNT) and multi-walled carbon nanotube (MWCNT),

respectively. Carbon nanotubes reported by Iijima (and others before 1991) were of multi-

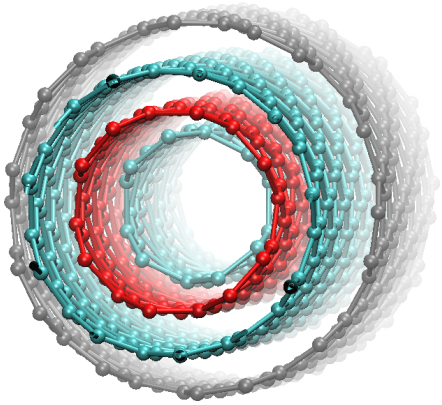

Figure 4.2: Model of multi-walled carbon nanotube.

walled type with the inner diameter of 4 nm [165]. The formation of SWCNTs was introduced in 1993 simultaneously by two groups (Japanese and American) [181, 182], during failed attempts to synthesize MWCNTs filled with transition metals. Among CNTs with specific features are also double-walled CNTs (DWCNTs) with two layers of graphene rolled into a nanotube [183]. It is considered that the minimal diameter of a CNT is that for a fullerene C_{60} [184], approximately 0.7 nm. Single-walled carbon nanotubes synthesized by Bethune et al. [182] had diameter of c.a. 1.2 nm, while Iijima [181] reported SWCNTs with diameters in the range of c.a. 0.7–1.6 nm with the average diameter of 1.05 nm. Multi-walled CNTs are characterized with the inner diameter in the range of c.a. 1.5–15.0 nm and the outer diameter of 2.5–30.0 nm. As one would expect, different types of CNTs are obtained in different synthesis procedures, therefore, they possess different properties, for example, SWCNTs are formed at higher temperatures, c.a. 900–1200°, while MWCNTs are synthesized at c.a. 500–700° [185].

The structural differences between SWCNTs, DWCNTs and MWCNTs can be analyzed performing different measurements. Among the most valuable technique to analyze carbon nanotubes is transmission electron microscopy (TEM), which enables to see the characteric CNTs structural features and estimate their purity. Figure 4.3 is an examplary TEM image, representing different types of carbon nanotubes.

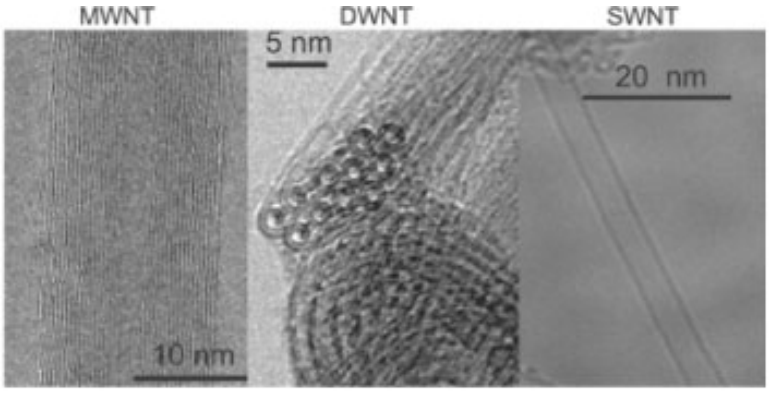

Figure 4.3: TEM images of multi-, double- and single-walled carbon nanotubes (labeled by author as MWNT, DWNT, SWNT, respectively). Data collected on the Creative Commons Attribution-ShareAlike License from Wikimedia Commons [186].

Different ways of graphene rolling up into a nanotube, i.e. arrangement of hexagons around the circumference, are possible. Therefore, CNTs are distinguished as either high-symmetry structures, zigzag and armchair CNTs, or chiral CNTs with helically structure around the tube axis. In his *historical* paper [165] Iijima reported that carbon nanotubes are prone to grow in a helical manner as they have a repetitive step at the growing edge. This suggests the helical CNTs, i.e. chiral ones, are more likely to be synthesized than zigzag and armchair ones, which require the repeated nucleation of a new ring of hexagons. Nowadays, chiral carbon nanotubes are believed to be the most commonly formed. It should be also noted that in most cases the CNTs synthesized are the mixture of different types and chiralities. Three main structural motifs of chiral and achiral (zigzag and armchair) CNTs are shown in Figure 4.4.

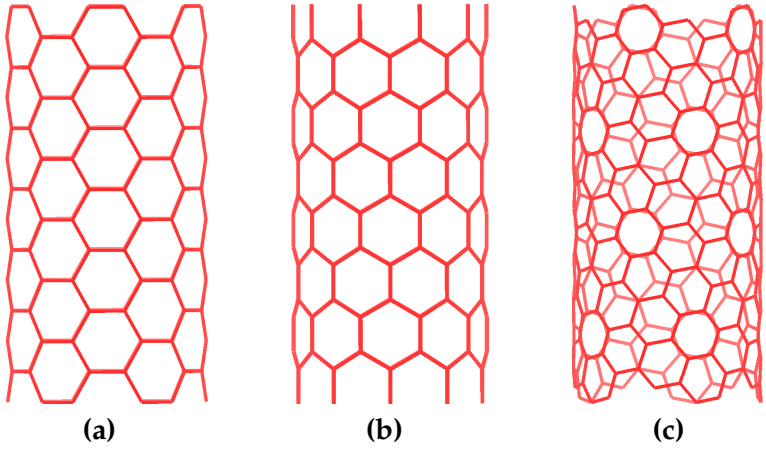

Figure 4.4: Types of the chirality of carbon nanotubes: (a) armchair CNT(6,6), (b) zigzag CNT(10,0) and (c) chiral CNT(5,10).

The structure of carbon nanotube can be defined as vector C, which links together two equivalent points of the graphene lattice and can be defined as:

$$C = na_1 + ma_2, \tag{4.1}$$

where a_1 and a_2 are the unit cell base vectors of the graphene sheet, n and m are integers used to index each SWCNT [187]. The mentioned vector C is shown with red color in Figure 4.5. It can be considered that every CNT is defined by this vector, which needs to map only two

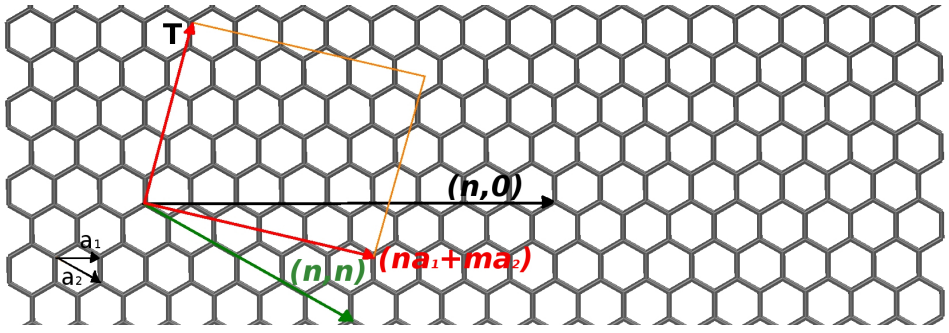

Figure 4.5: The ways of rolling up the graphene sheet to form carbon nanotube of certain chirality. Zigzag carbon nanotube (colored in black) is formed when m=0; armchair carbon nanotube (colored in green) is formed when m=n. Chiral nanotube (colored in red) is formed when n and m are different and form a vector as a sum of the unit vectors a_1 and a_2 of graphene in real space multiplied by the number n and m, respectively. T is a nanotube axis.

atoms onto the surface of a cylinder of a specific radius. Later, using the rotational and helical symmetry operators are used to estimate the remainder atoms of a tube [187]. Therefore, on the basis of different (n,m) integer pairs and wrapping angles, one can define the exact type of SWCNT structure. The armchair SWCNT is constructed when $n = m$ and wrapping angle is 30° [188]. Zigzag structures are formed when $m = 0$, therefore the wrapping angle is 0°. In all other cases chiral SWCNTs are produced. For the detailed *(n,m)* integer pairs and CNTs formed see Figure 4.5.

On the basis of the *(n,m)* integer pair the radius of carbon nanotube can be calculated [184]. Taking into account that a_0 is the carbon-carbon bond length (approximately is 1.42 Å), the CNT radius is:

$$R = a_0 \cdot \frac{\sqrt{3(n^2 + m^2 + nm)}}{2\pi}. \tag{4.2}$$

As a result, the theoretical radius of a zigzag SWCNT(n,0) is:

$$R = \frac{a_0}{2\pi} \cdot \sqrt{3}n = 0.392n \tag{4.3}$$

and armchair SWCNT (n,n) is:

$$R = \frac{a_0}{2\pi} \cdot 3n = 0.678n. \tag{4.4}$$

Chirality of carbon nanotubes significantly influences on their properties, especially on electronic ones. Theoretical calculations predicted that nanotubes are metallic, when $n = m$ or $(n - m) = 3q$, where q is an integer. In all other cases SWCNTs are a moderate-band-gap semiconductors [187] with an energy gap of c.a. 0.5 eV [189]. This means that all armchair SWCNTs are metallic, while zigzag and chiral nanotubes are either metallic or semiconducting. There are also exceptions, but both chiral and achiral CNTs with $(n - m) \neq 3q$ have band gaps inversely proportional to their radius. The differences between metallic and semiconducting CNTs enable to separate carbon nanotubes of a specific chirality using current-based methods [190], annealing treatment [191], dielectrophoresis [192], physisorption [193, 194] or covalent functionalization [195]. It is known that metallic single-walled CNTs can be more reactive than semiconducting ones [193, 196]. It was also reported that metallic SWCNTs of diameter less than 1.1 nm are destroyed by some oxidation treatments [197], whereas semiconducting ones stay stable. More detailed description of the electronic properties of CNTs is given in Subsection 4.1.2.

All structural properties of CNTs disscussed before, describe *perfect* carbon nanotubes. In practice, it is very hard to obtain such structures, because of very complicated synthesis procedures at high temperatures and with the usage of catalyst particles (see Section 4.3). Therefore, carbon nanotubes synthesized are characterized with additional defective regions on their surface. J.-C. Charlier classifies possible CNT defective structures into four main parts: 1) topological, 2) rehybridization, 3) incomplete bonding and 4) doping with other elements than carbon [198]. Topological defective structures are formed when rings other than hexagonal are introduced. Rehybridization is based on the ability of the carbon atom to hybridize between sp^2 and sp^3. Incomplete bonding are known as vacancies, dislocations etc. An examplary vacancy and divacancy defects on the carbon nanotube surface are shown in Figure 4.6.

Among widely known defects in the sidewall of the carbon nanotubes are:

- abrupt elbow-like bends [199],
- pentagon-heptagon pairs, known as 5-7-7-5 defect [198, 200],
- vacancy and divacancy [198, 201],

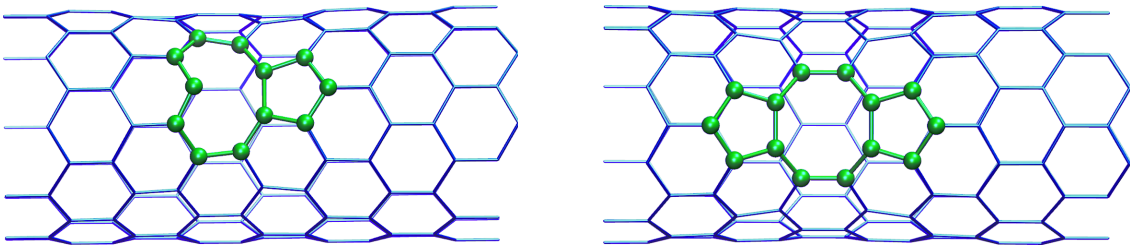

(a) (b)

Figure 4.6: The structure of the sidewall of the carbon nanotube: (a) vacancy-defective SWCNT, (b) divacancy-defective SWCNT.

- adatoms,
- Stone-Wales defect etc.

Elbow-like bends are formed when armchair CNTs are joined to zigzag ones by elbow connections making pentagonal and heptagonal rings on the outer and inner side of the elbow, respectively. The juction of carbon nanotubes, which cause an elbow-like bend is depicted in Figure 4.7. Such structures can be used as molecular-size metal–semiconductor, metal–

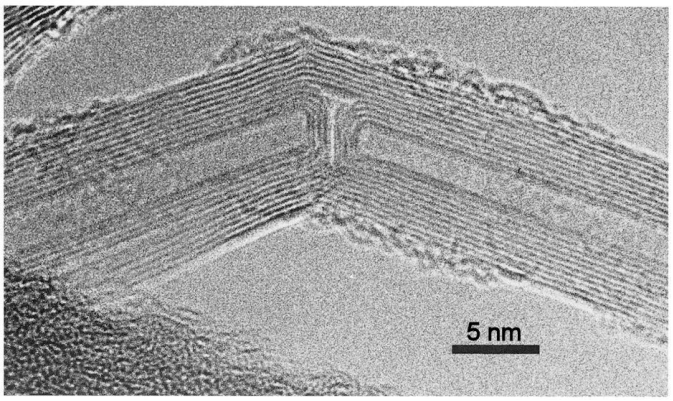

Figure 4.7: Transmission electron microscope image of carbon nanotube junction. Data collected on the Creative Commons Attribution-ShareAlike License from Wikimedia Commons [202].

metal or semiconductor–semiconductor junctions [203, 204]. Different CNT connections to form pentagon-heptagon pairs are possible, e.g. SWCNT(12,0) and (11,0), SWNCT(10,0) and (9,0) [205], SWCNT(8,0) and (7,1) [206] etc. The formation of such pairs is a topological defect with minimal local curvature, therefore low energy cost. Such defects can change the helicity of the CNT [199, 207] and can be responsible for the change of the CNT radius. As the result, the quantum conductance of CNT junctions can be changed [208]. In comparison to vacancy defect, the formation of pentagon-heptagon pairs do not induce additional state near Fermi energy, because they do not alter the sp^2 hybridization of the carbon atoms [209]. Carbon nanotubes can be deformed even by van der Waals forces [210]. It was reported that smaller CNTs, which contain less concetric layers, are weaker and more prone to be deformed [211].

The introduction of sp^3-like defects in the structure of a CNT, e.g. during covalent functionalization, significantly changes the properties of the surrounding carbon network of sp^2 type [211, 209]. They can act as non-conducting barriers, which separate structures in the whole CNT network. Such defects can occur along the symmetry axes resulting the formation of seven possible conformations, described by H. Hiura et al. [211], and are considered as the reason of folding, rippling and tearing of CNTs along the symmetry axes. It was reported that the introduction of the vacancy defect has similar influence on the electronic proper-

ties of semiconducting SWCNT(10,0) as covalent sidewall functionalization with COOH or F functional groups [209].

Among an interesting defect on the surface of CNTs is a Stone-Wales (SW) defect [212], which is formed as the result of the rearrangement of four six-membered rings of a carbon nanotube into two pentagons and two heptagons (see Figure 4.8) due to the rotation of a C–C bond by 90°. Pentagon-heptagon defect originated from SW is a low energy defect, which does not change the CNT helicity.

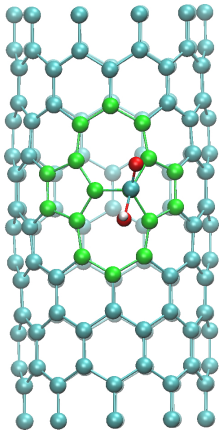

Figure 4.8: The structure of SWCNT sidewall with Stone-Wales defect and covalently attached carboxyl group. The defect motif is marked in green.

Defective regions of carbon nanotubes influence on their properties. On the one hand, they make the CNT surface more reactive [213], on the other one, they disrupt a normal transport of electrons along the nanotube axis, decreasing the level of the electric yield. It was found that some configurations of pentagon-heptagon pair defects in CNT junctions completely stop the flow of electrons [214]. Excepting the fact that defective CNT regions are formed unintentionally, some times defects are introduced on purpose, for example at post-processing processes using ion/electron irradiation [215].

Numerous experimental HRTEM (High-resolution Transmission Electron Microscopy) analyses and images show that the structure of single-walled CNTs can be a *perfect* one, but it mostly depends on the synthesis procedure. Generally, MWCNTs are more likely to get defective regions than SWCNTs, even those MWCNTs obtained during arc-evaporation, which is the best technique for high-quality multi-walled CNTs [185]. Therefore, SWCNTs are prone to be successfully used in nanoelectronic devices.

4.1.2 Electronic properties

Electronic band theory, which enables to analyze ranges of energies that an electron within the solid might have or not, classifies solids in four main groups differing with the filling of the electronic states in valence and conduction bands. Therefore, solids can be of metallic, semimetallic, semiconducting and insulating nature (see Fig. 4.9). Metals have partially filled conduction band, while semimetals have relatively small overlap between valence and conduction bands; both of them are characterized with no band gap between valence and conduction bands. Solids with the band gap lower than 4 eV are known as semiconductors [216], while those of the band gap larger than 4 eV are insulators. There are also some exceptions, e.g., the band gap of MgS, BeSe and AlN semiconductors at 300 K is 4.87 eV, 5.60 eV and 6.03 eV, respectively.

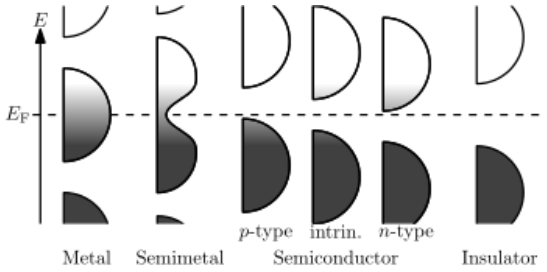

Figure 4.9: Band structure diagrams (filling of the electronic states) for metals, semimetals, semiconductors and insulators. Fermi level is noted as E_F, the shade of the valence and conduction bands denote the Fermi–Dirac distribution: states filled are in black, while states not filled are in white. Diagram is the own work of Nanite and available under the Creative Commons CC0 on Wikimedia Commons.

Carbon nanotubes can be either metallic or semiconducting depending on their structure: their electronic properties is a function of CNTs diameter and helicity. Taking into account experimental investigations on the types of CNTs synthesized, two-thirds of all possible SWCNTs are prone to be semiconducting ones. Type of the conducting process: with hole (p-type) or electron (n-type) carriers, depends on the position of the Fermi energy within the band gap (see Fig. 4.9). It should be noted that most of the electronic properties of carbon nanotubes was predicted theoretically due to the helical and rotational symmetries of CNTs. Only in 1998 the first investigations correlating the electronic properties of CNTs with their structure were made using the combination of Scanning Tunneling Microscopy (STM) and Scanning Tunneling Spectroscopy (STS) [189].

The electronic band structure of two different carbon nanotubes can be seen in Figure 4.10. In Figure 4.10 it is clealy seen that SWCNT(6,0) characterizes with metallic nature with no band gap between the electronic states, while SWCNT(10,0) is a semiconducting one with the band gap of c.a. 0.8 eV. In general, the value of the energy gap (E_{gap}) for semiconducting carbon

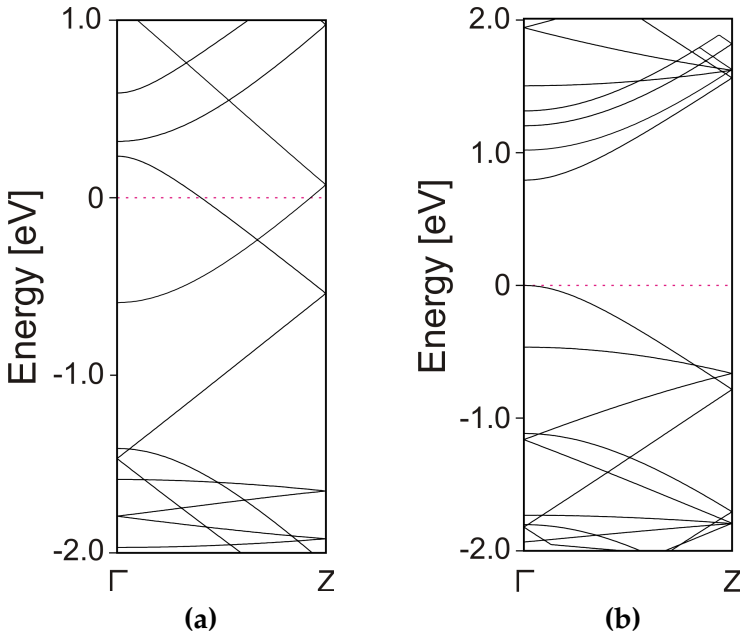

Figure 4.10: The calculated (DFT-D2, PBE) electronic band structure of two single-walled carbon nanotubes: (a) metallic SWCNT(6,0) and (b) semiconducting SWCNT(10,0). The Fermi level is marked with the dashed purple line.

nanotubes is in the range of 0.4–0.65 eV, while CNTs with the higher values of E_{gap} (c.a. 1.7–

2.0 eV) are classified to the metallic ones with the specific shape of the density of states peaks at the band edges [189]. The band gap of semiconducting CNTs depends on their diameter: for CNTs with the range of nanotube diameter of 1.0–2.5 nm the energy gap is inversely proportional to the tube diameter [189], for example: energy band gap for SWCNT with diameter of 1.0 nm, 1.4 nm and 2.0 nm is 0.85 eV, 0.60 eV and 0.43 eV, respectively [187, 189]. This dependence can be shown as:

$$E_{gap} = \frac{2\gamma_0 \cdot a_{C-C}}{d}, \tag{4.5}$$

where γ_0 is the C–C tight-binding overlap energy, a_{C-C} is the nearest neighbor C–C distance (c.a. 0.142 nm) and d is the CNT diameter. The C–C tight-binding overlap energy taken for the energy gap calculations in Ref. [189] was 2.7 eV. The effect of increasing radius of curvature on the moderate-band-gap properties of CNTs was predicted by C. T. White et al. [187]. Finally, it should be noted that when the nanotube diameter increases, the band gap tends to zero with the formation of zero-gap semiconductor (semimetal), which is electronically similar to the planar graphene sheet.

In some cases electronic band structure is characterized with a plenty of mutually crossed electronic states with different energy, therefore, the analysis of the diagram starts to be complicated. As a result, the density of these states (known as DOS – density of states) as the function of energy can be used. Figure 4.11 shows the density of states of the previously mentioned SWCNT(6,0) and SWCNT(10,0), which electronic band structure was depicted in Fig. 4.10. More electronic states of the same energy value, available for occupation, the higher is the intensity of the DOS. Density of states enables to distinguish easily pure metallic and semimetallic nature of the solid, because DOS of metals are fully filled at the Fermi level (similarly to Figure 4.11: a), whereas semimetals possess significantly lower intensity of DOS at this level. Zero DOS at the specific energy value means that no states can be occupied.

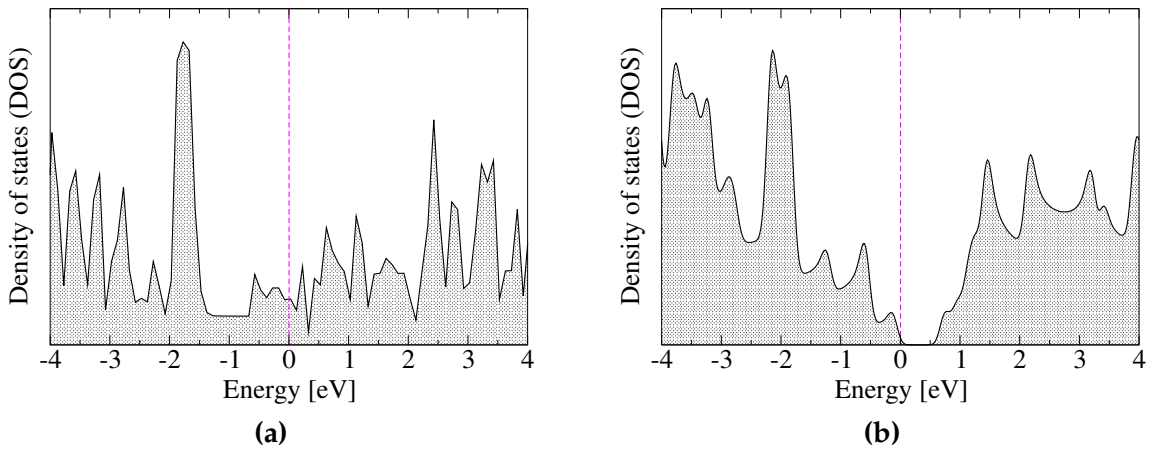

Figure 4.11: The calculated (DFT-D2, PBE) electronic density of states (DOS) of two single-walled carbon nanotubes: (a) metallic SWCNT(6,0) and (b) semiconducting SWCNT(10,0). The Fermi level is marked with the dashed purple line.

The allowed electronic states of CNTs are limited, as a result, the conduction process is well separated and is similar to the quantum wire with the ballistic transport [217]. Electrons in the material are confined in the radial direction in the singular plane of the graphene sheet and propagate only along the nanotube axis. Such electron transport is not affected by impurities or phonons, electrons face no resistance, therefore, no energy is dissipated. These means that carbon nanotubes can conduct large current without heating up. The studies

on the quantum transport in carbon nanotubes was presented in 1998 by Walt de Heer et al. [218].

Electronic properties of carbon nanotubes can be changed and controlled as the result of the defect formation, the introduction of atoms other than carbon or the covalent attachment of different functional groups [205, 209]. The magnetic field, applied perpendicularly to the nanotube axis, can also be used to change the energy band gap of CNTs [219, 220], therefore, to change the electronic character of the material. For example, it was reported that short semiconducting MWCNTs with the radius of 15 nm can be converted to the metallic ones [221]. Moreover, carbon nanotubes possess a high diamagnetic susceptibility, which increases at lower temperatures. There is no data concerning the direction of susceptibility (CNTs are randomly oriented in the material [222]), but is was confirmed that for nanotubes aligned parallel to the field the susceptibility is greater [223].

The superb electronic properties of carbon nanotubes have a great potential to be used in diodes [224], field effect transistors [190, 225], logic circuits [226], sensitive chemical sensors [227, 228, 229] etc. The limitation for the wide usage of the CNT materials in practice is the preparation of the nanotubes with a defined structure arranged into the specified way. On the one hand, single-walled CNTs possess much better electrical properties than multi-walled CNTs, because the inner walls of MWCNTs do not contribute significantly in their properties, but on the other hand, MWCNTs have higher degree of order and 3D-crystallinity, in comparison to SWCNTs, which make them more convenient in preparation. Concepts for the production of new materials and tools using electronic properties of carbon nanotubes are still developing.

4.1.3 Mechanical properties

Mechanical properties of CNTs, similarly to the electronic ones, were predicted, firstly, theoretically using both *ab initio* [230, 231] and potential-based methods [232, 233, 234]. In 1996, the first experiments have shown that carbon nanotubes possess high stiffness and axial strength, therefore, together with their low density, have a great potential to be used in lightweigh composite materials [235]. Nowadays, a plenty of different studies, concerning mechanical properties of carbon nanotubes, are available. In general, it is known that the Young's modulus and tensile strength of carbon nanotubes in the axial direction are in the range of 270–1000 GPa (in average) and 11-200 GPa (mean: 63 GPa), respectively [233, 236, 237]. Therefore, they are considered as the strongest material in nature. Moreover, CNTs are flexible and elastic. The breaking strain of strained single-walled carbon nanotubes was reported to be approximately 5% using theoretical models [234, 238], what was proven experimentally (c.a. 5.3% [239]). Using large-scale molecular dynamics simulations it was also predicted that CNTs are brittle under high strain and low temperature conditions. They are plastic (tubes with *(n,m)* integers larger than 14, see Subsection 4.1.1), if the strain is low and temperature is high. Carbon nanotubes with large *(n,m)* integers are moderately or completely brittle depending on their symmetry [234]. J.-P. Salvetat et al. [240] suggested that the reason of the CNT flexibility is not plastic deformation, but *"the high strength and the unique capability of the hexagonal network to distort for relaxing stress"*. Finally, carbon nanotubes were reported to be designed as a longest cable in the world, i.e a 23 000 mile cable from Space station to the Earth without suffering high gravitation force due to its own weight at that length [185].

Superb mechanical properties of CNTs are related to the sp^2 bond strength and are dependent on the lattice parameter [240]. Moreover, all mentioned properties are strongly dependent on the structural parameters of CNTs, defects and impurities, therefore, on the method of CNT synthesis and purification. Different experimental techniques were used to estimate mechan-

ical properties of CNTs. Among them are HRTEM, atomic force microscopy (AFM) [239], scanning probe microscopy [241] and electromechanical resonance [242].

Apart from the exraordinary properties of carbon nanotubes, there is a problem with their direct usage in enhancing the properties of composites, because of low load transfer from matrix to CNTs (see Subsection 4.4 for more details).

4.1.4 Optical properties

Carbon nanotubes are known to be black, but very thin layers of CNTs can be transparent [243]. At the same time, CNT material with vertically aligned carbon nanotubes, named as vantablack, is known as the blackest artificial substance, which absorb even 99.965 % light of the visible spectrum [244]. One of the most valuable optical property of CNTs, namely SWCNTs, which enables to examine their structural features, is characteristic Raman spectrum. A typical Raman spectrum of carbon nanotubes, depicted in Figure 4.12, consists of several peaks [245, 246]: radial breathing mode (RBM), D–band (D-disorder), G–band (G-graphite) and G'–band.

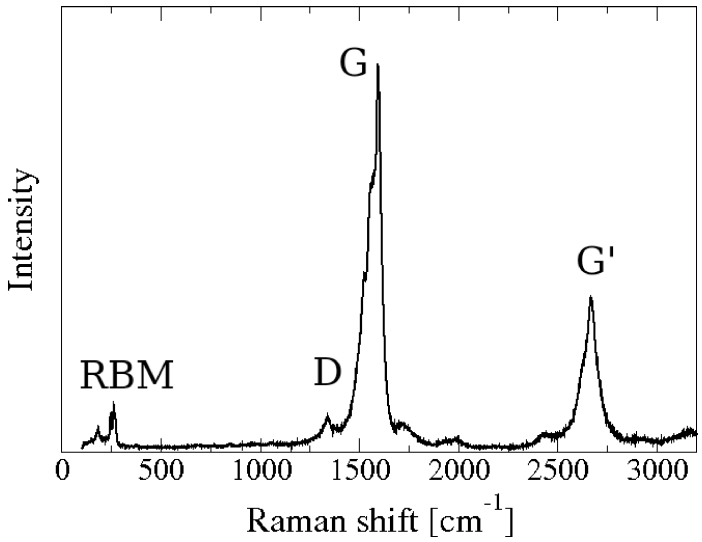

Figure 4.12: Raman spectrum of single-walled carbon nanotubes (spectrum measured on Renishaw Raman inVia Microscope; Ar ion laser (514 nm); incident power of the laser of 2.25 mW).

A low-frequency peak in the region 160–400 cm^{-1} is the radial breathing mode (RBM). RBM is often called as a bond-stretching out-of-plane phonon mode, because represents a symmetric movement of all carbon atoms in the radial direction. RBM is a unique fingerprint in the Raman spectrum, which is characteristic only for carbon nanotubes, therefore, its presence is the evidence that an examined sample contains carbon nanotubes. Moreover, for nanotubes with diameter in the range of 0.6–2 nm, the position of RBM can be used to estimate CNT diameter [247] using the following equation:

$$w_{RBM} = \frac{C_1}{d} + C_2, \tag{4.6}$$

where the values of C_1 and C_2 depend on the chosen value of a C–C bond (the average values are 220 cm^{-1} and 14^{-1}, respectively [248]). Peak in the region 1250–1450 cm^{-1} (the characteristic frequency is c.a. 1340 cm^{-1}), known as disorder-induced phonon mode (D-band), is a standard peak sensitive to the disordered structures in the carbon-based materials. It is induced due to the mode of boundaries in Brillouin zone.

The most intensive peak in the Raman spectrum of CNTs (see Figure 4.12) is a G–band, which is localized in the region 1550–1600 cm^{-1}. The G–mode is related to the tangential mode vibrations of the carbon atoms. This band is often divided into two peaks: G^+ and G^- with the frequencies of 1590 cm^{-1} and 1570 cm^{-1}, respectively. It was reported that G^+ peak, which describes in-plane vibrations along the tube axis, is sensitive to the SWCNT diameter, while G^-, which corresponds to the in-plane vibrations along the circumferential direction, is not [249]. G-band, together with RBM, can be used to distinguish metallic and semiconducting nanotubes [250, 245]. G'–band (in the region of 2500–2900 cm^{-1}) is the second order harmonic of the D–band. It is less sensitive to the defects of the carbon nanotubes, therefore, a lot of initial studies on the electronic and phonon structure of CNTs were made using this band.

Raman spectroscopy is often used to analyze the purity of single-walled CNTs using the ratio of the D/G band intensities. Moreover, it can give information about crystallite size, presence of sp^2–sp^3 hybridization (as the result of the covalent bond formation), clustering of the sp^2 phase, impurities, defects, crystal disorder, elastic constants, strain etc [251]. Raman spectroscopy is rarely used to analyze MWCNT samples.

4.1.5 Thermal properties

Thermal conductivity of carbon nanotubes is more than 9 times higher than copper. It is also higher than thermal conductivity of diamond and graphite, which is 2000–2500 $Wm^{-1}K^{-1}$ and 2000 $Wm^{-1}K^{-1}$, respectively. There is no one exact value for thermal conductivity of CNTs, because of heterogeneous structure of CNT material. J. Hone et al. [252] reported thermal conductivity of CNTs in the range of 1750–5800 $Wm^{-1}K^{-1}$, P. Kim et al. [253] measured values greater than 3000 $Wm^{-1}K^{-1}$, while S. Berber et al. [254] calculated thermal conductivity of isolated SWCNT(10,10) with the value of 6600 $Wm^{-1}K^{-1}$. In all cases the charateristic thermal conductivity of carbon nanotubes was higher than of other known materials. The conduction process of carbon nanotubes was reported to be quantized in phonon-based thermal conductance of semiconducting SWCNTs in low-temperature limit [255]. The reason of the quantization is the presence of some phonons in CNTs even at 0 K temperature.

High thermal conductivity of CNTs enables them to be extensively used in electronics, e.g., for producing thermal greases or nanoliquids [256] that improve thermal conductivity of the grease (c.a 1.4 times) and decrease temperature of the CPU (by 5–6°C). Additionally, carbon nanotubes are known as the most robust material, because they are atomically stable even at 3000°C [257].

4.2 Synthesis of carbon nanotubes in brief

There are three basic procedures to synthesize carbon nanotubes: arc-evaporation, laser-vaporization and chemical vapour deposition. The first method was used by Iijima in 1991 [165] and 1993 [181] for the synthesis of MWCNTs and SWCNT, respectively. This method is still the best one for the synthesis of high-quality multi-walled CNTs. Laser-vaporization [258, 259] is similar to arc-evaporation, because uses a graphite-metal mixture as a starting material and is based on the vaporization of this mixture proceeded by condensation in an inert atmosphere, but, at the same time, it uses a different source of energy to initiate CNTs production. The last procedure, chemical vapour deposition known as CVD [260], enables to use catalytic methods to synthesize arrays of aligned carbon nanotubes, even for large-scale production. Therefore, it is extensively studied and developed nowadays.

The first investigation on the catalytic growth of carbon filaments started in early 1970s [261]. Metal complexes were used as catalysts since 1990s [262]. The most frequently used metal

catalysts are based on Fe, Co, Mo and Ni [185, 263] or their combinations [264, 265, 266], but also Au, Ag and Cu [267, 268, 269] can be successfully used. The catalytic activity of the catalyst depends on the solubility of carbon in the metal [263]. Diameter of the synthesized CNTs depends on the particle size of the metal catalyst [270, 271]: nanoparticles of the size of 1.8 nm are the most active to grow SWCNTs [272], while those of above 9 nm are suitable to get MWCNTs [273]. Different carbon-rich compounds are used in this technique: hexane, methane [274, 275, 276], acetylene [262, 277], ethylene [278, 279], carbon monoxide [260, 280] etc. CVD is convenient and commonly used technique to synthesize SWCNTs, which quality is less dependent on the production method than in the case of MWCNTs [185]. There are also known other methods for CNT synthesis, including electrochemical synthesis [281] and plasma enhanced CVD [282]. Catalytically made CNTs possess more defects than those produced by arc, what reflects on their properties.

Carbon nanotubes, synthesized in the mentioned procedures, are not pure, because they are decontaminated by amorphous carbon, metal nanoparticles, support material etc. As a result, they need to be purified and selectively removed from the solution to enable their further usage. Among techniques for purification of CNTs, which mostly depend on the type of the carbon nanotube (SWCNT, MWCNT, metallic etc.) are:

- oxidation methods, e.g. acid treatment [283, 284],
- intercalation followed by oxidation [285, 286],
- high-temperature annealing [287],
- physical methods, e.g. centrifugation, laser treatment, filtration [288, 289],
- laser vaporization [290].

During either synthesis or purification the structure of CNTs may be changed, e.g. with the defect formation (see Subsection 4.1.1) or, when treated with oxidazing agents, with the attachment of COOH functional groups on their surface [291, 292, 293]. All structural changes of CNTs change their primary properties.

4.3 Functionalization procedures

Benzene-type hexagonal network, which is the basis of the carbon nanotube structure, impact high hydrophobic interactions: van der Waals and $\pi - \pi$ stacking interactions, between each nanotube unit causing CNTs to exist as ropes and bundles and form agglomerates in the scale of millimeters [294]. As a result, the unique CNT properties can not be successfully applied. Moreover, pristine carbon nanotubes are mostly inert and almost insoluble in polar solvents. Therefore, their direct usage in the pure form is limited. A lot of studies, devoted to the increasing of the CNTs solubility and reactivity, are undertaken until nowadays. Among them are exo- and endohedral, end-cap and sidewall functionalizations. All these functionalization types are based on two types of molecular interactions: covalent and noncovalent ones. Therefore, two main approaches for nanotube functionalization are known worldwide, i.e. covalent functionalization (CF) and noncovalent modification (NM) (often called functionalization too). Covalent functionalization is easier to handle, but the covalent attachment of molecules to the CNT surface deforms the local structure and directly influences their properties [31, 36]. Contrary to it, noncovalent modification has only a small influence on the electronic properties of nanotubes [37] due to weak van der Waals interactions between the CNT and the adsorbate, but it is based on much more subtle effects that are hard to control.

Functionalization of carbon nanotubes opens a variety of possible CNT applications, starting from the fabrication of field effect transistors and biosensors up to the drug delivery systems

and anticancer therapies. The detailed analysis of the CNT applications will be not given in the present PhD thesis; it was fully described in Ref. [295, 296, 297, 298, 299, 300, 301]. A brief introduction to the covalent and noncovalent functionalizations is presented below.

4.3.1 Covalent functionalization

Chemical modification of carbon nanotubes through the covalent attachment of the functional groups, such as COOH, OH, COH, NH_2, was the most appropriate and easy way to influence the dispersion of CNTs. An examplary scheme of the attachment of different

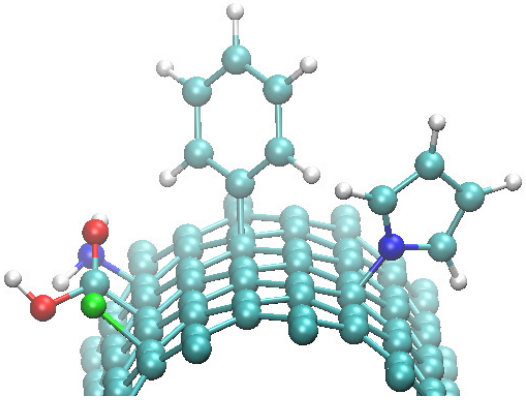

Figure 4.13: Simple scheme covalent attachment of different functional groups on the surface of carbon nanotube during covalent functionalization. Carbon atoms are cyan, H, O, N, F atoms are grey, red, blue and green, respectively.

functional groups to the CNT surface is shown in Figure 4.13. During CF, new covalent bonds between the carbon atoms from the nanotube and the specific functional groups are formed. It is connected with the change of the carbon atom hybridization from sp^2 to sp^3 and a simultaneous loss of π-conjugation system. If CF is occurred on the CNT end-caps (tips), only a highly localized transformation of the nanotube electronic structure is observed. Covalent functionalization of the CNT sidewalls can partially damage the intrinsic structural and electronic properties of SWCNTs [297]. It should be noted that CNT end-caps and the defective CNT regions are the most reactive CNT sites, therefore, CF will be occured firstly there [185], but better dispersion is observed when the sidewalls of carbon nanotubes are functionalized. In practice, carbon nanotubes are firstly purified from the amorphous carbon, catalysts particles etc., but also CNT tips are opened [302]. Such approach enables the functionalization of the CNT sidewalls and the increase of the CNT reactivity and dispersity. The initial functional groups, e.g. COOH or OH, can be attached to the CNT surface during the purification procedure [291, 292, 293]. Further chemical reactions between these groups and other molecules enable any surface functionalization. Here, the prominent solubility of CNT in dichloromethane, chloroform, toluene and other nonpolar solvents can be used to prepare the solution of the dispersed nanotubes. The covalent attachment of one functional group can influence the possibility of further covalent bonds formation, for example, the clustering effect during the COOH group attachment can take place [303].

The first example of the nondestructive sidewall functionalization by fluorination was carried in 1998 by Mickelson et al. [304]. Later, many chemical processes of the covalent functionalization of CNTs were reported: cycloaddition, such as Diels-Alder reactions [299], nitrene [305] and carbene addition [306], alkylation [307], arylation [308], hydrogenation [309], attachment of polymers [31, 60, 310] or bioconjugates [311] etc.

On the one hand, covalent functionalization gives more secure attachment of the functional

molecules on the CNT surface, but on the other hand, it is very difficult to control the chemo- and region-selectivity during such modification [312]. Additionally, CF often needs extreme conditions to form covalent bonds, as a result, the process of surface defects formation may also occur. Defects can impact not only the electronic properties of CNTs, but also reduce the high length-to-diameter ratios of SWCNTs by cutting them into short pieces [313].

Functionalization of CNTs allows to tune their chemical and physical properies. At the same time, the attachment of the functional groups on the CNT surface, change their properties. A. Garg and S. Sinnott [314] reported that covalently functionalized SWCNT(15,15) is less stiff and has 15% worst mechanical strength. I. Lara et al. [315] calculated that the electronic properties of SWCNT can be changed from semiconducting to metallic due to manipulating the amount of covalently attached COOH groups. J. Zhao et al. [209] demonstrated the significant change of the conductive properties of covalently functionalized CNTs and showed such CNTs are similar to the vacancy-defective ones.

4.3.2 Noncovalent functionalization

In comparison with CF, noncovalent modification (NM) gives the possibility to attach molecular species on the surface of the carbon nanotube without destroying their π-conjugated system. NM of carbon nanotubes is based on either *(i)* hydrogen bonds, vdW and $\pi - \pi$ stacking interactions between planar groups of the attached molecules and the nanotube sidewall or *(ii)* wrapping polymeric molecules helically around the CNT. The latter possibility of NM of SWCNT is depicted in Figure 4.14. Such interactions do not influence significantly the struc-

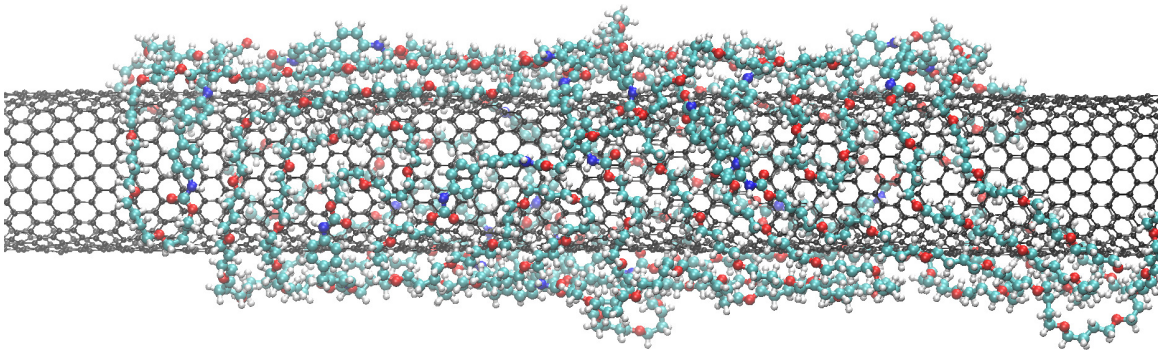

Figure 4.14: Noncovalent functionalization of single-walled carbon nanotube (20,0) with polytetramethylene ether glycol.

tural and electronic properties of CNTs, but change their dispersion in the solvent [295, 299]. NM can improve the interfacial characteristics of carbon nanotubes and keep their desired features [316]. Molecular systems modified noncovalently are easy to control but difficult to characterize in a quantitative way. The process can be even more complicated, because other interactions might take place and impact yield of NM (for example the solvent can replace the adsorbate [317]).

There are four main types of molecules used in NM of CNTs:

- specific planar (aromatic) molecules,
- surfactants,
- polymers,
- biomolecules.

Aromatic molecules, such as porphyrin, phtalocyanines, pyrene and their derivatives, interact with the CNT sidewall by $\pi - \pi$ stacking interactions and lead to either novel electron donor-

acceptor nanohybrid molecules [318, 319, 320], which undergo fast electron transfer, or new molecular systems used for protein immobilization [321].

Due to the usage of surfactants adsorbed on the surface of carbon nanotubes, the CNT surface tension is lowered, which efficiently prevents their aggregation. Such treatment overcomes vdW attraction interactions by electrostatic/steric repulsive forces [316]. The effectiveness of surfactant-based NM depends strongly on the physicochemical properties of the used adsorbate and its quantity. In the literature, there are a lot of investigations of such NM, using non-ionic (e.g. polyoxyethylene 8 lauryl [322], Triton X-100 [323]), anionic (e.g. sodium dodecylsulfate, sodium dodecylbenzenesulfonate, poly(styrene sulfate) [324]) and cationic surfactants (e.g. dodecyl tri-methyl ammoniumbromide [325]).

Polymers and biomolecules belong to the class of relatively large molecular systems, thus, different types of intermolecular interactions between each repeat unit and the CNT surface are merging into the wrapping process around the CNT. Taking into account the energetic factors and thermodynamically the most stable positions of polymers on the CNT surface, they are wrapping around it in a helical manner [295, 326]. A wide range of polymers have been used to functionalize carbon nanotubes, including, polyvinyl pyrrolidone [327], dextran [328], polystyrene sulfonate [329] etc. A special focus was given to the conjugated polymers, e.g. poly(9,9-dioctylfluorene), poly[(9,9-dioctylfluorene)-alt-1,1,2,2-tetramethyldisilane, which were shown to be excellent wrapping materials, especially for SWCNTs with smaller diameters [330, 331]. The wrapping process is a complex interplay between the structure of the polymer chain, its molecular weight and nature of the side groups. Thus, not only nature of the main polymer chain plays a decisive role, but also the length of the alkyl side chains. The usage of conjugated polymers gives an opportunity to separate selectively between semiconducting and metallic SWCNTs, to sort SWCNTs with specific *(n,m)* integer pair, or to separate SWCNT enantiomers [332].

The aim of CNT modifications with biomolecules was to insert molecules inside the nanotubes, which resulted in their additional adsorption and helical wrapping on the CNT surface [333]. The reason of such behavior is the existence of $\pi - \pi$ stacking interactions between amino acid residues of the proteins or nucleobases of DNA/RNA and π-surface of the carbon nanotubes. At the same time, when hydrophobic areas of biomolecules interact with the CNT surface, their hydrophilic functional groups are exposed toward the medium (e.g. water) and increase CNT dispersion. Among CNT immobilized biomolecules are metallothionein proteins [334], streptavidin [335], ferritin [336], different enzymes [337], single- and double-stranded deoxyribonucleic acid [305, 334, 338, 339] etc. Biomolecules have a high affinity to wrap around the CNTs, which even enables functionalized CNTs to pass through cell membranes [340]. Moreover, the wrapping process of the DNA molecules can be highly selective, for example, for specific SWCNT chirality [194]. Noncovalent functionalization of carbon nanotubes can be analyzed using electron microscopy techniques [313], described above.

Different modifications of CNTs in order to get desired properties of synthesized material are possible. Both, covalent and noncovalent functionalizations of carbon nanotubes open new opportunities for their applications in nanotechnology, medicine, electronics etc. Even if there is the variety of different ways to functionalize CNTs, the large-scale production of separated and monodispersed carbon nanotubes according to diameter, length and chirality is still a challenge.

4.4 Carbon nanotubes as a polymer filler

There is also a challenge to increase the dispersity of carbon nanotubes in the composite materials, where CNTs are used as a polymer filler in order to reinforce the characteristic

properties of the polymer matrix or even to give it new features. Dispersion, according to the conventional composites, means the distribution of polymer filler in a matrix medium without agglomerates [341]. The dispersion process in carbon-based composies can be defined as *(i)* nanoscopic dispersion, based on the unraveling of CNT agglomerates, or *(ii)* micro-, macrodispersion, based on uniform distribution of individual CNTs or their agglomerates in the composite material [342].

Dispersion of CNTs in the polymer matrix influences the transfer of their superior properties to it [19, 43, 240], thus efficient CNTs dispersion is needed. Unfortunately, carbon nanotubes are strongly connected with hydrophobic interactions, as a result it is very hard to separate them. Therefore, they form agglomerates like in Figure 4.15: a. Additionally, there are a lot of interfacial, intra- and intermolecular interactions between carbon nanotubes and polymer, which are hard to control, investigate and to obtain. There is no effective prescription how to synthesize a *good* CNT-based composite, where carbon nanotubes are equally dispersed (Figure 4.15: b) in the material.

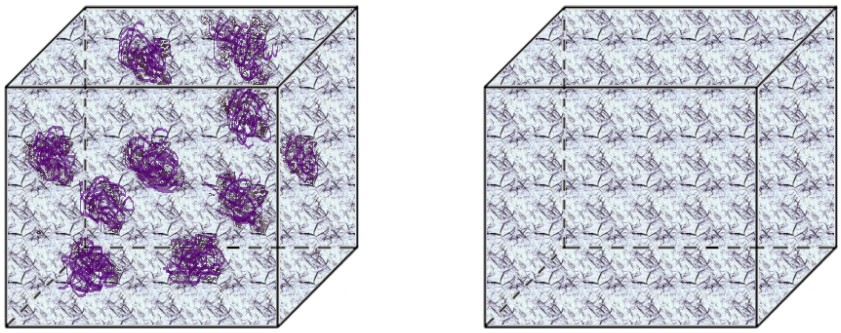

(a) **(b)**

Figure 4.15: Schematic dispersion of carbon nanotubes in a composite: (a) low CNT dispersion, carbon nanotubes exist as bundles, (b) carbon nanotubes uniformly dispersed in the polymer matrix.

The usage of experimental techniques to increase CNT dispersion in the polymeric medium, e.g. ultrasonication or high shear mixing [341], were proposed, but they are connected with the breakage of the CNT structure or degradation of the medium [343]. Covalent and non-covalent functionalizations of CNTs, described in the previous Section, are widely used too. Recently, it was reported that modification of CNT surface with introducing of hydrogen bonding sites changes the CNT dispersity in the composite, improving its mechanical properties [344]. Due to the surface modification of the carbon nanotubes with polydopamine, their dispertion, during the synthesis of composite based on polyurethane, was increased, therefore, the effective load transfer and 40%/100% increase of the tensile modulus and tensile strength, respectively, was observed [345]. It should be mentioned that the amount of CNTs used to produce a composite with enhanced properties is in the range of 0.01–2.0%, for example, G. Pircheraghi et al. [346] used CNTs of the concentration of 0.05vol% to produce CNT-based thermoplastic polyurethane nanocomposite with 99.7% better thermal conductivity. There are also studies which show very low reinforcing effect after the addition of the CNT filler [341], what is explained with weak interactions of CNTs with a polymer due to low CNT distribution in the composite. Even if the amount of the carbon nanotubes added to the polymer is very low, it is very hard to separate them.

Dispersion of CNTs in the polymer matrix is not the only one factor influencing the properties of the synthesized composite. Interfacial adhesion between carbon nanotubes and the polymer also defines the way of transferring the superb CNT properties, therefore, the reinforcing effect. Both dispersion and interfacial adhesion are mutually connected. Is was

improved that homogeneous dispersion of CNTs in the polymer matrix causes strong interfacial adhesion between CNTs and matrix, which directly influences the enhancement of mechanical and shape memory properties of polyurethanes [347]. F. Gojny et al. [348] have shown that the improved interfacial adhesion increases thermal resistance of CNT-based composite. N. Sahoo et al. [349] have reported that the interfacial adhesion between CNT and polyurethane matrix increases if the CNTs are functionalized with carboxyl groups.

As a result, the main challenge now is to understand molecule-molecule interactions in the composite and to discover the effective way for the dispersion of carbon nanotubes in the polymer matrix without CNTs agglomeration and high CNT/polymer interfacial adhesion. In the present PhD thesis, molecular modeling and theoretical approaches are used to understand the fundamental interactions between the monomeric molecules, used in the synthesis of CNT-based composite, and the surface of single-walled carbon nanotubes, in order to enable the explaination of the interfacial adhesion of the polymer filler and matrix.

4.5 Theoretical investigations

To solve the problem of the carbon nanotube dispersion and to examine extraordinary CNTs properties, both experimental and theoretical methods are used. As it was mentioned in the text above, most of CNTs properties were firstly predicted using theoretical calculations taking into account characteristic CNT structure and symmetry. There are a lot of theoretical investigations of these carbon allotropes, where different levels of theory and techniques are used. Most of them are focused on the CNT sidewalls, because carbon nanotubes are very long, as a result the effects of the end caps are neglected. The two main techniques used to calculate carbon nanotubes are known as:

- cluster approach
- periodic approach.

Figure 4.16 represents the main differences of these approaches. Cluster approach takes into

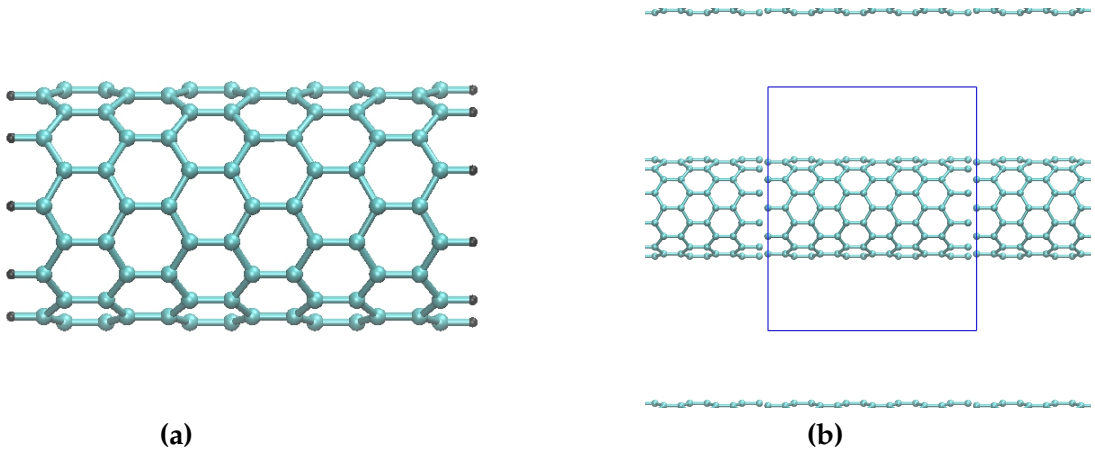

(a) (b)

Figure 4.16: Theoretical approaches which cover the field of the carbon nanotubes: (a) cluster approach, (b) periodic approach.

consideration a fragment of the carbon nanotube surface, which is hydrogenated on the CNT ends [62, 64, 314]. The size of the CNT fragment is unrestricted. The only one condition is the scalability of the theoretical method used for the calculations. The "cluster", i.e. fragment, can be modified and changed in different ways and with desired molecular species. On the one hand, the lack of the severe restrictions enables to study various CNT surfaces, but,

at the same time, real nature, therefore, superb properties, of carbon nanotubes are not imitated, because real CNT is very long. Additionally, the added hydrogen atoms change the distribution of the electron density in the system. As a result, additional approximations or other tricks should be used to make such calculations correct.

The second approach, the periodic one, is directly connected to the real nature of CNTs. Carbon nanotubes have a translational symmetry in the Z direction (nanotube axis), as a result they are known as 1-D translationally periodic systems. Due to the symmetry, periodic boundary conditions (PBC), with the specially designed unit cell, can be used to get the periodic nature of CNTs [209, 350, 351]. In this approach the CNT periodic unit cell, which mimics the real CNT properties, is calculated with imitation that these unit cell is infinitely multiplied in the calculations. Therefore, the length of the CNT calculated, using this technique, is infinitely long. This approach is more computationally demanding than the previous one and needs a specially designed and optimized CNT unit cell. The translational unit cell significantly depends on the *(n,m)* integers, not on CNT radius. For example, the SWCNT(10,9) has the radius of c.a. 7.0 Å, but the translational unit cell contains 1084 carbon atoms [187], whereas the radius of SWCNT(10,0) is c.a. 3.9 Å, but the unit cell consists of 160 carbon atoms [352]. The CNT translational unit strongly depends on the chirality, for example, the length of the translational unit for semiconducting SWCNT(10,0) is 17.1 Å (160 carbon atoms), while for SWCNT(9,4) is 49.2 Å (532 carbon atoms). Uncorrect definition of the unit cell can change the properties of the CNT calculated and the results obtained will be untrue. It should be noted that CNTs can be either metallic or semiconducting depending on the boundary conditions without changing any hybridization [188]. Therefore, it is an important task to choose the periodic boundary conditions for the CNT carefully.

The computational cost of cluster and periodic approaches significantly depends on the level of theory used in the calculations. There are two main computational methods which cover the field of the carbon materials:

- classical approach,
- quantum-chemistry based approach.

The classical approach, which is most frequently used for composites, is based on the classical molecular dynamics. It is complex method requiring parametrization techniques and approximations, but it gives a possibility to simulate the large fragments of the composite material, such as long large-diameter tubules or nanotube bundles [67]. The classical approach enables to calculate molecular systems of thousands of atoms [2, 35, 63]. Such calculations are based on the Newton equation and classical force fields, which do not include the electronic structure effects and bond breaking/formation. Therefore, such approach can not be used to describe the molecule-molecule interactions and specific bonding formation in the system, as they do not take explicitly electrons in their analyses. Theoretical methods based on the classical approach were used to calculate interactions between polymers, such as poly(3-hexylthiophene-2,5-diyl), P3HT and poly[2-methoxy-5-(2-ethylhexyloxy)-1,4-phenylenevinylene], MEH-PPV, with single-walled carbon nanotubes [64], where the influence of temperature and SWCNT structure on the polymer adhesion was analyzed. The diffusion of polystyrene chains among SWCNT was estimated using the classical molecular dynamics simulations with the COMPASS force field [66]. Moreover, high-temperature molecular dynamics simulations with the usage of the Reax force field were performed [353] to study the metal catalyst activity during the formation of the carbon nanotubes.

The quantum-chemistry approach is based on the quantum mechanical calculations (see Section 6), therefore, considers real electronic structure of the system. This approach is more computationally expensive (including time resouces) and implicate the application of more simplified models. For example, most static quantum calculations consider the non-defective

carbon nanotubes with no pollution from amorphous carbon material or catalysts. Theoretical calculations for the noncovalent interactions, including hydrogen bonds breaking and formation and vdW interactions, are only possible to be taken into account during calculations based on the quantum-chemistry approach. For the carbon-based interacting systems, where the main contribution to the energy of interactions is originated on the basis of dispersion interactions, require the usage of high-level *ab initio* methods, like coupled cluster one. But the size of the examined systems limits the appropriate approximations to the density functional theory (DFT) and modern semiempirical approaches. In general, systems of 200–300 atoms can be calculated using DFT method. This method was used, for example, to calculate noncovalent interactions between either conjugated polymers [351] or epoxy polymer chains [62] with the surface of single-walled carbon nanotubes and graphene. The influence of covalent sidewall functionalization of carbon nanotubes was also examined using this approach [209]. Both cluster and periodic techniques can be applied in the *ab initio* approach. In the first one, the localized basis sets are used, whereas the second one is based on the plane waves basis set.

There is also a possibility to combine classical and quantum approach to treat large systems with some chosen molecular area calculated from first principles. T. Kar et al. [354] used ONIOM (our own n-layered integrated molecular orbital and molecular mechanics) method to calculate theoretical IR spectra of armchair and zigzag single-walled carbon nanotubes.

Carbon based molecular systems can be calculated using different techniques. It is necessary to accurately study various possible models of the materials taking into account the aims of research and the available computational resources. In the present thesis, the quantum-chemistry approach, used to calculate structural and energetical properties of carbon nanotubes systems, is based on the density functional theory. More detailed description of the method used is available in Section 6.

Chapter 5

Diisocyanates and polyethylene glycol

The reaction for polyurethane synthesis, reported by Otto Bayer in 1937, was the first example of the polyaddition reaction used to produce a polymer [355]. This reaction was shown in Figure 2.2 in the Introduction (Chapter 2). As it was mentioned in Chapter 2, among two main *original* substrates for PU synthesis are diisocyanates and polyols. As the result of their toxicity, diisocyanates, nowadays, are being partially substituted by other chemical compounds, e.g. di-tert-butyl dicarbonate or alkyl bis-vinyl carbonates [356], but still bulk industry uses simple Bayer's method to produce PUs. The urethane bond, formed during the PU synthesis by Bayer's method, is not easily reversible, as the result, isocyanate foams made of diisocyanates, i.e. TDI and MDI, possess high thermal stability with the low degradation at the temperature below 270° [357]. That is why diisocyanates are still popular.

Diisocyanates and polyols are the main ingredients of the polyurethane polymer, but other functional compounds are also added to control the reaction process and the final properties of the synthesized polymer. Among such compounds are chain extenders, crosslinkers, catalysts, blowing agents, antidegradants etc. The type of the added reagents is directly dependent on the demanded properties of the PU polymer. Due to enormous possibilities to synthesize PU, their application field is extremely wide: starting from flexible foams even to artificial-heart blood vessels.

5.1 Chemistry of diisocyanates

Diisocyanates – isocyanates that contain two isocyanate (NCO) functional groups – were produced and investigated for the first time by Wurtz and Hoffman before 1850 [355], but their real commercial interest started in 1937 when Otto Bayer produced polyurethanes made from them and polyols. There are distinguished aliphatic, cycloaliphatic, polycyclic and aromatic diisocyanates, for example: 1,6-hexamethylene diisocyanate, 2,4-diisocyanato-1-methylbenzene (known as 2,4-toluene diisocyanate, TDI), 1,1'-methylenebis(4-isocyanatobenzene) (known as 4,4-methylene-bis-(phenylisocyanate), MDI), naphthalene 1,5-diisocyanate, isophorone diisocyanate etc. The structural formulae of these diisocyanates are shown in Figure 5.1.

The reactivity of diisocyanates is caused by the special geometry of double bonds in the isocyanate group, thus, the distribution of the electron density within it. The resonance structures of the NCO group is shown in Figure 5.2. The cumulated double bond sequence in NCO: R–N=C=O, enables the isocyanate group to react through the oxygen or nitrogen atoms, which are attacked by electrophiles [358]. In the literature, no exact place of the attack (O or N atom) is given, but most probable attack is via N atom (e.g. in the urethane bond

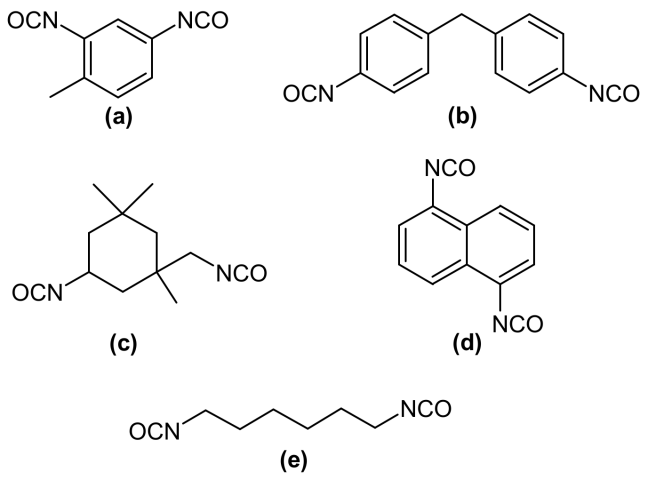

Figure 5.1: The structural formulae of examplary diisocyanates used for the synthesis of polyurethanes: (a) 2,4-diisocyanato-1-methylbenzene (TDI), (b) 1,1'-methylenebis(4-isocyanatobenzene) (MDI), (c) isophorone diisocyanate (IPDI), (d) naphthalene 1,5-diisocyanate (NDI), (e) 1,6-hexamethylene diisocyanate (HDI).

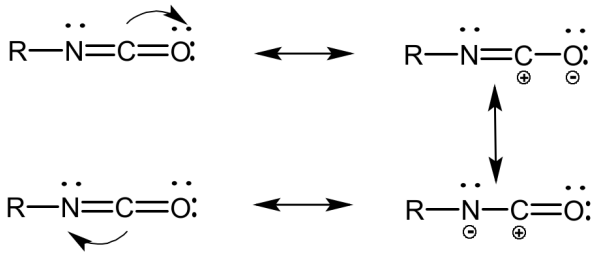

Figure 5.2: Resonance in the isocyanate group.

formation). At the same time, the positive character of the carbon atom involves attacks of nucleophiles.

Isocyanates belong to a group of very active chemical compounds, which are characterized with the toxic effects, especially to the respiratory system [357]. NCO functional groups are extremely active in the reactions with other molecules that contain an active hydrogen atom, i.e. amines, water, alcohols, urea, carboxylic acids. The general mechanism of these reactions is presented in Figure 5.3. The reactivity of isocyanate group in the reaction with

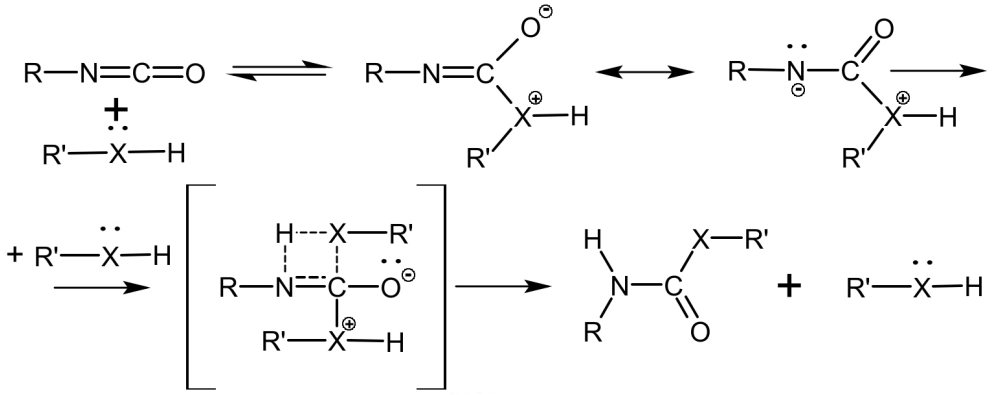

Figure 5.3: General mechanism of the isocyanate group reaction with active hydrogen compounds. The transition state is shown in the square brackets.

the active hydrogen atom is a complex process, because the reactivity of NCO groups is different in different diisocyanates and in the first/second reaction step. Starting from the latter, the reactivity of the first NCO group is much higher in the addition reaction then of the second one [359]. It is caused by the symmetrical differencies of two isocyanate molecules, as the result, the electron releasing effect [357]. Diisocyanate reactivity depends also on the nature of the substituent (R): aromatic diisocyanates are more reative than the aliphatic ones [42]. In can be clearly seen in Figure 5.4, where the negative charge is delocalized onto the aromatic substituent. Moreover, the reactivity of this aromatic R depends on the

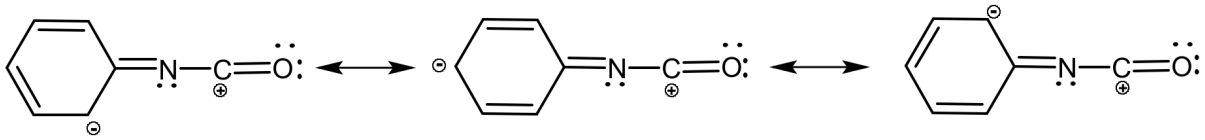

Figure 5.4: Resonance in the aromatic isocyanates.

nature of the functional groups attached to the aromatic ring: lower reactivity is observed if the electron donating groups are bounded, while higher reactivity is characteristic for the electron attracting substituents in ortho or para position [358]. Taking into account the steric hindrance connected with the ortho attaching to the aromatic ring, para-substituted diisocyanates are more reactive.

In the present PhD thesis diisocyanate reaction with the carboxylic acid, located on the surface of carbon nanotubes, is taken into consideration, so only the scheme of this reaction is described. In Ref. [42, 38, 356, 359] one can find a lot of useful information about other reactions of isocyanates. In general, diisocyanates have lower reactivity in the reaction with carboxylic acids in comparison to the amines, alcohols or water. Schematic reaction between isocyanates and carboxylic acids is shown in Figure 5.5.

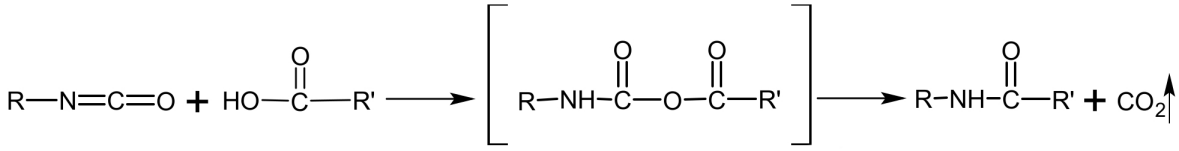

Figure 5.5: The general reaction of isocyanate group with the carboxylic acids. Unstable structure of anhydride is shown in the square brackets.

It should be noted that isocyanates can even react with themselves with the formation of the oligomeric and polymeric products [359]. Moreover, the formation of dimers of aromatic NCO-containing molecules is highly possible. It is influenced by the nature of the aromatic ring: TDI can not form such structures at ambient conditions, while MDI is one of the best representatives of such a behavior [357]. Together with aliphatic isocyanates and the additional heating, aromatic isocyanates can form trimeric structures.

On the one hand, isocyanates are toxic reagents, but on the other hand, their high reactivity enables a lot of versatile and flexible reactions to produce PU polymer. Among the most important and frequently used commercially isocyanates for the polyurethane synthesis are: TDI, 2,4-diisocyanato-1-methylbenzene and MDI, 1,1'-methylenebis(4-isocyanatobenzene) [71, 357] (see Figure 5.1: a, b). TDI diisocyanate is often used in different mixtures of 2,4-TDI and 2,6-TDI, which differ with the position of the second isocyanate group. MDI and TDI are taken as the diisocyanates representatives in the studies conducted in the present PhD thesis.

5.2 Polyethylene glycol: new perspectives for polyurethanes

The second main type of monomer used to obtain polyurethanes is polyol, which builts the soft segments of the polymer (see Chapter 2). Polyols is a huge group of chemical compounds which contain several hydroxyl groups. The main chain of the polyol can be of different nature. We can distinguish two main types of polyols used to produce the PU polymers: polyether and polyester. The schematic structural formulae of polyols are depicted in Figure 5.6. These compounds belong to the low molecular weight polymers that are used

(a) (b)

Figure 5.6: The general structural formulae of polyols: (a) polyether polyol, (b) polyester polyol.

in PU synthesis with molecular weight in the range of 500–3000 g/mol. Polyols of higher molecular weight are also possible, but they are used in other applications. Polyols belong to the group of hydrogen active compounds, therefore, they react with isocyanates according to the mechanism shown in Figure 5.3.

One of the popular polyether type polyol, used to synthesize polyurethanes, is polyethylene glycol (PEG). PEG is an amphiphilic polyol [360] which consists of the ethylene glycol/ethylene oxide (–O–CH_2–CH_2–) repeat units (Figure 5.6: a). PEG has high structural flexibility, extremely low immunogenicity and nontoxicity [361, 362]. It is characterized with an excellent pharmacokinetic and biodistribution behavior [363]. Polyethylene glycol has various applications, which are directly dependent on its molecular weight [364]. This chemical compound is used in medical [365, 366], chemical [367, 368] and biological [369] applications, for example for the conjugation of proteins, drugs, oligonucleotides [370], liposomes [371], polymeric nanoparticles [372] or carbon nanotubes [373, 374, 375]. Moreover, PEG characterizes with high viscosity (e.g. 50 cP for PEG(200) at 25°C), as a result, it can be used as solvent to disperse and stabilize carbon nanotube solutions [368, 376] and to prevent agglomeration of metal nanoparticles [367]. Generally, the process of the surface modification with PEG molecules is known as PEGylation [366, 377], which is used in drug delivery, targeting and vaccination. The main aim of the PEGylation is to obtain high concentrations of PEGylated drugs in aqueous solutions with the lowering of their cytotoxicity and immunogenicity, and with longer circulation time of the drug [366, 370].

In the polymer synthesis, PEG can be used as either monomer or chain extender. It was reported to be used in the production of shape memory PUs [365, 378], thermo-responsive PU hydrogels [379], PU-based materials for medical devices [380] and in tissue engineering applications [6, 72, 381] etc. Moreover, biodegradable polyurethanes [382] are also produced with PEG, which increases water permeability both in bulk and surface, making the polymer material more sensitive to the degradation [72, 73]. As the result of its excellent physical and mechanical properties [38, 383], and high biocompatibility, PEG is mainly used to obtain materials for biomedical applications [384, 385]. PEG-modified single-walled carbon nanotubes were investigated as diagnostic devices and controlled drug-release systems [386]. It was also reported that the toxicity of carbon nanotubes can be effectively reduced with the additional modification with PEG [386, 387]. H. Shi et al. [387] have investigated PEG-modified polyurethanes with carbon nanotubes in preparing infection-resistant wound dressings.

In the literature there are a lot of recently reported investigations on the usage of PEG-based

materials. The usage of polyethylene glycol in the polyurethane synthesis opens new perspectives of the potential usage of these polymer materials. Such materials, additionally modified with carbon nanotubes, can be of great importance for the biomedical applications. This fact, together with the simplicity of its molecular structure, influenced PEG to be analyzed in the present PhD thesis.

5.3 Composites based on diisocyanates, polyethylene glycol and carbon nanotubes

Introduction to the present thesis (Chapter 2) covers the general aspects of the polyurethane popularity, synthesis and various applications. Also, there was described the novel usage of carbon nanotubes as a polymer filler to enhance and reinforce the properties of the PU polymer matrix. Different types of PUs were modified with CNTs [2, 8, 19, 21, 24, 30, 44, 55, 56]. Among them are polyurethanes based on such monomers as:

- TDI and PEG (used as controlled drug delivery systems [74]),
- MDI and PEG (used as new shape memory materials [75]).

Different types of carbon nanotubes are taken to modify such polymer matrices, for example CNTs with covalently attached carboxyl groups [8, 44]. Such CNTs were found to have better interfacial adhesion with PU polymer matrix than the noncovalently modified carbon nanotubes [388]. As a result, CNT-COOH are often used in PU synthesis. Y. Jung et al. [389] also reported that CNT-COOH carbon nanotubes, which are easily formed during CNT purification, have better dispersion in the polyurethane matrix. The same conclusions were made during the studies of the reinforcing effects in the shape memory PU polymers after their modification with CNTs [347]. Authors have clearly showed that the CNT-COOH carbon nanotubes have better reinforcing effects as the result of better dispersion efficiency between the CNT and the polymer. Moreover, they have proven that functionalization of COOH-modified carbon nanotubes with MDI significantly influences the CNT dispersion and increases the strength of interactions between the filler and PU matrix, where filler acts like a chain extender. The increase of CNT-COOH dispersion after the covalent attachment with diisocyanate molecules was also shown in Ref. [390]. The mechanism of diisocyanate reaction with the COOH-modified surface of carbon nanotubes was established by M. Dresselhaus et al. [36] on the basis of IR measurements. Chemically active isocyanate groups reacts significantly with the carboxyl groups on the CNT surface.

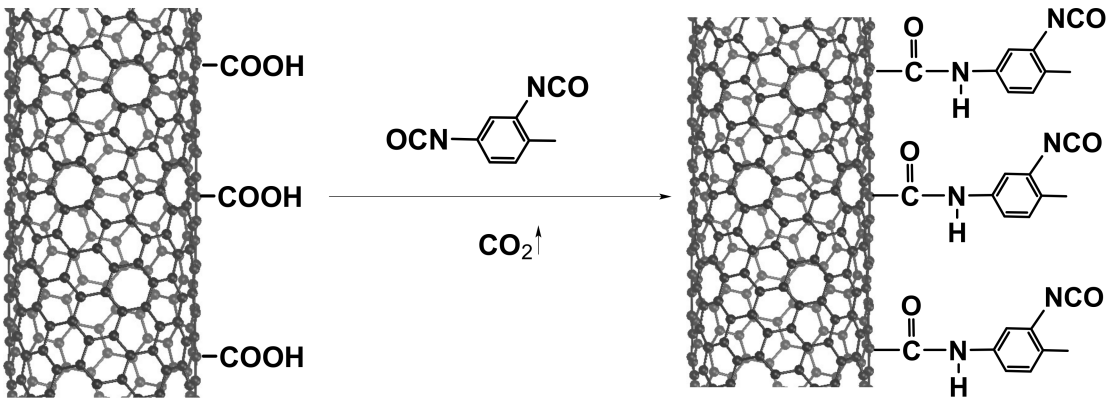

Figure 5.7: Schematic attachment of 2,4-diisocyanato-1-methylbenzene (TDI) to the surface of COOH-modified single-walled carbon nanotube by the urethane bond formation.

Better reinforcing properties of CNT-modified polyurethanes, where MWCNTs were addi-

tionally covalently functionalized by the MDI molecules, were also recently reported by M. Lopes et al. [391]. They used different techniques, including High Resolution Magic Angle Spinning Nuclear Magnetic Resonanse of ^{13}C spectra, to identify the exact structure of the MDI molecules covalently attached to the CNT surface. The confirmed structure of CNT-MDI system was the same as reported previously by C. Zhao et al. [390], Y. Jung et al. [36] and T. Richardson et al. [347]. The reaction between COOH-functionalized carbon nanotubes and diisocyanates, described in the mentioned publications to obtain CNT-MDI and CNT-TDI surfaces, is summarized in Figure 5.7.

In the literature, there are a lot of experimental studies on the usage of CNT-MDI and CNT-TDI during the PU synthesis, but there is no explanation of the increase of CNT dispersity after their surface modification with diisocyanates. Moreover, there is no detailed investigation of the additional hydrogen bonds in such systems. Taking into account the reported structures of CNTs modified by diisocyanates, the quantum-chemistry calculations and molecular dynamics simulations are used in the present PhD thesis to estimate the fundamental interations in either these systems or PEG-modified. Even if PEG is used to increase CNT dispersion during polyurethane synthesis [368, 376], CNT were reported to be in the form of bundles [386] in the PEG solutions. A lot of noncovalent interactions are responsible for such behavior, but there is the lack of such information.

Chapter 6

Methods

Nowadays, theoretical prediction of the properties of chemical compounds and their possible reaction mechanisms is an inherent part of the experimental investigation of novel materials, drugs, devices and various molecular systems. Since the high development of the nanotechnology in the previous century, scientists are interested in obtaining nanoscale systems, which are characterized with the better properties and higher activities, e.g. catalytic activity, in comparison with the macroscopic systems. In many cases, it is very hard task to obtain and analyze such systems using only experimental techniques. The same problem was mentioned in case of carbon nanostructures in Section 4.4. Properties of nanomaterials strongly depend on their structural parameters and purity. As it was mentioned before, the equal dispersion of carbon nanotubes in the polymer matrix significantly depends on the intermolecular and interfacial interactions. Such interactions can not be analyzed precisely using the experimental methods only. As a result, additional studies, based on theoretical calculations, should be made.

6.1 Introduction and main approximations

Modern computational chemistry consists of two main branches, i.e. quantum mechanics (QM) and molecular mechanics (MM) methods. Most of QM methods (i.e. *ab initio*, first principles), which calculate electronic structures and properties of molecules and solids, are based on the Schrödinger equation, which describes a many-body system consisting of nuclei and electrons by introducing a many-electron wavefunction ψ and Hamiltonian operator $\hat{H}$:

$$\hat{H}\psi = E\psi \tag{6.1}$$

Here, Hamiltonian operator is defined as:

$$\hat{H} = -\frac{1}{2}\sum_{i}^{el}\nabla_i^2 - \frac{1}{2}\sum_{A}^{nuclei}\frac{1}{M_A}\nabla_A^2 - \sum_{i}^{el}\sum_{A}^{nuclei}\frac{Z_A}{r_{iA}} + \sum_{i<j}^{el}\sum\frac{1}{r_{ij}} + \sum_{A<B}^{nuclei}\sum\frac{Z_A Z_B}{R_{AB}}, \tag{6.2}$$

where Z is the nuclear charge, M_A is the ratio of mass of nucleus A to the mass of an electron, R_{AB} is the distance between nuclei A and B, r_{ij} is the distance between electrons i and j and r_{iA} is the distance between electron i and nucleus A. Exact prediction of ground state energy of the system is very complicated task. It is possible only for small molecular systems consisted of several simple atoms. Among the most known QM methods are Hartree–Fock method, Møller–Plesset Perturbation Theory, Configuration Interaction and Coupled–Cluster. All of them are based on the wavefunction calculations. The most sophisticated method is Coupled–Cluster, which approach with single and double and perturbative triple excitations, CCSD(T), is known as a "golden standard" in quantum chemistry.

The computational cost of the mentioned methods is very high (except Hartee–Fock method, but it does not take into consideration correlation effects), e.g. N^5–N^7, where N is the amount of electrons in the system. Therefore, such calculations can be performed only for small systems. Theoretical approach, which is based on Hartree–Fock formalism, but has many additional approximations is known as semi-empirical QM method. It can be used for large systems, but still it possesses a great amount of approximations. Later, Density Functional Theory (DFT) approach, which is based on electron density calculations instead of wavefunction, was introduced. Its scalability is similar to Hartree–Fock method (N^3), but the accuracy of DFT calculations is close to post-Hartree–Fock methods, which are known as high-level *ab initio* wavefunction theory methods. As the result, larger molecular systems can be effectively calculated with the precision of *ab initio* methods.

Pure QM methods can be applied only for several atoms. To solve this problem some approximations are used, i.e. Born–Oppenheimer approximation, lack of the relativistic effects, some approaches to calculate correlation energy, pseudopotentials for atoms, periodic boundary conditions, and others. Born–Oppenheimer (BO) approximation was proposed in 1927 by M. Born and R. Oppenheimer [392] and it simplifies the mentioned Schrödinger equation (Equation 6.1). BO approximation separates the motion of heavy nuclei from that of light electrons. According to the approximation, nuclei do not move, because they are too heavy comparing with electrons, therefore, their motion is skipped in the calculations (the last term in the Hamiltonian, Equation 6.2), i.e. the value of this term in Hamiltonian is constant. As a result, only motion of "fast" and "hot" electrons is taken into account.

Contrary to QM methods, molecular mechanics (MM) methods represent atoms as balls connected with springs and do not include the description of the electronic structure of the system. They use empirical force fields (potentials), parametrized againt experimental data, to predict the properties of the system. MM methods are based on a classical Newton equations of motion in the simulation of molecular dynamics. The most important limitation of MM is the lack of the description of reactive events, because the parameters are fixed and force fields used are unable to adapt to changes in chemical enviroment. MM methods are efficient and computationally cheap tools for the description of huge molecular systems, but they can not be used to analyze bond breaking and formation, taking into account electronic structure of the system.

In our case the analyzed systems are quite complex and typical *ab initio* methods cannot be directly applied due to a high computational cost. At the same time, MM methods can not be used to analyze inter- and intramolecular interactions in detail. From this reason, Density Functional Theory approach, which is often used to tackle intermolecular interactions in large systems, is used. Additionally, Car–Parrinello molecular dynamics (CP–MD) simulations are used to analyze the structural changes and bond breaking/formation in the systems analyzed at finite temperature and time.

6.2 Density Functional Theory

6.2.1 General information

Density Functional Theory (DFT) is based on the fact that the electron density $\rho(r)$, which depends only on the three coordinates (x, y, z), defines the ground-state energy of the system. As it was mentioned above, here $\rho(r)$ is used instead of the many-electron wavefunction in the Schrödinger equation (Equation 6.1). The first *seed* of DFT was the Thomas-Fermi theory, introduced in 1927 [393, 394]. It was a new method for finding the electronic structure of atoms using only the one-electron ground-state density. According to this theory, electrons are distributed uniformly in each small volume element of atom, while the electron density

ρ(r) varies from one small volume element to the next. Thus, energy of the system depends on density fluctuations. This theory has a lack of exchange effects and the kinetic energy is very approximate, as a result, it gives a poor description of real systems.

In 1964 P. Hohenberg and W. Kohn formulated two theorems [395], which lie in the base of the original DFT approach. The first theorem states that the external potential V(r), therefore, the total energy of the system, is a unique functional of the electron density ρ(r). Thus, the energy can be demonstrated in the following way:

$$E[\rho(r)] = \int \rho(r)V(r)dr + F[\rho(r)] \tag{6.3}$$

$$\rho(r) = \frac{\delta E[V]}{\delta V(r)}, \tag{6.4}$$

where F[ρ(r)] is an unknown universal functional of the electron density.

$$F[\rho(r)] = T[\rho(r)] + V_{ee}, \tag{6.5}$$

where T[ρ(r)] and V_{ee} are the kinetic energy and the electron–electron repulsion energy. The electron density ρ(r) depends on three spatial coordinates, as a result, electrons determine the positions of the nuclei in a system, and also all ground-state electronic properties. Hamiltonian of the system (Equation 6.2) is defined by the mentioned external potential V and F. The second theorem formulates that the density that minimizes the total energy is the exact ground-state density, which can be obtained variationally:

$$\frac{\delta F[\rho(r)]}{\delta \rho(r)} = 0. \tag{6.6}$$

Two Hohenberg–Kohn theorems can be used to any system, which consists of electrons that move under the influence of the external potential V(r). At the same time, they are held only for non-degenerate ground states when there is a lack of magnetic field. The mentioned theorems are very powerful, but they do not propose a good way to calculate the ground-state density of the system. The solution is the Kohn–Sham equations [396].

W. Kohn and L. Sham suggested to replace the kinetic energy T[ρ(r)] in Equation 6.5 with that of an equivalent non-interacting system, because it can be easily estimated [396]. Therefore, in Kohn–Sham equations F[ρ(r)] consists of the classical Coulomb repulsion J[ρ(r)] and the kinetic energy T_s[ρ(r)] corresponding to the non-interacting orbitals, known as KS orbitals, ψ_i. The density of ψ_i equals to the density of the real system with interacting electrons. It can be represented as follows:

$$F[\rho(r)] = T_s[\rho(r)] + J[\rho(r)] + E_{xc}[\rho(r)] \tag{6.7}$$

$$T_s[\rho(r)] = -\frac{1}{2}\sum_i^N < \psi_i|\nabla^2|\psi_i > \tag{6.8}$$

$$J[\rho(r)] = \frac{1}{2}\int drdr' \frac{\rho(r)\rho(r')}{|r-r'|} \tag{6.9}$$

$$\rho(r) = \sum_i^N |\psi_i(r)|^2. \tag{6.10}$$

All underfined contributions to the energy, including non-classical part of electron–electron interactions, the difference in kinetic energy between the KS non-interacting and real interacting system, are presented by the exchange-correlation functional E_{xc}[ρ(r)] in Equation 6.7.

Exchange-correlation functional, $E_{xc}[\rho(\mathrm{r})]$, can be found exactly, but only for small systems. In practice, different approximated exchange-correlation contributions are used [397].

Taking into account the minimization of the energy when $<\psi_i \mid \psi_j> = \delta_{ij}$, the Kohn–Sham equation can be formulated (see Equation 6.1 for comparison) as:

$$(-\frac{1}{2}\nabla^2 + v(r) + \frac{\delta J}{\delta\rho(r)} + \frac{\delta E_{xc}}{\delta\rho(r)})\psi_i = \varepsilon_i\psi_i, \tag{6.11}$$

where

$$\frac{\delta J}{\delta\rho(r)} = \int dr' \frac{\rho(r')}{|r - r'|} \tag{6.12}$$

$$\frac{\delta E_{xc}}{\delta\rho(r)} = v_{xc}. \tag{6.13}$$

The sum in Equation 6.11:

$$v_{eff} = v(r) + \int dr' \frac{\rho(r')}{|r - r'|} + v_{xc} \tag{6.14}$$

is known as effective potential v_{eff} of Kohn and Sham. It should be also noted that in case of the true expression of v_{xc}, the solving of Kohn-Sham equations is the same as the solving of exact Schrödinger equation (Equation 6.1) with Born–Oppenheimer approximation.

Kohn–Sham formulation of DFT (known as KS–DFT) gives a useful method to the calculation of the ground-state energy and electron density. Moreover, it uses similar algorithms as Hartree–Fock theory (as the result the scalability of DFT and Hartree–Fock is similar), but it gives more realistic parameters of the calculated systems, taking into account exchange and correlation energies.

6.2.2 Approximations and functionals

The correct description of the ground-state energy in DFT significantly depends on the accuracy and the exchange-correlation energy. Unfortunately, the correct form of the exchange-correlation energy v_{xc}, thus, the exchange-correlation functional E_{xc} (Equation 6.11), is not known. Several methods to approximate DFT exchange-correlation functional were proposed. Among them is local density approximation (LDA), which is the simplest one, but it assumes that the system behaves locally, i.e. as a uniform gas:

$$E_{xc} = \int \rho(r)\varepsilon_{xc}^{LDA}(\rho(r))dr, \tag{6.15}$$

where ε_{xc}^{LDA} is the density of exchange-correlation energy per electron of a uniform electron gas of density ρ. The exchange part of ε_{xc}^{LDA} is analytical value:

$$\varepsilon_x^{LDA} = -\frac{3}{4}(\frac{3}{\pi})^{1/3}\rho^{1/3} \tag{6.16}$$

and correlation energy was obtained from accurate quantum Monte Carlo calculations [398] with additional parametrization [399]. LDA approximation is applicable to systems with slowly changing density, therefore, it usage for inhomogeneous systems, such as atoms and molecules, is insufficient.

Among the non-local or gradient-corrected approximations of the exchange-correlation functional is generalized gradient approximation (GGA), in which E_{xc} depends on the electron density, $\rho(\mathrm{r})$, and its gradient, $\nabla\rho(\mathrm{r})$, at a given point in space:

$$E_{xc} = \int \rho(r)\varepsilon_{xc}^{GGA}(\rho(r), \nabla\rho(r))dr. \tag{6.17}$$

In comparison to LDA, GGA can be successfully used for the systems with rapid changes of the density. There is no only one form of ε_{xc}^{GGA}, like in LDA, because different GGA functionals can be used, which differ in the amount of empiricism in their construction and in the number of other parameters. Different exchange GGA functionals, e.g. Perdew–Burke–Ernzerhof (PBE), Perdew–Wang 1986 (PW86), Becke 1988 (B88), and gradient-corrected correlation functionals, e.g. Lee–Yang–Parr (LYP), are known. The best results are obtained in case of the combination of exchange and correlation functionals, e.g. Becke–Lee–Yang–Parr (BLYP) functional. Among the most popular exchange-correlation functional in solid-state calculations, which gives accurate geometries and qualitatively correct electronic band structures, is PBE functional [400], which is non-empirical one. PBE, together with BLYP functional, are used in the present PhD thesis to estimate the properties of different systems.

Even if GGA is better than LDA approximation, it still possesses some differences in comparison with the experimental values. As a result, hybrid GGA and meta-GGA functionals were reported. In hybrid GGA, e.g. B3LYP functional, the exact amount of exchange and correlation contributions are introduced. That is why, hybrid functionals are no longer semilocal. It was estimated that the exchange contribution is significantly larger than the correlation one, so the introduction of the exact exchange influence positively on the obtained calculations. Hydrid GGA are more expensive than GGA for solid state calculations, so they are not often used. Among meta-GGA are Minnesota funtionals, known as M05, MN-15, MN15-L etc. Meta-GGA functionals include additionally the Kohn-Sham kinetic energy density and the Laplacian of the electron density, so the functional is more "flexible":

$$E_{xc} = \int \rho(r)\varepsilon_{xc}^{GGA}(\rho(r), \nabla\rho(r), \nabla^2\rho(r), \tau_{KS}(r))dr, \tag{6.18}$$

$$\tau_{KS}(r) = -\frac{1}{2}\sum_i |\nabla_i(r)|. \tag{6.19}$$

There are no density functionals able to describe the dispersion interactions in the analyzed systems. As it was mentioned in Section 3.1, London dispersion interactions exist in all atoms and molecules. They are decisive forces in case of non-polar compounds and complex structures formed with these molecules. As a result, pure DFT method is not accurate in the calculation of noncovalent interactions. This problem can be solved with the addition of extra dispersion corrections. Different types of such corrections are known nowadays, for example: Grimme D2 [142], Grimme D3 [143], Tkatchenko–Scheffler [144]. Moreover, the usage of specially designed pseudopotentials, e.g. Dispersion-Corrected Atom-Centered Potentials, DCACP [145, 146], increase the accuracy of DFT. In the present studies, the dispersion correction Grimme D2 is used to treat the precisely noncovalent interactions.

DFT-D functionals (Grimme functionals) are common known and widely used dispersion corrections nowadays. They are based on the pairwise dispersion energy correction $E_{disp}^{(2)}$, which is the leading term in the multipolar expansion of the intermolecular interaction:

$$E_{disp} = E_{disp}^{(2)} + E_{disp}^{(3)} + ... \tag{6.20}$$

$$E_{disp}^{(2)} = E_6^{(2)} + E_8^{(2)} + E_{10}^{(2)} + ... = -\sum_{n=6,8,10,...}\sum_{A>B} C_n^{AB} R_{AB}^{-n} f_n(R_{AB}), \tag{6.21}$$

where C_n^{AB} is the dispersion coefficient, R is an intermolecular distance, f_n is a family of functions that account for the approximate nature of the multipolar expansion at the short range. $E_{disp}^{(2)}$ contains terms of order higher than the dipole–dipole interactions.

The first reported Grimme correction [401] is based only on the C_6 coefficient and a global scaling factor s_6:

$$E_{DFT-D} = -s_6 \sum_{i>j} \frac{C_6^{AB}}{R_{AB}^6} f_{damp}(R_{AB}), \tag{6.22}$$

where the damping function $f_{damp}(R)$ is formulated as a function:

$$f_{damp}(R) = \frac{1}{1 + exp(-\alpha(R/R_0 - 1))}, \tag{6.23}$$

where R_0 is a quantity that represent the atomic size. In Grimme D2 dispersion correction, which was the most popular dispersion correction for the last years (before the introduction of the latest Grimme D3 in 2010), the dispersion coefficient is defined as:

$$C_6^{AB} = \sqrt{C_6^{AA} C_6^{BB}}. \tag{6.24}$$

For homoatomic coefficients:

$$C_6^{AA} = 0.05 N I_p^A \alpha^A, \tag{6.25}$$

where N is the atomic number of the noble gas on the same period as A, I_p^A is the atomic ionization potential, α^A is the atomic static polarizability in vacuum. Because of its popularity Grimme D2 was implemented in various software packages. In some of them it is still used, but in others Grimme D2 is replaces by the Grimme D3 dispersion correction, which is based on more complicated than D2 and has coefficients dependent on the geometry, not on the electron density. DFT-D3 is based on the pre-computed quantities using time-dependent DFT method.

6.2.3 Plane waves and pseudopotentials

Basis set is a set of functions, which are mixed in linear combinations to create molecular orbitals used in the QM calculations. Among different types of basis set used in QM are plane waves (PW), which form a complete and orthonormal basis. PW are defined as:

$$f_G^{PW}(r) = \frac{1}{\sqrt{\Omega}} exp[iG \cdot r], \tag{6.26}$$

where Ω represents the cell volume and G is the reciprocal space vector. For a particular QM calculations using DFT the exact amount of Kohn–Sham orbitals (see Equation 6.10) is needed. Kohn–Sham orbitals can be expanded:

$$\psi_i(r) = \frac{1}{\sqrt{\Omega}} \sum_G c_i(G) exp[iG \cdot r] \tag{6.27}$$

and this expansion should be truncated at the energy cutoff:

$$E_{cut} = \frac{1}{2} G^2. \tag{6.28}$$

The value of the energy cutoff estimates the amount of the PW used to calculate the system:

$$N_{PW} = \frac{1}{2\pi^2} \Omega E_{cut}^{3/2} \tag{6.29}$$

therefore, determines the accuracy of the calculations. Larger cutoff results in greater amount of PW and more accurate calculations. At the same time, such calculations are expected to be more computationally expensive.

PW do not depend on the nuclei positions, they have lack of basis set superposition error in the estimation of the interaction energy. Moreover, PW are expanded on the whole periodic cell (initially estimated before the calculations maintaining the periodic boundary conditions, PBC) uniformly without favoring any region. From this reason, PW basis set enables to calculate systems with periodic nature, taking into account influence of the PBC images. PW is an ideal basis set for the obtaining properties of such translational systems as carbon nanotubes, which are the main subjects of the present PhD thesis. One of the disadvantages of PW is the lack of the way to add more basis functions into the regions in the space, where they are more necessary than in the other regions.

To decrease the number of the PW necessary for calculations, core electrons are replaced by pseudopotentials (PP), which belong to a kind of approximation, where only the valence electrons are considered in the calculations, whereas the energy of the core states is constant, so the core electrons are "frozen". Such approach enables to produce pseudo wavefunctions, which mimic the full wavefunctions outside a core radius. There are different types of PP in DFT, e.g. norm-conserving (Troullier–Martins [402], Goedecker–Teter–Hutter [403] etc.) or ultrasoft pseudopotentials, known as Vanderbilt Ultrasoft Pseudopotentials (USPP) [404, 405]. Depending on the PP type chosen for calculations the energy cutoff E_{cut} is defined, which directly influences the accuracy of such calculations.

6.2.4 Advantages and disadvantages

As one can see, DFT method is based on different approximations, which make such approach to recede from *ab initio* calculations. From this reason, some scientists do not classify DFT to first principles calculations. Most of quantum chemists, nowadays, suggest that, with the usage of efficient and reliable exchange-correlation functionals and fitted pseudopotentials, DFT is a powerful tool that enables to perform theoretical calculations on the QM level. Taking into account extremely high computational cost of pure *ab initio* methods, DFT is one of the most reliable tool to estimate properties of larger systems using their electron structure. With the development of high-accuracy dispersion corrections, DFT can be also used to calculate noncovalent interactions in various molecular systems. Finally, with the usage of PW approach, DFT is a resonable method in the calculation of properties of solids and periodic systems. There are a lot of scientific reports concerning the usage of DFT in obtaining properties of such periodic systems as carbon nanotubes. Among them are sidewall functionalization of SWCNT with carboxyl, amine and amide functional groups [209, 350, 406], mechanism of carboxylation of vacancy-defective SWCNT and its influence on the electronic properties of carbon nanotubes [407], noncovalent functionalization of SWCNT by conjugated or epoxy polymers [62, 351] etc. The recent review on the development of DFT and its usage, which covers this approach in more detailed manner, is available in Ref. [397, 408, 409].

6.3 Car–Parrinello molecular dynamics

In computational chemistry both static and dynamical calculations can be performed. During static calculations the wavefunction and the geometry of the system analyzed are obtained using the predefined structure and position of the molecules. Static calculations are performed at the temperature of 0 K, so the parameters do not correspond directly to the real conditions. This disadvantage of static calculations is fulfilled with the usage of molecular dynamics (MD) simulations, in which desired temperature and preassure can be taken into account. MD simulations are able to mimic real conditions of the system at the given timescale, therefore, structural rearrangements and changes of the properties of the system, as the result of different interactions, can be obtained.

MD simulations can be performed with the usage of *ab initio* methods or molecular mechanics, i.e. classical methods. Because of the fact that classical MD methods are not able to describe intermolecular interactions in the system on the basis of its electron structure, the *ab initio* MD (AIMD) methods are performed to get the understanding of functionalization of carbon nanotubes. From this reason, a brief description of AIMD is presented here.

6.3.1 *Ab initio* molecular dynamics in brief

The main idea of *ab initio* MD is to generate the dynamical trajectory of the molecular system with the usage of forces computed directly (on the fly) from electronic structure calculations, for example, based on DFT calculations. For this purpose, AIMD is the combination of *ab initio* electronic structure methods and molecular dynamics based on Newton's equations of motion. AIMD is the best tool for the description structural rearrangements of the system, taking into account bond breaking and formation. With its algorithms, AIMD simulations are much more computationally demanding than the classical methods, so the system size and the simulation time are restricted to hundred of atoms and the picosecond timescale. There are two main *ab initio* MD approaches used in the simulation: Born–Oppenheimer molecular dynamics (BO–MD) and Car–Parrinello molecular dynamics (CP–MD). They both are based on the mentioned Born–Oppenheimer approximation, according to what: the ionic and electronic degrees of freedom can be separated adiabatically at all points in the phase space.

In general, Born–Oppenheimer MD is more accurate approach for the obtaining the real properties of the molecules in the simulated trajectory. It uses the re-minimization of the electron wavefunction, i.e. calculate the electronic structure of the system, at each timestep of the simulation, therefore, the computational cost of such calculations is very high. BO–MD is limited only for the simulation of small molecular systems (tens of atoms).

In the second approach, Car–Parrinello MD, the electron structure of the system is calculated only once, for the initial structure, as the result, the computational cost of such simulations decreases dramatically and systems consisted of hundreds of atoms can be analyzed. This approach is an extended Lagrangian formulation, where both nuclear and electronic degrees of freedom act as dynamic variables [410]. Car–Parrinello molecular dynamics was proven to be in good comparison with Born–Oppenheimer MD [69, 70].

6.3.2 CP–MD: general information

Car–Parrinello molecular dynamics approach is based on the transformation of quantum adiabatic time-scale separation of fast electron and slow nuclear motion into the classical adiabatic energy-scale separation for molecular dynamics. As a result, the time-independent Schrödinger equation (Equation 6.1) is solved only once and on its basis the MD trajectory, using Euler–Lagrange equations (in the CP form) of motion, is calculated. Taking into account Euler–Lagrange equations of motion:

$$\frac{d}{dt}\frac{\partial \mathcal{L}_{CP}}{\partial \dot{R}_I} = \frac{\partial \mathcal{L}_{CP}}{\partial R_I} \tag{6.30}$$

$$\frac{d}{dt}\frac{\delta \mathcal{L}_{CP}}{\delta \dot{\psi}_i^*} = \frac{\delta \mathcal{L}_{CP}}{\delta \psi_i^*} \tag{6.31}$$

the Car–Parrinello equations can be written as:

$$M_I \ddot{R}_I(t) = -\frac{\partial}{\partial R_I} < \Psi_0 | \mathcal{H}_e | \Psi_0 > + \sum_{ij} \Lambda_{ij} \frac{\partial}{\partial R_I} < \psi_i | \psi_j >, \tag{6.32}$$

$$\mu\ddot{\psi}_i(t) = -\frac{\delta}{\delta\psi_i^*} < \Psi_0|\mathcal{H}_e|\Psi_0 > + \sum_j \Lambda_{ij}\psi_j. \tag{6.33}$$

As a result, the Car–Parrinello Lagrangian (equation of motion) can be formulated as:

$$\mathcal{L}_{CP} = \frac{1}{2}\sum_I M_I\dot{R}_I^2 + \frac{1}{2}\sum_i \mu < \dot{\psi}_i|\dot{\psi}_i > - < \Psi_0|\mathcal{H}_e|\Psi_0 > + \sum_{ij}\Lambda_{ij}(< \psi_i|\psi_j > -\delta_{ij}). \tag{6.34}$$

Its first and second elements denote the kinetic energies of the nuclei and the electrons; the third part is the Kohn–Sham energy (potential energy), while the last one is responsible for the orbitals to stay orthonormal. R. Car and M. Parrinello introduced an additional value in their equation, i.e. fictitious mass μ (an inertia parameter), which is assigned to the orbital degrees of freedom. Fictitious mass parameter is responsible for maintaining the adiabatic separation of nuclear and electronic degrees of freedom. Car–Parrinello scheme can be described with "cold electrons" ("low electronic temperature"), which enable the electronic subsystem to be close to Kohn–Sham energy, therefore, close to the exact Born–Oppenheimer surface. It can be made only when a ground-state wavefunction, optimized at the beginning, will stay close to its ground state during MD simulations. That is why, it is so important to separate the motion of nuclei and electrons [411, 412]. The energy transfer between ion and electron subsystems can be assured via vibration spectra from both subsystems, which main frequency domain can not overlap. To control the energy transfer between subsystems specially designed thermostats might be used. Among them are, e.g., Berendsen thermostat, Langevin thermostat, Nosé–Hoover thermostat.

Nosé–Hoover thermostat [413, 414] is often used in the canonical ensemble calculations, when the constant temperature of the simulations should be kept. In CP–MD method thermostating on both ions and fictitious electrons is possible. With the addition of Nosé–Hoover thermostat in the CP–MD, the mentioned CP–MD equations (see Equations 6.32, 6.33) are changed:

$$M_I\ddot{R}_I(t) = -\frac{\partial}{\partial R_I} < \Psi_0|\mathcal{H}_e|\Psi_0 > + \sum_{ij}\Lambda_{ij}\frac{\partial}{\partial R_I} < \psi_i|\psi_j > -M_I\dot{R}_I\dot{x}_R \tag{6.35}$$

$$\mu\ddot{\psi}_i(t) = -\frac{\delta}{\delta\psi_i^*} < \Psi_0|\mathcal{H}_e|\Psi_0 > + \sum_j \Lambda_{ij}\psi_j - \mu\dot{\psi}_i\dot{x}_e, \tag{6.36}$$

where the last terms in both equations 6.35 and 6.36 are added. They are friction terms which couple atoms and wavefunctions dynamics to the thermostats; x_R and x_e can be obtained from the equation:

$$Q_R\ddot{x}_R = 2[\frac{1}{2}\sum_I M_I\dot{R}_I^2 - \frac{1}{2}gk_bT], \tag{6.37}$$

where $g = 3N$ is the number of degrees of freedom, k_b is a Boltzmann constant and T is the physical temperature of the system, and equation:

$$Q_e\ddot{x}_e = 2[\sum_i \mu < \dot{\psi}_i|\dot{\psi}_i > -E_{kin,e}]. \tag{6.38}$$

The average kinetic energy of the ionic and fictitious electronic subsystem is presented by the last term in Equation 6.37 and Equation 6.38, respectively.

6.3.3 CP–MD in practice

Car–Parrinello MD scheme is a common known algorithm used for various analyses and predictions. It is a good choice in theoretical simulations to include temperature and conformational dynamics with entropic effects, which are taken into account directly during

computations. In CP–MD no parametrization of an empirical potential is needed, thus only nature of molecules determines the reaction path. As a result, CP–MD scheme can be used for different purposes. In general, Car–Parrinello MD is mainly used to solve problems in the field of physics, but in the last decade it was extended to chemistry and biochemistry. There are a lot of reports concerning the usage of CP–MD to analyze intra- and intermolecular interactions, their strength, lifetime and rearrangements for different molecular systems at finite temperature. Among the most extensive studied system using CP–MD is liquid water. Using different CP–MD simulations of water, this MD approach was proven as a good substituent [415, 416, 417, 418] for BO–MD in case of larger systems, which are too expensive to be calculated by BO–MD.

CP–MD was also used to estimate structural and dynamical properties of thiophene in supercritical CO_2, where the special focus was given to microscopic interactions and solvation dynamics [419]. It is often used to analyze the hydrolysis reactions and the structure of the solvation shell around different ions, e.g. electroactive vanadium cations [420]. In such calculations quantum effects of water, proton transfer and diffusion coefficients are efficienly taken into account, therefore, the results obtained are close to the real nature of molecular systems analyzed. Moreover, the results from CP–MD can be directly compared with high-resolution experimental investigation of molecules trapped in different matrices at very low temperatures (e.g. 10–30 K) [421]. Finally, this approach is of great importance in the analysis of biomolecules, especially when the electronic properties of their specially designed regions (e.g. places of inhibition, places of enzymatic reactions) should be obtained. One of the latest overview in this field is decribed in Ref. [422].

Since CP–MD can be successfully used with periodic boundary conditions (the usage of plane waves basis set for DFT calculations), e.g. in CPMD code [423], this approach can be utilized to simulate such systems as carbon nanotubes. In the literature, there are a lot of reports devoted to the studies of CNT using CP–MD, e.g. investigation of chemisoption process on different CNT surfaces [424], analysis of magnetic properties and interactions between iron atoms and SWCNT [425], description of the process of growth of gallium nitride on CNTs [426] etc. Moreover, CP–MD simulations were used to understand the Stone–Wales transformation and intramolecular reorganization in carbon nanotubes [427], as also to estimate the influence of structural defects on the surface of CNT on the adsorption of NO_2 [428]. Functionalization of the surface of carbon nanotubes was also investigated with CP–MD, for example the effect of endo- and exohedral functionalization with fluorine with the detailed analysis of the density of states (DOS, see Section 4.1.2) and interactions in such systems [429]. Car–Parrinello MD was also used to characterize the surface reactivity of different catalysts based on the carbon materials with the evaluation of the interactions between the catalyst surface and reagents.

Chapter 7

Computational details

The present PhD thesis is focused on the analysis of different intra- and intermolecular interactions between molecules during covalent and noncovalent functionalization of single-walled carbon nanotubes (SWCNTs). To describe such subtle interactions theoretical calculations, either static or dynamic, are employed. In this Chapter the initial test calculations and the computational set-up of theoretical calculations made are presented. It should be noticed that the molecular systems analyzed in the thesis, i.e. models of functionalized SWCNT with diisocyanate molecules, carboxylated models of pristine and defective SWCNT etc., were constructed on the basis of the experimental data reported previously [36, 347, 389, 391].

7.1 Set-up of the calculations

The present work is a complex investigation of different molecules and their interactions, which were analyzed to solve specific scientific problems, but they all are connected with the functionalization of carbon nanotubes. From this reason, different parameters for theoretical calculations were used for some of the studies presented here. To make the description of the parameters used more clear, the parameters, that are changing within a particular investigation, are given in Table 7.1. The main parameters of the used theoretical approach remain the same in all calculations. Among them are:

- the usage of plane waves basis set (see Section 6.2.3),
- dispersion correction Grimme D2 (see Section 6.2.2),
- Nosé–Hoover thermostat (see Section 6.3.2),
- the canonical ensemble (NVT),
- fictitious mass of electrons μ with the value of 400 a.u. (see Section 6.3.2),
- the temperature of CP–MD simulations of 300 K,
- the Velocity–Verlet integration algorithm [430].

All calculations were made in the PWscf [431] (version v4.3.2) and CPMD [423] (version 3.17.1) program packages, in which the density functional theory approach with plane waves is implemented. Theoretical calculations, using the mentioned software, were performed at the Interdisciplinary Centre for Mathematical and Computational Modelling (ICM) at Warsaw University under the grants number G55-1, G57-23 and G63-0. Vizualization of the results obtained was made using VMD program [432].

The methodology of all studies was the same for all types of calculations performed to accomplish the PhD thesis. At the beginning, the geometry of the molecular systems was

Table 7.1: List of several differing parameters used in static DFT calculations and CP–MD simulations for systems analyzed in the work. SWCNT(x) means all types of carbon nanotubes analyzed, i.e. pristine and defective. E_{cutoff} and E_{kin}^{fict} denote the cutoff energy of plane waves and the fictitious kinetic energy of electrons, respectively. PBE and BLYP are exchange–correlation DFT functionals of Perdew–Burke–Ernzerhof and Becke–Lee–Yang–Parr, respectively. USPP means Vanderbilt ultrasoft pseudopotentials. In case of covalently attached molecules to SWCNT (i.e. SWCNT(x)) additional local spin density approximation (LSD) was used as a result of odd number of electrons in the system.

System analyzed	Static calculations (functional; E_{cutoff}; PP)	MD simulations (MD run; timestep; E_{kin}^{fict}; thermostat ions/electrons)
TDI (gas phase)	PBE; 30 Ry, USPP	10 ps; 4 a.u.; 0.03 a.u.; 2300 $^{-1}$ / 15000 cm^{-1}
MDI (gas phase)	PBE; 30 Ry, USPP	10 ps; 4 a.u.; 0.03 a.u.; 2900 $^{-1}$ / 15000 cm^{-1}
PEG (gas phase)	BLYP; 120 Ry, Trouiller–Martins	25 ps; 2 a.u.; 0.004 a.u; 2920 cm^{-1} / 15000 cm^{-1}
SWCNT(x)–TDI	PBE+LSD; 30 Ry, USPP	10 ps; 4 a.u.; 0.03 a.u.; 2300^{-1} / 15000 cm^{-1}
SWCNT(x)–MDI	PBE+LSD; 30 Ry, USPP	10 ps; 4 a.u.; 0.03 a.u.; 2900^{-1} / 15000 cm^{-1}
SWCNT(x)–PEG	PBE+LSD; 30 Ry, USPP	–

optimized with the usage of DFT method with additional dispersion correction. The local minima structures obtained were analyzed during the vibrational analysis procedure. Before the geometry optimization, computational parameters were firstly checked and optimized to prevent systematic errors. Among such parameters were: 1) the choice of the unit cell (box) calculated, 2) the plane waves energy cutoff, 3) the DFT functional and other parameters, which are discussed below. In all cases the size of the PBC box was optimized to exclude the interactions of its neighbor images, so the size of the box was set up to have the minimum distance between the molecule and its image of 10 Å.

After the geometry optimization, the atomic coordinates of the most stable structures were used to produce a trajectory using Car–Parrinello MD. Before starting the MD simulations, the wavefunction was optimized and the electronic degrees of freedom were quenched to the Born–Oppenheimer surface. Before collecting data for the production MD run, the heating of the system, starting from 100 K until 300 K (1 ps for every 100 K), and the equilibration procedure (2 ps) at 300 K, were performed. During all mentioned steps of calculation the specific parameters were checked and analyzed to keep the system in stable adibatic conditions, which are required for CP scheme. Using such methodology we were able to observe structural rearrangements and changes of the molecular systems, as a result of different interactions in the system, in real time and at finite temperature, using geometry of the molecules obtained using electronic structure calculations.

7.2 Static calculations

7.2.1 Single-walled carbon nanotubes

Two types of single-walled carbon nanotubes are considered in the present research, i.e. metallic SWCNT(6,0) and semiconducting SWCNT(10,0), see Figure 7.1. Both carbon nanotubes were initially optimized and fully relaxed with the length of 17.065 Å/17.139 Å (four unit cells along the tube axis, Z-axis), what corresponds to 96/160 carbon atoms in the nanotube for SWCNT(6,0) and SWCNT(10,0), respectively. The diameter of the optimized SWCNT(6,0) and SWCNT(10,0) was 4.84 Å and 7.94 Å, respectively.

In the case of noncovalent and covalent functionalization of SWCNT with several diisocyanate molecules, SWCNT with five unit cells was taken into account to prevent interactions

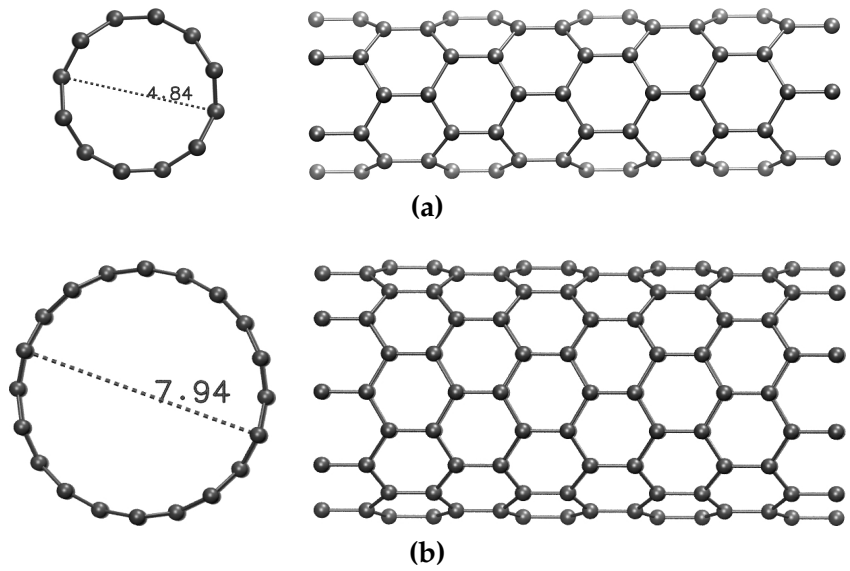

Figure 7.1: Single-walled carbon nanotubes (a) SWCNT(6,0) and (b) SWCNT(10,0) used in the present research.

of the neighbor images in PBC. Therefore, the extended SWCNT(6,0) and SWCNT(10,0) were of the length of 21.331 Å and 21.424 Å, respectively. In all cases, the vacuum space in the lateral direction was set to be larger than 10.0 Å to avoid redundant interactions between periodic images. The length of the unit cell in x- and y-direction was chosen according to the size of the molecule adsorbed noncovalently or attached covalently on the CNT surface. At the same time, to compare the results quantitatively the size of the unit cell in x- and y-direction was chosen with respect to the largest adsorbate, i.e. MDI molecule. Resulting unit cell was of the size of 28.0 Å·28.0 Å·17.065 Å and 28.0 Å·28.0 Å·17.139 Å for SWCNT(6,0) and SWCNT(10,0), respectively.

The adsorption energy (E_{ads}) in the case of noncovalent modification and binding energy (E_{bind}) in the case of covalent functionalization of carbon nanotubes were obtained using the subtraction of the total energies of global minimum structures of the carbon nanotube and the attached molecule in the gas phase from the total energy of the interacting system:

$$E_{ads} = E_{SWCNT-ads} - (E_{SWCNT} + E_{ads}) \tag{7.1}$$

$$E_{bind} = E_{SWCNT-R} - (E_{SWCNT-} + E_R), \tag{7.2}$$

where $E_{SWCNT-ads}$ ($E_{SWCNT-R}$) is the total energy of the carbon nanotube with adsorbed (covalently attached) molecule, E_{SWCNT} is the total energy of the SWCNT and E_{ads} is the total energy of the gas-phase global minimum structure of the adsorbate. In case of covalent functionalization of SWCNT E_{SWCNT-} for the SWCNT with odd number of electrons was used. The negative values of the energy mean the stabilization of the system, thus, the attractive interactions. **The lower the energy value – the higher energy gain as the result of the additional interactions – the more stable is the system**. In the case of positive values, the destabilization of the system is observed.

7.2.2 The choice of the DFT functional

As it was mentioned in Section 6.2.2, the density functional theory is unable to describe dispersion interactions correctly. Taking into account the analyzed molecular systems in the present research, which are mainly of π-nature, an adequate choice of DFT functional with the dispersion correction should have been found. To estimate the influence of different

approximations in calculating the noncovalent interactions between carbon nanotubes and adsorbates, i.e. MDI and TDI diisocyanates, during the noncovalent functionalization of SWCNTs, the initial tests of model π-system interactions with CNT were made. Due to its structural simplicity, the benzene molecule was chosen as a model π-system (see Figure 7.2). Previous calculations [433] have shown that the parallel arrangement of the benzene molecule

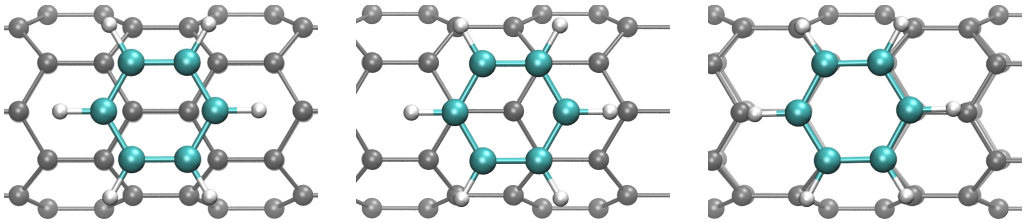

Figure 7.2: Adsorption sites of benzene molecule on SWCNT(6,0): (a) Bridge position, (b) Top position, (c) Hollow position. Carbon nanotube is marked in gray, carbon and hydrogen atoms from the benzene molecule are cyan and white, respectively.

on the surface of single-walled CNT is more stable than the perpendicular one. From this reason, several specific parallel arrangements of the benzene molecule on the surface of SWCNT(6,0) were analyzed with the usage of both LDA and GGA approximations with the additional correction to the GGA approach. In Figure 7.2 the most characteristic positions of benzene on SWCNT are presented, i.e. bridge, top and hollow.

In order to estimate the adsorption energies of the π-molecule on the carbon nanotube, several DFT approximations were used (Section 6.2.2): LDA and GGA. In the GGA approximation the exchange-correlation functional PBE (Perdew–Burke–Ernzerhof) was used, because it is often used DFT functional for solid-state calculations, especially in the case of carbon-based materials. We used generalized gradient approximation with and without Grimme D2 dispersion correction, which is implemented in both PWscf and CPMD program packages that were used to perform calculations. In Table 7.2 the calculated adsorption energies and the shortest C–C distance between the benzene molecule and the CNT surface are listed.

Table 7.2: Impact of dispersion correction on the parameters of the benzene adsorption on the surface of SWCNT(6,0). E_{ads} and l_{C-C} are the adsorption energy and the shortest distance between the carbon atom from the benzene molecule and the carbon atom from the SWCNT. The negative values of the energy mean higher stabilization of the system, therefore, the highest energy gain as the result of intermolecular interactions. The position of benzene molecule on SWCNT surface corresponds to those in Figure 7.2.

Position	**E_{ads} [kJ/mol]**			**l_{C-C} [Å]**		
	LDA	PBE	PBE+D2	LDA	PBE	PBE+D2
Bridge	-22.0	-2.7	-27.7	3.33	4.20	3.39
Top	-21.2	-2.6	-26.8	3.18	3.99	3.22
Hollow	-14.2	-1.9	-20.8	3.23	4.00	3.25

As it can be noticed, the best values of the adsorption energy (the highest absolute values) are obtained in the PBE approach with the dispersion correction. Moreover, the "zero" adsorption was obtained in the case of pure GGA approach ("PBE" column in Table 7.2). This proves that the dispersion interactions are involved in the $\pi - \pi$ interactions and additional

corrections must be used to describe properly the π-systems. The most stable arrangement of benzene on SWCNT is not the sandwich one (Figure 7.2: c), but the position similar to parallel-displaced one, which is one of the most stable in the case of benzene dimer (see Section 3.4). Similar results with the same order of the stability of adsorption sites were reported by L. Woods et al. [434] for SWCNT (8,0). The results obtained are also comparable with those calculated by high level MP2 calculations of the benzene molecule adsorption on SWCNT(10,0) [433], where the adsorption energy for bridge and hollow positions was -24.5 kJ/mol and -19.4 kJ/mol, respectively, while in the present calculations the obtained energy is of -27.7 kJ/mol and -20.8 kJ/mol.

The initial test calculations of the benzene molecule on the surface of SWCNT(6,0) confirmed the necessity of the usage of dispersion correction in the DFT method. Additionally, the results obtained were similar to the previously reported in the literature, including those from MP2 method, therefore, the approach chosen is reliable and accurate one for the description of carbon-based systems, such as carbon nanotubes. That is why, PBE functional with Grimme D2 dispersion correction is used in case of all calculations in the present PhD thesis. The only exception is in the case of PEG molecule, where the exchange-correlation BLYP functional is used to describe properly hydrogen bonds in the system.

7.2.3 Energy cutoff

According to the parameters listed in Table 7.1, two different cutoff energies, E_{cutoff}, for plane waves basis set were used. It should be noted that the value of the energy cutoff E_{cutoff} directly influences on the amount of the plane waves used in the particular calculations (see Equation 6.29). In case of larger amount of PW, more accurate results can be obtained. For such huge molecular systems as carbon nanotubes, where 160 carbon atoms are used in the calculations (in case of SWCNT(10,0)), without counting the molecules attached, the energy cutoff should be tested carefully to estimate the most efficient value with saving of the computational resources. To save the computational time we have used common

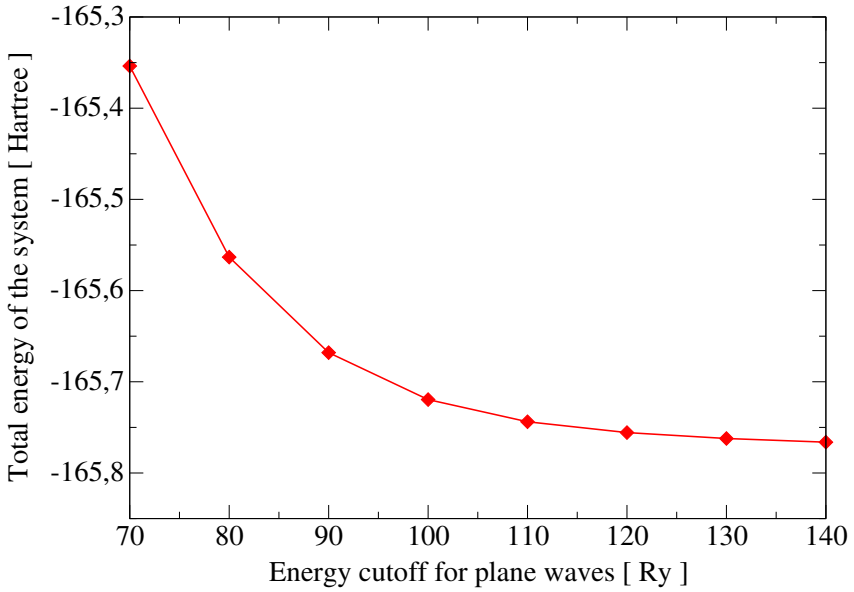

Figure 7.3: Influence of energy cutoff of plane waves on the total energy of the system using normconserving pseudopotentials of Trouiller–Martins. System analyzed: polyethylene glycol molecule with five repeat units (Section 8.2).

known Vanderbilt ultrasoft pseudopotentials (USPP), for which the reduced value of E_{cutoff} is

required. The most frequently used E_{cutoff} for plane waves in case of USPP is 30–35 Ry [435]. With the usage of higher values of E_{cutoff} the difference in the total energy of the system changes insignificantly. Before our choice of the energy cutoff of 30 Ry (Table 7.1) we have made test calculations for the system consisted of the SWCNT(6,0) and the benzene molecule, where the change of E_{cutoff} from 30 Ry to 35 Ry gave the difference in the total energy of the system of 0.096 kJ/mol [436]. Taking into account the increase of the computational time in case of higher value of E_{cutoff} and the value of the total energy of the system, 30 Ry was chosen as a good compromise.

For the detailed estimation of the intramolecular interactions in different polyethylene glycol molecules (see Section 8.2), the normconserving pseudopotentials of Trouiller–Martins (TM) were used (see Table 7.1). The usage of TM pseudopotentials requires higher values of E_{cutoff}, i.e. 60–100 Ry [423]. As a result, several test calculations for the wavefunction optimization were made to find a reasonable value of the energy cutoff. In Figure 7.3 the dependence of the total energy of the system as the result of the increasing value of E_{cutoff} is shown. It can be seen that with the increase of the energy cutoff, the total energy changes reaching closer the ground-state energy. In Table 7.3 the total energy and the differences between the

Table 7.3: Total energy of the system (polyethylene glycol molecule with five repeat units), E_{tot}, and the differencies, $\Delta\ E_{tot}$, between the total energies obtained using different energy cutoff, E_{cutoff} of plane waves (CPMD). The time of one step of the calculations, t, was estimated using 64 CPU at ICM.

$\mathbf{E}_{cutoff}$ [Ry]	$\mathbf{E}_{tot}$ [Hartree]	$\Delta\ \mathbf{E}_{tot}$ [Hartree]	$\Delta\ \mathbf{E}_{tot}$ [kJ/mol]	**t** [s]
70	-165.3537	–	–	2.29
80	-165.5633	-0.2095	-550.2520	2.80
90	-165.6681	-0.1048	-275.1921	3.30
100	-165.7195	-0.0514	-135.0261	3.69
110	-165.7439	-0.0244	-64.0010	4.86
120	**-165.7557**	**-0.0119**	**-31.1460**	**5.40**
130	-165.7622	-0.0064	-16.8716	5.93
140	-165.7662	-0.0041	-10.7184	6.87

total energy values as the result of increasing E_{cutoff} are shown. For clear presentation of the influence of E_{cutoff} on the computational cost, the time for one step of the calculation is also shown in Table 7.3. With the increasing of the value of energy cutoff, the differences in the total energy are decreasing and the results obtained are tending to more accurate ones, but, at the same time, the computational time increases. Starting from the value of E_{cutoff} of 120 Ry, the total energy changes slightly, what is seen in Figure 7.3. From this reason, this value was chosen as the energy cutoff in our calculations.

7.3 Testing parameters for Car–Parrinello MD

To estimate adequate parameters for Car–Parrinello molecular dynamics simulations, additional test calculations considering the timestep and the fictitious kinetic energy were made. Here, several examples are presented.

7.3.1 Timestep and fictitious mass

In Car–Parrinello scheme for collecting MD trajectory, the wavefunction is quenched to the Born–Oppenheimer surface at the beginning of the simulation, then the forces calculated are used as initial parameters for MD simulations, which are performed using Newton (Euler–Lagrange) equation of motion. In such approach there is a possibility to move away from the BO surface, therefore, the calculated data can be untrue. To keep the system close to BO surface, stable adiabatic conditions should be fulfilled. Among parameters to control the adiabatic conditions in CP–MD is fictitious electron mass μ, which was described in Equation 6.36 in Section 6.3.2. The common used values of μ are in the range of 300–1500 a.u. [423], but larger fictitious masses are more *aggresive* and they have trend to go away from BO surface. As a result, fictitious mass of c.a. 400 a.u. is the most often used [69].

Among other parameters influencing the stability of the system during CP–MD is a timestep, which indicates the moment when the forces for the MD steps are calculated. Generally, the timestep of 2–10 a.u. is used, but it is strongly connected to the value of the energy cutoff of plane waves and the fictitious mass:

$$\Delta t^{max} \propto \left(\frac{\mu}{E_{cutoff}}\right)^{1/2}, \tag{7.3}$$

where Δt^{max} is the maximum value of the timestep. Taking into account previous test calculations of the energy cutoff for PEG calculations (Section 7.2.3), where the cutoff of 120 Ry was chosen, the timestep was set to 2 a.u. (0.048 fs). In case of MD simulations with the energy cutoff of 30 Ry, the timestep of 4 a.u. (0.096 fs) was used. In all calculations the fictitious mass of 400 a.u. (0.219 a.m.u) was used.

7.3.2 Keeping adiabatic conditions

Even if fictitious mass and timestep are chosen correctly and the system is stable in the calculations, there is a possibility for the drift of the fictitious kinetic energy during longer

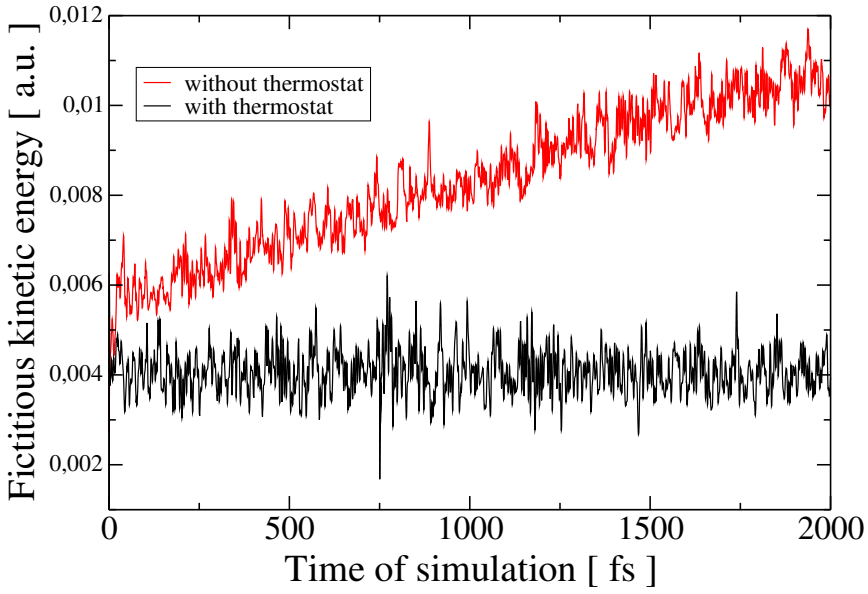

Figure 7.4: Evolution of fictitious kinetic energy during equilibration procedure of CP–MD simulations with and without additional thermostat on electrons. Test calculations made for MD simulations of polyethylene glycol molecule at 300 K.

MD simulations. An examplary drift of the fictitious kinetic energy is shown in Figure 7.4 (marked in red).

The energy is slightly rising with every step of the simulation to the moment when its value indicates that the system is far from BO surface. The additional procedure, which is making for such "unstable" systems is switching on the Nosé–Hoover thermostat on electrons, which requires the initial value of the fictitious kinetic energy of electrons. This value should be as small as possible, but still it should be characteristic for the system analyzed. To estimate this value, the free-run MD simulations are performed. During free-run simulations at the finite temperature the value of fictitious kinetic energy for electrons sets up. This value is the corresponding one for the fictitious kinetic energy in Nosé–Hoover thermostat on electrons, which keeps the energy oscillating around the estimated value (see black plot in Figure 7.4). Using the described methodology the values of fictitious kinetic energy for all systems analyzed were chosen (Table 7.1).

Chapter 8

Gas-phase calculations for polyurethane monomers

The initial gas-phase calculations of the molecules used to functionalize carbon nanotubes were made. The aim of the static calculations was to establish the most stable structure of the molecule, which is used in further analysis. Car–Parrinello molecular dynamics simulations at finite temperature were made to collect data about structural rearrangements of the molecules attached without the influence of the neighbor molecules to compare the MD results with those obtained for the covalent functionalization of SWCNTs. In this Chapter both static and dynamics studies of MDI, TDI and different PEG molecules are presented.

8.1 Diisocyanates molecules

The investigation of the structure of diisocyanate molecules enables the understanding of the intra- and intermolecular interactions in the polymer matrix and the affinity of the molecule to interact with the surface of carbon nanotube. It helps to study hydrogen bonds between hard-hard and hard-soft polymer segments, which directly influence the macroscopic properties of the polymer.

Among the most often used diisocyanates in the polyurethane polymer industry are MDI, 1,1'-methylenebis(4-isocyanatobenzene), and TDI, 2,4-diisocyanato-1-methylbenzene. The structural formulae of these diisocyanates were depicted in Figure 5.1 in Section 5.1, where the chemistry of these chemical compounds was described. In comparison to the TDI molecule, which consists of one phenyl ring with two isocyanate functional groups, the MDI molecule possesses two phenyl rings connected with the $–CH_2–$ group. As a result of the planar nature of both phenyl ring and the isocyanate group, the TDI molecule is very stiff and its conformers do not differ significantly. From this reason, only the optimized conformers of MDI are analyzed in the static calculations. At the same time, the conservative behavior of the TDI molecule is shown in the Car–Parrinello MD.

8.1.1 Geometry optimization

Recently, it was reported that phenyl rings of the MDI molecule have mutual barrierless rotation with the energy barrier with respect to the rotation of one phenyl ring of c.a. 0.89 kJ/mol [437], which is less than the "chemical accuracy". The influence of the rotation of the isocyanate group on the total energy of the molecule is also small, with the difference of 0.02 kJ/mol. Slight differences in the values of the relative energy of different MDI conformers can be also seen from the Figure 8.1, where the selected optimized local minima of MDI are shown. All local minima in Figure 8.1 are positioned in such a way that the top phenyl

ring has always a fixed position, therefore, the differences on the orientation of the second phenyl ring are well visible. It can be seen that MDI molecule is highly symmetrical in the range of the C-C-C-C dihedral angle of -180° → 0°, 0° → 180°, 90° → -90°. This means that

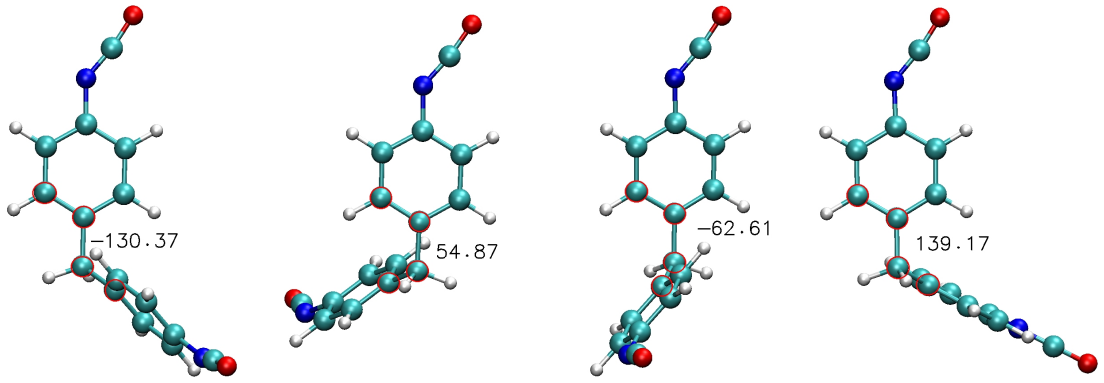

(a)	(b)	(c)	(d)
E_{rel} = 0.00 kJ/mol	E_{rel} = 0.09 kJ/mol	E_{rel} = 0.11 kJ/mol	E_{rel} = 0.13 kJ/mol

Figure 8.1: Selected structures of the local minima of MDI diisocyanate molecule. The C-C-C-C dihedral angle is marked with red circles, the corresponding value of C-C-C-C dihedral angle is written next to the molecule.

the MDI molecule is very flexible with the tendency for free rotation of the phenyl rings. Together with phenyl rings, the isocyanate group are changing being always in the same plane as the phenyl ring.

The structure of the MDI phenyl rings prevents to stay either in one single plane or to acquire the wing-like orientation of both phenyl rings. As a result, there is no evidence for intramolecular $\pi - \pi$ stacking, but there is a possibility for the stabilization due to C-H$\cdots\pi$ hydrogen bonds. It was estimated that C-H$\cdots\pi$ H-bonds in MDI are very weak and they can not be detected using standard methods for the analysis of hydrogen bonding [437]. We can estimate the real influence of C-H$\cdots\pi$ H-bonds on the structural rearrangements of MDI using MD simulations at 300 K.

The most stable MDI and TDI local minima were taken for the further MD simulations and the functionalization of the carbon nanotubes, which is presented in the next sections.

8.1.2 Structural diversity

The TDI molecule is rather simple molecule, because it possesses only one phenyl ring, which is planar, methyl and isocyanate functional groups. As a result, it was expected that this molecule will not show significant structural rearrangements during the MD simulations in the gas phase. It was proven by performing the MD run at 300 K. Selected snapshots from the MD simulation are depicted in Figure 8.2, where two views of the molecule are shown simultaneously. The MD simulation for the TDI molecule was made to obtain a comparative data for further investigations.

It can be seen that the isocyanate groups are slightly changing their position with respect to the phenyl ring, but most of the time they stay in the same, planar, position. Mutual changes of NCO group with respect to the aromatic ring are shown in Figure 8.3, where the time evolution of the C-C-N-C dihedral angle, formed between two carbon atoms from the phenyl ring and the isocyanate group, is shown. The C-C-N-C dihedral angle of 0° correspond to the position of the isocyanate group in the same plane as the phenyl ring. Changes of the dihedral angle show that the maximal deformation of the NCO group is around 75° down

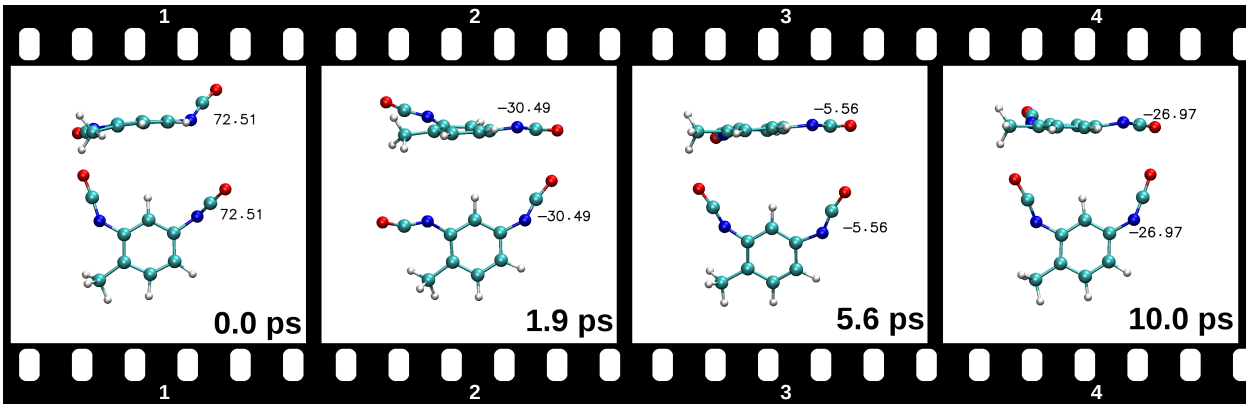

Figure 8.2: Selected snapshots of the structural rearrangements of the TDI molecule obtained from CP–MD simulations at 300 K. Two views (side view and top view) of the TDI conformation are given. The values of the corresponding C-C-N-C dihedral angle are marked in each snapshot. Each snapshot is presented with the corresponding timestamp.

or up (for example, in the snapshot "1" in Figure 8.3), but the average value of the C-C-N-C dihedral angle is 60° with respect to the ring plane.

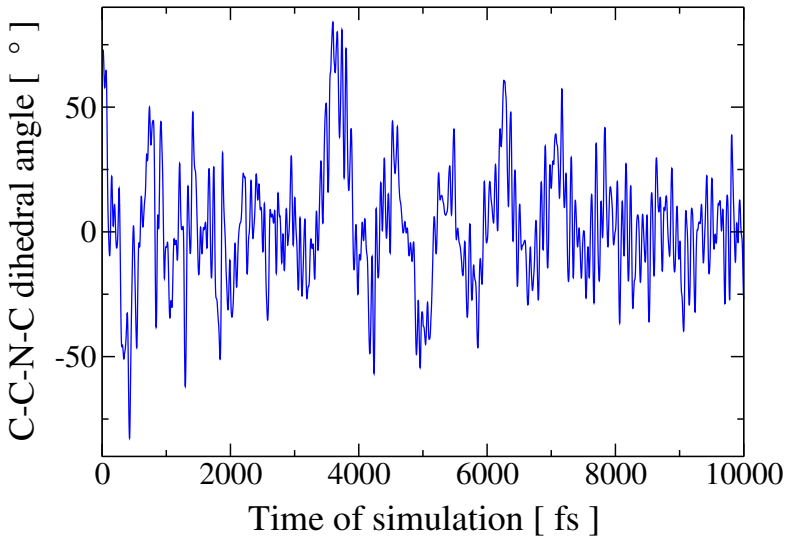

Figure 8.3: Time evolution of the C-C-N-C dihedral angle between the TDI aromatic ring and the isocyanate group.

The MDI molecule has additional aromatic ring, but its structural rearrangements in the gas phase are different than for the TDI molecule. The only one similar feature between these molecules is the structural changes of the isocyanate groups, which prefer to stay in the same plane as the corresponding phenyl ring. The oscillations of the NCO group from the plane of the phenyl ring are about 60° and are slightly more stable than for the TDI molecule (see Figure 8.4). Such oscillations are similar to those reported by P. Rodziewicz et al. [437] for the MDI molecule at 350 K.

Taking into account the results from the static DFT calculations, the MDI molecule is highly able to change its conformation, because of the significantly low energy differences between different MDI conformers. Therefore, it can possess barrierless rotation of the phenyl rings. The full rotation of the two phenyl rings in the MDI molecule was confirmed during the CP–MD simulations at 350 K [437]. In the present investigations, the CP–MD simulations

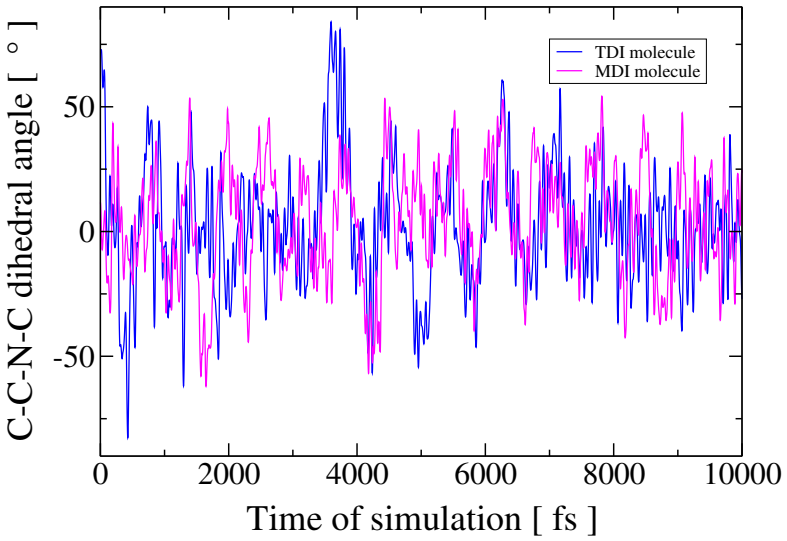

Figure 8.4: Time evolution of the C-C-N-C dihedral angle between the TDI/MDI aromatic ring and the isocyanate group. The changes of the TDI and MDI molecules are shown with the blue and pink curve, respectively.

at 300 K were made. The selected MDI structural conformers from the CP–MD run, which correspond to the most important MD geometries, are depicted in Figure 8.5. For the clear analysis of the changes of the MDI structure, the MDI molecule in Figure 8.5 is depicted in the same view, when the upper phenyl ring is in a fixed position and only the second phenyl ring is moving. The values of the dihedral angle, marked in the each snapshot, correspond to the C-C-C-C dihedral angle shown in Figure 8.1.

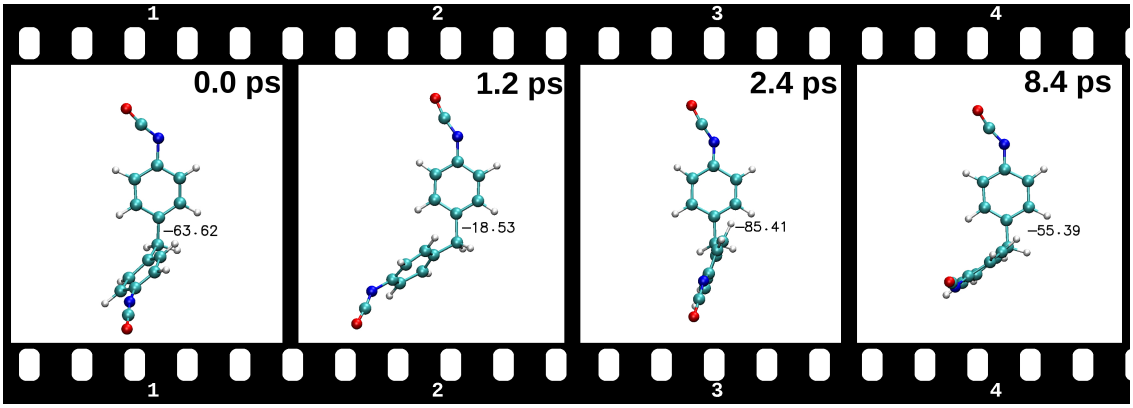

Figure 8.5: Selected snapshots of the structural rearrangements of the MDI molecule obtained from CP–MD simulations at 300 K. The values of the corresponding C-C-C-C dihedral angle between the MDI phenyl rings (as shown in Figure 8.1) are marked in each snapshot. Each snapshot is presented with the corresponding timestamp.

From the selected snapshots of the MDI structural rearrangements it can be seen that the second phenyl ring is rotating only in the same, perpendicular-like plane, without the full rotation of the fixed phenyl ring. For more clear understanding of the mutual rotation between phenyl rings, the time evolution of the C-C-C-C dihedral angles between the phenyl rings was plotted (see Figure 8.6). The black curve corresponds to the top C-C-C-C dihedral angle with marked values (Figure 8.5), while the green curve corresponds to the opposite (bottom) C-C-C-C dihedral angle. The two rest dihedral angles between the MDI aromatic rings behave the same as the selected ones and are skipped here. From Figure 8.6 it is seen that there

is no full rotation between the MDI phenyl rings, as they are rotating on only c.a. 80°. In

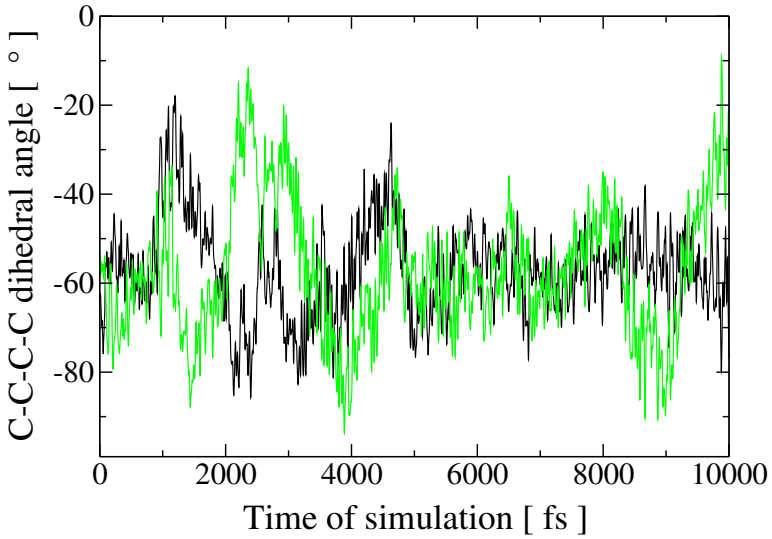

Figure 8.6: Time evolution of the top (as shown in Figure 8.1) and bottom C-C-C-C dihedral angles between the phenyl rings in the MDI molecule, corresponding to their mutual rotation.

case of higher temperatures, e.g. 350 K, the full rotation of the MDI rings is possible [437], but at the room temperature their mutual structural rearrangements are suppressed. It can be of high importance during the attaching the MDI molecule to the surface, for example, during the SWCNT functionalization, and during the PU synthesis, where more branched or more stiff polymer structures can be formed. Generally, the values of the C-C-C-C dihedral angle of the MDI molecule are changing from c.a. -20° to -90° with the most preferable C-C-C-C dihedral angle of 40°–60°, which is consistent which the potential energy surface of the mutual phenyl rings rotation reported in Ref. [437]

Among the similar features between the MDI structural rearrangements at 300 K and 350 K is the existence of the weak C-H$\cdots\pi$ contacts. These interactions can not be classified as hydrogen bonds, as defined by IUPAC [118], because they do not fit the critea for H-bonds formation, so the definition of "contacts" is used. C-H$\cdots\pi$ contacts are formed when the MDI phenyl rings are in the perpendicular position with respect to each other (the inner $\angle$(CCC) angle of 113.79°), when the C-C-C-C dihedral angle is close to the value of 20°. The formation of this weak hydrogen bonding can be seen in snapshots "2" and "4" in Figure 8.5. As the result of the steric effects, which are connected with the perpendicular arrangement of the phenyl rings, these intramolecular interactions are weak and temporary with the lifetime in the range of 0.38–0.52 ps.

The CP–MD simulations for diisocyanates molecules were made as a comparative data for the molecular dynamics simulations of the covalently functionalized SWCNT(10,0), which are presented in Section 10.3.

8.2 Polyethylene glycol molecules

The usage of the DFT static calculations is connected to the limits in the size of the systems amalyzed. Taking into account the computational cost, we have decided to analyze the noncovalent interactions between the polyol molecules and the surface of the carbon nanotube on the model systems, consisted of low molecular polyethylene glycol molecules (PEG). Generally, different PEG molecules are used in the polymer synthesis and the functionalization of the CNT during the synthesis of PU/CNT composites. Four representatives

of the PEG molecule with two to five repeat –O–CH_2–CH_2– subunits were chosen to analyze their primary interactions with SWCNT(10,0). There are investigations reported, concerning the adsorption of the PEG molecules on the carbon nanotube surface [438], but the reported simulations were made for PEG with high molecular weights, using the classical molecular dynamics with the initially parametrized force fields. The Authors in Ref. [438] have shown that the PEG chains wrap the carbon nanotubes, but no information about the intermolecular interactions was given. From this reason, the main aim of the present research is the observation of the forces responsible for the adsorption of the PEG molecules on the CNT, therefore, smaller molecules of similar structural motifs as PEG of higher molecular weights were analyzed. In this subsection, the initial DFT static calculations and CP–MD simulations at 300 K of the isolated gas-phase PEG molecules are presented.

8.2.1 Static calculations of low molecular weight PEG

Polyethylene glycol is a known biocompatible polymer, which is used in different formulations and for various purposes. Depending on the aim of the usage of this polymer, different types of PEG, varing in the amount of the repeat subunits, thus the molecular weight, are used. In the present analysis only small PEG molecules with two, three, four and five subunits are investigated. At the beginning, the static DFT calculations were used to estimate the most probable structures of the PEG molecules mentioned. For this purpose, minimum five and maximum twelve PEG conformers, depending on the length of the PEG molecule, were optimized with the convergence of orbitals and geometry of $1x10^{-8}$ and $1.2x10^{-5}$ a.u., respectively. All calculated local minima were also checked with the vibrational analysis for the absence of the negative frequencies. Several local minima were chosen to show the possible PEG conformers with differing energy and intramolecular bonding pattern. The structures of the PEG with two to four subunits are depicted in Figure 8.7, while PEG conformers with five subunits are shown in Figure 8.8.

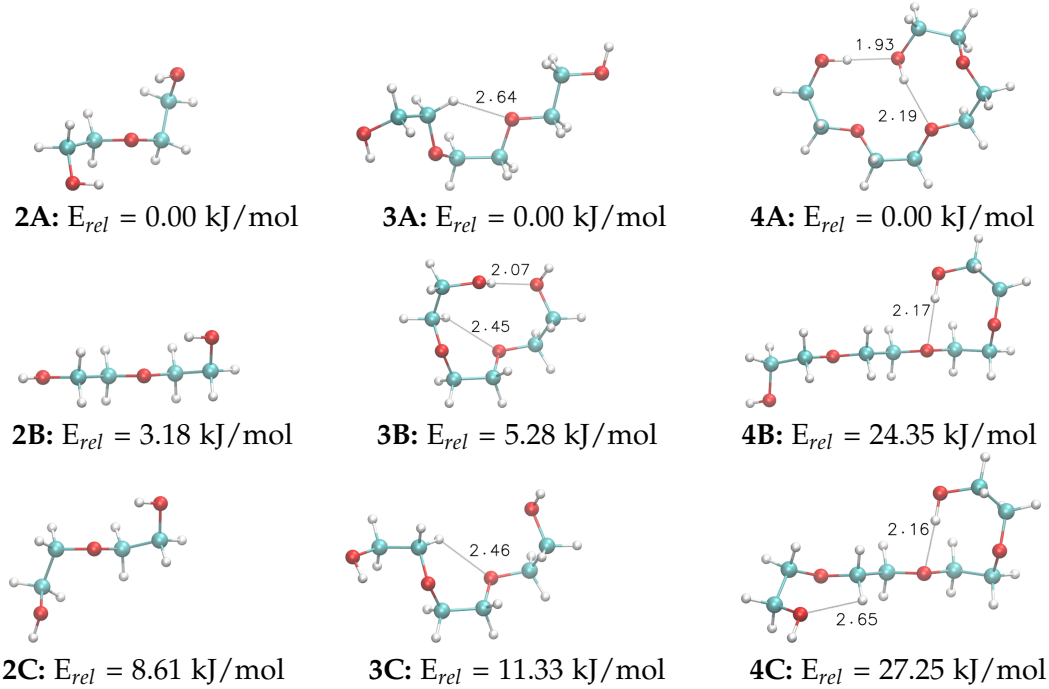

2A: E_{rel} = 0.00 kJ/mol **3A:** E_{rel} = 0.00 kJ/mol **4A:** E_{rel} = 0.00 kJ/mol

2B: E_{rel} = 3.18 kJ/mol **3B:** E_{rel} = 5.28 kJ/mol **4B:** E_{rel} = 24.35 kJ/mol

2C: E_{rel} = 8.61 kJ/mol **3C:** E_{rel} = 11.33 kJ/mol **4C:** E_{rel} = 27.25 kJ/mol

Figure 8.7: Selected optimized structures of low molecular polyethylene glycol molecule with two (2A–2C), three (3A–3C) and four (4A–4C) –O–CH_2–CH_2– subunits. Hydrogen bonds, confirmed by QTAIM analysis, are marked with the dashed lines.

The global minimum structures, which represent the most stable structures and possess the lowest absolute energies, are labeled with the letter "A" and have the values of the relative energy set to 0.00 kJ/mol. The relative energies, E_{rel}, of less stable local minima structures were obtained as a subtraction between the absolute energies of less stable local minimum, $E^{abs}_{local-min}$, and the global minimum, $E^{abs}_{global-min}$, structures:

$$E_{rel} = E^{abs}_{local-min} - E^{abs}_{global-min}. \tag{8.1}$$

Positive values of the relative energy denote less stable structures of the same molecule.

PEG molecule is able to exist in different local minima characterized with different relative energies because of its specific nature, which impact the PEG molecule to have additional hydrogen bonds. In PEG, both C-H and O-H groups play the role of the hydrogen bond proton donor, whereas the oxygen atom, either hydroxyl or etheric, plays the role of the proton acceptor. Therefore, two types of hydrogen bonding are possible, i.e. strong red-shifted O-H$\cdots$O and weak blue-shifting C-H$\cdots$O. The blue-shifting and red-shifted nature of the analyzed hydrogen bonds was proven and described in detail in our recent publication [439]. Both types of H-bonds can be seen in structures depicted in Figure 8.7, where only hydrogen bonds confirmed by the QTAIM analysis are shown. The detailed structural and topological parameters of those H-bonds are listed in Table 8.1. The description of the theoretical bases of the QTAIM analysis was given in Section 3.4.1. The formation of intramolecular hydrogen

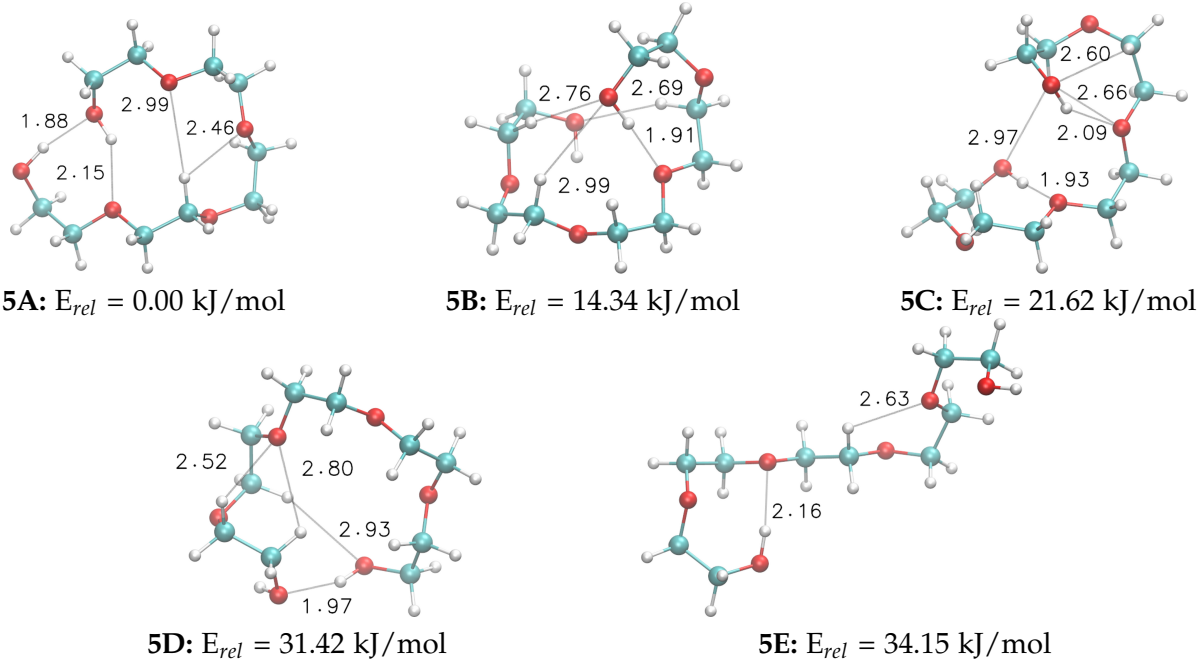

5A: E_{rel} = 0.00 kJ/mol **5B:** E_{rel} = 14.34 kJ/mol **5C:** E_{rel} = 21.62 kJ/mol

5D: E_{rel} = 31.42 kJ/mol **5E:** E_{rel} = 34.15 kJ/mol

Figure 8.8: Selected optimized structures of low molecular polyethylene glycol molecule with five –O–CH_2–CH_2– subunits. Hydrogen bonds, confirmed by QTAIM analysis are marked with the dashed lines.

bonds in PEG, which can stabilize the structure and lead to the higher energy gain depends on the amount of the repeat subunits in the PEG molecules. It can be easily seen from the structural parameters of the hydrogen bonds, for example, with three subunits in comparison to five.

Polyethylene molecule with two repeat subunits has the smallest conformational space among all PEG molecules analyzed. The local minima structures of these PEG molecules have small energy difference, e.g. the energy difference between the global minimum (**2A**) and the first local mimimum (**2B**) is only 3.18 kJ/mol, which is less than the chemical accuracy. This

means that there is a high possibility of the barrierless change between different PEG conformers. The reason of the energy difference of 3.18 kJ/mol is caused by the existence of two stabilizing interactions via H-bonds between the hydroxyl groups and the oxygen atom from the main chain of the global minimum structure (**2A**). These interactions are not marked in Figure 8.7, because they were not detected in the QTAIM analysis, but they were confirmed in the NCI index analysis (see Figure 8.9, where the reduced density gradient is shown (green areas denoting intramolecular interactions). The mentioned interactions are similar to O-H$\cdots$O H-bonds, but they are characterized with lower linearity (the OHO angles are 105.2° and 109.7°), which should be fulfilled in the AIM code. The same feature is the characteristic one for the local minimum structure **2B** with the OHO angle of the interaction of 105.3°. The least stable PEG structure with two subunits (**2C**) has very similar geometry as the global minimum structure **2A**, but it also possesses extra hydrogen repulsion caused by the deformation of the O-C-C-O chain (see Figure 8.7). As a result the energy gain as the result of the formation of the intramolecular interactions is lower that the energy loss because of H–H repulsion and the structures differ by 8.61 kJ/mol.

The existence of typical hydrogen bonds was detected in the PEG molecules with three repeat subunits (see Figure 8.7: 3A–3C). The electron density and the Laplacian of the electron density at bond critical points (BCP) that describe the C-H$\cdots$O and O-H$\cdots$O hydrogen bonds in the first local minimum structure (**3B**) are 0.0103 a.u. (0.0388 a.u.) and 0.0206 a.u. (0.0663 a.u.), respectively (see Table 8.1). These values are in range of the criteria for hydrogen bonds (see Section 3.2 and Section 3.4.1), reported by U. Koch an P. Popelier [159], i.e. the hydrogen bond exists if the value of electron density in BCP is in the range of 0.002 to 0.034 a.u. and the Laplacian of the electron density is in the range of 0.024–0.139 a.u. Even if the valence angle of the C-H$\cdots$O hydrogen bond in the global minimum structure **3A** is low, i.e. 109.6°, this weak blue-shifting hydrogen bond, of the distance of 2.64 Å, was detected by QTAIM and NCI index (see Figure 8.9). The O-H$\cdots$O hydrogen bond in the structure **3A** was not detected by QTAIM, because of its low linearity (OHO angle of 106.6°), but this intramolecular interaction of the length of 2.43 Å was proven by NCI index (Figure 8.9), which uses different criteria for the noncovalent interactions and is able to detect even very weak interactions of the London dispersion nature.

The first local minimum of the PEG molecule with three subunits (**3B**) is characterized by stronger hydrogen bonds than the global minimum structure (**3A**), but its relative energy is 5.28 kJ/mol higher, so it is slightly less stable. This is caused by the higher stress of the molecule during the H-bonds formation and the additional hydrogen–hydrogen repulsion interactions. As a result, the gain of the energy from the formation of additional hydrogen bond is lower than its loss caused by the change of the PEG geometry. The same scenario was observed for the least stable PEG structure (**3C**) with th relative energy of 11.33 kJ/mol. Even if this conformation is very similar to the global minimum one, the detailed analysis of the structural parameters indicated that the main chain of the molecule is more deformed in case of the structure **3C**, where the dihedral angles C-C-O-C (in the left end) and C-C-O-C (in the right end) are 85.8° and 83.2°, respectively, whereas the values of these dihedral angle are 169.7° and 178.2° for the global minimum structure. That is why, it can be concluded that the stability of the PEG molecule depends on the formation of the intramolecular hydrogen bonds, H–H repulsion interactions and internal stress of the molecule caused by the changing of the conformation.

The addition of the next –O–CH_2–CH_2– repeat subunit increases the tendency of the PEG molecule to form intramolecular hydrogen bonds. In case of the most stable PEG with four –O–CH_2–CH_2– (structure **4A**), the formation of four hydrogen bonds of O-H$\cdots$O nature is possible. Two of them were detected by QTAIM analysis and are marked in Figure 8.7, the third and the forth ones are the weakest ones, but still they were proven after the NCI

Table 8.1: Structural and topological parameters of the hydrogen bonds in the local minima structures of low molecular PEG molecules with three, four and five repeat subunits obtained using DFT static calculations with plane waves. Relative energies (E_{rel}) are given in kJ/mol, interatomic distances (H$\cdots$O) and valence angles [$\angle$(XHO)] are given in Å and $^\circ$, respectively. The values of the electron density and the Laplacian of the electron density at bond critical points (BCPs) of hydrogen bonds, detected using QTAIM approach, are given in a.u.

Label	$\mathbf{E}_{rel}$ [kJ/mol]	**H-bond type**	**H$\cdots$O** [Å]	**$\angle$(XHO)** [$^\circ$]	$\rho_{H\cdots O}$ [a.u.]	$\nabla^2_{H\cdots O}$ [a.u.]
3A	0.00	C-H$\cdots$O	2.64	109.6	0.0076	0.0278
3B	5.28	O-H$\cdots$O	2.07	150.7	0.0206	0.0663
		C-H$\cdots$O	2.45	122.5	0.0103	0.0388
3C	11.33	C-H$\cdots$O	2.46	124.7	0.0100	0.0368
4A	0.00	O-H$\cdots$O	1.93	172.6	0.0278	0.0775
		O-H$\cdots$O	2.19	156.0	0.0157	0.0507
4B	24.35	O-H$\cdots$O	2.17	150.6	0.0166	0.0542
4C	27.25	O-H$\cdots$O	2.16	150.4	0.0171	0.0556
		C-H$\cdots$O	2.65	108.5	0.0075	0.0284
5A	0.00	O-H$\cdots$O	1.88	166.8	0.0322	0.0849
		O-H$\cdots$O	2.15	141.6	0.0162	0.0566
		C-H$\cdots$O	2.46	116.3	0.0108	0.0397
		C-H$\cdots$O	2.99	173.9	0.0034	0.0111
5B	14.34	O-H$\cdots$O	1.91	173.1	0.0279	0.0812
		C-H$\cdots$O	2.69	161.0	0.0059	0.0184
		C-H$\cdots$O	2.76	163.4	0.0052	0.0161
		C-H$\cdots$O	2.99	142.5	0.0030	0.0106
5C	21.62	O-H$\cdots$O	1.93	169.4	0.0267	0.0795
		O-H$\cdots$O	2.09	149.7	0.0186	0.0644
		C-H$\cdots$O	2.60	112.3	0.0091	0.0325
		C-H$\cdots$O	2.66	110.0	0.0083	0.0310
		C-H$\cdots$O	2.97	148.1	0.0032	0.0105
5D	31.42	O-H$\cdots$O	1.97	159.1	0.0262	0.0756
		C-H$\cdots$O	2.52	110.8	0.0097	0.0370
		C-H$\cdots$O	2.80	116.5	0.0054	0.0199
		C-H$\cdots$O	2.93	158.9	0.0036	0.0116
5E	34.15	O-H$\cdots$O	2.16	150.0	0.0171	0.0555
		C-H$\cdots$O	2.63	112.1	0.0077	0.0283

index analysis (see Figure 8.9). The length of two O-H$\cdots$O H-bonds, listed in Table 8.1, is 1.93 Å and 2.19 Å and they are characterized with relatively high linearity of 172.6° and 156°. That is why, their corresponding electron density at the BCP are among the highest ones, i.e. 0.0278 a.u. and 0.0157 a.u., respectively. From the visualization of the noncovalent interactions in this structure, it can be seen that due to the formed hydrogen bonds an additional *pseudo* ring is formed, which makes this conformation more than 20 kJ/mol more stable than the rest local minimum structures, i.e. structures **4B** and **4C**. The increase of the reduced gradient of the electron density in the place of the formation of this "ring" is shown in Figure 8.9: g with huge green surfaces. Due to such specific PEG structure (**4A**) one O atom from the terminal hydroxyl group plays the role of the hydrogen bond donor and acceptor. Moreover, it plays a role for the H-bond donor for three oxygen atoms. In

general, the bifurcated hydrogen bonds are less stable than one-to-one bondings, but in the analyzed structure there is an extra stabilization and mutual sharing of the electron density, therefore, it has strong effects on the stability of the molecule. It can be stated that these hydrogen bonds are the associated ones.

The local minimum structures **4B** and **4C** are 24.35 kJ/mol and 27.25 kJ/mol less stable than the global minimum one, as the result of the lack of a specific net of stabilizing hydrogen bonds. According to QTAIM analysis, these structures are characterized by one O-H$\cdots$O (structure **4B**) and two: O-H$\cdots$O and C-H$\cdots$O (structure **4C**), hydrogen bonds with the length of 2.17 Å, 2.16 Å and 2.65 Å, respectively (see Table 8.1). The analysis of their topological parameters shows that the O-H$\cdots$O H-bonds in these structures are very similar and the electron density in their BCPs is 0.0166 a.u. and 0.0171 a.u, respectively. They differ by one C-H$\cdots$O hydrogen bond, which exists in the structure **4C**, which is 2.9 kJ/mol less stable than the structure **4B**. The formation of the second H-bond deforms the geometry of the CH_2 group in the main chain of the molecule (instead of the the value of the OCH valence angle of 110.0°, it is 105.5°) and the total energy of the system is changing to the less stable. This example clearly shows that the formation of the hydrogen bonds can be unfavourable on the overall energy gain of the system. It can disrupt the stable geometry of the system, which has strong consequences on the absolute energy of the system.

The last analyzed PEG structure consists of five repeat subunits, therefore, it is characterized with the formation of different conformers of extremely differing structural patterns. The selected local minima with the most interesting properties are depicted in Figure 8.8. All of the PEG local minima presented possess intramolecular hydrogen bonds. Even if the starting PEG structure was the linear one, it was changed to the structure with the hydrogen bonds in the ends of the molecule, where the terminal hydroxyl groups are engaged (see structure **5E** in Figure 8.8). This means, that longer PEG molecules can not exist in purely linear configuration without any hydrogen bond formation. The global minimum structure (**5A**) possesses four hydrogen bonds, which were confirmed by either QTAIM or NCI index analyses. No extra hydrogen bonds were proven by NCI analysis, as it was mentioned for all previously described, smaller, PEG structures. Among the H-bonds of the structure **5A** are two bonds of O-H$\cdots$O nature and two C-H$\cdots$O ones. Their structural and topological parameters are given in Table 8.1. All these H-bonds are of relatively high linearity in the range of 116°–174°. The C-H$\cdots$O hydrogen bond of the length of 2.99 Å, is the weakest one, but still it is characterized by the electron density and the Laplacian of the electron density of 0.0034 a.u. and 0.0111 a.u., respectively, and is able to stabilize the molecule. As the structure **4A**, the global minimum structure **5A** has the associated and bifurcated hydrogen bonds, where one oxygen atom simultaneously plays the role of the hydrogen bond donor and acceptor or one hydrogen bond is interacting in two different H-bonds, respectively.

The formation of the associated hydrogen bonds is characterized also for the local minimum structures **5B**, **5C** and **5D**, but only the global minimum structure has two strong O-H$\cdots$O hydrogen bonds without additional deformation of the main PEG chain. The structure **5B** has only one strong O-H$\cdots$O hydrogen bond with the length of 1.91 Å and the valence OHO angle of 173.1°. This is one of the reason why this conformer has 14.34 kJ/mol worst total energy. At the same time, this H-bond has slightly lower strength the O-H$\cdots$O H-bond of the length of 1.88 Å in the global minimum structure. The structure **5C** is 21.62 kJ/mol less stable than the structure **5A** and it is very twisted in comparison to **5A**. The formation of five H-bonds: two O-H$\cdots$O and three C-H$\cdots$O, in this conformer is not a favourable process. Moreover, C-H$\cdots$O H-bonds in this structure are of low linearity, therefore they are weaker, but cause the additional structural deformation. With the lack of one O-H$\cdots$O hydrogen bond in the structure **5D** in comparison to structure **5C**, the system loses 9.8 kJ/mol. The highest energy difference is between the global minimum structure and the structure **5E**

(34.15 kJ/mol), which is caused by the absence of the mentioned stabilizing intramolecular interactions. Instead of it, only two hydrogen bonds are formed with the electron density of 0.0171 a.u. and 0.0077 a.u., respectively. The real possibility of the PEG molecule with the five repeat subunits to take all of the mentioned structures (or similar ones) can be checked performing the Car–Parrinello molecular dynamics simulations at finite temperature, what is described in the next subsections.

8.2.2 Electron density analysis

As it was described above, there is a tendency for the formation of intramolecular hydrogen bonds in the PEG molecule. The strength of such NCI interactions can be estimated using the electron density distribution over the analyzed molecule. Hydrogen bonds are formed when there is sharing of the electron density between some parts of the molecule. The visualized PEG structures with depicted distribution of the electron density of the isovalue of 0.2 a.u. are shown in Figure 8.9: a–d. They were obtained using the postprocessing analysis of the converged wavefunctions using the BLYP functional and Dunning basis set (aug-cc-pVTZ) in the Gaussian09 program package. The postprocessing was based on the generation of cube files from the data in a formatted checkpoint file with the number of points per side in the cube of 80 using the cubegen function in Gaussian09.

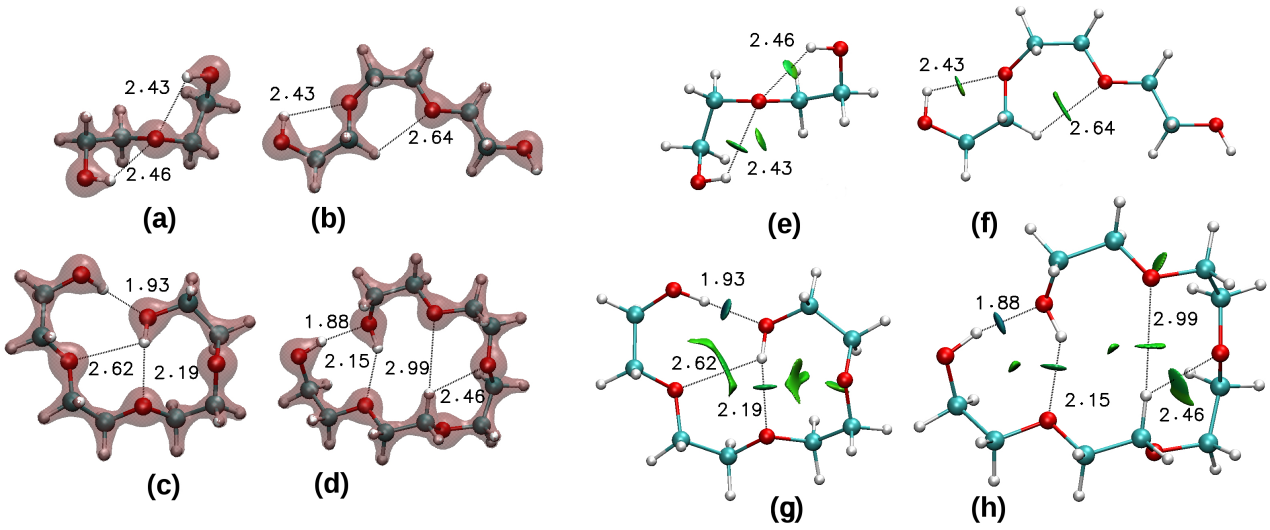

Figure 8.9: Electron density isosurface (isovalue of 0.2 a.u.): (a)–(d) and NCI surface (the reduced density gradient of 0.5 a.u.): (e)–(h) of the polyethylene glycol molecule with (a, e) two, (b, f) three, (c, g) four and (d, h) five –O–CH_2–CH_2– subunits obtained using DFT with BLYP/aug-cc-pVTZ. The color scale for the NCI surfaces is of -0.05 $< \rho <$ 0.05 a.u.

Taking into account that the noncovalent interactions in PEG have the maximum value of the electron density at the hydrogen bond BCPs of 0.0322 a.u. (see Table 8.1), no NCI interactions are seen in Figure 8.9: a–d. Using an additional tool, i.e. NCI index (see Section 3.4.2), where the reduced density gradient and the sign of the second eigenvalue of the electron-density Hessian are used, it is possible to visualize these NCI interactions. The PEG molecules after the NCI index analysis are shown in Figure 8.9: e–h, where the noncovalent interactions, including hydrogen bonds and vdW interactions are shown with the green surfaces of different shapes.

It is very hard to distinguish type and strength of the NCI interaction using only visualization in Figure 8.9: e–h. For this purpose NCI interactions were plotted in Figure 8.10 as the dependence between the reduced electron density gradient, s, and the sign of the second

eigenvalue of the electron-density Hessian, λ_2, together with the value of the corresponding electron density, ρ.

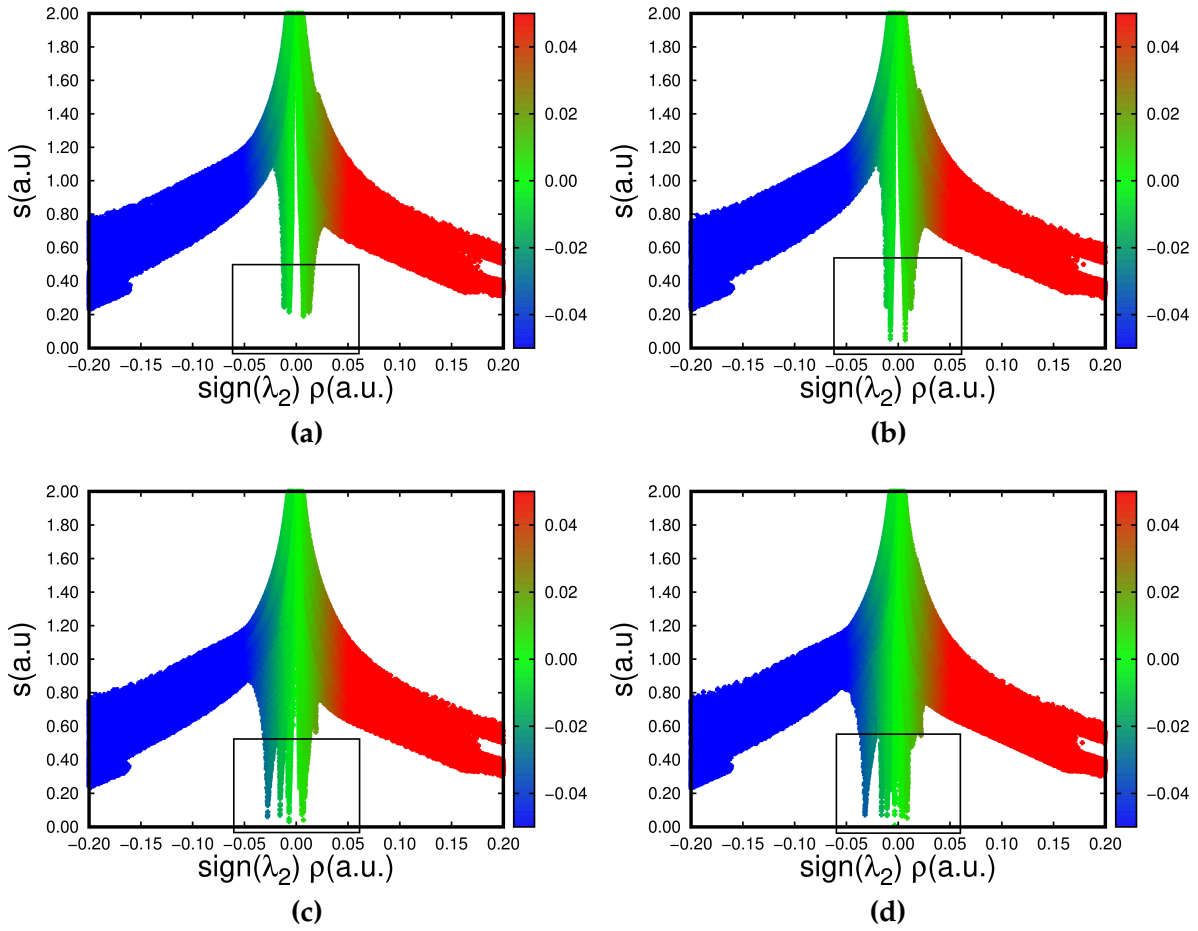

Figure 8.10: NCI analysis: the relationship between the reduced density gradient and the sign of the sign of the second eigenvalue of the electron-density Hessian, of the global minimum structures of PEG with (a) two, **2A**, (b) three, **3A**, (c) four, **4A**, and (d) five, **5A**, repeat subunits. The corresponding PEG structures analyzed are given in Figure 8.9: e–h. The region of the NCI interactions is marked with the black square.

NCI intramolecular interactions in different PEG molecules are localized in the electron density range of c.a. –0.05–0.05 a.u. marked with the black square in Figure 8.10. Negative sign of the second eigenvalue of the electron-density Hessian, λ_2, indicates the attractive interactions, such as hydrogen bonds, positive sign means the repulsion forces, while the both positive and negative signs with the density values of c.a. 0.005 a.u. indicate the the existence of weak vdW interactions, including dispersion interactions. In Figure 8.10 it is clearly seen that all global minimum structures of the PEG molecule, described in Section 8.2.1, are characterized with the hydrogen bonds formation (dark green and blue peaks), dispersion interactions (light green areas) and slight repulsion forces (dark green to red areas). The repulsion forces, which are of the greatest value in the case of the PEG molecule with two repeat subunits (see Figure 8.10: a) and still exist in the PEG molecule with three subunits, are generated by the deformation of the main PEG chain and additional hydrogen–hydrogen repulsion, described in the previous subsection. The repulsion forces disappear in the case of larger PEG molecules, i.e. starting from four subunits (structures **4A** and **5A**). The latest PEG molecules possess a net of different hydrogen bonds of different strength (more strong H-bonds are colored in blue color), which were explained in detail. In Figure 8.10: a, one can

notice that the repulsion forces are of the similar strength as the attractive ones: the value of the reduced density gradient, therefore, the electron density, are more less the same. This explains why the traditional hydrogen bonds, reported by IUPAC, were not confirmed with the QTAIM analysis. In the case of the structure **3A** (Figure 8.10: b) the existence of vdW interactions, which are stronger than the repulsion forces, is indicated by the highest green peaks with the values of the reduced density gradient close to 0 a.u., which means the high electron density and very strong vdW interaction (see Section 3.4.2).

8.2.3 Car–Parrinello molecular dynamics simulations

Static DFT calculations confirmed that the PEG molecules can exist in different conformational structures, which depend on the formed hydrogen bond pattern. In the literature, only O-H$\cdots$O hydrogen bonds in PEG were previously studied experimentally and were taken into consideration during classical simulations of larger PEG molecules. The data presented in the current PhD thesis show that additional C-H$\cdots$O H-bonds can be formed, which are of the great importance in case of the PEG molecules with four and five repeat subunits. To estimate the lifetime and the impact of the hydrogen bonds in the structural rearrangements of different PEG molecules, Car–Parrinello MD simulations of 25 ps in the gas phase at 300 K were performed.

PEG molecule with two repeat units

Due to its small size and the limited number of possible local minima structures, PEG molecule with two repeat subunits changes its geometry between several structures at 300 K. Six selected snapshots representing the formation of different conformers are depicted in Figure 8.11. The formation of the global minimum structure from the static calculations can

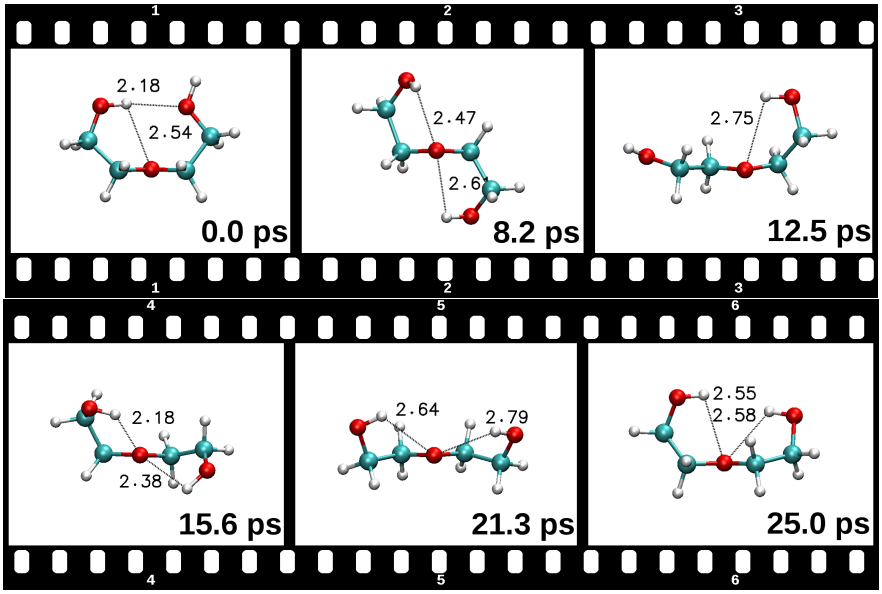

Figure 8.11: Selected snapshots of the structural rearrangements of the PEG molecule with two subunits from CP–MD simulations at 300 K. Each snapshot is presented with the corresponding timestamp. Hydrogen bonds are marked with the dashed lines.

be seen in the snapshot "2", where the simultaneous formation of two hydrogen bonds, of the length of 2.47 Å and 2.61 Å, is seen. Even if the structure **2A** is the most stable at 0 K, it is not the preferable conformation at 300 K. It can be seen from Figure 8.12, where the time evolution of two O-H$\cdots$O hydrogen bonds of PEG with two subunits is shown (each color

denotes one hydrogen bond). Changes of both: H···O distance and OHO angle, are shown here to confirm the formation of these weak interactions. When the distance is less than c.a. 3.0 Å and the OHO angle is more than 110°, the hydrogen bond is formed. Therefore, the structures with the simultaneous formation of two hydrogen bonds are taking place only for c.a. 0.8 ps in time of the simulation of 8 ps and temporary after the 15th ps. Most of the time of the simulation the molecule exists in the structure stabilized only by one of the hydrogen bonds mentioned. The lifetime of such structures is in the range of 1.4–2.2 ps.

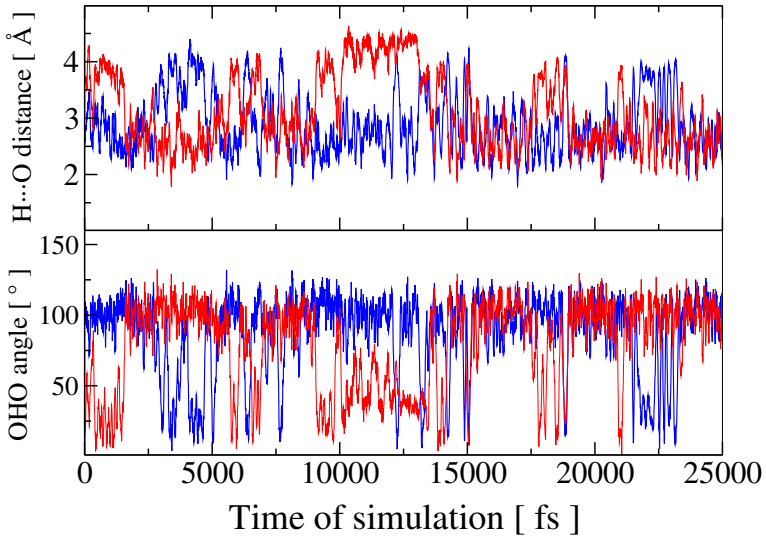

Figure 8.12: Time evolution of the structural parameters: H···O distance and OHO angle, of the O-H···O hydrogen bonds in PEG with two subunits. Blue and red curves denote parameters of the same O-H···O H-bonds formed between the terminal hydroxyl group and the etheric oxygen atom.

Among interesting PEG structures in the gas phase is the structure in the snapshot "1" in Figure 8.11, when two hydrogen bonds, originated from one hydrogen bond donor, are formed. This structure was changing to the one from the snapshot "2", due to the frequent movements of the hydrogen atoms from the terminal hydroxyl groups. Because of the H–H repulsion between the hydrogen atoms from the terminal OH groups, the structural rearrangements of the PEG molecule are starting from the configurations with two H-bonds, as in the snapshot "1", "5" or "6", to the structures with one H-bond, similar to the molecule in the snapshot "3". Later, the structure is changing to the conformer with two H-bonds as in the global minimum structure (similar to the structure in the snapshot "2"). Moreover, such PEG structural changes are repetitive since the second picosecond, when the rearrangements from the structure **2C** to **2A** are changed to **2B** and, once again, from the structure **2C** etc. It should be mentioned that during the simulation time of 25 ps no fully opened PEG molecule was observed.

PEG molecule with three repeat units

The formation of two simultaneous hydrogen bonds is making more probable in the case of the PEG molecule with three repeat subunits. It is clearly seen in Figure 8.13, where, similarly as for the previous PEG molecule, the time evolution of the H···O distance and the OHO angle is shown. These hydrogen bonds are of the same linearity, i.e. 100°–120°, as the previously described H-bonds, but most of the time the H···O distance and the OHO angle stay stable, forming the structures such as in the snapshot "3", "4" and "6" in Figure 8.14. Two O-H···O hydrogen bonds, as in the snapshot "3", are characterized with the average H···O distance of 2.45 Å and the full range of the H···O distance of 1.65–4.14 Å. They are

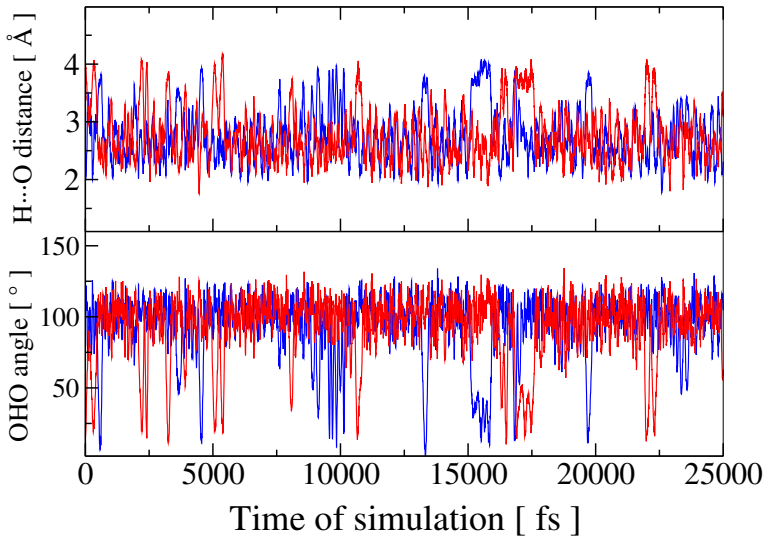

Figure 8.13: Time evolution of the structural parameters: H···O distance and OHO angle, of the O-H···O hydrogen bonds in PEG with two subunits. Blue and red curves denote parameters of the same O-H···O H-bonds formed between the terminal hydroxyl group and the closest etheric oxygen atom.

the typical noncovalent interactions in case of this PEG molecule.

The structure, similar to the global minimum one (structure **3A**), is shown in the snapshot "1", where the O-H···O and C-H···O H-bonds of the length of 2.00 Å and 2.59 Å, are formed. Unfortunately, such structure is not stable at 300 K, where the PEG structure, e.g. in the snapshot "3" or "4", is most probable to be formed. The formation of the associated hydrogen bonds, which was shown in the static DFT calculations to be the characteristic feature of the PEG molecule, is also possible. It is shown in the snapshot "5" in Figure 8.14, where the formation of four O-H···O hydrogen bonds of the H···O distance of 1.98 Å, 2.27 Å, 2.44 Å and 2.92 Å, occurs. Such H-bonds are stable for approximately 0.3 ps.

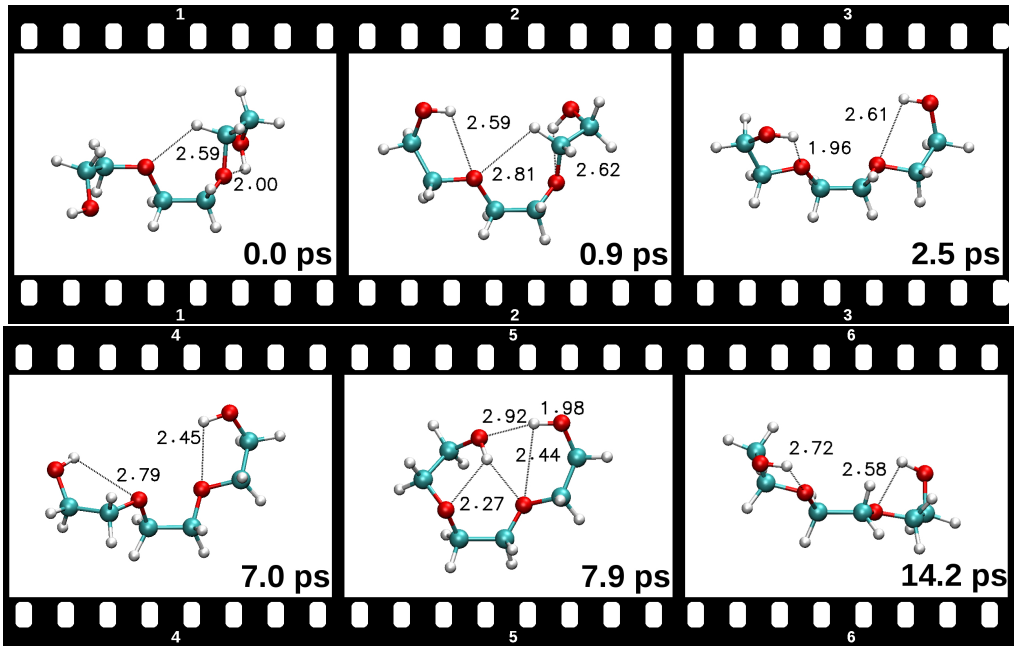

Figure 8.14: Selected snapshots of the structural rearrangements of the PEG molecule with three subunits from CP–MD simulations at 300 K. Each snapshot is presented with the corresponding timestamp. Hydrogen bonds are marked with the dashed lines.

PEG molecule with four repeat units

The polyethylene glycol molecule with four repeat subunits plays the role of the special form of the PEG molecule between PEG with three and five subunits. This molecule possesses the highest structural diversity and the possibility of forming interesting combinations of the hydrogen bonds, which can be seen in Figure 8.15. The structure similar to the global minimum structure (see **4A** in Figure 8.7) is shown in the snapshot "1", where the formation of four hydrogen bonds, as confirmed by NCI index analysis (Figure 8.9: g), is taking place. All these H-bonds are of O-H···O nature with the length of 1.91 Å, 2.44 Å, 2.66 Å and 2.77 Å, and form the associated hydrogen bonds. Because of the temperature influence such intramolecular interactions are not stable for the long time of the simulation, but they can be formed again and again during the MD run, e.g. in the snapshot "3", where slightly changed hydrogen bond pattern is formed.

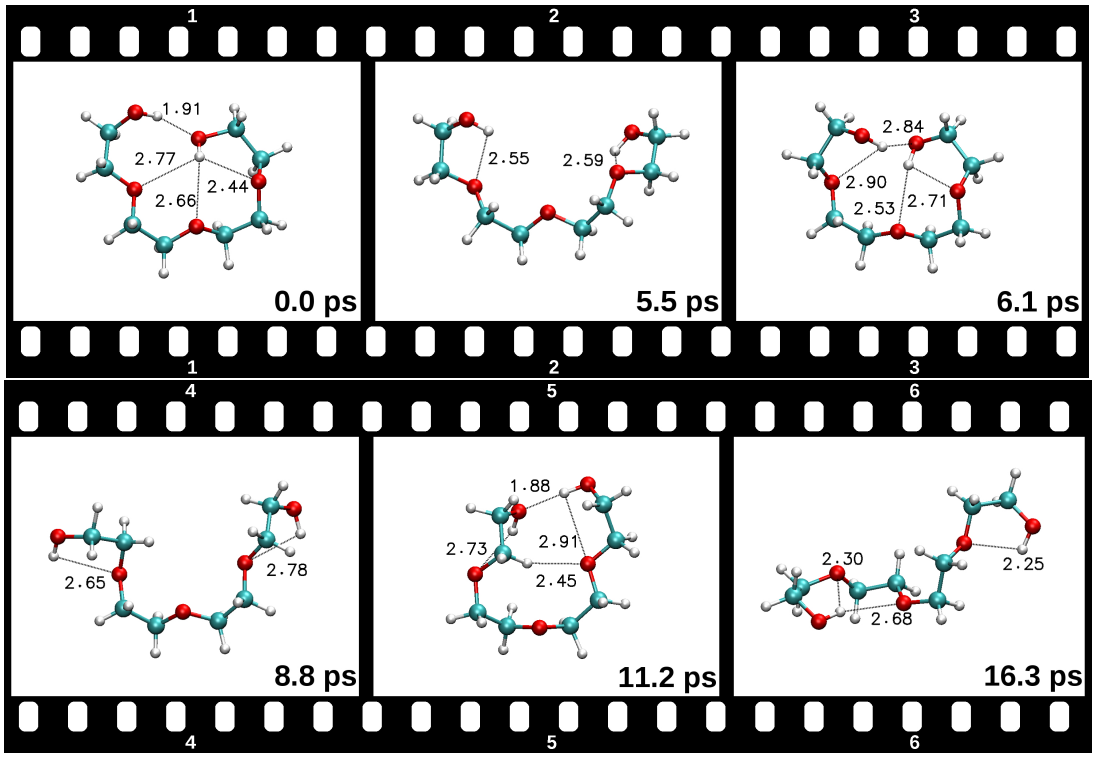

Figure 8.15: Selected snapshots of the structural rearrangements of the PEG molecule with four subunits from CP–MD simulations at 300 K. Each snapshot is presented with the corresponding timestamp. Hydrogen bonds are marked with the dashed lines.

In general, we have detected different: seven O-H···O and three C-H···O, hydrogen bonds in the simulation time of 25 ps for the PEG molecule with four ethylene oxide subunits. For the analysis of all these noncovalent interactions, several groups of H-bonds were classified, which enabled to understand the mutual hydrogen bond breaking and formation in different PEG conformations. Time evolution of six selected O-H···O hydrogen bonds (the most prominent ones) and three C-H···O ones is shown in Figure 8.16 and Figure 8.17. The first H-bond group is O-H···O (1) and O-H···O (2), which denote hydrogen bonds formed between the terminal hydroxyl groups. The formation of these bonds can be seen in the snapshot "1" and "5" with the corresponding H···O distance of 1.91 Å and 1.88 Å. These hydrogen bonds exist during the first 15 ps of the MD simulation (upper panel in Figure 8.16). Due to their formation, the PEG molecule reminds the closed PEG structure. The second set consists of O-H···O (3) and O-H···O (4) H-bonds, formed between one terminal hydroxyl

group and the fourth O atom (starting from the right side of the molecule). Therefore, for the left hydroxyl group this H-bond is formed between the closest etheric oxygen atom as the acceptor of the H-bond (hydrogen bonds of the length of 2.55 Å in the snapshot "2" in Figure 8.15). This hydrogen bond, i.e. O-H···O (3), is stable during the whole simulation time (blue curve in the lower panel in Figure 8.16). O-H···O (4) H-bond is formed in the PEG structure in the snapshot "1" with the length of 2.77 Å. The last hydrogen bond exists only three times during the simulation time and denotes the formation of the associated H-bonds like in the global minimum structure, i.e. **4A**.

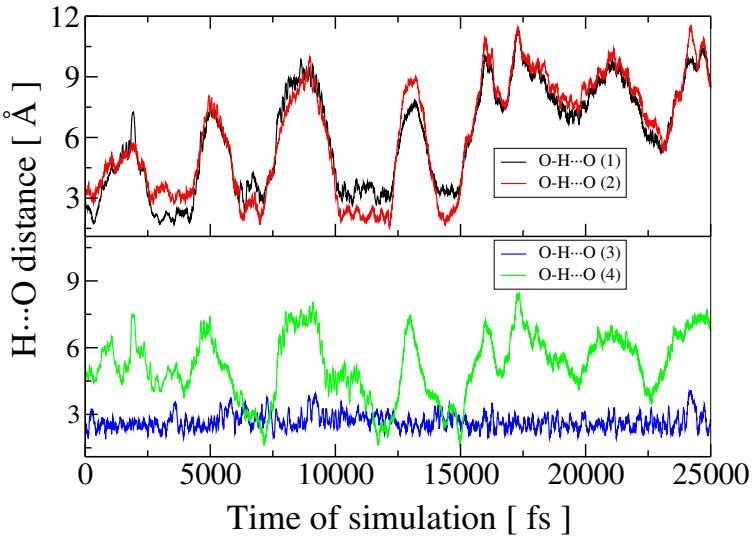

Figure 8.16: Time evolution of the H···O distance of O-H···O hydrogen bonds in PEG with four subunits. The description of the nature of the formed hydrogen bonds is explained in the text.

The third group of the analyzed hydrogen bonds is formed from O-H···O (5) and O-H···O (6), corresponding to the intramolecular interations between the terminal hydroxyl groups as H-bond donors and central etheric oxygen atom as H-bond acceptor. PEG structures

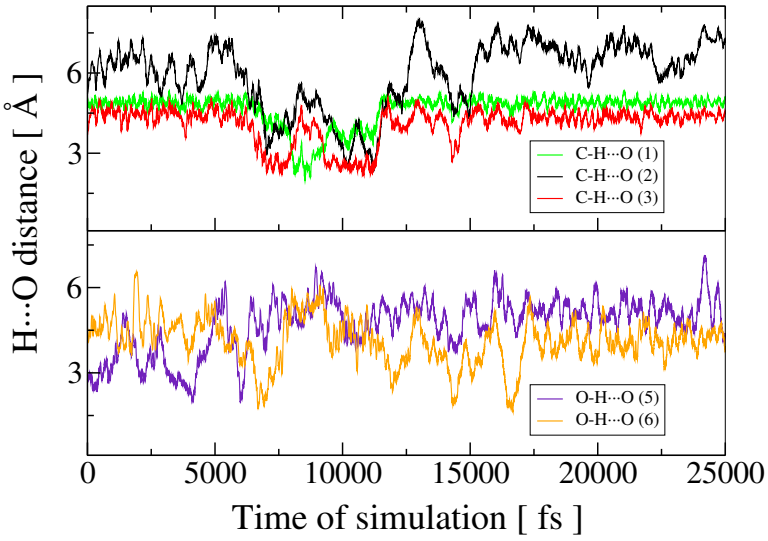

Figure 8.17: Time evolution of the H···O distance of O-H···O and C-H···O hydrogen bonds in PEG with four subunits. The description of the nature of the formed hydrogen bonds is explained in the text.

stabilized with these H-bonds exist several times during the MD simulation (see lower panel

in Figure 8.17) with the maximum lifetime of c.a. 1 ps. These hydrogen bonds can be seen in the snaphot "1" or "6" with the H···O distance of 2.77 Å and 2.68 Å, respectively. From the time evolution of these H-bonds, one can see that the PEG molecule is not able to transform in the structure where both of the mentioned hydrogen bonds exist.

The last group of the selected H-bonds consists of three C-H···O hydrogen bonds, formed, for example, in the structure from the snapshot "5" in Figure 8.15. All these H-bonds are weaker than the O-H···O ones, but still they are effectively formed during the other PEG rearrangements connected with the changing of the one conformer to the other one. The existence of these bonds was confirmed at the simulation time from 6.6 ps to 11.4 ps (see upper panel in Figure 8.17). Their lifetime is longer than for the PEG with three subunits. It is in the range of 0.5–2.0 ps. Even if there is a tendency to form various hydrogen bonds in the PEG molecule, the most stable conformer is that from the snapshot "1" with the formation of the associated H-bonds.

PEG molecule with five repeat units

All previously described low molecular PEG molecules have a tendency to increase the possibility for the formation of intramolecular hydrogen bonds with the addition of the next ethylene oxide subunit. In case of the last examined PEG molecule with five subunits, this tendency starts to be slightly decreased. From Figure 8.18, where several examplary PEG con-

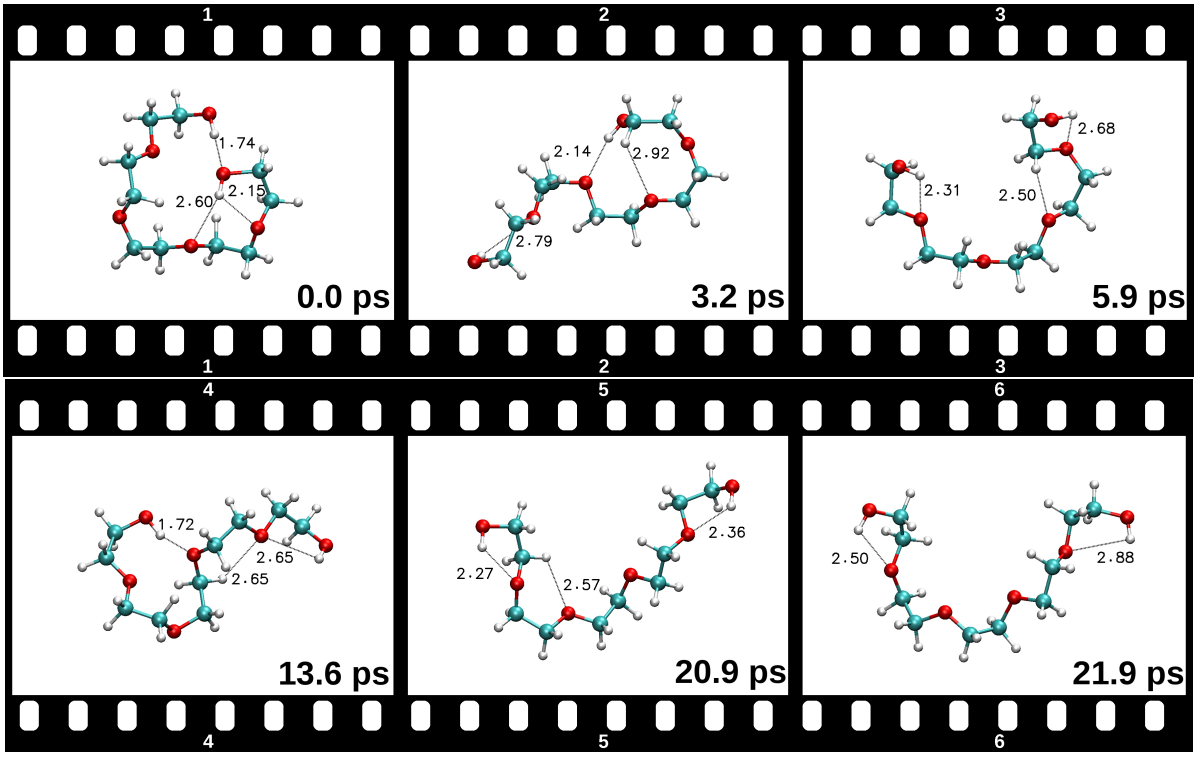

Figure 8.18: Selected snapshots of the structural rearrangements of the PEG molecule with five subunits from CP–MD simulations at 300 K. Each snapshot is presented with the corresponding timestamp. Hydrogen bonds are marked with the dashed lines.

formers at 300 K are depicted, it can be noticed that the molecule starts to be more opened than closed, with the additional stabilization due to the hydrogen bonds formation. Because of its larger size and the formation of extra structural deformations and H–H repulsion during the process of closing the molecule, it tends to form stable hydrogen bonds "on the ends", when the terminal hydroxyl groups and the closest etheric oxygen atom are engaged.

Structures with these hydrogen bonds are shown in the snapshots "3", "5" and "6" with the corresponding H···O distances of 2.31 Å, 2.68 Å, 2.27 Å, 2.36 Å, 2.50 Å and, finally, 2.88 Å. The stability of the mentioned hydrogen bonds is confirmed by their time evolution shown in Figure 8.19 (lower panel).

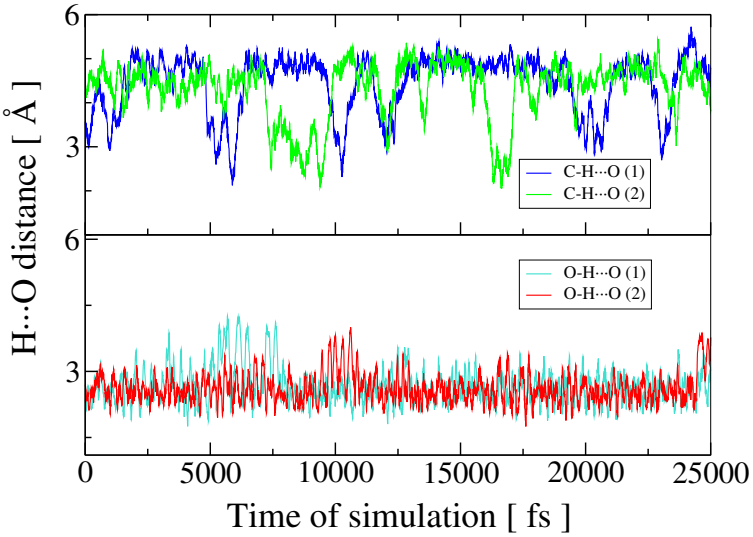

Figure 8.19: Time evolution of the H···O distance of O-H···O and C-H···O hydrogen bonds in PEG with five subunits. O-H···O hydrogen bonds denote H-bonds formed between the terminal hydroxyl groups as H-bond donors and the closest etheric oxygen atom as the H-bond acceptor.

The formation of temporary C-H···O H-bonds is also possible, e.g. in the snapshot "2", "3", "4", where their lengths equal to 2.92 Å, 2.50 Å and 2.65 Å, respectively. Their lifetime is c.a. 0.3 ps and they are formed, the same as in case of the PEG molecules with four subunits, only during transition of one structure to the other one. The formation of the associated H-bonds is also possible for this PEG molecule, but they are weaker in comparison to the smaller PEG. The examplary structure with such hydrogen bonds is shown in the snapshot "1", when three O-H···O H-bonds of the length of 1.74 Å, 2.15 Å and 2.60 Å, are formed. PEG local minima of higher relative energy are also seen during the simulation time, for example structures similar to the local minimum **5E** are in the snapshots "3" and "5". All PEG local minima can be detected in the form of different structural rearrangements of the PEG molecule, but only several examples were described here.

Polyethylene glycol molecule is a simple molecule, but it is very flexible, especially at room temperature or higher ones. It is stabilized by strong O-H···O and weak C-H···O hydrogen bonds, which can be formed between different parts of the molecule, i.e. hydrogen bond donors and acceptors. The highest structural diversity is characterized for the PEG molecule with four subunits, which have a specific hydrogen bond pattern and the ability to form associated intramolecular H-bondings. Starting from the PEG molecule with five repeat subunits, the molecule starts to be more "linear" than "closed", but still the formation of the hydrogen bonds with the participation of the terminal hydroxyl groups is possible.

Chapter 9

Noncovalent functionalization of carbon nanotube

During the synthesis of the composites, based on the carbon nanotubes as polymer fillers and polyurethanes as the polymer matrices, different processes, concerning intermolecular interactions between molecules, can take place. In the *grafting to* procedure, the PU polymer is attaching to the surface of the carbon nanotubes. Such approach is not suitable to obtain composites with the equal, high, dispersion of CNTs in the polymer matrix, which importance was described previously. Therefore, *grafting from* technique is used, when the composite is produced from the carbon nanotubes together with PU monomers, which react on the CNTs, and the polymer can be directly attached to the surface of the polymer filler. Different *grafting from* synthetic variations are possible, but all of them use the PU monomers mixed with the carbon material. This approach gives better dispersion of CNTs in PU, but there is no information about intermolecular interactions between the molecules in such polymer "mixture". Moreover, both covalent and noncovalent interactions between PU monomers and CNTs are possible during the synthesis of such composites. Both types of the interactions should be taken into account in order to understand processes responsible for the structure of the produced material and the origin of its properties.

In this Chapter the studies of the noncovalent interactions between PU monomers, i.e. diisocyanates and polyol, are analyzed. Static density functional theory calculations are used here to estimate the affinity of the molecules to be adsorbed on the single-walled carbon nanotubes (6,0) and (10,0).

9.1 Diisocyanates molecules

Two, of the most commonly used, diisocyanates were used to understand the noncovalent interactions between diisocyanates and single-walled carbon nanotubes, i.e. MDI and TDI. They are of aromatic nature and are more reactive than the aliphatic diisocyanates. The only one structural difference between the chosen diisocyanate molecules is the amount of the phenyl rings, therefore, different strength of the noncovalent interactions and the position on the SWCNT surface are expected.

9.1.1 Noncovalent interactions between TDI and SWCNT

TDI, 2,4-diisocyanato-1-methylbenzene, is similar to the most known aromatic molecule, i.e. benzene, therefore, the similar interaction pattern with the surface of the single-walled carbon nanotube is possible. The difference between these two molecules is the presence of the isocyanate and methyl functional groups in the TDI aromatic ring (see Figure 5.1). Taking

into account our initial test calculations for the adsorption of the benzene molecule on the SWCNT(6,0), described in Section 7.2.2, nine different structures of various orientation of the TDI molecule on SWCNT(6,0) were examined. All of the analyzed systems were made in such a way that enables to compare different alignments of the molecule on SWCNT. As a result, bridge, top and hollow positions, as shown in Figure 7.2, were analyzed in the noncovalent functionalization of SWCNT by TDI. Two of the systems analyzed have converged to the same local minimum (structure **A**, which is the global minimum structure) and, finally, eight different structures of the TDI adsorption on SWCNT(6,0) were obtained. These structures in two different views: top view and side view, are depicted in Figure 9.1 and Figure 9.2. In Figure 9.1, the structures with the initial TDI in the bridge position, as the most stable, are given, whereas top and hollow orientations are presented in Figure 9.2. The

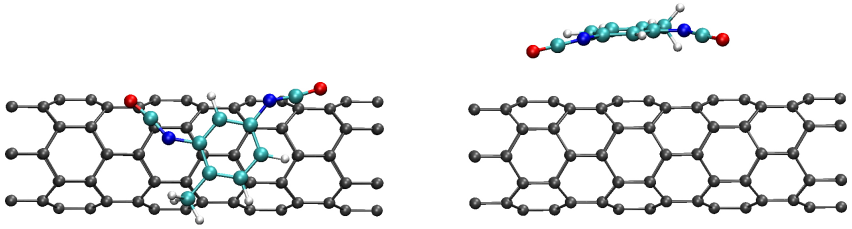

(A): E_{ads} = -49.21 kJ/mol

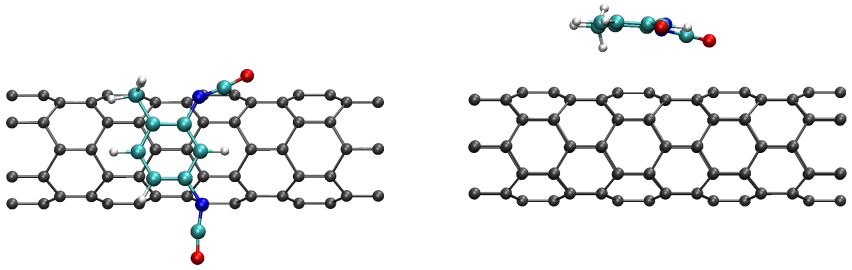

(B): E_{ads} = -43.90 kJ/mol

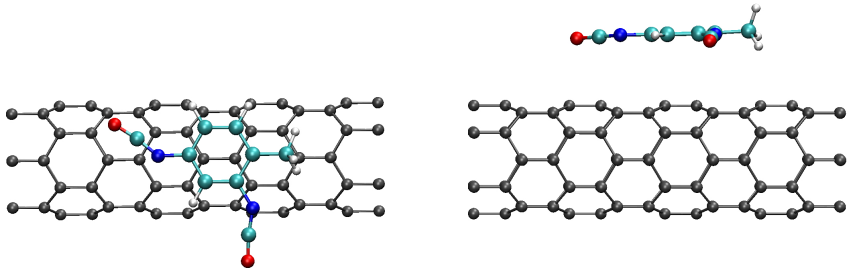

(C): E_{ads} = -41.97 kJ/mol

Figure 9.1: Optimized structures of noncovalent functionalization of SWCNT(6,0) with TDI molecules: top view and side view, with the corresponding values of the adsorption energy. Only the initial starting configurations in bridge position are shown.

adsorption energies of the TDI molecule on the SWCNT(6,0) are listed in Table 9.1. They were calculated using Equation 7.1 in Section 7.2.1. Negative value of the adsorption energy indicates attractive interactions between SWCNT and the molecule adsorbed, and stabilizing effect of the formation of such system in comparison to the individual components. To enable a transparent analysis of the results obtained, Table 9.1 was completed with the most important structural parameters of all local minima depicted.

The global minimum structure for the TDI adsorption on the surface of SWCNT(6,0) is the structure **A** in Figure 9.1 with the adsorption energy of -49.21 kJ/mol. In this structure, the TDI molecule is positioned in the top position with respect to the nanotube surface, which

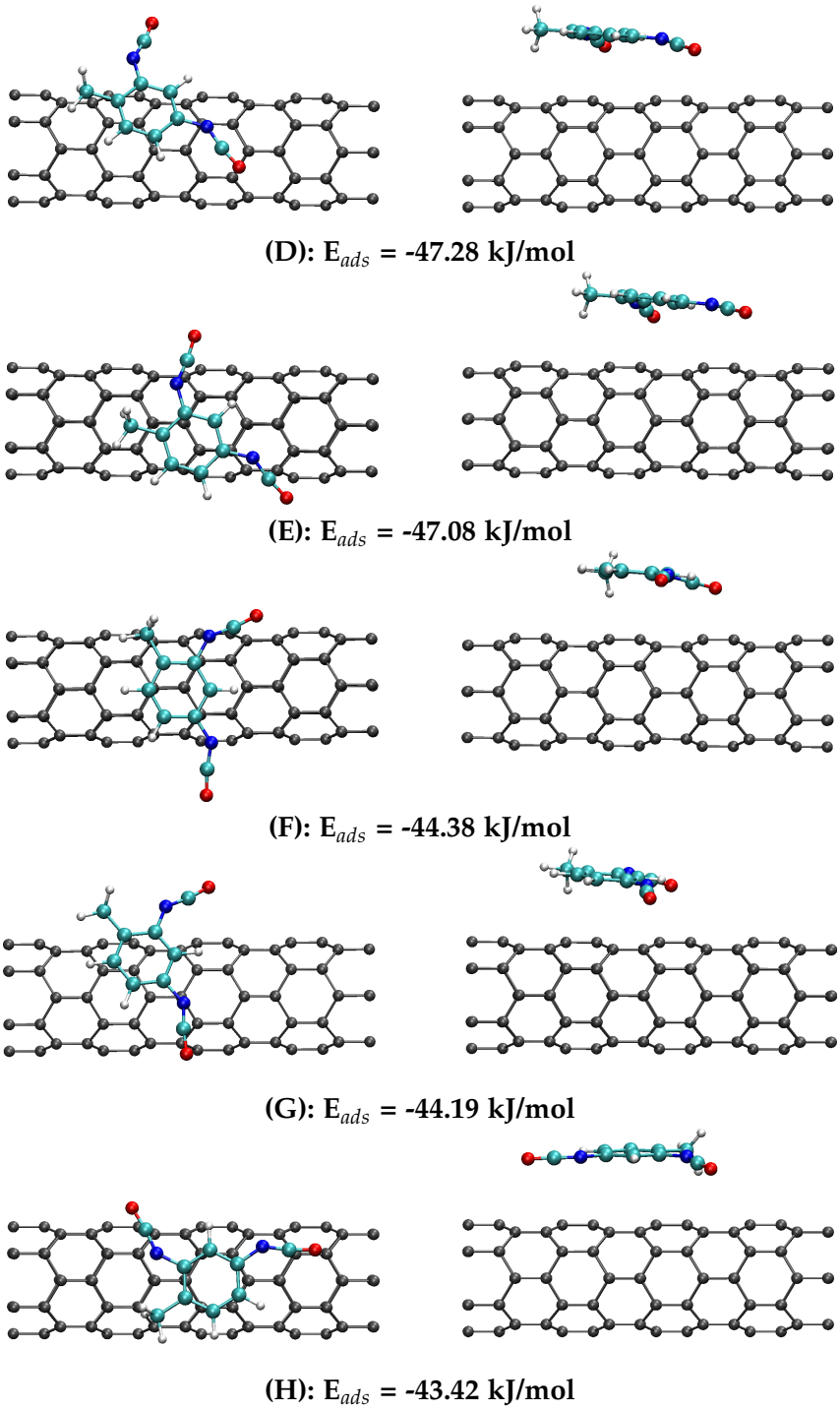

Figure 9.2: Optimized structures of noncovalent functionalization of SWCNT(6,0) with TDI molecules: top view and side view, with the corresponding values of the adsorption energy. The initial starting configuration in top and hollow positions are shown.

is clearly seen in the top view of the system. It should be mentioned that the starting configuration of this structure was in the most stable position (in case of the benzene molecule), i.e. bridge one, but after the geometry optimization, it has been changed to the top one. Both bottom and bridge positions of the π-molecules on the SWCNTs are the most stable, which are similar to the parallel-displaced position of two benzene molecules in the benzene dimer (see Section 3.3). The difference between the bridge and top positions of benzene on SWCNT(6,0) is only 0.87 kJ/mol, what was reported during the initial calculations, summed

in Table 7.2. Therefore, the positions can be easily changed depending on the nature of the molecule adsorbed. Results obtained, concerning the adsorption of the TDI molecule on the SWCNT(6,0), listed in Table 9.1, show that the top position of TDI on SWCNT(6,0) is the most preferable one with the best adsorption energies of such arrangement. Even the initial hollow position was changed to the top one, but no changes from top to other positions were seen.

Such orientation can be explained on the basis of the distribution of the charge density of the SWCNT(6,0) and TDI, what is depicted in Figure 9.3: b, where the charge density of isovalue of 0.2 a.u. is shown. The electron density is localized on the carbon-carbon bonds in the carbon nanotube, which are most preferable interacting places for the adsorbate. As a result, the TDI molecule is interacting with the CNT surface via dispersion and quadrupole–quadrupole interactions. As it was mentioned in case of the NCI index, weak vdW interactions are characterized with the electron density of c.a. 0.005 a.u. From Figure 9.3: c one can see that the visualization of the charge density with the isovalue of 0.005 a.u. shows the intermolecular interactions between TDI and SWCNT. Top position of the interacting molecule enables the effective, dispersion-based "sharing" of the electron density between adsorbate and SWCNT, therefore, the system is stabilized. The shortest C–C distance between the TDI molecule and the CNT surface is in the range of 3.06–3.27 Å (see Table 9.1) and corresponds to the dispersion nature of the $\pi - \pi$ stacking interactions, what was described in Section 3.4 for the benzene dimer.

Table 9.1: The values of the adsorption energy, E_{ads}, the initial/final position and the list of the structural parameters of the TDI molecule adsorbed on the surface of SWCNT(6,0). Among the listed structural parameters are: the shortest C–C distance between the carbon atom from TDI and SWCNT, l_{C-C}, the C-C-N-C dihedral angle between the TDI phenyl ring and the NCO groups and the shortest distance between O atom from NCO groups and the carbon atom from SWCNT.

Label	**E_{ads}** [kJ/mol]	**l_{C-C}** [Å]	**C-C-N-C** [°]	**C-C-N-C_{CH_3}** [°]	**Initial**	**Final**	**$O_{NCO} \cdots$ CNT** [Å]
A	**-49.21**	**3.17**	**13.73**	**11.99**	**Bridge**	**Top**	**3.35; 3.43**
B	-43.90	3.06	5.88	9.87	Bridge	Bridge	3.45; 4.84
C	-41.97	3.25	4.35	7.52	Bridge	Bridge	3.40; 4.69
D	**-47.28**	**3.08**	**11.81**	**15.92**	**Hollow**	**Top**	**3.58; 4.08**
E	**-47.08**	**3.07**	**10.41**	**14.25**	**Top**	**Top**	**3.74; 3.62**
F	-44.38	3.17	7.52	12.04	Top	Top	3.51; 4.93
G	-44.19	3.19	8.43	16.78	Hollow	Top	3.69; 4.69
H	-43.42	3.27	2.01	11.88	Hollow	Hollow	3.38; 3.57

The adsorption energy of the benzene molecule on the SWCNT(6,0) is -27.69 kJ/mol for the bridge position and -26.82 kJ/mol for the top position (Section 7.2.2). In case of the TDI molecule, the adsorption energy is -49.21 kJ/mol, which is 22.39 kJ/mol more stable concerning the top position. The results for all calculated TDI-SWCNT systems indicate that the range of the adsorption energy of the TDI on SWCNT(6,0) is -49.21 – -41.97 kJ/mol, which is still 15.15 kJ/mol more stable than for the benzene molecule. The reason of such relatively high differencies can be the specific nature of the TDI molecule in comparison to the benzene molecule. TDI has two electron-withdrawing substituents, i.e. isocyanate functional groups, which possess a double effect on the affinity of the TDI molecule to adsorb on the SWCNT(6,0).

Firstly, according to the Hunter–Sanders model [91], NCO groups change the local orientation of the π-electron density in the phenyl ring of TDI, slightly changing the quadrupoles localized from the both sides of the aromatic ring. This substituent effect is significantly larger than the electron donating effect of the methyl group, because it is enhanced with the mutual *meta* orientation of both isocyanates groups. The influence of the isocyanate groups on the electron density distribution can be seen from Figure 9.3: d, where the vizualization of isovalue of 0.3 a.u. is shown. Comparing to the charge density distribution on the carbon-carbon bonds in the carbon nanotube, the carbon-carbon bonds of the TDI molecule are characterized by higher charge density, because of the electron-withdrawing effect of the NCO substituents. Substituted aromatic molecules have better $\pi - \pi$ interactions, which was shown previously by M. Sinnokrot and C. Sherrill [90].

Secondly, the presence of the substituents in the TDI molecule increase the electrostatic and dispersion interactions between the substituents and the surface of the SWCNT, which have stabilization effect on the adsorption affinity. Moreover, S. Wheeler and J. Bloom [140] have suggested that the effect of the substituent interactions with the surface of the carbon nanotube is higher than the increase of the $\pi - \pi$ interactions, existing between the molecule adsorbed and the surface. Therefore, the adsorption of the TDI molecule on the SWCNT(6,0) is the interplay between the local density changes in the aromatic ring and the additional dispersion interactions between the isocyanate groups and the CNT surface. In both cases, the significant influence of the substituents, on the adsorption affinity of the TDI molecule on the carbon nanotube, is observed.

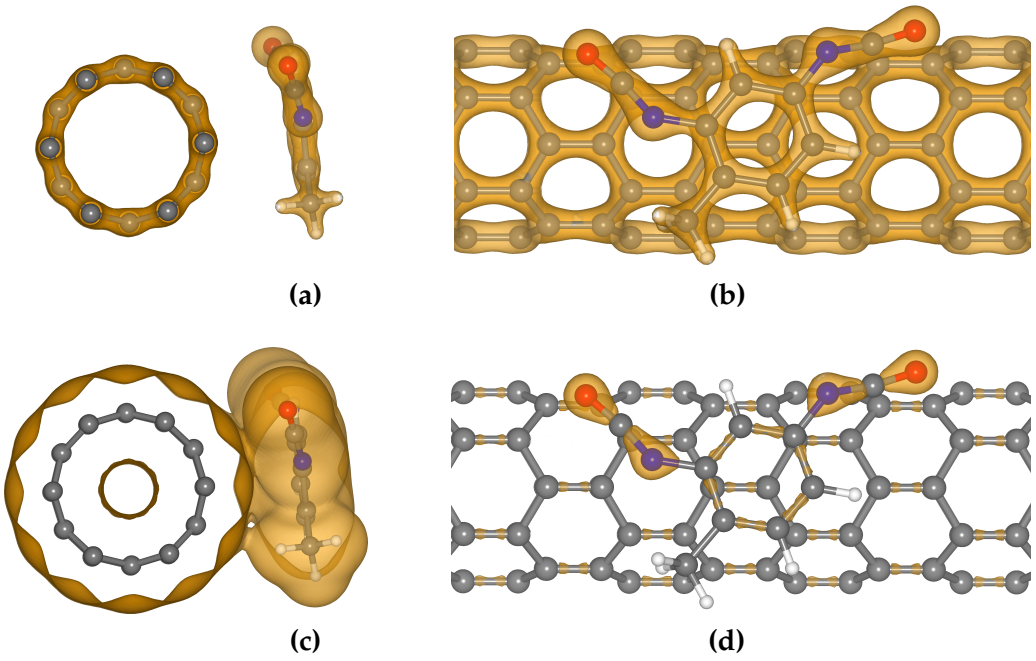

Figure 9.3: Vizualization of the charge density for the global minimum structure (**A**) of the noncovalent functionalization of SWCNT(6,0) by the TDI molecule. Different isosurfaces are presented: (a) profile view, isosurface of 0.2 a.u., (b) top view, isosurface of 0.2 a.u., (c) profile view, isosurface of 0.005 a.u., (d) top view, isosurface of 0.3 a.u.

The role of the isocyanate functional groups on the adsorption of the TDI molecule on the surface of the SWCNT(6,0) can be proven using the detailed analysis of the structural parameters of the adsorbed molecule on the CNT surface. The most important parameters are listed in Table 9.1. Among them are the deformation of the NCO groups from the plane of the aromatic ring and the distance between the oxygen atom from the isocyanate group and the closest carbon atom from the carbon nanotube. Taking into account the nature of the NCO

group, described in Section 5.1, it prefers to be in one planar plane with the TDI aromatic ring. All changes of the mutual position of the NCO group, with respect to the TDI phenyl ring, can be monitored by the C-C-N-C dihedral angle, introduced in Section 8.1.2. From data in Table 9.1, it can be noticed that the higher deformations of two isocyanate groups in TDI are characterized to the most stable structures of the TDI adsorption on SWCNT(6,0), i.e. structures **A**, **D** and **E** with the adsorption energy of -49.21 kJ/mol, -47.28 kJ/mol and -47.08 kJ/mol, respectively. In the mentioned structures both NCO groups of the TDI molecule are deformed on 13.73°/11.99°, 11.81°/15.92° and 10.41°/14.25°, respectively, from the plane of the aromatic ring. Moreover, NCO groups in different TDI arrangements on the SWCNT(6,0) are oriented close to the CNT surface with the O$\cdots$CNT distance in the range of 3.35–4.08 Å (see Table 9.1). Higher O$\cdots$CNT distances, c.a. 3.8 Å, correspond to the non-interacting, with the CNT surface, isocyanate groups, which are located too far away from the carbon nanotube (see structures in Figure 9.1 and Figure 9.2).

The mentioned values indicate that the isocyanate groups have a significant influence on the noncovalent interactions between TDI diisocyanate molecule and the carbon nanotube. Is it possible to estimate what parameter is of greater importance during the noncovalent functionalization of the SWCNT with TDI: the position of the molecule with respect to the surface or the orientation of the isocyanate groups? Second the closest position of the TDI isocyanate groups to the SWCNT surface has the structure **H** with the O$\cdots$CNT distances of 3.38 Å and 3.57 Å, but the corresponding C-C-N-C dihedral angles are of 3.27° and 2.01°, which indicate lower interactions via NCO groups. This structure is characterized with lower absolute value of the TDI adsorption of -43.42 kJ/mol, which is close to the adsorption energy of the structure **B** (-43.90 kJ/mol), where one of the NCO groups is not interating with the CNT surface. It can be explained on the basis of the position of TDI on SWCNT. In the structure **H**, the TDI molecule is localized in the hollow position (see Figure 9.2: H), which is less stable than the top one (see Figure 7.2). As a result, the system is less stable than the global minimum by 5.79 kJ/mol.

All the facts mentioned stand for the top position as the most influential element during the adsorption of TDI. The second parameter is the position of the isocyanate groups: the deformation directed to the SWCNT surface and the distance between NCO and the surface. The mentioned structural parameters should be fulfilled for both isocyanate groups to gain the best adsorption of the TDI molecule on the surface of SWCNT. The systems with the higher adsorption affinity of the TDI molecule to the SWCNT surface are characterized with either proper position of the π-molecule or the geometry of the isocyanate group with respect to the SWCNT surface.

The noncovalent functionalization of the SWCNT(6,0) with the TDI molecule is based on two types of the noncovalent interactions, i.e. $\pi - \pi$ interactions and the additional London dispersion interactions originated from the presence of the isocyanate groups in the molecule. $\pi - \pi$ interactions during this functionalization can be increased as the result of the electron-withdrawing substituent effect, which changes the local orientation of the π-density located within the TDI aromatic ring. The electron-withdrawing effect of the substituent in TDI is enhanced, as the result of the specific *meta* position of both isocyanate groups. The mentioned interactions can be seen using the charge density analysis and its visualization with the isovalue of 0.005 a.u.

9.1.2 Noncovalent interactions between MDI and SWCNT

The MDI molecule, which has an additional phenyl ring (see Figure 5.1), shows slightly different adsorption affinity on the surface of SWCNT(6,0). As it was estimated in the previous Section, the TDI molecule has better adsorption energy on SWCNT(6,0), in comparison to the

benzene molecule, on 21.52/22.39 kJ/mol (depending on the position chosen for the benzene adsorption, i.e. bridge or top, respectively). The addition of the second phenyl ring to the MDI molecule changes the intermolecular interactions between MDI and SWCNT, and the adsorption energy equals to -64.74 kJ/mol for the global minimum structure (see Figure 9.4: A). In comparison to the most stable TDI molecule on SWCNT(6,0), the MDI-SWCNT system is 15.53 kJ/mol more stable, which is less than the gain of the adsorption energy as the result of the "pure" adsorption of the benzene molecule, i.e. 21–22 kJ/mol. Therefore, it can be stated that the additional phenyl ring of the MDI molecule generates less stable intermolecular interactions with the carbon nanotube sidewall. What is the source of such, lower, energy gain?

There are two main reasons of the decreased adsorption of MDI on the carbon nanotube in comparison to TDI, namely, *(i)* "non-planar" aromatic rings of MDI with respect to the CNT and *(ii)* the decreased electron-withdrawing effect of the isocyanate groups. The first factor is caused by the presence of the CH_2 group between two phenyl rings of the MDI molecule, which prevents MDI to exist in the one planar plane with respect to the CNT surface and to get the most effective arrangement of the aromatic rings involving $\pi - \pi$ interactions. The results of the MDI structural diversity in the gas phase at 300 K, reported in Section 8.1.2, indicate that there is no possibility of MDI to exist in the "planar" form (see Figure 8.6; the most probable mutual orientation of two MDI phenyl rings is with the dihedral angle of 40°–60°), therefore, there is no possibility to obtain better adsorption sites with more "planar" MDI. The second factor was described in case of TDI adsorption on SWCNT(6,0), where two isocyanate groups are attached to the same phenyl ring in *meta* position, which increases the overall substituent effect and can increase the strength of the adsorption of the molecule. In case of the MDI molecule, only one NCO is attached to the phenyl ring. Both these factors influence the strength of the $\pi - \pi$ interactions between the MDI molecule and the SWCNT, thus, the obtained energy of adsorption is lower. The influence of the dispersion interactions between the isocyanate groups and the surface of the carbon nanotube can be neglected here, because of the similar structural changes of the NCO groups in both MDI and TDI, which are discussed below.

We have chosen five, the most important, structures of the noncovalent functionalization of the SWCNT(6,0) by MDI. They are depicted in Figure 9.4 and Figure 9.5 with the corresponding values of the adsorption energy. Among the chosen local minima, the arrangements of the MDI molecule across (structures **A** and **B**) and along (structures **C**, **D** and **E**) the Z-axis of the carbon nanotube with different types of possible interactions are shown. The most stable structures of the noncovalent functionalization of the SWCNT(6,0) with MDI are the structures with the across position of MDI, i.e. structure **A** and structure **B**, with the corresponding energy of adsorption of -64.74 kJ/mol and -63.68 kJ/mol. The across position enables the maximum overlap of π-electron density and quadrupole moments [91] of both phenyl rings of MDI with the surface of SWCNT. Only in the case of such orientation the interactions of both phenyl rings with CNT are possible, therefore, these structures are of the best adsorption energies. The visualization of the noncovalent interactions between the carbon nanotube and the MDI molecule in the structure **A** is depicted in Figure 9.6: c. Analysis of the charge density in case of TDI and MDI molecules adsorbed on the SWCNT(6,0) indicates the similarity of the noncovalent interactions that exist during the functionalization of the CNT (see Figure 9.3 and Figure 9.6) with these aromatic diisocyanates.

The position of the MDI phenyl rings, with respect to the CNT surface, is different in case of the structures **A** and **B**. One of the phenyl rings of MDI in the structure **A** is localized in top position on the CNT hexagon, while the second one is in the bridge position. It is depicted in Figure 9.6: b, d, where the charge density of the molecules is visualized. In case of the structure **B**, both phenyl rings are located in the top position. This structural difference is not

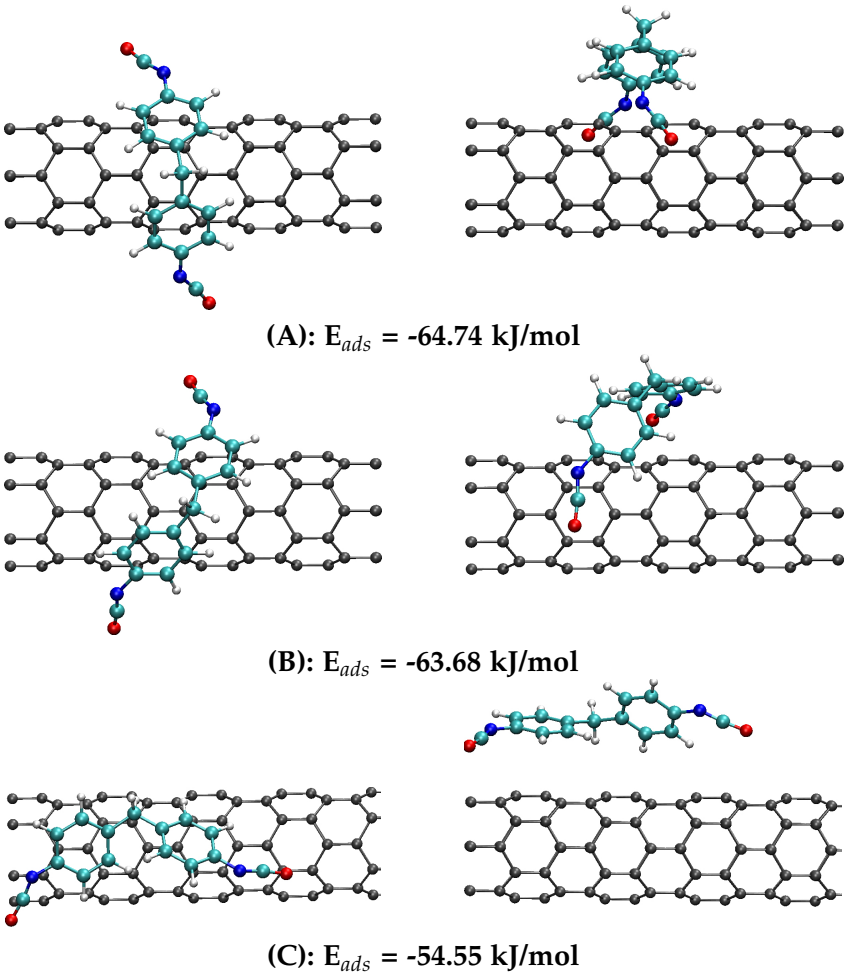

Figure 9.4: Optimized structures of noncovalent functionalization of SWCNT(6,0) with MDI molecules: top view and side view, with the corresponding values of the adsorption energy.

so important, here, as the distance between the MDI molecule and the CNT. In case of the structure **B**, the second phenyl ring is located slightly further from the CNT surface – instead of the shortest C–C distance of 3.13 Å (structure **A**), the distance is 3.22 Å (see Table 9.2). Such small differences induce a difference of the adsorption energy of 1.06 kJ/mol, which is less than the chemical accuracy and can be neglected.

The structure **C** in Figure 9.4 represents the position of MDI along the CNT, when one phenyl ring is more parallel to the nanotube axis than the other one. The detailed analysis of the structural parameters of all mentioned structures (listed in Table 9.2) indicates that the MDI intramolecular parameters, as a result of the adjusting to maximum interaction with the surface, are changed for the most in the case of the structure **C**. It can be seen from the increase of the CCC valence angle between the phenyl rings by 3.58°, in comparison to the gas-phase MDI molecule. This change is the highest one among all analyzed MDI adsorption sites on SWCNT. The energy difference between the across and along position of MDI on SWCNT is 10.19 kJ/mol.

The structure **D** (see Figure 9.5) with the adsorption energy of -43.22 kJ/mol, which is close to the typical adsorption energies of the TDI molecule on SWCNT(6,0), shows the possibility of the MDI molecule to attach carbon nanotube by only one phenyl ring. The position of MDI in this structure is similar to the TDI one with the top on-plane orientation. As it could be expected, the lack of the interaction with both phenyl rings decreases the adsorption affinity, so such adsorption pattern is less probable with the relative energy of 21.52 kJ/mol,

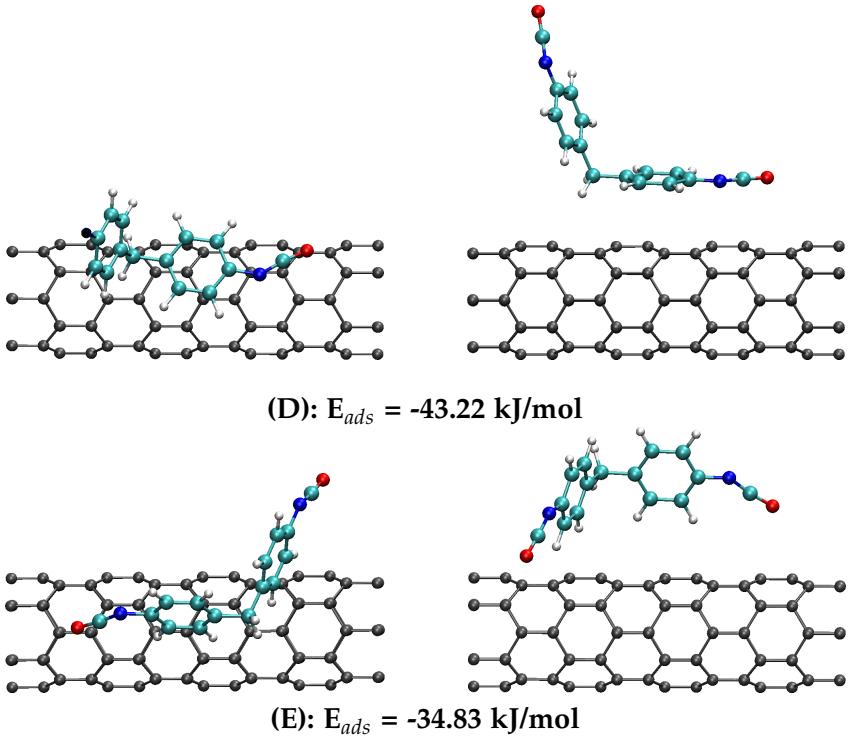

(D): E_{ads} = -43.22 kJ/mol

(E): E_{ads} = -34.83 kJ/mol

Figure 9.5: Optimized structures of noncovalent functionalization of SWCNT(6,0) with MDI molecules: top view and side view, with the corresponding values of the adsorption energy.

with respect to the global minimum structure. The distance between MDI and CNT in the structure **D** is 3.29 Å, what is in the range of the typical $\pi - \pi$ interactions, and is more than in the global minimum TDI and MDI structures, 3.13 Å and 3.17 Å, respectively.

Table 9.2: The values of the adsorption energy, E_{ads}, and the list of the structural parameters of the MDI molecule adsorbed on the surface of SWCNT(6,0). For more clear comparison the structural parameters for the MDI molecule in the gas phase is also given. Among the listed structural parameters are: the shortest C–C distance between the carbon atom from the MDI phenyl rings and SWCNT, l_{C-C}, the C-C-C-C dihedral angle and $\angle$(CCC) valence angle between the MDI phenyl rings, the C-C-N-C dihedral angle between the MDI phenyl ring and the NCO groups and the shortest distance between O atom from NCO groups and the carbon atom from SWCNT.

Label	**E_{ads}** [kJ/mol]	**l_{C-C}** [Å]	**C-C-C-C** [°]	**$\angle$(CCC)** [°]	**C-C-N-C** [°]	**$O_{NCO} \cdots$ CNT** [Å]
MDI	–	–	**-127.48; -127.13**	**113.79**	**0.75; 1.05**	–
A	-64.74	3.14; 3.13	-93.37; -86.72	111.59	-11.96; -10.37	3.61; 3.68
B	-63.68	3.13; 3.22	-130.12; -94.92	112.64	-13.25; -14.37	3.51; 3.71
C	-54.55	3.29; 3.23	137.66; 159.31	117.37	-5.94; -8.53	3.37; 3.51
D	-43.22	3.29; –	-99.12; -99.93	112.43	0.20; 0.40	3.31; –
E	-34.83	–; –	-83.10; 83.19	112.51	2.02; -1.33	3.29; 5.23

The last example of the CNT functionalization with MDI was created to show the strength of C-H$\cdots\pi$ hydrogen bonds, therefore, no $\pi - \pi$ stacking interactions are present here (see the structure **E** in Figure 9.5), but the interactions similar to the π-interactions in the T-shaped benzene dimer, with the energy of dimerization close to the typical $\pi - \pi$ interactions (see Section 3.4), are present. That is why, the adsorption in such MDI position has a relatively

high energy of -34.83 kJ/mol, but still it is less possible than the previously analyzed models. It should be mentioned that the highest changes in the dihedral angle between the phenyl rings in the MDI molecule are characterized to the MDI in the structure **E**, where the changes of c.a. 44° (see Table 9.2) were detected. The H$\cdots\pi$ distances of the four possible C-H$\cdots\pi$ hydrogen bonds, which lie in the basis of the mentioned types of interaction, are in the range of 2.63–3.01 Å (2.63 Å, 2.64 Å, 2.84 Å and 3.01 Å) and are characteristic for typical hydrogen bonds, defined in Ref. [118].

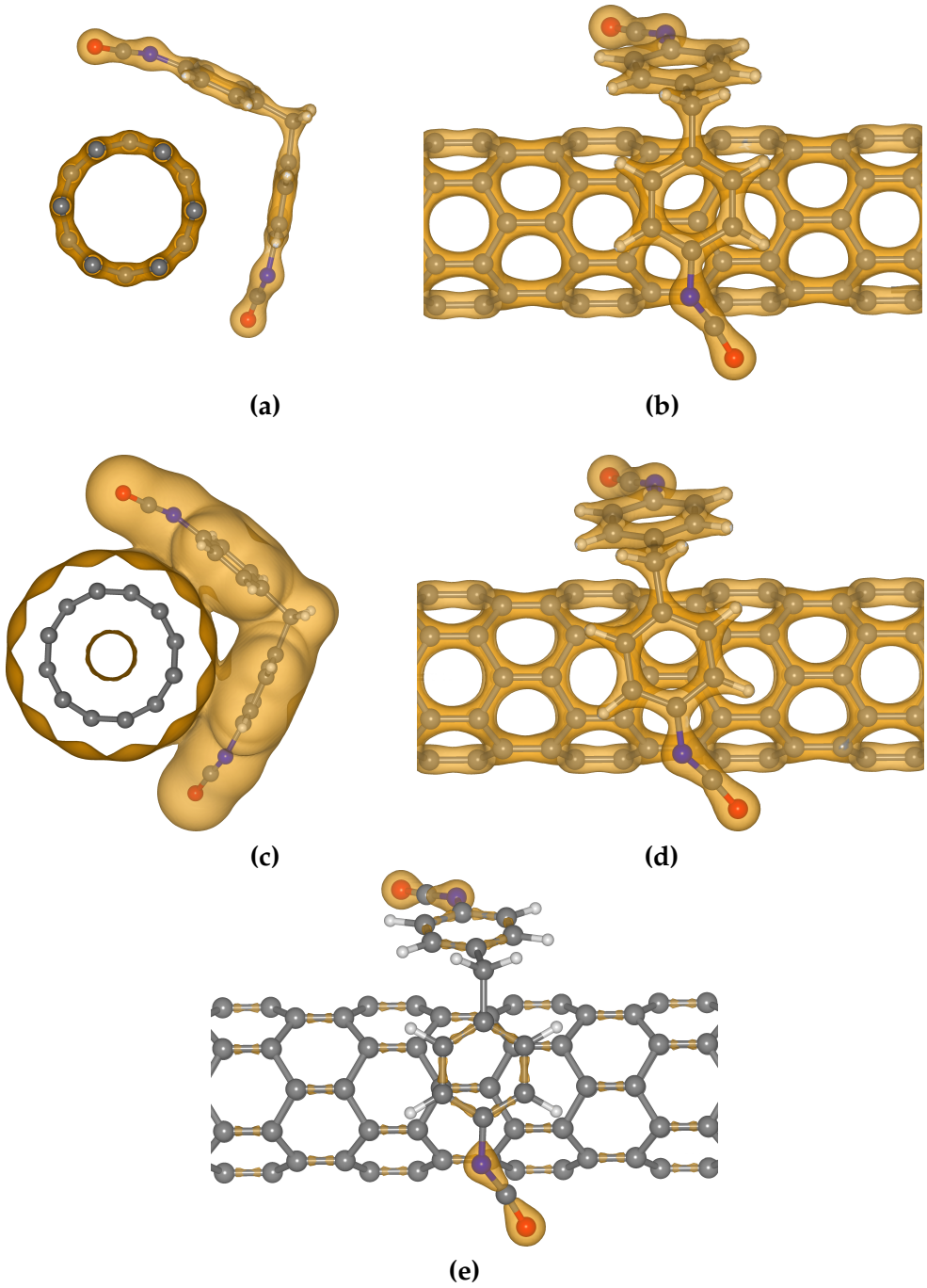

Figure 9.6: Vizualization of the charge density for the global minimum structure (**A**) of the noncovalent functionalization of SWCNT(6,0) by the MDI molecule. Different isosurfaces are presented: (a) profile view, isosurface of 0.2 a.u., (b) top view, isosurface of 0.2 a.u., the first phenyl ring, (c) profile view, isosurface of 0.005 a.u., (d) top view, isosurface of 0.2 a.u., the second phenyl ring, (e) top view, isosurface of 0.3 a.u.

Similarly as for the TDI molecule, MDI interacts with the surface of SWCNT via isocyanate groups too. It was proven due to the analysis of the C-C-N-C dihedral angle, indicating the deformation of the NCO group from the planar plane of the corresponding phenyl ring, and the distance between the oxygen atom from the NCO group and the closest carbon atom from the carbon nanotube, O$\cdots$CNT. All measured values are given in Table 9.2. As it was for TDI, in the MDI molecule the isocyanate groups prefer to be in one plane with the phenyl ring, which corresponds to the C-C-N-C dihedral angle close to 0°. The values of this angle in the case of MDI in the gas phase are 0.75° and 1.05°. The same as for TDI, the highest deformations of the NCO co-planarity with the phenyl ring are characteristic to the most stable structures, i.e. structure **A** and **B**, where the deformations in the range of 10°–14° are seen. The lowest deformation is seen for the structure **D**, which is characterized with one of the closest positions of the isocyanate groups to the CNT surface, i.e. 3.31 Å.

Both TDI and MDI molecules induce relatively strong noncovalent interactions during the noncovalent functionalization of SWCNT(6,0). These NCI are based on the physisorption of the aromatic molecules on the surface of the carbon nanotube. The best interaction pattern of the TDI adsorption on SWCNT(6,0) is characterized with the adsorption energy of -49.21 kJ/mol, while the adsorption of MDI is connected with the energy gain of -64.74 kJ/mol. In both cases two main types of NCI interactions are possible: $\pi - \pi$ interactions in the top position of the phenyl ring from the adsorbate on the hexagonal ring from the CNT surface and dispersion interactions between the isocyanate functional groups and the surface of CNT. Moreover, the increase of the strength of $\pi - \pi$ interactions has been also detected as the result of the substituent effect of the electron-withdrawing nature, which changes the distribution of the π-electron density in the molecule attached. This effect has lower impact on the NCI interactions between the CNT and the MDI molecule, which has only one isocyanate group in the phenyl ring. Contrary to it, TDI is characterized with relatively high adsorption energy than MDI, because of the enhancing of the substituent effect as the result of the *meta* position of the isocyanate groups in the aromatic ring. The additional NCI interactions between NCO and the SWCNT surface were estimated due to the detailed analysis of the structural parameters of the adsorbed molecules comparing to their gas-phase global minimum structures, analyzed in Section 8.1.1 and Section 8.1.2.

9.1.3 Influence on electronic properties

Noncovalent functionalization of carbon nanotubes, when only comparatively weak interactions are taking place, has small influence on the electronic properties of SWCNT. It is caused by the lack of the significant disruption of the *unique* structure of the carbon nanotubes, which is characterized to the covalent functionalization of CNTs. Such small changes of the electronic properties of metallic SWCNT(6,0), during its noncovalent functionalization by MDI and TDI, were also obtained in the present research. The density of states of the pristine SWCNT(6,0) and the noncovalently modified SWCNT by MDI and TDI are depicted in Figure 9.7. The Fermi level in Figure 9.7 is marked with the red dashed line. The given analysis concerns only the global minimum structures of the noncovalent functionalization of SWCNT(6,0) by TDI and MDI, namely the structure **A** in Figure 9.1 and the structure **A** in Figure 9.4.

It is clearly seen that the Fermi level for the TDI and MDI adsorption on SWCNT is only slightly shifted by 0.06 eV and 0.15 eV, respectively, with respect to the Fermi level of the pristine SWCNT(6,0). There are also minor changes of the shape of DOS close to the Fermi level, but they do not change the electronic properties of the nanotube. The most noticable differences in both adsorption sites are seen on approximately 1.6 eV/2.2 eV and 1.5 eV/3.0 eV below the Fermi level for the MDI and TDI adsorption, when the additional bands, originated from the adsorbate molecules, are located. There are also some changes above the

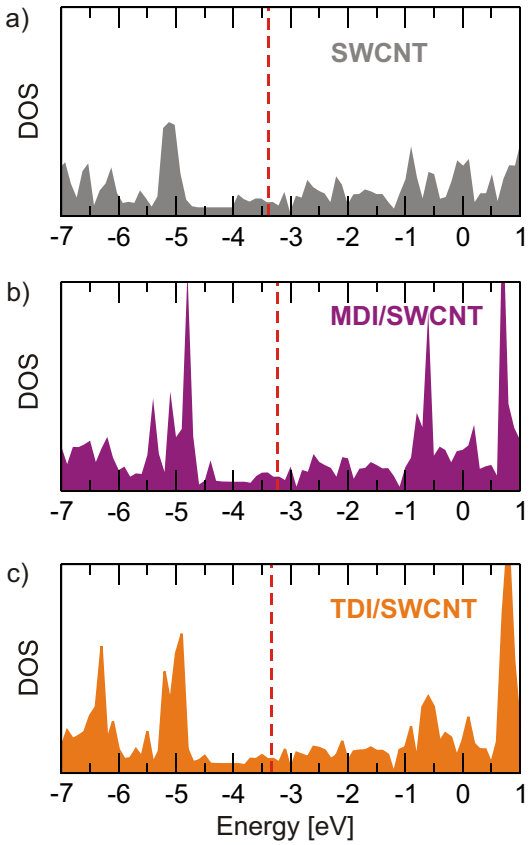

Figure 9.7: Density of states (DOS) of (a) pristine SWCNT(6,0), (b) noncovalently modified SWCNT(6,0) with the MDI molecule, (c) noncovalently modified SWCNT(6,0) with the TDI molecule. Fermi level is marked with the red dashed line.

Fermi level, but they are relatively far from it, i.e. starting from approximately 2.2 eV from the Fermi level.

The DOS analysis of the electronic properties of the metallic single-walled carbon nanotube after its noncovalent functionalization with aromatic diisocyanates TDI and MDI confirms only slight influence of diisocyanate adsorption on the CNT electronic properties, as the result of adsorption, based on the physisorption steered by $\pi - \pi$ stacking in CNT–adsorbate system and dispersion interactions between the isocyanate groups and the carbon nanotube sidewall.

9.2 Polyethylene glycol molecules

The second type of the monomer used to produce PU polymer is of polyol nature. Polyethylene glycol was chosen as a model polyol molecule for the adsorption on the SWCNT, because it is rather simple molecule, which can be calculated using DFT approach. To limit the computational time of the DFT calculations of noncovalent functionalization with PEG, we have chosen the smallest possible PEG molecules with two to five repeat subunits. The detailed analysis of the selected PEG structures and the description of different intramolecular interactions in PEG molecules was introduced in Section 8.2. Taking into account that PEG molecules, used to produce polyurethanes, are of higher molecular weights (more than 200 g/mol) than the analyzed PEG (the largest examined PEG weighs 238 g/mol), the examined, in the present PhD thesis, polyethylene glycol molecules are only the model systems representing possible types of intermolecular interactions between PEG and CNT.

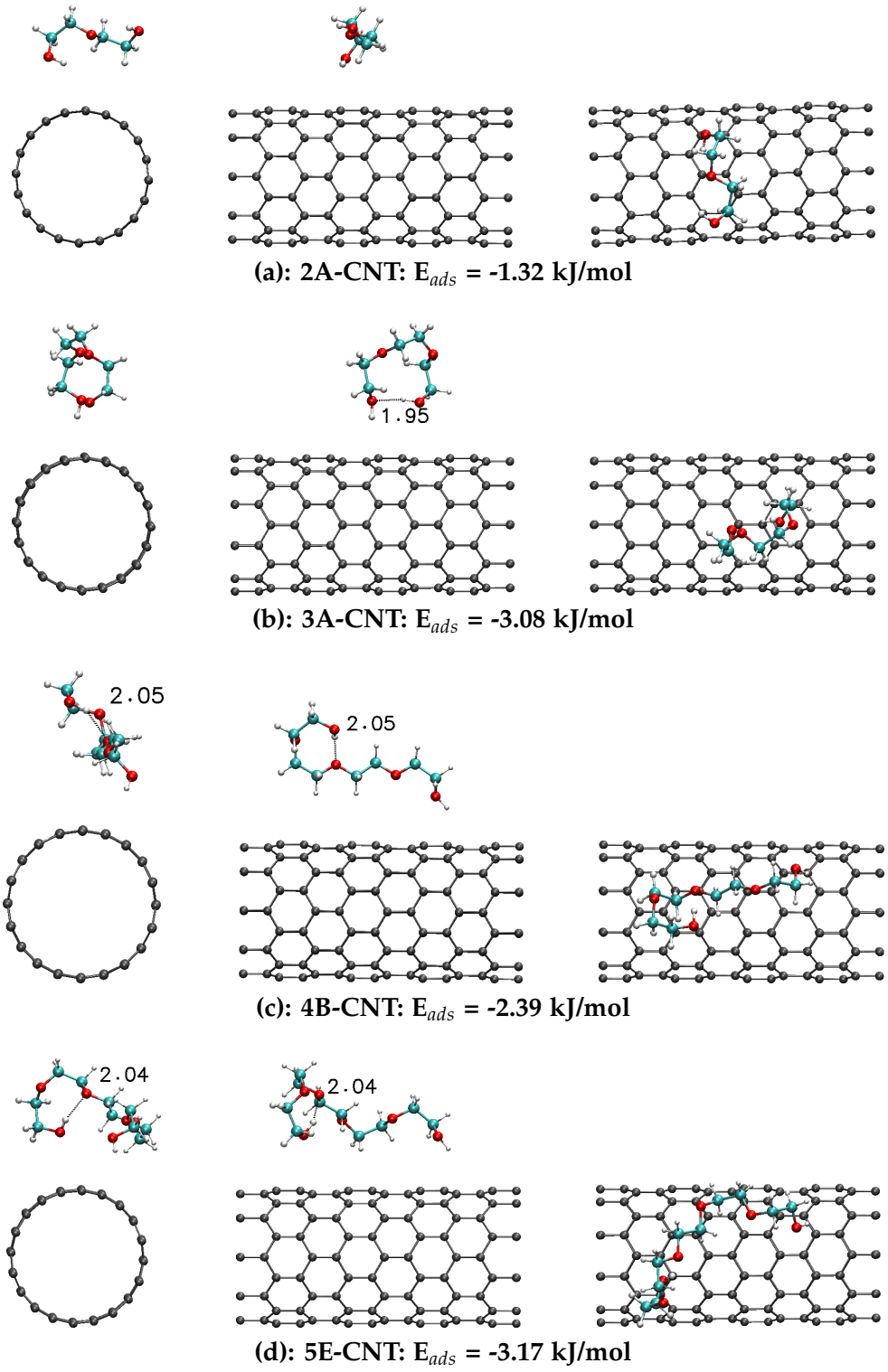

(a): 2A-CNT: E_{ads} = -1.32 kJ/mol

(b): 3A-CNT: E_{ads} = -3.08 kJ/mol

(c): 4B-CNT: E_{ads} = -2.39 kJ/mol

(d): 5E-CNT: E_{ads} = -3.17 kJ/mol

Figure 9.8: Selected structures (in three types of views: profile, side and top) of the noncovalent functionalization of SWCNT(10,0) with different PEG molecules: (a) PEG with two repeat subunits, (b) PEG with three repeat subunits, (c) PEG with four repeat subunits, (d) PEG with five repeat subunits, with the corresponding adsorption energy.

In Section 8.2 it was shown that the PEG molecules have a high tendency to form different patterns of intramolecular hydrogen bonds, which cause the additional stabilization of the system. Moreover, during the formation of intramolecular H-bonds in PEG there is an interplay between the energy gain as a result of the H-bond attractive interaction and the energy

loss connected to the hydrogen–hydrogen repulsion and deformation of the main chain of the molecule. Overall, the PEG molecule, e.g. with five repeat subunits, can be stabilized even by 34.15 kJ/mol due to the formation of hydrogen bonds. This effect descreases for smaller PEG molecules.

To analyze the noncovalent functionalization of carbon nanotubes by low molecular weight PEG molecules, 50 different structures have been calculated with various adsorption sites of the adsorbate on the surface of SWCNT(10,0). The global minimum structures, with the best values of the adsorption energy, are depicted in three views in Figure 9.8. Taking into account the PEG structure and possible intermolecular interactions with SWCNT, the analyzed structures were made concerning the formation of both C-H$\cdots\pi$ and O-H$\cdots\pi$ hydrogen bonds. Therefore, the adsorbed molecules were put on the SWCNT sidewall on the average distance of 2 Å, where the formation of the mentioned interactions is highly possible. Different positions of the PEG molecules, i.e. along, across or perpendicularly to the nanotube axis, were considered. Additionally, two different types of PEG local minima were analyzed: the corresponding global minimum structure and the structure of the highest relative energy, thus the least stable one (see Figure 8.7 and Figure 8.8 for clarity).

After the geometry optimization, no significant changes of the "adsorbed" PEG molecules have been noticed (some parameters of the PEG–SWCNT system are listed in Table 9.3). Therefore, the results from static DFT calculations indicate slight influence of the CNT surface on the properties of PEG. The H$\cdots$O distances of the intramolecular PEG hydrogen bonds were decreased causing higher stabilization of the molecule, e.g. the H$\cdots$O distance of the H-bonds in PEG with two subunits changed from 2.43 Å and 2.46 Å to 2.38 Å and 2.41 Å. At the same time, the PEG molecules detach from the CNT surface, which is seen from the shortest distances between the PEG molecule and the carbon atom from the CNT sidewall (values of $H_{OH}\cdots$CNT and $H_{CH_2}\cdots$CNT in Table 9.3). The initial position of the PEG molecule was c.a. 2 Å from the CNT, whereas the final position is in the range of 2.56–3.48 Å. The last parameter indicating the adsorption affinity of PEG on SWCNT(10,0), i.e. adsorption energy, finally explained such weak interactions in the PEG-SWCNT system. For all analyzed systems the adsorption energy is less than 4 kJ/mol, which indicates no specific interactions between the PEG molecules with carbon nanotube and probably no adsorption.

Table 9.3: The values of the adsorption energy, E_{ads}, and the list of the structural parameters of the PEG molecules adsorbed on the surface of SWCNT(10,0). Label of the structure indicates the type of the PEG local minimum taken for the analysis. Among the listed structural parameters are: the shortest distances between the hydrogen atom from the OH or CH_2 groups in PEG and the carbon atom from the SWCNT, $H_{OH}\cdots$CNT and $H_{CH_2}\cdots$CNT, respectively, and the distance between the hydrogen and oxygen atoms during the formation of intramolecular PEG H-bonds. The corresponding values of the hydrogen bonds in gas-phase PEG molecules are also given for clarity.

Label	$\mathbf{E}_{ads}$ [kJ/mol]	$\mathbf{H}_{OH}\cdots\mathbf{CNT}$ [Å]	$\mathbf{H}_{CH_2}\cdots\mathbf{CNT}$ [Å]	$\mathbf{H}\cdots\mathbf{O}_{PEG}$ [Å]	$\mathbf{H}\cdots\mathbf{O}_{PEG}^{gas-phase}$ [Å]
2A-CNT	-1.32	3.10	3.48	2.38; 2.41	2.43; 2.46
3A-CNT	-3.08	2.56	–	1.95; 2.38	2.43; 2.64
4B-CNT	-2.39	2.84	3.28; 3.41	2.05	2.17
5E-CNT	-3.17	2.82	3.28	2.04; 2.82	2.16; 2.63

It should be mentioned that it the beginning, the smallest PEG molecules were put on SWCNT sidewall. After the analysis of the adsorption energy (its negligible values), the list of the starting configurations was extended to the least stable PEG structures to check

if the starting configuration of PEG influences the interaction strength, but no increase in the adsorption energy was noticed. PEG interacts with SWCNT only via ubiquitous London dispersion interactions with no specific adsorption via C-H$\cdots$O and O-H$\cdots$O hydrogen bonds. Moreover, there were some structures with the positive values of the adsorption energy indicating unfavorable effect of the formation of PEG-SWCNT system, because of the destabilizing deformation of the PEG structure and no attraction interactions with the surface. Our previous experince in the DFT calculations of such unstable systems with further CP–MD simulations at 300 K prompts no possibility for the adsorption of this molecule in real conditions. *From this reason, in our further investigations we are only focused on the interactions of diisocyanates with carbon nanotubes.*

In general, the noncovalent functionalization of the CNT with larger PEG molecules, e.g. with 86 repeat subunits [438], were calculated using classical MD simulations. Carbon nanotubes used in Ref. [438] were OH-functionalized and the interaction energy obtained was high as the result of the strong O-H$\cdots$O hydrogen bonds between OH groups and PEG. In our case, the pristine carbon nanotube, the adsorption energies indicate higly impossible interactions between CNT and small PEG. It might be changed with the increase of the PEG chain, which can wrap the carbon nanotube, causing better CNT dispersion in PEG solutions. Still additional tools should be used to increase the stability of the PEG adsorption on the carbon nanotubes, for example, the initial modification of PEG with pyrene fragments [440, 441], which serve as the stable linkers between the PEG and the carbon-based surface.

Chapter 10

Covalent functionalization of carbon nanotubes

There are different methods to produce composites based on polyurethanes and carbon nanotubes. Most of them use initially functionalized CNTs, because they have better dispersion of the nanotubes in the polymer solution [344, 442]. Among such modified carbon nanotubes are CNTs initially functionalized by diisocyanates, when TDI or MDI is covalently attached to the sidewall of the carbon nanotube. The experimental investigations have proven that such CNTs are characterized with higher dispersity in the polymer synthesized and better enhancing of the mechanical properties of the composite [347, 391]. The common used way to get the SWCNT-MDI carbon nanotube is the chemical reaction between the carboxylated carbon nanotubes and diisocyanate molecules. This reaction was described in detail in Section 5.3. Taking into account the reported experimental data, concerning the structure of the obtained SWCNT-MDI system, confirmed with the usage of novel, high-resolution, techniques [36, 347, 391], the models of the SWCNT(6,0) and SWCNT(10,0) with covalently attached TDI and MDI were produced. In this Section the analysis of the single-walled carbon nanotubes with covalently attached one TDI and MDI, and two TDI and MDI are presented. The influence of the covalent functionalization on the electronic properties of metallic and semiconducting single-walled carbon nanotubes is also explained. Additionally, the static calculations are completed by the Car–Parrinello molecular dynamics simulations at 300 K.

10.1 Static calculations of TDI and MDI diisocyanates on SWCNT

As the result of the chemical reaction between the carboxyl group, located on the surface of the SWCNT, and the isocyanate group of TDI or MDI, the formation of the urethane (-CO-NH-) bond occurs, which is a linker between the attached molecule and the surface of SWCNT. This is a characteristic property of the isocyanate functional group, which was previously described (see Section 5.1).

Two types of carbon nanotubes were used to estimate the influence of the diisocyanate covalent attachment on the electronic and structural properties of single-walled CNTs, i.e. metallic SWCNT(6,0) and semiconducting SWCNT(10,0). Firstly, the attachment of the smaller diisocyanate was tested. Two initial TDI orientations were checked for the global minimum structure. Among the structures analyzed were TDI with the parallel and perpendicular positions of the phenyl ring with respect to the carbon nanotube axis during their covalent attachment to CNT sidewall. During the procedure of the geometry optimization, the parallel position was changed to the perpendicular one, which was estimated to be the most stable way of the covalent attachment of TDI to SWCNT. The structures of the optimized geometry of TDI attached to SWCNT(6,0) and SWCNT(10,0) are shown in Figure 10.1.

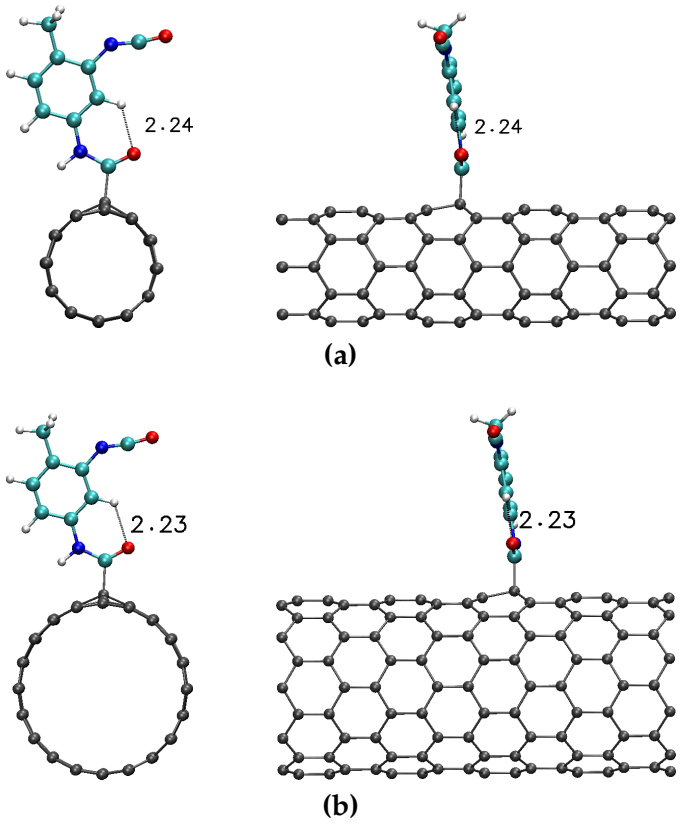

Figure 10.1: Optimized structures of carbon nanotubes (a) SWCNT(6,0) and (b) SWCNT(10,0) with covalently attached TDI molecule (profile view and side view). Hydrogen bond is marked with a dashed line.

Apart from the initial tests on the position of the phenyl ring of the TDI molecule, the position of the second isocyanate group, which does not interact with the surface, was checked. For this purpose, structures with the isocyanate group on one side and opposite side with respect to the carbonyl fragment of the urethane (amide) bond were calculated. The orientation of the NCO at the same side as the CO group is 1.64 kJ/mol more stable than the opposite one, so this geometry was taken for further analysis and investigation. Using the initial results for TDI covalent attachment to the SWCNT(6,0) and SWCNT(10,0), the models of the MDI bonding to the carbon nanotubes were made. They are depicted in Figure 10.2.

During the formation of the covalent bond between diisocyanate and the carbon nanotube, the geometry of the CNT region, where the attachment occurs, changes. It is caused by the change of the hybridization of the carbon atom, which is directly connected to the functional group: from sp^2 to sp^3. That is why, the C–C bond lengths, in the corresponding CNT hexagon, change. In the case of the TDI and MDI attachment, the average C–C bond length changes from 1.44 Å (pristine SWCNT) to 1.52 Å (functionalized SWCNT). The latter value is close to the C–C length in the diamond phase with sp^3-hybridized carbon atoms. Moreover, the $\angle$CCC angle, where the middle carbon atom is sp^3-hybridized, changes from typical 119° to the values in the range of 103.9°–113.2° (detailed values are listed in Table 10.1). More significant changes have been estimated for the metallic SWCNT(6,0). The change in the geometry of the area of the formation of the covalent bond is clearly seen from the optimized structures in Figure 10.1 and Figure 10.2. Even if there are only slight structural changes of the CNT geometry as a result of the covalent bond formation, there is a significant influence on the electronic properties of the single-walled carbon nanotubes, which is a common known fact in the chemistry of CNTs. It should be mentioned that in the present research the formation of one covalent bond is analyzed, but in practice there is a huge amount of such bonds on the CNT sidewall and the overall effect of the covalent functionalization, i.e. dis-

ruption of the π-system of the CNT, is extremely high and can be estimated using standard techniques used to analyze the structural parameters and purity of carbon nanotubes (more information is in Chapter 4).

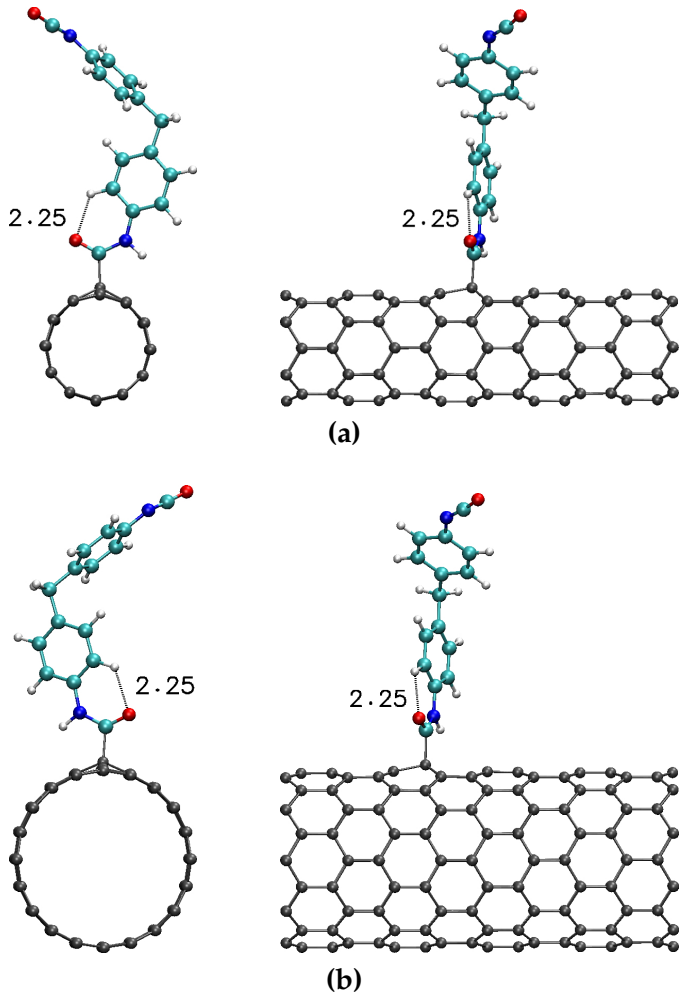

Figure 10.2: Optimized structures of carbon nanotubes (a) SWCNT(6,0) and (b) SWCNT(10,0) with covalently attached MDI molecule (profile view and side view). Hydrogen bond is marked with a dashed line.

There is a high possibility for the covalent attachment of the diisocyanate molecule to the CNT sidewall, because of the positive effect of the formation of the covalent bond. The binding energy of the attachment of TDI and MDI, with the direct comparison with the -$CONH_2$ group linkage, was calculated using Equation 7.2 given in Section 7.2.1. Negative values of the binding energy indicate the favourable reaction. The calculated binding energies for the covalently attached TDI and MDI, see Table 10.1, clearly indicate that energetically more favourable is the covalent functionalization of the metallic SWCNT(6,0), which characterizes with approximately two times higher values of the binding energy (c.a. 154 kJ/mol) than the functionalization of the semiconducting SWCNT(10,0) with the binding energy of c.a. 75 kJ/mol. Therefore, the binding energy is inversely proportional to the SWCNT diameter. This evidence was also reported for other covalently modified carbon nanotubes [196]. Higher affinity of SWCNT(6,0) to be modified can be proven by the formation of stronger C–C covalent bond between the SWCNT and the attached molecule, marked in Table 10.1 as C_{CNT}–C′ bond, where C_{CNT} means the carbon atom from the carbon nanotube directly connected to TDI or MDI, and C′ is the carbon atom from the urethane bond. C_{CNT}–C′ bond is shorter during the covalent functionalization of SWCNT(6,0), i.e. 1.58 Å, comparing to

C_{CNT}–C' bond for SWCNT(10,0), i.e. 1.60 Å.

Table 10.1: List of structural parameters of the covalently functionalized SWCNT(6,0) and SWCNT(10,0) with TDI and MDI molecules: values of the binding energy, E_{bind}, the length of the carbon-carbon bond formed between the C atom from SWCNT (C_{CNT}) and the C atom from the attached molecule (C'), C_{CNT}–C', values of the valence angle within sp^3-hybridized carbon atom from CNT, $\angle(CCC)_{CNT}$, the C-C-C-N dihedral angle between the attached molecule and the CNT surface, and the C-C-N-C dihedral angle between the TDI/MDI phenyl ring and the NCO group. For comparison data calculated for the covalent attachment of the $CONH_2$ group are added.

Label	$\mathbf{E_{bind}}$ [kJ/mol]	$\mathbf{C_{CNT}}$**–C'** [Å]	$\mathbf{\angle(CCC)_{CNT}}$ [°]	**C-C-C-N** [°]	**C-C-N-**$\mathbf{C_{NCO}}$ [°]
SWCNT(6,0)–TDI	-154.47	1.585	104.1/112.2/112.7	-88.57	-1.31
SWCNT(6,0)–MDI	-154.00	1.588	103.9/112.2/112.6	-99.78	1.37
SWCNT(6,0)–$CONH_2$	-148.20	1.586	–	–	–
SWCNT(10,0)–TDI	-75.16	1.602	107.9/112.8/113.2	-90.60	0.81
SWCNT(10,0)–MDI	-73.91	1.605	107.8/112.8/113.2	-106.61	0.98
SWCNT(10,0)–$CONH_2$	-67.73	1.603	–	–	–

Due to the additional calculations of the covalent attachment of the amide group, the influence of the nature of the attached molecule/group on the value of the binding energy was obtained. In Table 10.1 the data for SWCNT-$CONH_2$ functionalized CNTs are also given. There is only small influence (the energy difference of c.a. 6–7 kJ/mol) of the aromatic nature of TDI and MDI on the binding energy. This effect for MDI attachment is even smaller, because of the additional unfavourable structural deformations of MDI as the result of the bond formation. The geometrical parameters are slightly changed for MDI, covalently attached to SWCNT, in comparison to its gas-phase analogue, for example the valence angle $\angle(CCC)$ increases only on 1.22° and 0.4° in case for MDI attached to SWCNT(6,0) and SWCNT(10,0), respectively. The C-C-C-C dihedral angle between the MDI phenyl rings changes more significantly – it is decreasing by 22.26° and 20.75°, changing the mutual orientation of the phenyl rings. Higher differences of the mentioned parameters in case of functionalization of SWCNT(6,0) indicates its higher reactivity in comparison to SWCNT(10,0).

Both TDI and MDI are attached to the sidewall of carbon nanotubes at the perpendicular orientation with the angle in the range of 88°–106°. Among the possible ways to estimate the angle of the attachment is the C-C-C-N dihedral angle formed between two carbon atoms from the surface of the SWCNT and a fragment of the urethane bond, directly connected to the CNT. In general, the position of the TDI molecule is more perpendicular than for MDI, which is attached at the angle of 99.78° and 106.61° for SWCNT(6,0) and SWCNT(10,0), respectively (see Table 10.1). This is caused by the presence of the second phenyl ring in the MDI molecule, which has a specified orientation.

Among highly similar structural parameters of both molecules attached is the geometry of the isocyanate group and the formation of C-H$\cdots$O intramolecular hydrogen bond via CH group from the phenyl ring and the oxygen atom from the urethane bond (this bond is marked in all structures analyzed). The latter one charaterizes with the H$\cdots$O distances in the range of 2.23–2.25 Å and $\angle(CHO)$ of 118°–119° (see Figure 10.1 and Figure 10.2). Isocyanate group, which is not participating in the described reaction, has no significant changes in comparison to the gas-phase TDI and MDI. It is localized far from the CNT surface, therefore, no additional interactions are possible.

As the result of the covalent bond formation between diisocyanates and the SWCNT, the structure of them both is changing, enabling to form the most stable and reactive systems. Higher reactivity and affinity for the covalent attachment is obtained for the carbon nanotube with smaller diameter, which is in agreement with the previously reported studies. This means that in the case of the mixture of SWCNTs with different chiralities, here SWCNT(6,0) and SWCNT(10,0), the SWCNT(6,0) will be more reactive and more possible to be modified. On this basis new ways of the separation of SWCNTs with different chiralities can be investigated.

10.1.1 Attachment of two TDI molecules

In practice, lots of functional groups are attached to the surface of the carbon nanotube. The most probable position of the second attached molecule (and etc.) can be estimated with the theoretical calculations of different structures with the two groups (or more) connected to the SWCNT sidewall. This knowledge can help to understand the possible mechanism of the formation of the PU/SWCNT composite: are the polymer chains, covalently connected to the SWCNT surface, strained equally and parallelly one to another in the perpendicular position with respect to the carbon nanotube axis, or there is a high possibility for different, chaotic, attachments of the initial monomers, therefore, the synthesized polymer chains are mixed in an uncontrollable way? This knowledge is a basic one, but it significantly influences the transfer of the unique properties from the carbon nanotubes to the polymer.

To analyze the covalent attachment of the second TDI molecule to the CNT, several model structures were made. The selected structures, representing different types of the possible interactions between the molecules, are depicted in Figure 10.3. The carbon nanotube with the extended length of 21.424 Å (five unit cells; for detailed information see Section 7.2.1) was used. Only the covalent attachment to the SWCNT(10,0) was taken into consideration, because of the higher available CNT surface, comparing to the SWCNT(6,0) one. Among the structures selected, the structure labeled as **A**, corresponds to the non-interacting TDI molecules attached to the CNT sidewall. This structure was the reference one to estimate the positive or negative effect of the position of two diisocyanate molecules. The relative energy of this system was set as 0.00 kJ/mol and the energies calculated for other structures were compared to the energy of the non-interacting system. The relative energy was obtained as the difference between the total energy of the corresponding structure and the energy of the reference, non-interacting structure:

$$E_{rel} = E_x^{abs} - E_{non-int}^{abs}, \tag{10.1}$$

where E_x^{abs} is the corresponding total energy of the local minimum and $E_{non-int}^{abs}$ is the total energy of the non-interacting system (structure **A** in Figure 10.3). The negative value of the relative energy indicates the favourable process of the attachment of the molecule and additional intermolecular interactions, while the positive value is characteristic to the unfavourable attachment.

The most stable system, with two TDI molecules attached, is the structure **B** with the relative energy of -17.75 kJ/mol. The molecules are slightly displaced here, which is seen in the profile view of the structure (see Figure 10.3: B). The type of displacing is not characteristic to the $\pi - \pi$ parallel displaced structure, which is energetically more stable than the sandwich stacking, but seems to be originated from the strong dispersion interactions between the isocyanate groups, which are located close to each other. The distance between the NCO groups and, accordingly, the distance between the TDI molecules, is in the range of 3.53–3.69 Å. It is close enough to enable the electrostatic interaction between NCO. The slight displacing of the TDI aromatic rings and the deformation of the NCO group from the planar plane of the aromatic ring (by c.a. 4°) are caused by the optimizing the strength of such

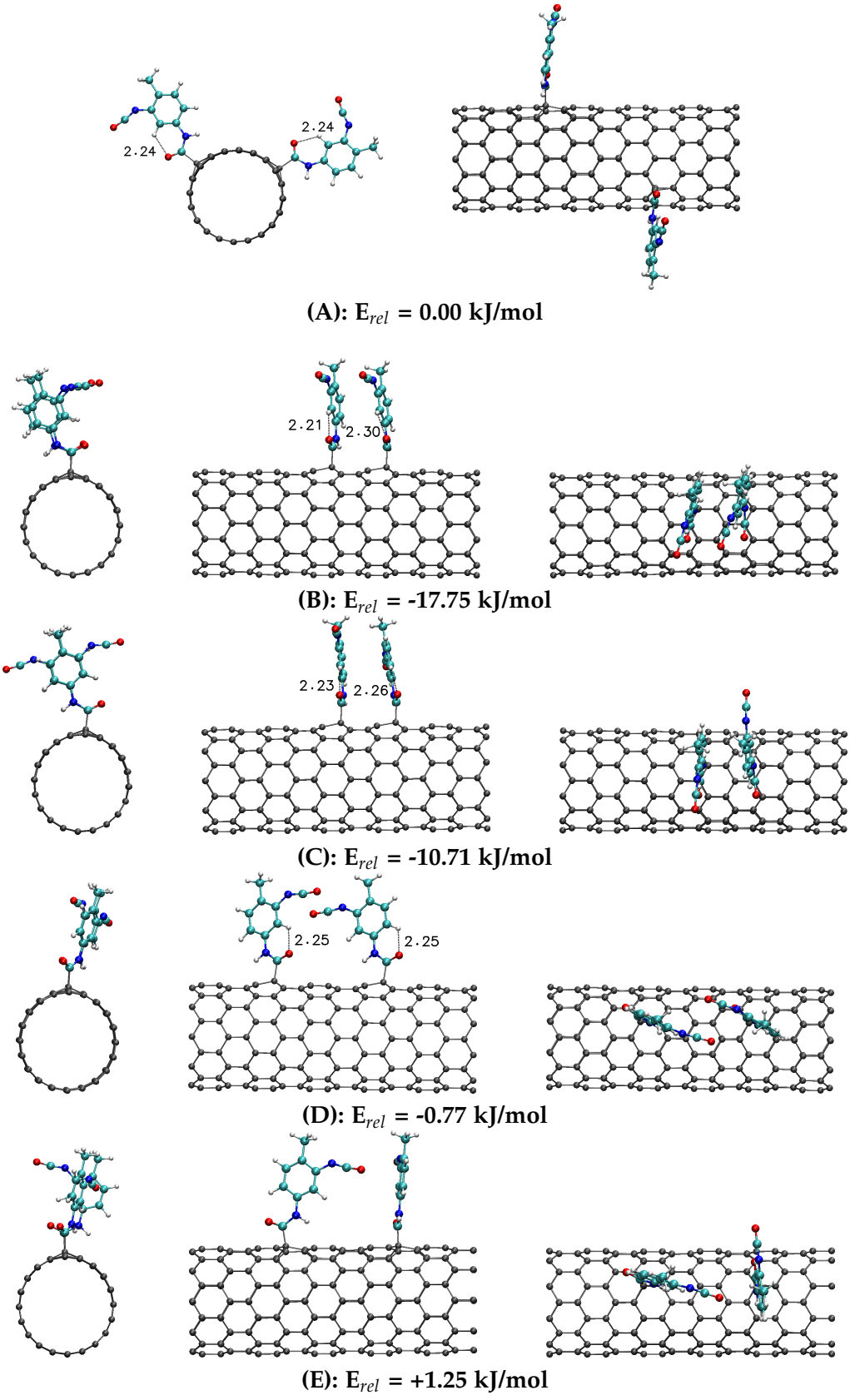

Figure 10.3: Optimized structures of carbon nanotube SWCNT(10,0) with two covalently attached TDI molecules (profile view, side view and top view). Each local minimum is given with the corresponding relative energy with respect to the non-interacting structure, marked as **A**.

interaction, but not through the N–N, C–C and O–O overlaping, but two interactions via O–C contacts. Moreover, both phenyl rings of TDI are located at different angles of attachment to the CNT than their non-interacting analogues. It can be estimated on the increasing of the C-C-C-N dihedral angle of one phenyl ring by c.a 6° and decreasing of the C-C-C-N of the second phenyl ring by c.a. 3° (see Table 10.2). This indicates the existence of $\pi - \pi$ interactions between the molecules attached, which stabilize the structure.

The relative energy of the structure **C** is c.a. 7 kJ/mol higher than for the structure **B**, which means the lower stability of such system. The main difference between the structure **B** and **C** is the position of the isocyanate groups, which are localized in the opposite position with respect to each other. Therefore, no electrostatic interactions between the NCO groups are present here. The molecules are localized on slightly larger distance of 3.60–3.76 Å than in the structure **B**. The change of the angle of attachment (C-C-C-N dihedral angle) and the deformation of the NCO group from the planarity with the phenyl ring are close to the non-interacting TDI molecules. Therefore, only $\pi - \pi$ interactions stabilize this structure.

Table 10.2: List of structural parameters of two TDI molecules covalently attached to SWCNT(10,0): values of the relative energy, E_{rel}, the C-C-C-N dihedral angles between the attached molecules and the CNT surface (absolute value), the C-C-N-C dihedral angle between the TDI phenyl ring and the NCO groups, H···O distance and ∠(CHO) angle of the C-H···O hydrogen bond. Values for both TDI molecules are given.

Label	$\mathbf{E_{rel}}$ [kJ/mol]	**|C-C-C-N|** [°]	**C-C-N-C_{NCO}** [°]	**H···O** [Å]	**∠(CHO)** [°]
A	0.00	97.09/91.91	-1.11/-0.01	2.24/2.24	119.38/119.34
B	-17.75	103.11/88.99	-4.98/0.67	2.21/2.27	119.86/117.12
C	-10.71	95.53/81.95	-0.79/0.62	2.23/2.26	119.49/119.01
D	-0.77	82.83/82.82	19.25/17.21	2.25/2.25	118.45/118.36
E	+1.25	84.23/95.80	0.39/-0.56	2.25/2.24	118.38/119.32

The lack of the stabilization of the system by $\pi - \pi$ interactions and electrostatic interactions between isocyanate groups cause the relative energy of the system be close to the non-interacting attached molecules. Even if the molecules are close to each other (see structure **D** in Figure 10.3), no evidence for the intermolecular interactions is seen. Moreover, there is a huge deformation of the isocyanate groups from the co-planarity with the phenyl ring (by c.a. 17–18°, see Table 10.2), which indicates the maximization of the interactions between carbon and oxygen atoms from the NCO. The angles of attachment have been also changed by 14.26° and 9.09° with respect to the structure **A**, indicating the overall deformation of the covalent bond between TDI and the CNT. Such deformations are not preferable, therefore, the total energy of the system lowers (in absolute value).

The last example (structure **E** in Figure 10.3) depicts the T-shaped structure of two TDI molecules, when the isocyanate group of one TDI is oriented to the π-electron density of the second TDI. Such arrangement of the molecules is highly impossible, because it is even more unfavourable than the non-interacting attachment. It is caused by the repulsion interactions between the C=O fragment from the isocyanate group and the π-electron density, which was previously reported by Y. Imai et al. [443]. As a result of the repulsion interactions and no strong attractive interactions, the relative energy of this system is a positive one, therefore, the structure is unstable.

In all analyzed systems the structural parameters of the C-H···O hydrogen bond are very

similar: the H···O distance is in the range of 2.21–2.27 Å and the ∠(CHO) angle is in the range of 117°–120° (see Table 10.2).

10.1.2 Attachment of two MDI molecules

With the knowledge of the interaction pattern for two TDI molecules covalently attached on the SWCNT(10,0), the addition of the second MDI molecule was made. The optimized

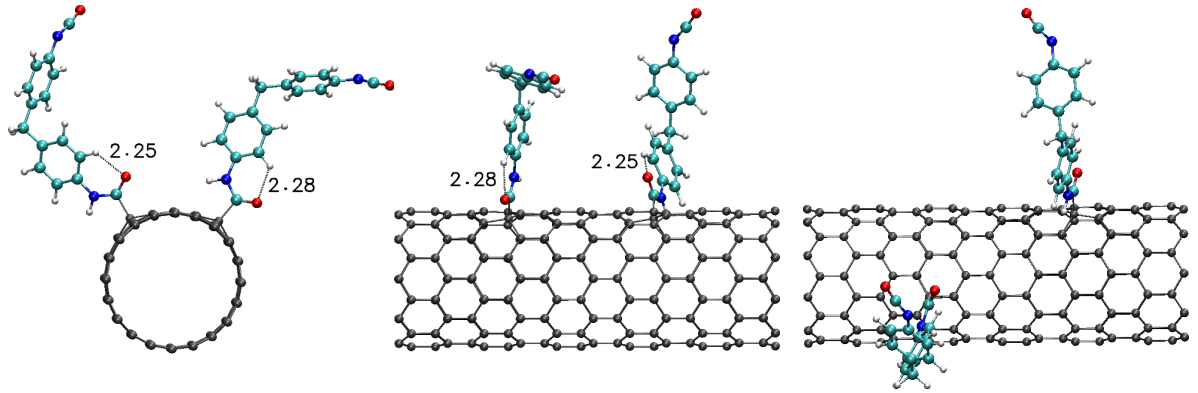

(A): E_{rel} = 0.00 kJ/mol

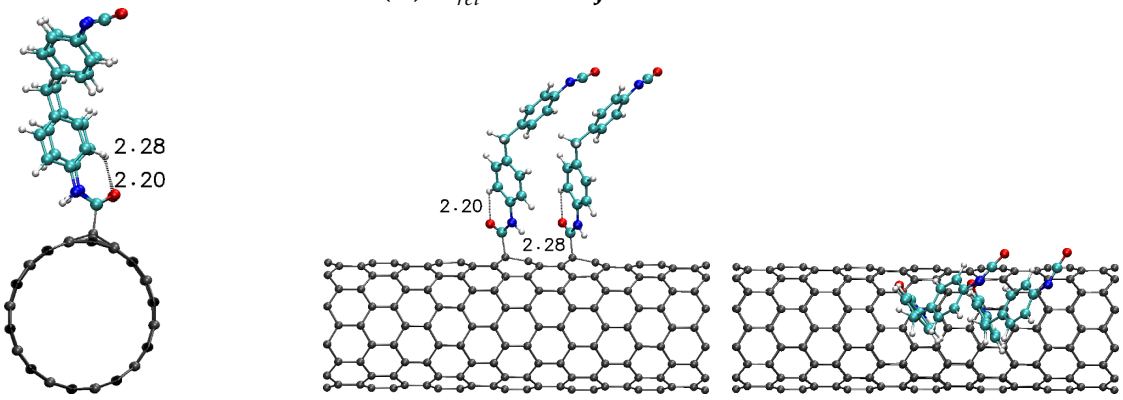

(B): E_{rel} = -31.45 kJ/mol

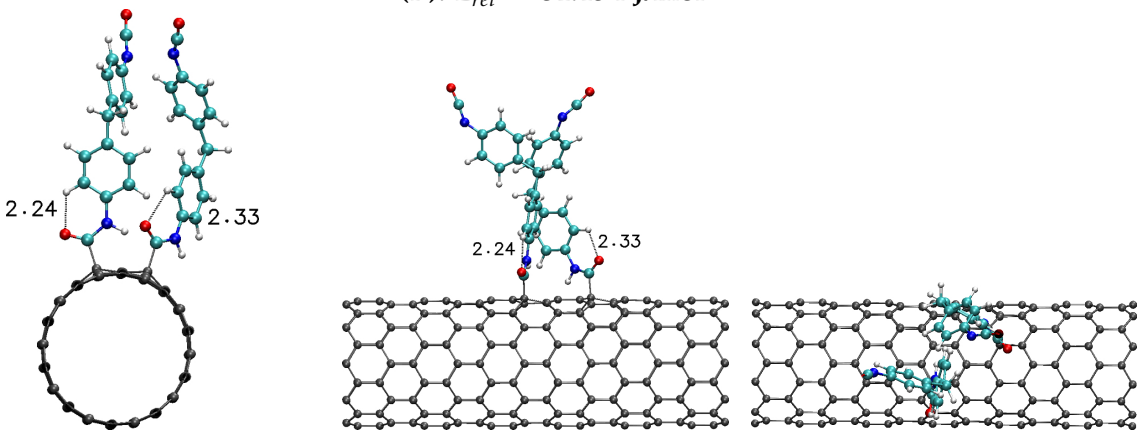

(C): E_{rel} = -33.38 kJ/mol

Figure 10.4: Optimized structures of carbon nanotube SWCNT(10,0) with two covalently attached MDI molecules (profile view, side view and top view). Each local minimum is given with the corresponding relative energy with respect to the non-interacting structure, marked as **A**.

structures are shown in Figure 10.4, where one non-interacting system is also marked with

the label **A**, as it was used for the SWCNT-$(TDI)_2$ system. The same method of the obtaining the interaction energies was used as for the two TDI molecules, described in the previous subsection. As a result, the energy gain of -33.38 kJ/mol and -31.45 kJ/mol for the intermolecular and additional intramolecular interactions between two attached MDI was estimated. In comparison to the SWCNT-$(TDI)_2$ molecular system, where the relative energy of the global minimum is -17.75 kJ/mol, the relative energy of the global minimum for SWCNT-$(MDI)_2$ is approximately 2 times higher, i.e. -33.38 kJ/mol. One can suggest that such increase in the interaction energy is caused by the presence of the second phenyl ring in the MDI molecule, therefore, the additional set of $\pi - \pi$ interactions. The detailed analysis of the results obtained explained that it is not fully true, because the interaction pattern of two MDI molecules on the surface differs with the TDI–TDI noncovalent interactions.

The first selected local minimum with the relative energy of -31.45 kJ/mol imitates the TDI–TDI system, when the molecules interact via $\pi - \pi$ interactions and the additional dispersion interactions between isocyanate groups, localized close to each other (structure **B** in Figure 10.4). Because of the second phenyl ring in the MDI molecule, the same strength of $\pi - \pi$ interactions can not be gained and the distance between the phenyl rings on the bottom part is in the range 4.20–4.50 Å, while rings on the top part are localized on the distance in the range of 4.48–4.63 Å. Both distances are larger then for the TDI molecules, which interacts on 3.53–3.69 Å (structure **B** in Figure 10.3). That is why, the effect of the π-interactions is different. It should be also noted that the mentioned $\pi - \pi$ interactions are more in parallel-displaced manner than the sandwich manner, as it was for the TDI–TDI interactions. Thus, one phenyl ring, directly connected to the CNT surface, is positioned over the C–C bond of the second phenyl ring. The phenyl rings in the upper part of the MDI molecules are not interacting via $\pi - \pi$ interactions, but instead of them, the additional dispersion interactions between one phenyl ring and the C-H bond are possible. Moreover, the isocyanate groups are interacting by only one C$\cdots$O contact, not two as it was for TDI–TDI. The distance between the carbon and oxygen atoms in this contact is 3.50 Å. There is also the deformation of the NCO group from the co-planarity with the corresponding phenyl ring on c.a. 5–6° (see values of C-C-N-C dihedral angle in Table 10.3).

Table 10.3: List of structural parameters of two MDI molecules covalently attached to SWCNT(10,0): values of the relative energy, E_{rel}, the C-C-C-N dihedral angles between the attached molecules and the CNT surface (absolute value), the C-C-N-C dihedral angle between the MDI phenyl ring and the NCO groups, the $\angle$(CCC) and C-C-C-C dihedral angle between the MDI phenyl rings. Values for both MDI molecules are given.

Label	**E_{rel}** [kJ/mol]	**|C-C-C-N|** [°]	**C-C-N-C_{NCO}** [°]	**$\angle$(CCC)** [°]	**C-C-C-C** [°]
A	0.00	102.77/109.64	-0.91/-1.26	114.55/113.73	-108.66/-112.11
B	-31.45	53.86/65.45	-4.87/6.89	115.33/114.86	-148.28/-142.44
C	-33.38	80.65/**134.79**	-1.50/1.00	115.20/115.98	-103.66/**-17.02**

Both MDI molecules in the structure **B** in Figure 10.4 are very twisted with respect to their non-interating conformers. The initially defined angle of the attachment, C-C-C-N is highly changed here, from c.a. 100° to 50°–60° (Table 10.3), but it is caused by the twist when the position of the nitrogen atom is changed. Overall, the molecule in attached in the perpendicular way, which is clearly seen in the figure. The specific twist of the molecule, as a result of the twist of the bottom phenyl rings in order to maximize the area of the interaction, changes the mutual geometry of the phenyl rings in both MDI. The C-C-C-C dihedral angle increases

(in the absolute value) and enables the formation of one intermolecular C-H$\cdots\pi$ hydrogen bond between the CH_2 group of one MDI with the upper phenyl ring of the other MDI. It can be seen from the side view of the structure **B**. The average distance between the hydrogen atom from CH_2 and the carbon atoms from the neighbor phenyl ring is 2.75 Å, which is close enough to form a stable H-bond. The *standard* C-H$\cdots$O hydrogen bond, which exists in both TDI and MDI after the covalent functionalization of the CNTs, possesses the similar values of the length and the valence angle as the previously analyzed systems, H$\cdots$O distance is of 2.20 Å and 2.28 Å with the correponding valence angle of 119.69° and 119.07°. To sum up, the structure **B** with two MDI molecules covalently attached to the SWCNT sidewall is stabilized by one $\pi-\pi$ interaction site, one C$\cdots$O contact in the NCO dispersion interactions and one stable C-H$\cdots\pi$ hydrogen bond.

The last structure (Figure 10.4: C) is the stablest one and have the relative energy slightly higher (in absolute value) than the structure **B**, but possesses completely different interaction pattern. Instead of two MDI molecules interacting via $\pi-\pi$ interactions, new types of interaction exist. The distance between the molecules is higher than in the structure **B** (the initial position of the molecules was one carbon atom far from the initial MDI; see top view of the system in Figure 10.4: C), which prevents $\pi-\pi$ interactions. Because of more space between the molecules attached, they are significantly twisted with respect to each other with the change of the angle of attachment (from standard c.a. 100° to 134.79°, see Table 10.3), which makes the molecules to be closer (side view of the structure) and the formation of additional C-H$\cdots\pi$ hydrogen bonds. There are four C-H$\cdots\pi$ H-bonds in the structure **C**: two of them are of intermolecular character and two are intramolecular. Due to the adjusting of one MDI to the other one, the C-C-C-C dihedral angle between the phenyl rings decreases to the values when the formation of the intramolecular C-H$\cdots\pi$ hydrogen bond is possible, i.e. in the range of 20° (Section 8.1.2). Here, this dihedral angle is of 17.02°, see Table 10.3.

The four mentioned C-H$\cdots\pi$ hydrogen bonds are the most influencing noncovalent interactions that stabilize the global minimum structure. All of them are originated only by the atoms from the phenyl ring, without the contribution of the CH_2 group. The distances between the hydrogen atom from the CH as hydrogen bond donor and the carbon atoms from the interacting phenyl ring in the intramolecular C-H$\cdots\pi$ H-bonds are in the range of 2.59–4.08 Å and 2.56–4.06 Å. The H$\cdots$C distances of the intermolecular C-H$\cdots\pi$ H-bonds are in the range of 2.68–3.57 Å and 2.89–3.05 Å. As the result of the twist of the molecule, the geometry of one of the C-H$\cdots$O hydrogen bond changes: the H$\cdots$O distance increases to 2.33 Å (instead of 2.24–2.25 Å) with the decrease of the CHO valence angle (116.12° instead of c.a. 119°). The second C-H$\cdots$O H-bond stays unchanged (2.24 Å and 119.63°). Finally, it should be noted that there are no interactions via isocyanate groups in the structure **C**. NCO groups are far from each other, therefore, there is no deformation from the plane of the phenyl ring (values of C-C-N-C dihedral angle in Table 10.3). The angle between the phenyl rings, $\angle$(CCC), stays similar in all analyzed systems; it is changing maximally by 2.19°.

10.2 Electronic properties of covalently functionalized SWCNT

As the result of the covalent functionalization of the single-walled carbon nanotubes, their electronic properties are changed, because their unique π-electron structure is disrupted. To estimate this change the analysis of the electronic band structure of the pristine and diisocyanate-functionalized SWCNT(6,0) and (10,0) was made. Due to the similarity of the data obtained for TDI- and MDI-functionalized carbon nanotubes, only the results concerning the functionalization with the MDI molecule are presented here. In Figure 10.5 the electronic band structures of SWCNT(6,0) and (10,0) before and after the covalent attachment are shown. The Fermi level was set here as 0 eV for the clear comparison of the data.

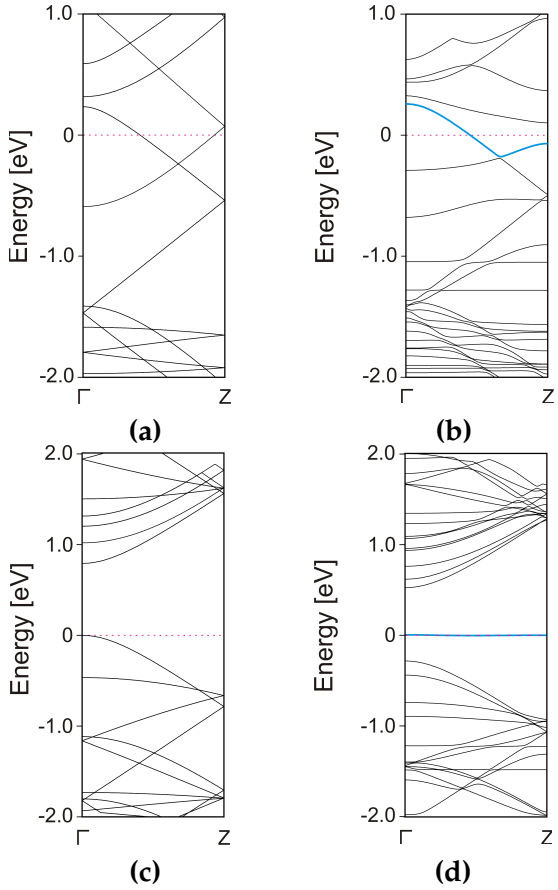

Figure 10.5: Electronic band structure along the Γ–Z line in the Brillouin zone for (a) pristine SWCNT(6,0), (b) MDI-modified SWCNT(6,0), (c) pristine SWCNT(10,0), (d) MDI-modified SWCNT(10,0). The Fermi level is marked with the dashed red line. The band changes close to the Fermi level are marked with the blue color.

The changes of the bands in the electronic band structure of the mentioned CNTs are different, because the electronic nature of both single-walled carbon nanotubes, i.e. metallic and semiconducting. After the addition of the MDI molecule to the SWCNT(6,0) sidewall, the strong reorganization of the bands close to the Fermi level (-1.0 eV to 1.0 eV) is seen. Moreover, the electron density in the Z-point wavefunction is slightly different: for the pristine SWCNT it is higher the Fermi level, while for the functionalized one is lower the Fermi level (see Figure 10.5: a, b). There are also additional conduction bands above and below the Fermi level. More significant changes of the electronic band structure were detected for the functionalization of SWCNT(10,0), which is of semiconducting nature with the band gap of c.a. 0.8 eV (see Figure 10.5: c). After the MDI covalent attachment to the sidewall, the additional band appears, which shows the descrease of the band gap to c.a. 0.5 eV. This band is depicted by the blue color in Figure 10.5: d. Additionally, there is also seen the reorganization of some bands close to the Fermi level with the addition of a new half-filled band comparing to the pristine SWCNT(10,0). The changes obtained are similar to the previously reported data for the functionalization of SWCNTs with other functional groups [209].

The analysis of the electron density corresponding to the Γ-point in the Brillouin zone of the systems analyzed (see Figure 10.6), indicates the existence of the impurity states as the result of the covalent bond formation. The impurity states are different for metallic and semiconducting SWCNT. For the first CNT, the partially occupied band with a large dispersion is seen with the extension of the Γ-point wavefunction over the CNT (Figure 10.6: a). The addition of the MDI molecule slightly changes the electron density distribution close to the

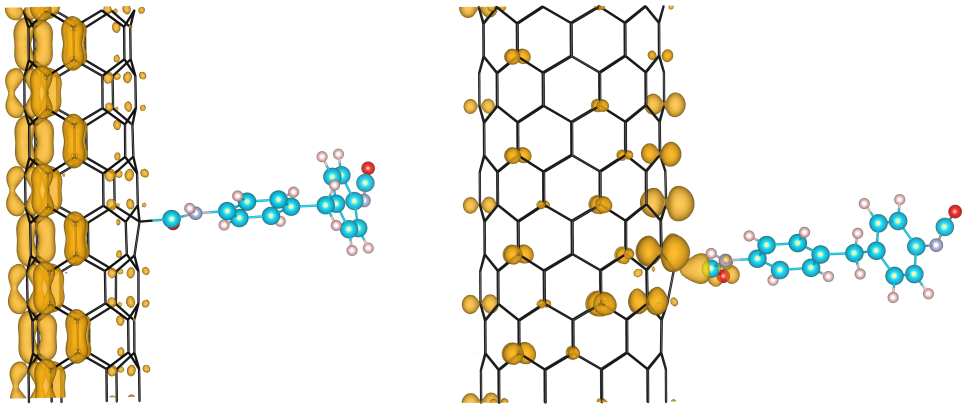

(a) (b)

Figure 10.6: Visualization of the electron density of the Γ-point wavefunction of the band crosing at the Fermi level, with the isovalue of 0.001 a.u., of the MDI-modified (a) metallic SWCNT(6,0) and (b) semiconducting SWCNT(10,0).

attachment site. In the case of the SWCNT(10,0), the perfectly flat band at the Fermi level has some impurity states localized around the functionalization site. It is clearly seen that such impurity states are extended with the molecular states around the amide bond, which change the distribution of the electron density in the place of the MDI attachment.

10.3 Structural rearrangements of diisocyanates covalently attached to SWCNT

The results obtained due to static DFT calculations of SWCNT(6,0) and SWCNT(10,0) with covalently attached TDI and MDI molecules have proven that the properties of the attached diisocyanates are very similar within the same type of the SWCNT. Apart from the similarity in the binding energy, as the result of the covalent bond formation, the structural parameters of the molecules, i.e. the angle of attachment, the geometry of the isocyanate group, the existence of C-H$\cdots$O hydrogen bond, the geometry of the attachment site etc., are similar too. All mentioned parameters were estimated on the basis of the static calculations, which do not include the entropy effects, only the calculation of the state of the system with minimum acting forces. To evaluate the changes of the molecules attached in comparison with their gas-phase analogues and to compare the structural flexibility of TDI and MDI covalently attached to SWCNT the Car–Parrinello MD simulations at 300 K were performed. The carbon nanotube with larger diameter, SWCNT(10,0), was chosen as a model structure of SWCNT, which characterizes with diameter close to the carbon nanotubes synthesized experimentally [444].

The molecular dynamics production run of 10 ps was estimated as a short, but fully representative time to estimate the most valuable structural changes and similarities. Moreover, the repetitive character of the analyzed parameters confirmed this fact. In Figure 10.7 the selected structural motifs from the MD run of TDI covalently attached to SWCNT are shown with the corresponding timestamp. For transparent analysis of the results obtained, several structural parameters were chosen and fully studied. Among the selected parameters are: the inclination angle and the rotation angle. The first parameter is defined as a valence angle between the surface of the carbon nanotube and the plane of the phenyl ring (directly connected to CNT) of the attached molecule. It is marked as CCC_{TDI} (or CCC_{MDI}) angle, where the first two carbon atoms indicate the carbon atoms from the CNT: one from the surface, while the second one is the atom directly connected to the attached molecule (see atoms

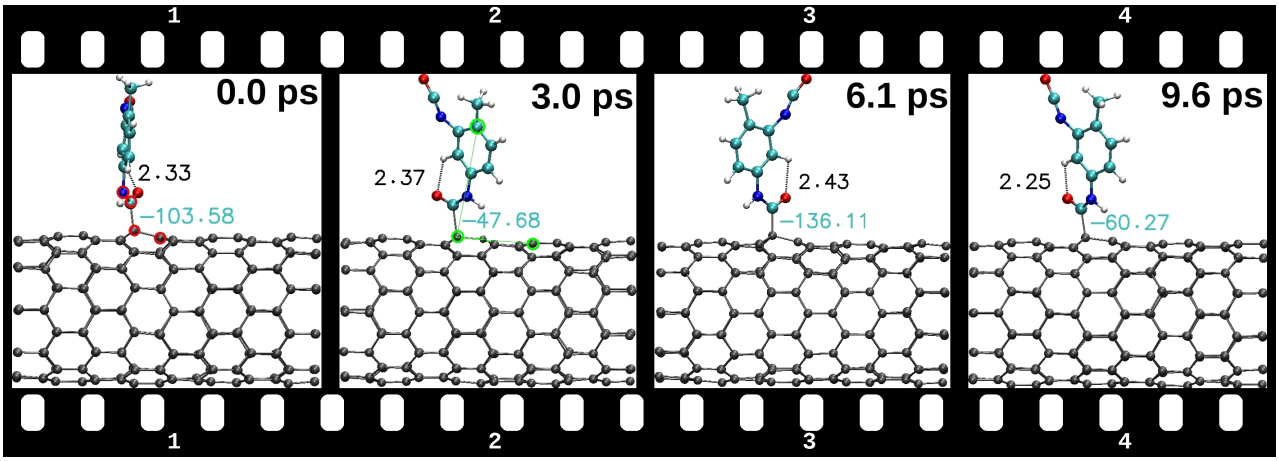

Figure 10.7: Selected snapshots from CP–MD simulation representing the structural rearrangements of TDI molecule covalently attached to the SWCNT(10,0). Car–Parrinello MD at 300 K. Each snapshot is given with the corresponding timestamp. Values marked in black correspond to the H···O distance in the C-H···O hydrogen bond, values marked in cyan indicate the rotation of the TDI with respect to the CNT surface. Detailed explanation is given in the text.

in green circles in snapshot "2" in Figure 10.7 or snapshot "3" in Figure 10.8). The third carbon atom is originated from the TDI/MDI phenyl ring as marked in snapshot "2" in Figure 10.7/snapshot "3" in Figure 10.8 with the green circle. The inclination angle substitutes here the mentioned C-C-C-N dihedral angle (Section 10.1) to show the angle of the TDI/MDI attachment. Previously used C-C-C-N dihedral angle is an ideal parameter to observe the rotation of the attached molecule with respect to the CNT surface, therefore, it is used here as a rotation angle, which is the second chosen parameter for the analysis. The rotation angle

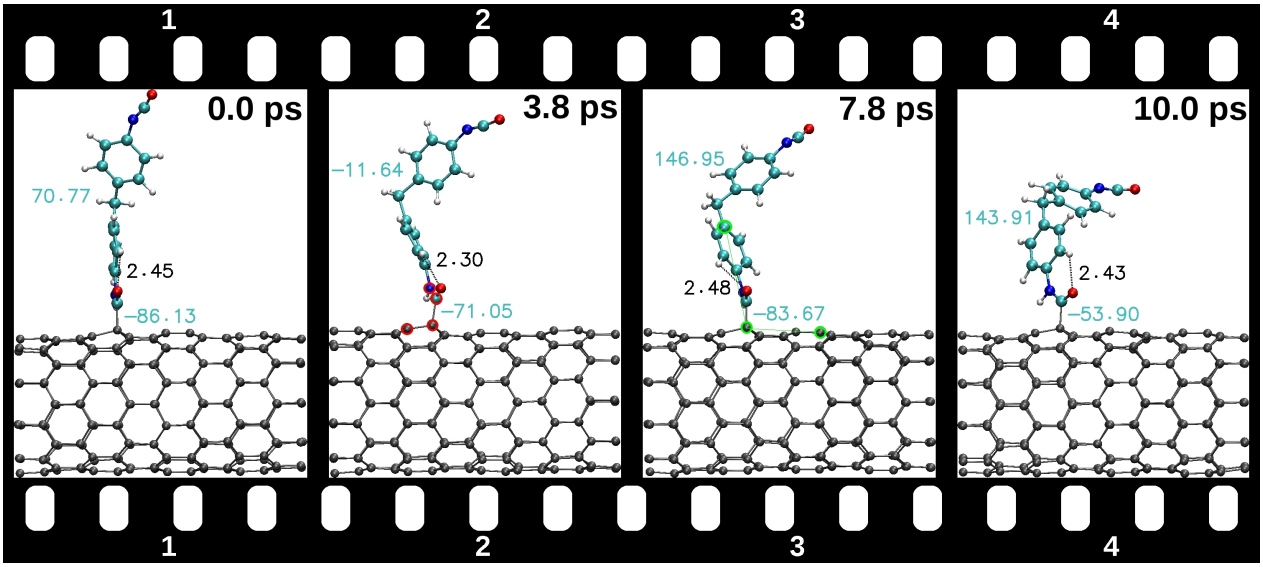

Figure 10.8: Selected snapshots from CP–MD simulation representing the structural rearrangements of MDI molecule covalently attached to the SWCNT(10,0). Car–Parrinello MD at 300 K. Each snapshot is given with the corresponding timestamp. Values marked in black correspond to the H···O distance in the C-H···O hydrogen bond, values marked in cyan indicate the rotation of the MDI with respect to the CNT surface and the C-C-C-C dihedral angle between two phenyl ring of MDI. Detailed explanation is given in the text.

is shown with red circles in snapshot "1" in Figure 10.7 or snapshot "2" in Figure 10.8. The values of the C-C-C-N dihedral angle are also given in each snapshot (in cyan). The same

parameters were also chosen to analyze SWCNT(10,0) with attached MDI (see Figure 10.8).

The angle of the attachment (or inclination angle) was estimated to be in the range of 88°–90° and 99°–107° for TDI and MDI attached to SWCNT, respectively (see Table 10.1). Molecular dynamics simulations show that this angle is changing in time as the result of the movements of the aromatic TDI and MDI rings. These changes are repetitive and depend on the type of the position of the phenyl ring with respect to the CNT surface. When the plane of the phenyl ring, directly connected to the SWCNT, is in the parallel position (see snapshot "2", "3" or "4" in Figure 10.7 or snapshot "4" in Figure 10.8), the values of the inclination angle are higher. When the phenyl ring rotates in the perpendicular plane (as in snapshot "1" in Figure 10.7), the values decrease. It can be seen in the upper plot in Figure 10.9, where the time evolution of the inclination angle for SWCNT-TDI and SWCNT-MDI is shown. The dependence described is clearly visible for the SWCNT-TDI system, which is characterized by higher changes in the values of the inclination angle.

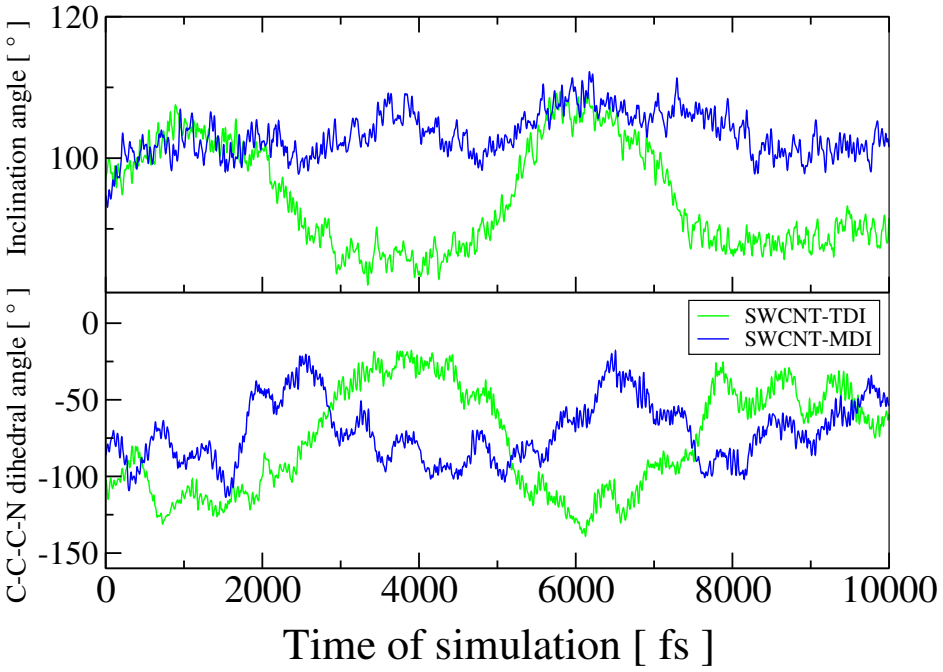

Figure 10.9: Time evolution of the inclination angle (CCC_{TDI}/CCC_{MDI}) and rotation angle (C-C-C-N dihedral angle) of the phenyl ring directly connected to the surface of SWCNT(10,0). Plots in green denote the SWCNT-TDI system, whereas plots in blue characterize the SWCNT-MDI system. The detailed explanation of the selected angles is given in the text.

The values of the inclination angle for TDI attached to SWCNT(10,0) are in the range of 83°–109°, while the SWCNT-MDI system is more stable with the CCC_{MDI} in the range of 98°–111°. Both ranges of the angles are close to the values estimated in the static DFT calculations and indicate no possibility of the attached molecules to interact with the CNT surface via $\pi - \pi$ interactions. The analysis of the inclination angle has shown that there is a difference in the changes of the angle depending on the size of the molecule attached. TDI is smaller molecule, which is more flexible and can rotate freerly with respect to the carbon nanotube axis, therefore, the changes of the inclination angle are higher, i.e. by 26° (see green plot in upper panel in Figure 10.9). At the same time, MDI should take into account the second phenyl ring, which, at some point, suppresses the movement of the whole molecule, therefore, the inclination angle is changing in less extend, only by 13° (blue plot in the upper panel in Figure 10.9). This indicates higher structural stability of the MDI molecule attached and higher arrangement of the polymer chains on the surface of the carbon

nanotubes. Moreover, the proven perpendicular position of TDI and MDI on SWCNT(10,0) at 300 K denotes the high possibility of the synthesized polymer chains to be oriented parallelly one to another in the same, perpendicular, position with respect to the CNT.

The second analyzed parameter is the rotation angle, which shows the way of the rotation of the phenyl ring with respect to the surface of the carbon nanotube. The time evolution of the C-C-C-N dihedral angle, corresponding to the rotation angle, is depicted in the lower panel in Figure 10.9. Both TDI and MDI molecules show similar rotational behavior: phenyl ring of TDI and MDI rotates on maximally 102° and 92°, respectively. Moreover, TDI is characterized with prolonged rotation states with the lifetime of c.a. 2.3 ps. During the simulation time of 10 ps there were observed four rotations of the phenyl ring of TDI (see molecule in the snapshots in Figure 10.7). The rotation of the phenyl ring of the MDI molecule has several additional oscillations on c.a. 32°, therefore, the changes are more smooth. No full rotation of the covalently attached phenyl rings has been observed.

Car–Parrinello MD simulations also confirm the existence of intramolecular C-H$\cdots$O hydrogen bond, formed between the C-H bond from the phenyl ring and the oxygen atom from the urethane bond, in both TDI- and MDI-modified SWCNTs. This hydrogen bond is marked in all selected snapshots with black color and dashed line. C-H$\cdots$O H-bond is very stable with the values in the range of 1.85–2.85 Å and 1.85–2.75 Å for SWCNT-TDI and SWCNT-MDI systems, respectively. The radial distribution function of the H$\cdots$O distance during the simulation time of 10 ps shows that the average H$\cdots$O distance is 2.25 Å for both systems analyzed. This value is highly compatible with the calculated one in the static DFT calculations. The corresponding $\angle$(CHO) angle is in the range of 100°–131° and 102°–128° for TDI and MDI functionalized SWCNT. It should be noted that C-H$\cdots$O hydrogen bond strongly influences the structural rearrangements of the molecules attached, especially, the rotation of the phenyl ring, which depends on the movement of the oxygen atom from the urethane bond, which participates in the H-bond formation. In the MD trajectory it is clearly visible that the phenyl ring directly mimics the movement of the oxygen atom. Taking into account that structural parameters of C-H$\cdots$O hydrogen bond in both systems are similar, the rotation of TDI and MDI phenyl rings is similar too.

Among the characteristic feature of the analyzed systems is the presence of the isocyanate functional group, which was proven to interact with the surface of the carbon nanotube during their noncovalent functionalization. In case of the covalent attachment of diisocyanate molecules, when one NCO group is engaged in the formation of the urethane bond with the COOH group on the SWCNT, the second NCO is located far from the CNT surface (see Figure 10.7 and Figure 10.8), therefore, no possibility for the additional intermolecular interactions was detected. The free isocyanate group is ready for further interactions to form PU polymer chains. The time evolution of the C-C-N-C dihedral angle, which corresponds to the deformation of the isocyanate group from the co-planarity with the phenyl ring, shows the same changes of the NCO geometry as the free NCO groups of TDI and MDI in the gas phase (see Figure 8.4).

The last part of the discussion of the result obtained is about the structural parameters of the MDI molecule attached to the SWCNT(10,0). The CP–MD simulations of the MDI molecule in the gas phase (see Section 8.1.2) have shown that there is no full rotation between two MDI phenyl rings at 300 K, as it was reported for the gas-phase MDI at 350 K [437]. The maximum rotation on c.a. 40° was characteric for MDI at 300 K. After the attachment of the MDI molecule to the SWCNT surface, the mutual rotation of the phenyl rings changes. The time evolution of both: gas-phase and covalently attached MDI at 300 K, are depicted in Figure 10.10. One phenyl ring of MDI is connected to the rigid surface, thus, starts to be stiffer. At that time, the second phenyl ring is rotating with larger amplitudes than it was for the gas-phase MDI. Two significant rotations in the opposite directions on c.a. 140° and 102°

take place during the time simulation of 10 ps (see Figure 10.10). Even if one phenyl ring is more suppressed, the second one is still flexible, but no full rotation was detected. The variety of different positions of the second phenyl ring is shown in Figure 10.8, where the corresponding values of the C-C-C-C dihedral angle are given with the cyan color (values positioned close to the C-C-C-C dihedral angle).

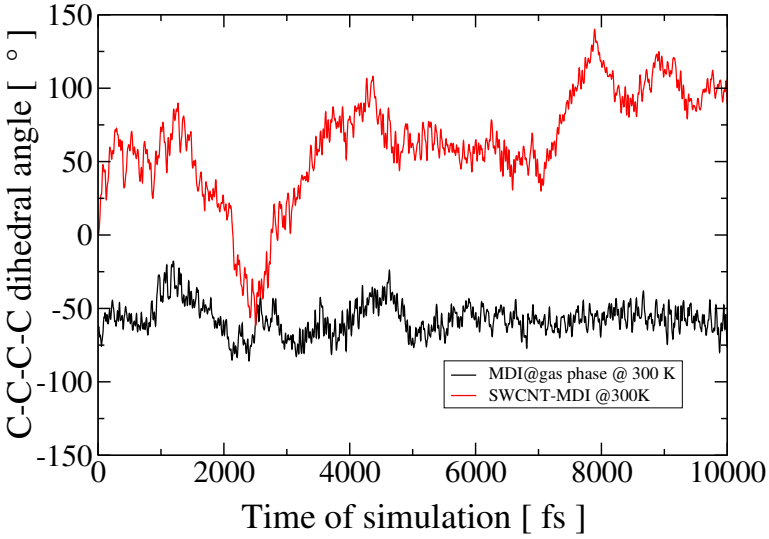

Figure 10.10: Time evolution of the C-C-C-C dihedral angle between two phenyl rings of MDI obtained from a CP–MD run. C-C-C-C dihedral angles for gas-phase MDI and covalently attached to SWCNT(10,0) at 300 K are marked in black and red, respectively.

The relatively free movement of the second phenyl ring enables the formation of additional weak intramolecular interaction, i.e. C-H$\cdots\pi$ hydrogen bond between the C-H H-bond proton donor from the upper phenyl ring and the π-density localized on the lower phenyl ring. The formation of this temporary interaction can be seen in the snapshot "3" and "4" in Figure 10.8. The existence of the C-H$\cdots\pi$ hydrogen bond (or C-H$\cdots\pi$ contacts, because it is very weak type of interaction) was reported during the MD simulations of the gas-phase MDI, where its lifetime was estimated as 0.38–0.52 ps. After the covalent attachment of MDI, this intramolecular interaction exists with significantly longer lifetime in the end of the simulation time (see Figure 10.11), when the formation of the structure depicted in the snaphot "4" in Figure 10.8 takes place. The shortest H$\cdots\pi$ distance is 2.55 Å and is connected with high internal stress of the molecule (the typical geometry of the $\angle$(CCC) valence angle between the rings changes, which is unfavourable), therefore, the lifetime of such interaction is very low. In comparison to other structural parameters of the MDI molecule, $\angle$(CCC) angle between the MDI phenyl rings is very stable with the values in the range of 112°–122°, which are close to the gas-phase ones.

There is a high tendency of the initially carboxylated carbon nanotubes to be modified by diisocyanate molecules. This fact is among the frequently used methods to increase the dispersion of the carbon nanotubes and to synthesize the polyurethane composites. The affinity of carboxylated CNTs to react with diisocyanates depends on the type of the carbon nanotube: the binding energy is inversely proportional to the diameter of the SWCNT, which was proven on SWCNT(6,0) and SWCNT(10,0) examples. As a result of the formation of the covalent bond, the geometry of the site, close to the attachment of the molecule, changes, which is connected with the change of the hybridization of the carbon atom from the SWCNT sidewall. This structural change influences the distribution of the electron density in close vicinity to the sp^3-hybridized carbon atom, therefore, impact the electronic properties of the

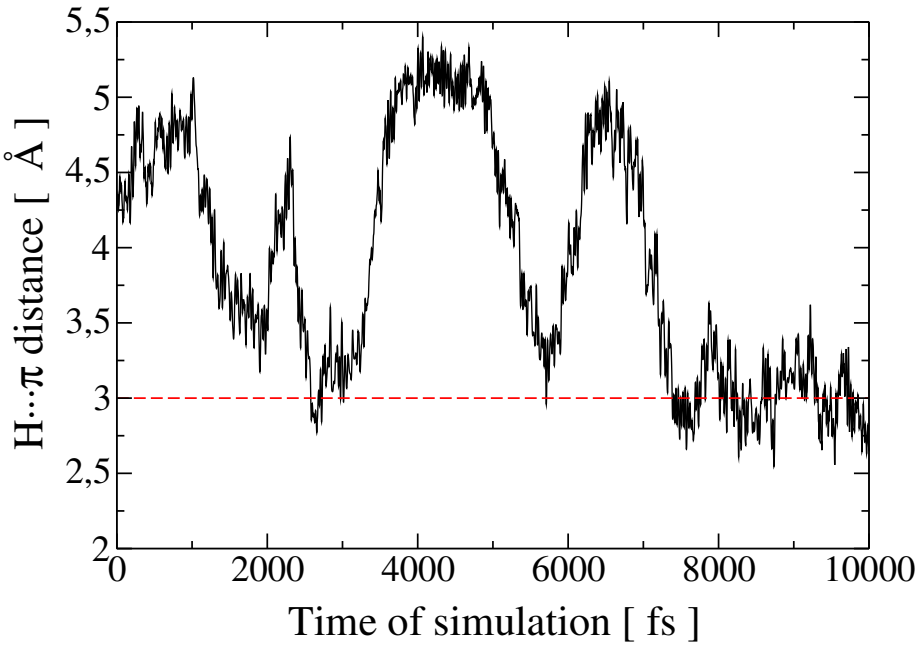

Figure 10.11: Time evolution of the H$\cdots\pi$ distance from the C-H$\cdots\pi$ hydrogen bond in SWCNT-MDI system, obtained from a CP–MD run. H$\cdots\pi$ distance corresponds to the distance between the hydrogen atom from a H-bond donor and the closest carbon atom from the second phenyl ring.

carbon nanotubes.

Noncovalent interactions are of great importance during the covalent attachment of the second molecule of diisocyanate. Among them are $\pi - \pi$ interactions, electrostatic interactions between isocyanate groups and C-H$\cdots\pi$ hydrogen bonds between the neighbor molecules. The strength and the detailed influence of the mentioned NCI were explained in this Section with the clear analysis of the model structures representing the possible covalent attachment of diisocyanates. The structural rearrangements of the TDI and MDI attached to the sidewall of SWCNT(10,0) were fully explained due to the Car–Parrinello molecular dynamics simulations at 300 K. Both TDI and MDI molecules prefer to be covalently attached to SWCNT in perpendicular position with respect to the nanotube axis with the rotation of the phenyl ring, directly connected to the surface, by maximally 102° and 92° for TDI and MDI, respectively. No evidence for full rotation of the molecules was confirmed. Moreover, the structural flexibility of the MDI molecule is more suppressed in comparison to TDI, which is caused by the presence of the second phenyl ring and the formation of weak intramolecular C-H$\cdots\pi$ hydrogen bond. The structural changes of the molecules attached directly depend on the behavior of the oxygen atom from the urethane bond, which steers the rotation of the molecules on the surface, due to the formation of strong intramolecular C-H$\cdots$O hydrogen bond.

Chapter 11

Influence of defective regions on carbon nanotube surface

As it was described in Section 4.1.1, most of the carbon nanotubes synthesized are rich in different defective regions, which are caused by the usage of high temperature and catalysts during the production of this carbon structures. There are developed methods to purify CNTs from them, but still it is extremely hard and expensive to obtain carbon powder consisted only from pristine carbon nanotubes with the specific chirality. Each type of the defect might cause different change of the properties of CNTs and decrease of their uniqueness. Moreover, during the further modification of the carbon nanotubes, the defective CNTs might have different activity and change the properties of the material comparing to the expected ones. In this Chapter, the influence of different defects, on the sidewall of single-walled carbon nanotubes, on their reactivity and electronic properties during the their carboxylation is described. Additionally, the CP–MD simulations at 300 K are used here to show the influence of the defects on the structural rearrangements of diisocyanate molecules, covalently attached in the close vicinity to the defective region. It serves as a simple example of the influence of the small structural changes on the surface on the structural properties of molecules covalently attached on SWCNTs.

11.1 Defective carbon nanotubes

Different types of defective CNT regions can appear as a result of synthesis, purification or post-processing of carbon nanotubes. Among them vacancies (both mono- and di-) and adatom defects are the most chatacteristic native and irradiation-induced structural defects. Apart from the defects that appear as the reorganization of the carbon atoms on the surface, defects based on heteroatom introduction and elbow-like bends are also possible. The present research is focused only on the analysis of defective CNT regions formed due to the reorganization of carbon-carbon bonds in the SWCNT sidewall as they were not investigated in detail previously.

11.1.1 Introduction

Five defective regions of SWCNT(10,0) are considered in the present PhD thesis. Among them are: vacancy-defective SWCNT(10,0), divacancy (5-8-5)-defective SWCNT(10,0), divacancy (555-777)-defective SWCNT(10,0), adatom-defective SWCNT(10,0) and SWCNT(10,0) with Stone-Wales defect, described in Section 4.1.1. The mentioned defective regions on the surface of the carbon nanotubes are depicted in Figure 11.1 with the green color. Vacancy defect is based on the lack of one carbon atom in the pure hexagonal structure of SWCNT, as a result the defect consists of one pentagonal ring and one larger ring with nine carbon

atoms (see Figure 11.1: a). When there is a lack of two carbon atoms, i.e. in the case of

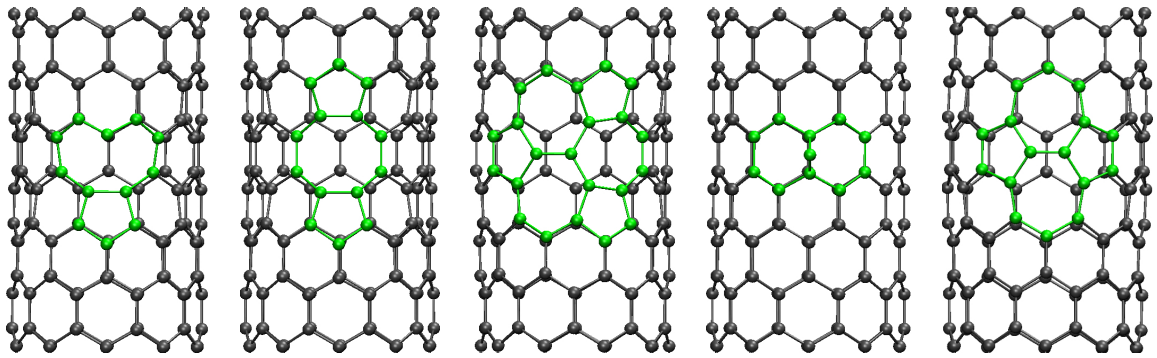

Figure 11.1: Optimized geometries of defective structures of SWCNT(10,0): (a) vacancy-defective, (b) divacancy(5-8-5)-defective, (c) divacancy(555-777)-defective, (d) adatom and (e) Stone-Wales defects. All defective regions (sites) are marked with the green color.

divacancy-defective CNTs, different structural rearrangements are possible to form a stable structure of the defect. Two of them, i.e. divacancy (5-8-5) and divacancy (555-777), are studied in the present work (see Figure 11.1: b, c). The energy of the formation of these defects is different, where the divacancy (5-8-5) was proven to be more stable and more likely to be formed. The energy difference between these two defects is 142 kJ/mol [213] or 154 kJ/mol [445], depending on the theoretical approach used. As it is seen from Figure 11.1, during divacancy (5-8-5) three defective rings are formed: two pentagonal and one octagonal, while divacancy (555-777) consists of six defective rings: three pentagonal and three heptagonal. The defective sites mentioned can be formed in a lateral (along the CNT axis) or vertical (perpendicular to CNT axis) orientation, but the lateral divacancies are more stable, so only they are considered here. In adatom defect the additional carbon atom is covalently attached to the sidewall of SWCNT with the formation of two bonds with the carbon atoms from the CNT hexagons (see Figure 11.1: d). The last defect studied is Stone-Wales defect formed by the rotation of one carbon-carbon bond of CNT by 90°, which results in the formation of four defective rings: two pentagonal and two heptagonal (see Figure 11.1: e).

The reactivity of all defective CNTs analyzed is different and significantly depends on the exact structural change, therefore, the change of the electronic properties comparing to the pristine carbon nanotube. In the present PhD thesis, the reactivity of the selected defective SWCNTs is analyzed during the carboxylation process, when one carboxyl group is covalently attached to the sidewall of SWCNT. More description is given in Section 11.2.

11.1.2 Influence on electronic properties

Small deviation from the equilibrium, pristine, structure of single-walled carbon nanotube causes the change of its original properties, especially electronic ones. To show this change, the electronic band structures in Γ–Z direction were obtained for all defective SWCNTs using static DFT calculations with Grimme–D2 dispersion correction. The electronic band structures in the range of -2.0–2.0 eV near the Fermi level are given in Figure 11.2. For all systems, the Fermi level was set as 0 eV and is shown with the red dashed line in the figure. For comparison, the electronic band structure of pristine, semiconducting, SWCNT(10,0) is also given in Figure 11.2.

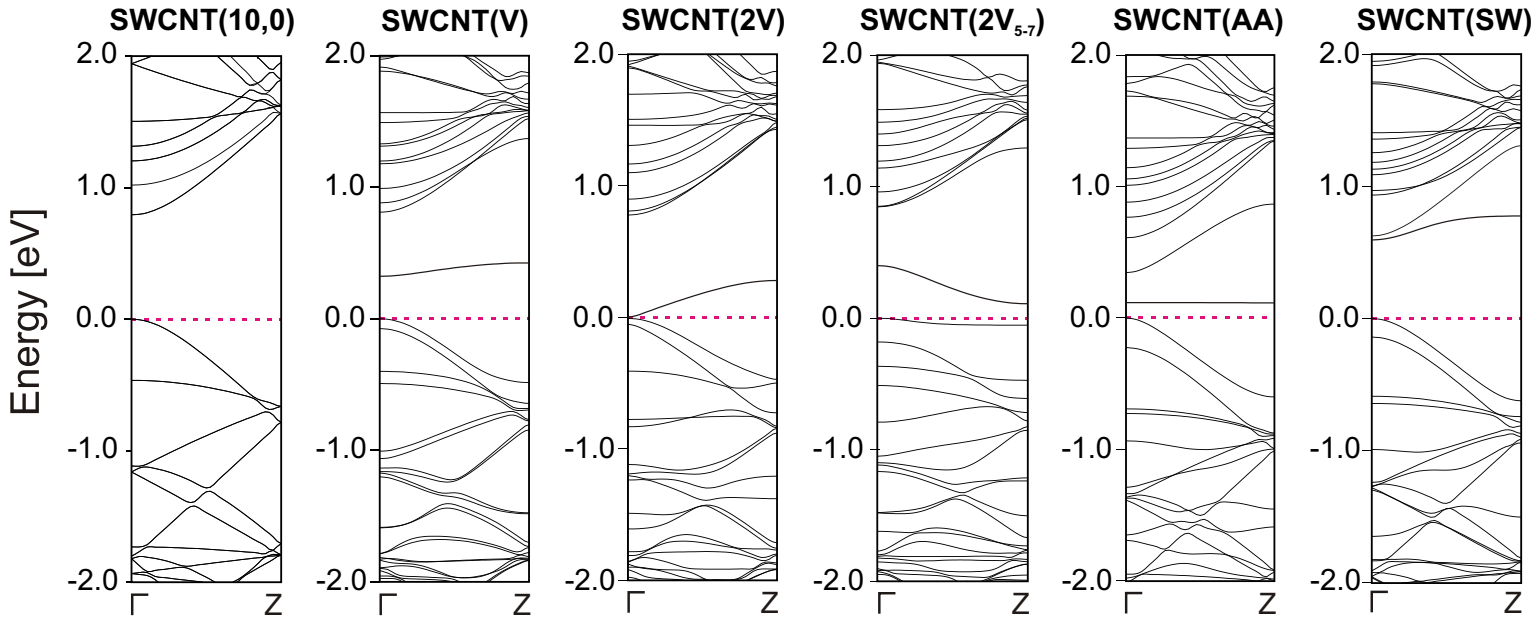

Figure 11.2: Electronic band structure in Γ–Z direction for defective SWCNT(10,0) with vacancy, divacancy: (5-8-5) and (555-777), adatom and Stone-Wales defects. The corresponding type of the defect is given in the caption for every plot. The Fermi level was set to 0 eV and is marked with the red dashed line.

The introduction of the defective regions in the SWCNT(10,0) sidewall disrupts the original π-electron density localized within the carbon nanotube and causes the descrease of the band gap of the defective SWCNT(10,0) in comparison to the pristine SWCNT(10,0). It is clearly seen in Figure 11.2, where new bands, close to the Fermi level, are formed, lowering the width of the band gap. The new bands are formed as a result of the introduction of new states during the defect formation. The highest change in the electronic band structure is seen for the adatom-defective SWCNT(10,0), labeled as SWCNT(AA) in Figure 11.2, and divacancy(5-8-5)-defective SWCNT(10,0), labeled as SWCNT(2V) in Figure 11.2. The energy band gap decreases to c.a. 0.15 eV for SWCNT(AA) and even to the values close to 0 eV for the SWCNT(2V). The smallest influence of the defect formation is seen in the case of Stone-Wales defect, where the band gap is changing from c.a. 0.8 eV (pristine SWCNT(10,0)) to c.a. 0.56 eV. In general, after the defect formation the conducting properties of the semiconducting carbon nanotube are changed, therefore, the the defective SWCNTs are expected to be more reactive than the defect-free SWCNT.

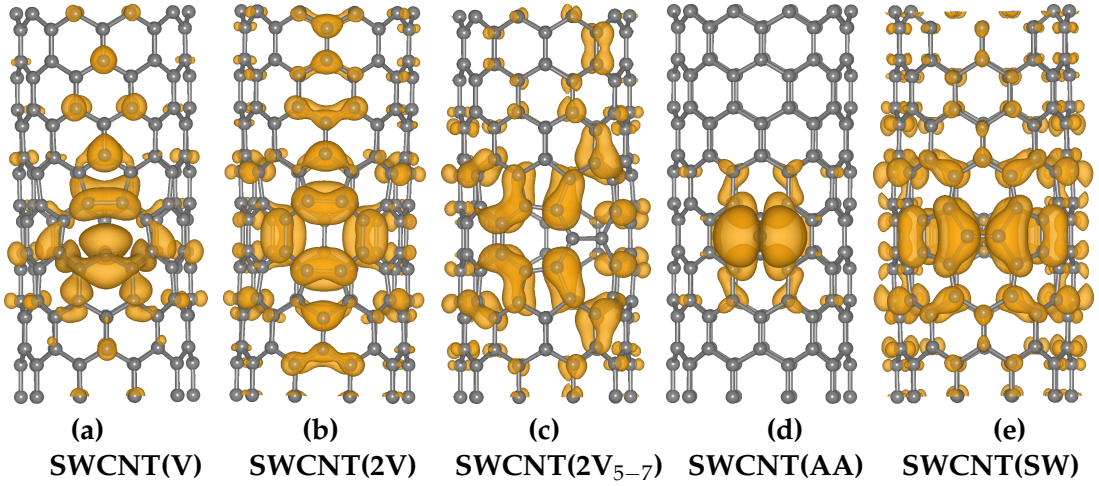

Figure 11.3: Charge density of the unoccupied states of defective SWCNT(10,0) localized directly above the Fermi level for: (a) vacancy-defective SWCNT(V), (b) divacancy(5-8-5)-defective SWCNT(2V), (c) divacancy(555-777)-defective SWCNT(2V$_{5-7}$), (d) adatom-defective SWCNT(AA) and (e) SWCNT with Stone-Wales defects SWCNT(SW). The orange surface represents the charge density of isovalue of 0.001 a.u.

The second fact indicating differences in the reactivity of the defective CNTs is the way of the distribution of the charge density localized directly above the Fermi level (unoccupied states) of the defective SWCNT. It is depicted in Figure 11.3. There are relatively small changes of the structure with the defect formation, but the unoccupied states of the defective single-walled CNTs are characterized with significantly different charge distribution, thus differences in the chemical reactivity.

11.2 Carboxylation of defective carbon nanotubes

There are a lot of possible methods to estimate the reactivity of carbon nanotubes. Taking into account that CNTs are usually covalently functionalized with OH and COOH groups before the synthesis of PU composites, the carboxylation reaction was used to obtain the most reactive defective CNT types and attachment sites.

11.2.1 Reactivity of defective SWCNT(10,0)

Different initial covalent attachment of carboxyl group was used to estimate the most probable place of the covalent bond formation. With the usage of the charge density distribution

(see Figure 11.3), one can suggest that each carbon atom located in the defective region has different affinity to form a covalent bond. To compare the reactivity of the carbon atoms within the defect, structures with different position of the attachment of COOH group were considered. Due to the symmetry of some attachment sites, the amount of possible structures was reduced. The carboxylated SWCNTs(10,0) with vacancy defect are shown in Figure 11.4. The binding energy for each the structure depicted is different (see Table 11.1). The most

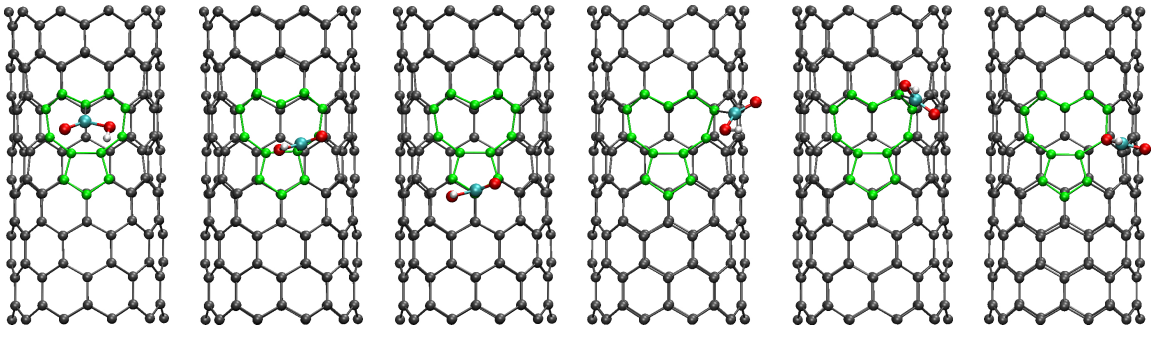

Figure 11.4: Optimized geometries of carboxylated vacancy-defective SWCNT(10,0) with different position of the carboxyl functional group. The defective region is marked with the green color.

reactive site of the covalent attachment of the carboxyl group is on the carbon atom with two dangling bonds (structure **V-1**), located directly on the central carbon atom of the defective ring with nine carbon atoms. In Figure 11.3: a, it is clearly shown that this carbon atom has a specific distribution of the charge density, which is sticking out from the CNT surface. The energetical cost of the formation of the C–C bond in this position is -325.16 kJ/-mol (see Table 11.1) and it is 4.27 times more reactive than the carbon atom from the pristine SWCNT(10,0). The corresponding length of the C–C bond formed between the carbon atom from the CNT surface and the carboxyl group (marked as C_{CNT}-C') is 0.114 Å shorter, which means that the bond formed is stronger than the traditional single carbon-carbon bond.

The rest, five, structures of vacancy-defective SWCNT(10,0) (see Figure 11.4) with attached COOH groups are characterized with significantly lower reactivity in the range of -155– -92 kJ/mol (see Table 11.1) as the origin of the C–C bond formation is different. Apart from the lower reactivity of these sites, the vacancy-defective SWCNT(10,0) are still more reactive than the pristine SWCNT(10,0). The length of C_{CNT}-C' bond is in the range of 1.564–1.592 Å, which is close to the carbon-carbon bond of the covalent attachment in the case of pristine carbon nanotube (1.569 Å).

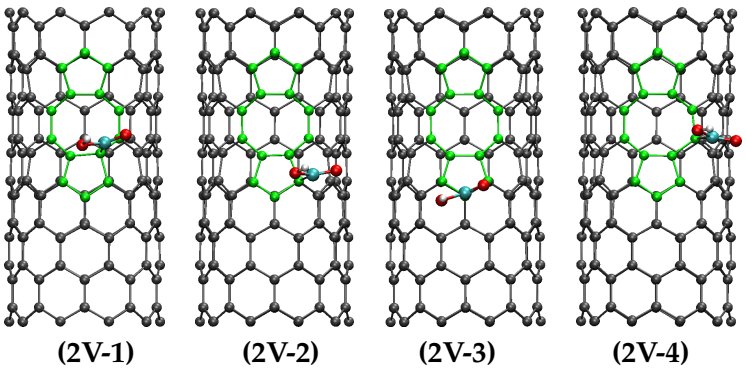

Figure 11.5: Optimized geometries of carboxylated divacancy(5-8-5)-defective SWCNT(10,0) with different position of the carboxyl functional group. The defective region is marked with the green color.

The second defect considered is a divacancy (5-8-5), which characterizes with c.a. 1.84 times lower reactivity than the vacancy-defective CNT. The most reactive site is the structure labeled as **2V-1**, where the COOH group is attached to the carbon atom belonging to pentagonal and octagonal defective rings simultaneously (see Figure 11.5). The binding energy of the attachment to this carbon atom is -176.57 kJ/mol, which is also more reactive than the carbon atom from the pristine SWCNT(10,0). The reactivity of other defective sites is similar to the less stable vacancy-defective regions (see Table 11.1). The second divacancy defect, (555-777), has similar influence on the carboxylation of defective SWCNT(10,0) as a divacancy (8-5-8). The structures analyzed are presented in Figure 11.6, where the structure **2V$_{5-7}$-1** is the global minimum structure with the binding energy of -182.36 kJ/mol. The charge distribution on this defect is relatively equal within the defect region (Figure 11.3: c), therefore the reactivity of the carbon atoms in the C–C bond formation is similar for all structures with the exception of the structure **2V$_{5-7}$-5**, where COOH group is attached to the carbon atom that connects three heptagonal rings, where the charge density is lower than 0.001 a.u. ("zero" value of the density in Figure 11.3: c). It is close to the carbon atom from the pristine SWCNT(10,0), therefore, the binding energy is close to the pristine one, i.e. -88.77 kJ/mol.

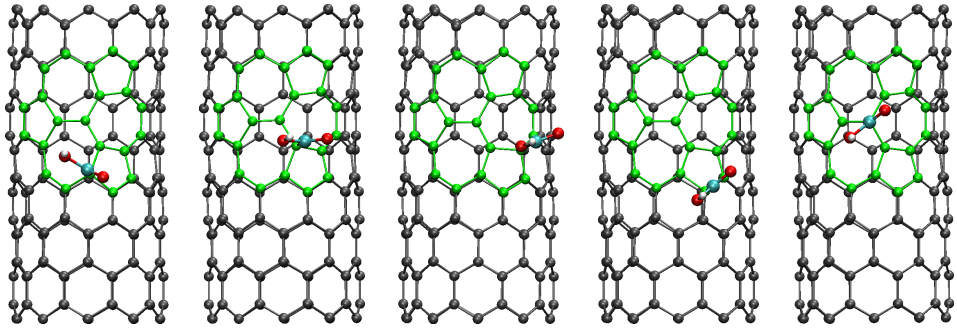

Figure 11.6: Optimized geometries of carboxylated divacancy(555-777)-defective SWCNT(10,0) with different position of the carboxyl functional group. The defective region is marked with the green color.

The forth defect considered, namely adatom, is the most reactive one from all defective regions analyzed. It is known as one of the native irradiation-induced structural defects of SWCNT, which appears during ion/electron irradiation of carbon nanotubes [446]. The most reactive carbon atom of this defect is the added carbon atom, which form a bridge-like connection with the two neighbor carbon atoms from SWCNT (see structure **AA-1** in Figure 11.7). As it was shown in Figure 11.3: d, the electron density is localized on this carbon

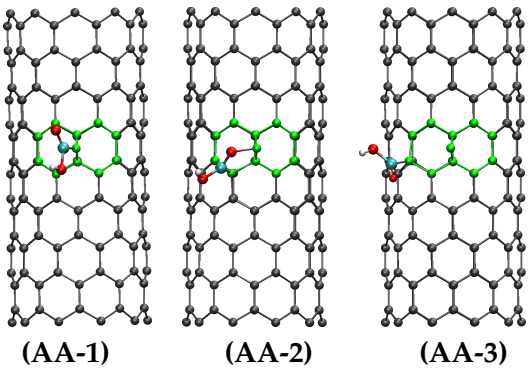

Figure 11.7: Optimized geometries of carboxylated adatom-defective SWCNT(10,0) with different position of the carboxyl functional group. The defective region is marked with the green color.

Table 11.1: Energetical, structural and vibrational parameters of carboxylated SWCNT(10,0) with different defective regions: the binding energy of the covalent attachment of COOH group, the length of C_{CNT}–C' bond between the carbon atom from the carbon nanotube and COOH group participating in the formation of the covalent bond, the characteristic vibrational frequencies, ν, and shift of the vibrational frequencies, $\Delta\nu$ (with respect to the COOH attached to the pristine SWCNT(10,0)) of CO and OH group from COOH attached to the different SWCNT surfaces.

Defect	**Label**	$\mathbf{E}_{bind}$ [kJ/mol]	$\mathbf{C}_{CNT}$**–C'** [Å]	$\nu_{C=O}$ [cm^{-1}]	$\Delta\nu_{C=O}$ [cm^{-1}]	ν_{O-H} [cm^{-1}]	$\Delta\nu_{O-H}$ [cm^{-1}]
SWCNT(10,0)		**-76.22**	**1.569**	**1763**	**0**	**3596**	**0**
	V-1	**-325.16**	**1.455**	**1667**	**-96**	**3619**	**23**
	V-2	-155.34	1.577	1740	-23	3601	5
SWCNT(V)	V-3	-137.97	1.565	1769	6	3596	0
	V-4	-110.00	1.577	1760	-3	3597	1
	V-5	-98.41	1.564	1772	9	3596	0
	V-6	-92.63	1.592	1747	-16	3596	0
	2V-1	**-176.57**	**1.564**	**1760**	**-3**	**3590**	**-6**
SWCNT(2V)	2V-2	-161.13	1.549	1761	-2	3591	-5
	2V-3	-138.94	1.561	1768	5	3597	1
	2V-4	-104.20	1.592	1754	-10	3603	7
	$2V_{5-7}$-1	**-182.36**	**1.545**	**1755**	**-8**	**3596**	**0**
	$2V_{5-7}$-2	-170.78	1.569	1761	-2	3600	4
SWCNT($2V_{5-7}$)	$2V_{5-7}$-3	-158.24	1.568	1760	-3	3596	0
	$2V_{5-7}$-4	-121.57	1.575	1769	6	3599	3
	$2V_{5-7}$-5	-88.77	1.560	1746	-17	3595	-1
	AA-1	**-401.38**	**1.439**	**1640**	**-123**	**3608**	**12**
SWCNT(AA)	AA-2	-189.11	1.513	1495	-268	3588	-8
	AA-3	-103.24	1.570	1769	6	3594	-2
	SW-1	**-148.59**	**1.539**	**1752**	**-11**	**3600**	**4**
	SW-2	-111.92	1.560	1762	-1	3602	6
SWCNT(SW)	SW-3	-104.20	1.564	1761	-2	3599	3
	SW-4	-104.20	1.563	1761	-11	3598	2
	SW-5	-94.56	1.562	1756	-7	3604	8

atom for the most, therefore, this atom is the most preferable to react with the formation of the covalent bond. The binding energy of this defective site is -401.38 kJ/mol (see Table 11.1) and it is more than 2 times more reactive than the formation of the C–C covalent bond in the structure **AA-2** and c.a. 4 times more reactive than the structure **AA-3**. The formed C–C bond is relatively shorter, i.e. 1.439 Å than the rest C–C bond formed, and is close to the C–C bond from the global minimum structure of vacancy-defective SWCNT(10,0), which is 1.455 Å. Both these structures: **V-1** and **AA-1** are the most reactive ones from all structures studied with the significant structural differencies among other structures.

The Stone-Wales defect belongs to the least reactive defective regions of SWCNT(10,0). The binding energy of the global minimum structure (**SW-1**) is -148.59 kJ/mol, which is in the range of typical less reactive defective regions considered for the previous structures (see Table 11.1). The most reactive are the carbon atoms localized on the border of 7-5-7 defective rings, where the electron density is localized (butterfly-like density distribution in Figure 11.3: e). Even if the Stone-Wales defect is less reactive than other defects, it is c.a. 2 times more reactive than the pristine SWCNT(10,0). That is why, the SW-defective SWCNT are more

likely to be functionalized than the pristine CNTs.

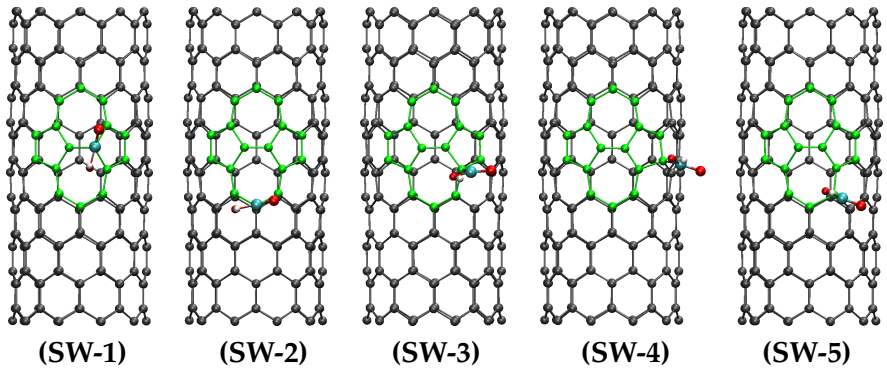

Figure 11.8: Optimized geometries of carboxylated SWCNT(10,0) with Stone-Wales defect and different position of the carboxyl functional group. The defective region is marked with the green color.

Defective carbon nanotubes are significantly more reactive than the pristine ones. Taking into account the investigation of the reactivity of defective SWCNTs(10,0) in the carboxylation reaction, their reactivity can be organized in the following order: adatom (AA) > vacancy (V) > divacancy(555-777) ($2V_{5-7}$) > divacancy(5-8-5) (2V) > Stone-Wales defect (SW).

11.2.2 Vibrational analysis

The carboxylation of carbon nanotubes can be investigated using experimental techniques, including Infrared (IR) and Raman spectroscopy, due to the characteristic vibrations of carbonyl and hydroxyl functional groups. The band between 1710 and 1760 cm^{-1} is characteristic to C=O stretching vibration ($\nu_{C=O}$), while the band between 3100 and 3600 cm^{-1} corresponds to O-H stretching vibration. The existence of both vibrations means the presence of the carboxyl group on the surface. Any change of the position of the characteristic vibration, with respect to the reference system, means the structural changes close to the place of functional group attachment. The sensitivity of the vibrational frequencies of COOH group, as a result of the introduction of the defective regions on the surface of the CNTs, can be obtained using static DFT calculations.

The pristine SWCNT(10,0) was selected as a reference system for the vibrational analysis of different defective SWCNTs. The characteristic vibrational frequencies calculated for C=O and O-H for the pristine SWCNT(10,0) are 1763 cm^{-1} and 3596 cm^{-1}, respectively. The shifts of these frequencies were calculated for all defective, carboxylated carbon nanotubes. They are listed in Table 11.1 together with the exact value of the characteristic C=O and O-H frequencies. The band corresponding to the C=O vibration is more sensitive to the existence of defective regions than the O-H one. The highest shift of 268/123 cm^{-1} and 96 cm^{-1} of the C=O vibration, $\Delta\nu_{C=O}$, is observed for the most reactive defective structures of SWCNT, i.e. adatom and vacancy-defective, respectively. At the same time, these defective structures possess the highest shift of the O-H vibration, $\Delta\nu_{O-H}$: 12 cm^{-1} for the global minimum structure of SWCNT(AA) and 23 cm^{-1} for the global minimum structure of SWCNT(V). Less reactive structures are characterized with relatively small shift in the range of 1–23 cm^{-1} and 0–8 cm^{-1} for C=O and O-H vibrational frequencies, respectively. It should be also noted that the values obtained of some frequencies calculated for COOH functional group on the SWCNT sidewall (see Table 11.1), e.g. 1640 cm^{-1} and 1667 cm^{-1}, are similar to the reported previously frequencies for COOH groups at the tips of the zigzag CNTs [354].

The vibrational analysis of the defective structures analyzed confirms that the characteristic vibrational frequencies of the carboxyl group are sensitive on the presence of the structural

changes on the surface of the carbon nanotubes and can be used to differentiate the type of the defect in SWCNTs.

11.2.3 Electronic band structure

Only two defects of the carbon nanotubes with different reactivity are taken for further analysis, i.e. vacancy-defective SWCNT(10,0) and divacancy(5-8-5)-defective SWCNT(10,0). These defects were selected, because they are the most primary and native defects of CNTs, commonly detected in the synthesized CNTs. Due to the differencies in their reactivity, the direct comparison of more and less reactive defective sites is possible.

The influence of the attachment of carboxyl group on the electronic structure of pristine and defective SWCNT(10,0) was obtained only for the global minimum structures of the selected defective carbon nanotubes. Due to the fact that after the attachment of the COOH group,

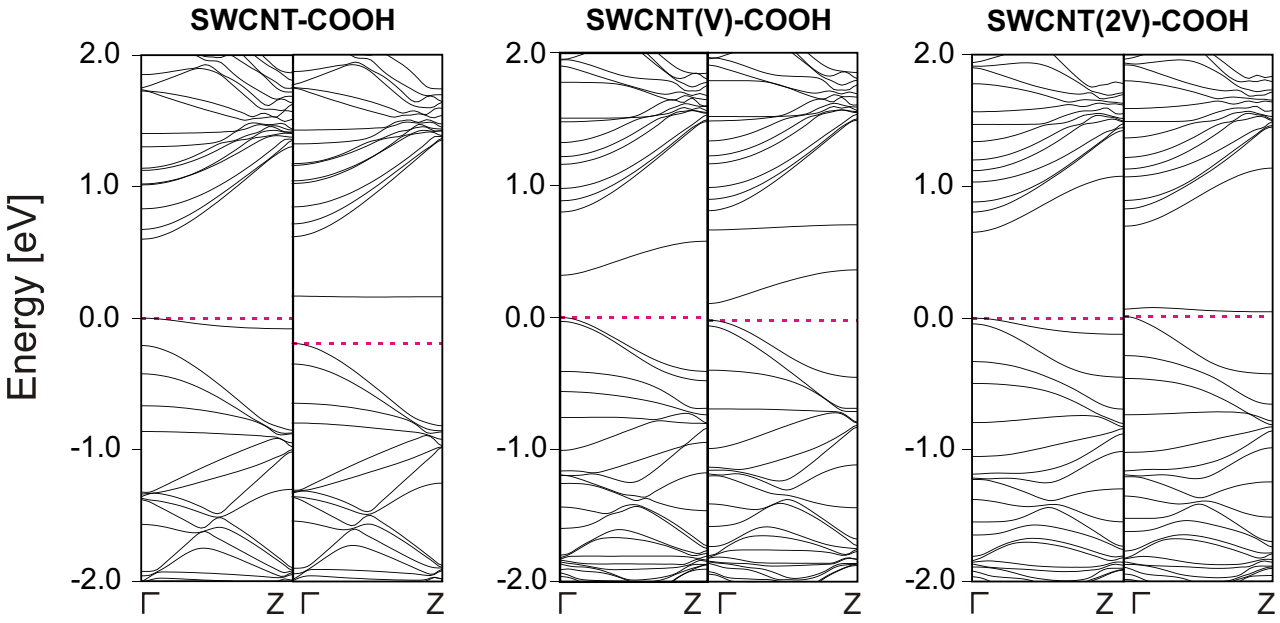

Figure 11.9: Electronic band structure of carboxylated pristine SWCNT(10,0) and defective: vacancy-defective and divacancy-defective SWCNT(10,0). Due to the spin polarization of the carboxylated system, both spin-up (plot in the left) and spin-down (plot in the right) electronic contribution is shown. The Fermi level was set to 0 eV. The maximally occupied spin-up and spin-down channels are marked with the red dashed line.

there is an odd number of electrons in the system, the local spin density approach was used to estimate the changes of both spin-up and spin-down electronic contribution. The obtained electronic band structures for two spin states for pristine, vacancy- and divacancy-defective SWCNT(10,0) are shown in Figure 11.9. The corresponding electronic band structures without the COOH attachment were given in Figure 11.2. It should be noted that all carboxylated single-walled carbon nanotubes are characterized with the p-doped character. The odd electron occupies the spin-up band, while the spin-down band is empty.

After the carboxylation of pristine SWCNT(10,0) the energy band gap decreases from 0.8 eV to c.a. 0.45 eV for the spin-up band due to the apperance of new dispersive half-filled band. At the same time, the new low-dispersive half-filled band close to the Fermi level is introduced. There is also reorganization of some bands at c.a. -1– -2 eV and 1–2 eV because of the breaking of the mirror symmetry of the carbon nanotube. The attachment of carboxyl group

to SWCNT(V) and the saturation of the two-coordinate carbon atom from the defect causes a significant shift down to the Fermi level. The spin-down band close to the Fermi level is more dispersive. The electronic band structure for SWCNT(2V) system changes after carboxylation too. The bands close to the Fermi level start to be less dispersive, but more splitted than the original ones. Moreover, some additional bands close to Fermi level appears. As a result, it can be stated that carboxylation of the defective SWCNTs induces different changes in the electronic band structure, therefore, the change of the electronic properties.

The properties of CNTs are changed because of the atom reorganization on the surface due to the formation of the defective regions or the attachment of the functional groups, e.g. COOH. The structural changes of the SWCNTs induce different behavior of the molecules attached, for example diisocyanates. Such changes are relatively small in the nanoscale, but might have huge effects on the macroscopic properties of the composites, e.g. transfering of the electronic properties, enhancement of the mechanical properties etc. To show the structural changes of the diisocyanate molecules attached as a result of the defect introduction to SWCNT, the further MD simulations were performed.

11.3 Structural rearrangements of diisocyanates on SWCNT with defects

Carbon nanotubes with the defective regions are very likely to be formed before their usage for the concrete purpose. They are several times more reactive than the pristine nanotubes. It means that during the carboxylation process of the mixture of SWCNTs with different structure of the sidewall, defective carbon nanotubes are the first to react with the attachment of the COOH group. Later, carboxylated SWCNTs are used to attach diisocyanate molecules, e.g. MDI or TDI, to increase the CNT dispersity in the polymer solution. Different arrangement of the attached MDI and TDI is possible on the pristine and defective carbon nanotubes. What is the influence of the defective regions on the SWCNT sidewall on the structural rearrangement of the attached MDI and TDI? To understand it, two defective SWCNTs with different reactivity were chosen as a model of the CNT sidewall. They are the vacancy- and divacancy(5-8-5)-defective SWCNT(10,0).

11.3.1 Static DFT calculations

The most reactive defective structures of the carboxylated single-walled carbon nanotubes, i.e. structures **V-1** and **2V-1** from Figure 11.4 and Figure 11.5, were used to obtain the corresponding TDI and MDI modified carbon nanotubes. For better comparison of the results, the previously described structures of TDI- and MDI-modified SWCNT(10,0), as a result of the covalent functionalization (see Section 10.1), are also given. The optimized structures of the TDI attachment to different SWCNT surfaces are depicted in Figure 11.10, whereas the structures of MDI covalently attached to SWCNTs are shown in Figure 11.11. All systems were optimized with the usage of PBE functional with Grimme D2 dispersion correction, which were explained in detail in Section 7.1. The binding energy, E_{bind}, was calculated using Equation 7.2 from Section 7.2.1, where it is the difference between the total energy of the supercell of the defective/defect-free SWCNT(10,0)–TDI/MDI system and the sum of the energy of the supercell for the defective/defect-free carbon nanotube and the isolated –CONH–TDI'/–CONH–MDI', where TDI' or MDI' means the modified TDI and MDI molecules as a result of the urethane bond formation. Negative value of the binding energy means that the process of covalent functionalization is energetically favorable.

Similarly as for the reactivity of the defective carbon nanotubes, during the carboxylation reaction, the vacancy defective region is approximately 1.8 and 4.2 times more reactive than

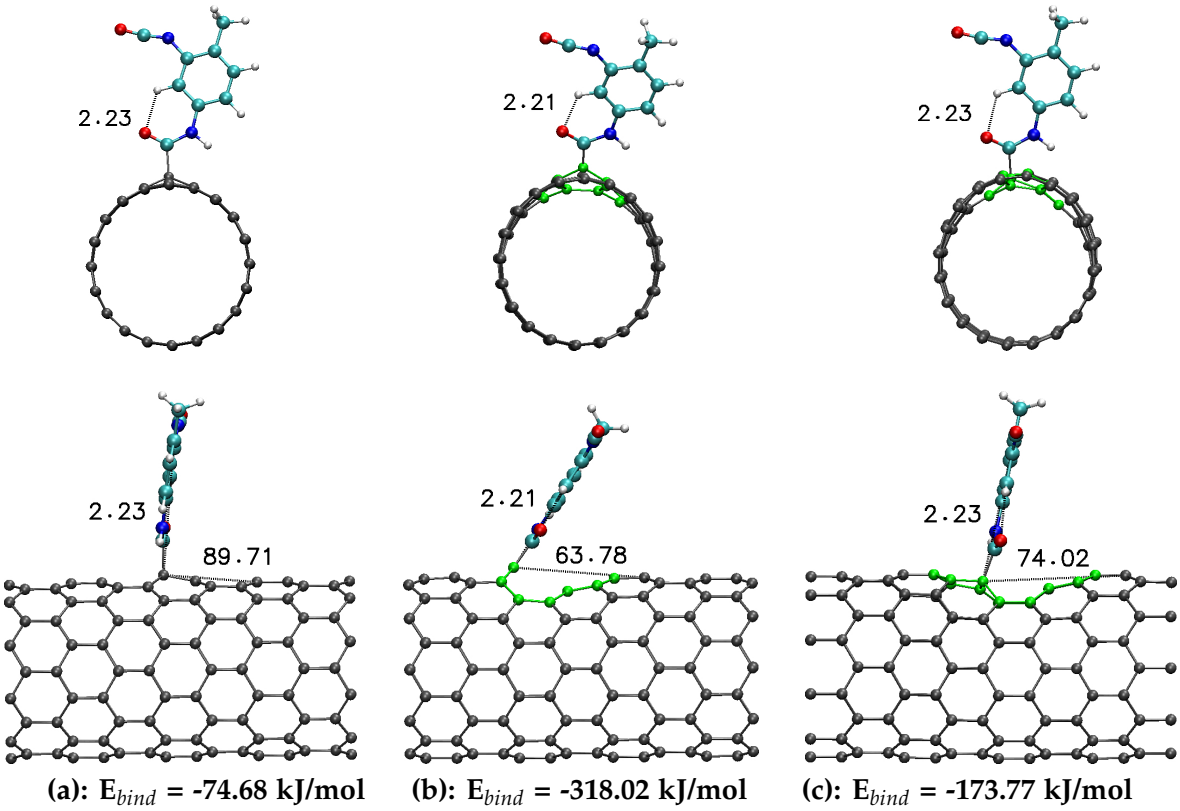

Figure 11.10: Optimized geometries of the global minimum structures (profile view and side view) of the TDI molecule covalently attached to (a) pristine SWCNT(10,0) and (b) vacancy-defective SWCNT(10,0) and (c) divacancy-defective SWCNT(10,0). The defective region is marked with the green color. The C-H$\cdots$O hydrogen bond and $\angle(\mathrm{CCC}_{TDI})$ inclination angle are marked with the dashed lines and are given with their corresponding values.

the divacancy(5-8-5)-SWCNT and pristine SWCNT, respectively. The binding energy for the vacancy-defective SWCNT(10,0) is c.a. -318 – -319 kJ/mol, while for the pristine SWCNT(10,0) it is c.a. -74 – -75 kJ/mol. For both diisocyanates the energy of the urethane bond attachment is very close within each type of the SWCNT surface. The influence of the second phenyl ring of the MDI molecule is negligible. That is why, the structural changes, due to the TDI and MDI attachment, are similar for the specific type of carbon nanotube (see Table 11.2). The vacancy defect is so reactive, because the carbon atom from the carbon nanotube, which participates in the molecule binding, is two-coordinated and have a great tendency to form a bond. Moreover, the bond formed is shorter than the traditional single carbon-carbon bond: the length of C_{CNT}–C' is c.a. 1.46–1.47 Å for SWCNT-V, while for other systems analyzed it is c.a. 1.59–1.60 Å. The lengths of the C_{CNT}–C' bond in pristine and divacancy-defective systems are close and are originated from the sp^3 hybridization of the carbon atom, but the way of the sp^3 hybridization in both cases is different. There are almost the same $(CCC)_{CNT}$ angles (108.0°, 112.9° and 113.2°) around the C_{CNT} atom with the similar lengths of the carbon–carbon bond in the attachment site, i.e. 1.52 Å, which form traditional hybridization of the C_{CNT} atom. In the case of the divacancy-defective SWCNT, the values of the $(CCC)_{CNT}$ angles around C_{CNT} atom vary in the higher extent and are 110.8°, 100.0° and 119.9° with different carbon–carbon lengths in the range of 1.52–1.57 Å. Therefore, the geometry of the sp^3-hybridized C_{CNT} atom is different in the case of the pristine and divacancy-defective SWCNT(10,0) systems.

As a result of higher reactivity of vacancy defect, the molecule attached, both TDI and MDI, changes its position on the surface of CNT: instead of the perpendicularly-like position (on

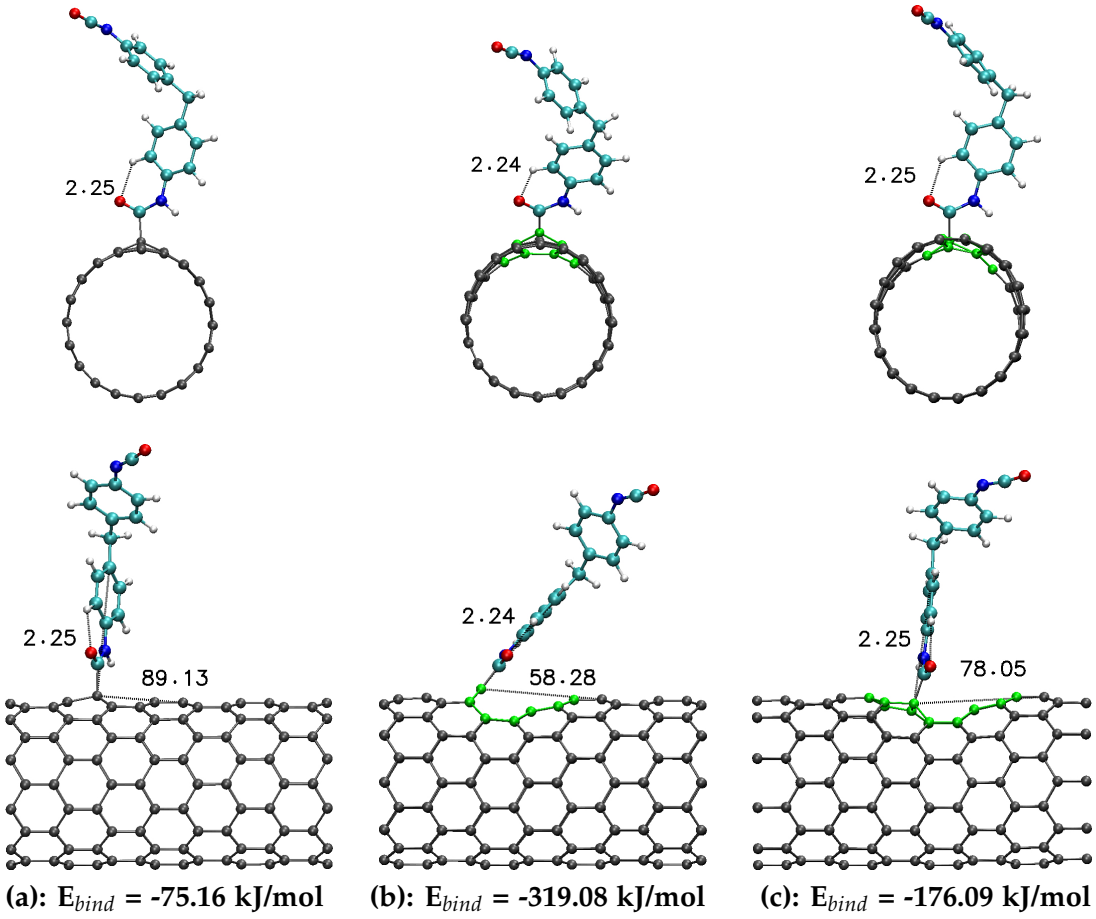

Figure 11.11: Optimized geometries of the global minimum structures (profile view and side view) of the MDI molecule covalently attached to (a) pristine SWCNT(10,0) and (b) vacancy-defective SWCNT(10,0) and (c) divacancy-defective SWCNT(10,0). The defective region is marked with the green color. The C-H$\cdots$O hydrogen bond and $\angle(\mathrm{CCC}_{MDI})$ inclination angle are marked with the dashed lines and are given with their corresponding values.

pristine SWCNT), the molecule has a significantly different inclination angle in the range of 51–52° (see structures with label **(b)** in Figure 11.10 and Figure 11.11). The $\angle\mathrm{CCC}_{TDI/MDI}$ inclination angle was mentioned in Section 10.3, when the structural rearrangements of diisocyanates covalently attached to pristine SWCNT were analyzed. It is formed from three carbon atoms: two from the surface of the CNT and the third originated from the central carbon atom in the first phenyl ring attached to the surface. The corresponding values of the inclination angle are given in each of the structure shown with the additional dashed line for the transparent analysis. The inclination angle is decreasing (molecule is positioned closer to the defect site) with the increase of the SWCNT reactivity: 51–52° $\rightarrow$ 77–78° $\rightarrow$ 89–90°, consequently for SWCNT-V, SWCNT-2V and pristine SWCNT (see Table 11.2). The change of the $\angle\mathrm{CCC}_{TDI/MDI}$ angle from 90° to 51° decreases the dispersion of the carbon nanotubes, because of higher packing of the molecules attached and the decrease of "buffer" layer between the neighbor CNT. This small structural difference might be of great importance on the macroscopic properties of the material.

The same as it was for the covalent attachment of diisocyanates to pristine SWCNT, for the defective SWCNTs no intermolecular $\pi - \pi$ interactions between the MDI phenyl rings and the CNT surface are possible. Both diisocyanate molecules are highly planar in the regions of the phenyl ring connected to CNT. The values of the C-C-N-C dihedral angle, which is formed from the C atom at the attachment site and C-N-C atoms from the attached molecule,

Table 11.2: List of structural differences between TDI and MDI molecules covalently attached to pristine and defective (vacancy and divacancy) SWCNT(10,0): the values of the binding energy, E_{bind}, the length of the carbon-carbon bond formed between the C atom from SWCNT (C_{CNT}) and the C atom from the attached molecule (C'), C_{CNT}–C', the $\angle(CCC_{TDI/MDI})$ mentioned as inclination angle, the C-C-N-C dihedral angle between the attached molecule and the CNT surface, and the C-C-N-C dihedral angle between the TDI/MDI phenyl ring and the NCO group.

Label	$\mathbf{E_{bind}}$ [kJ/mol]	$\mathbf{C_{CNT}}$–C' [Å]	$\angle$**(CCC$_{TDI/MDI}$)** [°]	**C-C-N-C** [°]	**C-C-C-N$_{NCO}$** [°]
SWCNT(10,0)–TDI	-74.68	1.602	89.7	169.93	0.03
SWCNT(10,0)-V–TDI	**-318.02**	**1.469**	**52.8**	**178.69**	**-0.22**
SWCNT(10,0)-2V–TDI	-173.77	1.595	78.4	173.07	-2.24
SWCNT(10,0)–MDI	-75.16	1.605	89.1	177.06	0.79
SWCNT(10,0)-V–MDI	**-319.08**	**1.471**	**51.6**	**174.13**	**1.47**
SWCNT(10,0)-2V–MDI	-176.09	1.598	77.0	169.02	0.67

is close to the linear one (see Table 11.2), indicating the planar orientation of the urethane bond and the phenyl ring with no $\pi - \pi$ interactions with the surface. The second phenyl ring of the MDI molecule acquires the characteristic to the gas phase orientation with respect to the first phenyl ring with the $\angle$(CCC) valence angle between the phenyl ring of 115.32° and 114.96° for the vacancy- and divacancy-defective system (the corresponding value for the gas phase is 113.79°). At the same time, the C-C-C-C dihedral between the aromatic rings is changing from -130.37° (gas-phase MDI) to -87.80° (SWCNT-V) and -109.83° (SWCNT-2V).

Similarly to the covalently attached diisocyanates to the pristine SWCNT (see Section 10.1), in the case of defective CNTs the intramolecular C-H$\cdots$O hydrogen bond is also formed between the oxygen atom from the -CO-NH- group and the closest hydrogen atom from the phenyl ring of the TDI/MDI molecule. It is marked in the structures depicted. The H$\cdots$O distances, i.e. 2.21 – 2.25 Å, are almost the same for all systems studied. Finally, free isocyanate group has no possibility to interact with the CNT surface, because of the distance criterium, that is why, it is not deformed from the co-planarity with the phenyl ring (see Table 11.2), as it was reported for the noncovalently modified SWCNTs.

11.3.2 CP–MD simulations of diisocyanates covalently attached to vacancy-defective SWCNT

The DFT static calculations confirmed that the geometrical parameters of both TDI and MDI molecules, attached to the specific carbon nanotube, are very similar. Therefore, it can be suggested that the influence of the second phenyl ring is insignificant. Taking into consideration the most stable SWCNT(x)-TDI and SWCNT(x)-MDI structures (where x denotes that the carbon nanotube is defective), the CP–MD simulations at 300 K were performed with the usage of the same computational set-up as it was for the pristine SWCNT (for details see Section 7.1). From the *dynamics* of the system during 10 ps, the most characteristic structures were selected. They are depicted in Figure 11.12 and Figure 11.13, where the time evolution of the structural rearrangements of TDI and MDI on vacancy-defective SWCNT(10,0) is shown with the corresponding timestamp.

The first noticable feature of the attached molecules is the position with respect to the carbon nanotube. Both molecules are attached on perpendicularly-like position on the pristine SWCNT (see Figure 10.8), but after the vacancy defect formation, the inclination of

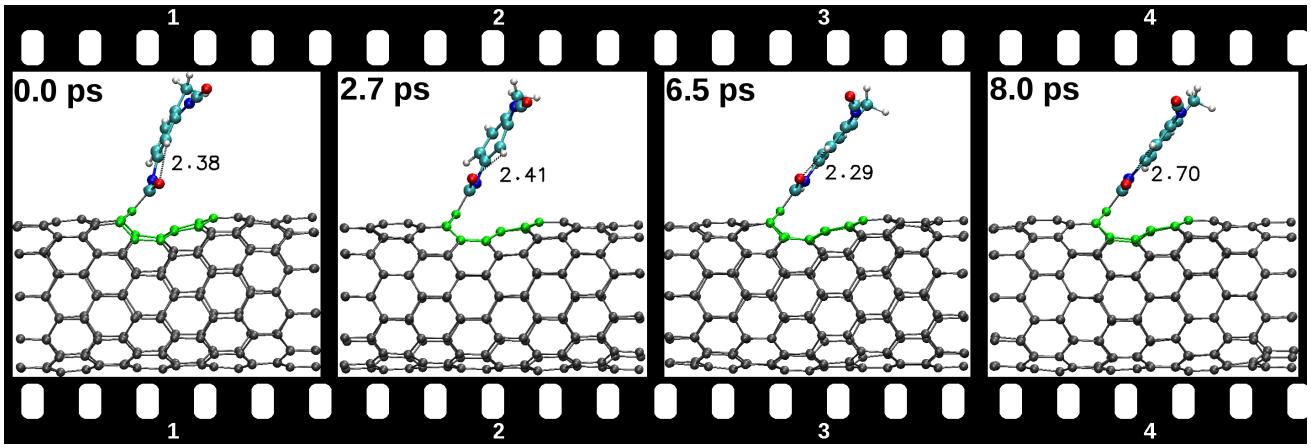

Figure 11.12: Time evolution of the TDI structural rearrangements on vacancy-defective SWCNT(10,0) after the covalent functionalization. Defective region is marked with the green color. C-H···O hydrogen bond is marked with the dashed line.

the molecules on the surface changes strongly. Instead of the perpendicular position, the attachment at the inclination angle of c.a. 50°–70° is seen. As it was explained above, the inclination angle was measured using three carbon atoms, which denote the attachment of the molecule on the surface. As a result of the continuous movement of the molecules, the angle of inclination is changing around the value of c.a. 52°, which was reported during the static calculations (see Table 11.2).

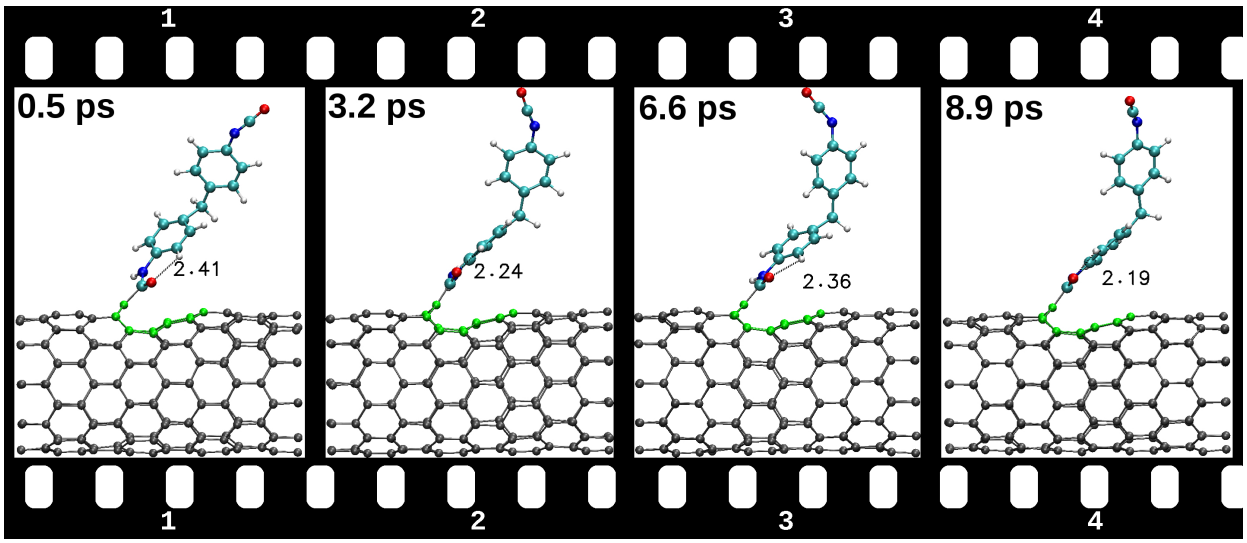

Figure 11.13: Time evolution of the MDI structural rearrangements on vacancy-defective SWCNT(10,0) after the covalent functionalization. Defective region is marked with the green color. C-H···O hydrogen bond is marked with the dashed line.

The time evolution of the inclination angle is shown in the upper panel in Figure 11.14, where the plots of the structural changes of both systems are given together to estimate the influence of the second phenyl ring. Similarly as it was reported for the diisocyanate attachment to the pristine carbon nanotube (see Section 10.3), the inclination angle depends on the position of the plane of the phenyl ring with respect to the nanotube axis: parallel or perpendicular. That is why, every deformation of the plane of the phenyl ring from the perpendicular position, with respect to the CNT axis, can be detected: the increase of the inclination angle corresponds to more parallel position (see snapshot "1" in Figure 11.13).

In comparison to the attachment to the pristine carbon nanotubes, there is no fully parallel position of the plane of the phenyl ring on the vacancy defective surface. Most of the time the molecule attached is positioned in the perpendicular plane position, which is seen in the snapshot "1" , "3", "4" in Figure 11.12 and "2", "4" in Figure 11.13. The change of the inclination angle is smoother with slight deformations from the perpendicular position of the plane of the phenyl ring. Moreover, the *dynamics* of the inclination angle is different for TDI and MDI molecules. The inclination angle of phenyl ring of the TDI molecule is changing in the range of 57°–72°, while of the covalently attached phenyl ring of the MDI molecule is changing in the range of 48°–62°. That is why, the effect of the second phenyl ring on the inclination angle is present and it stabilizes the molecule to be positioned closer to the defect site.

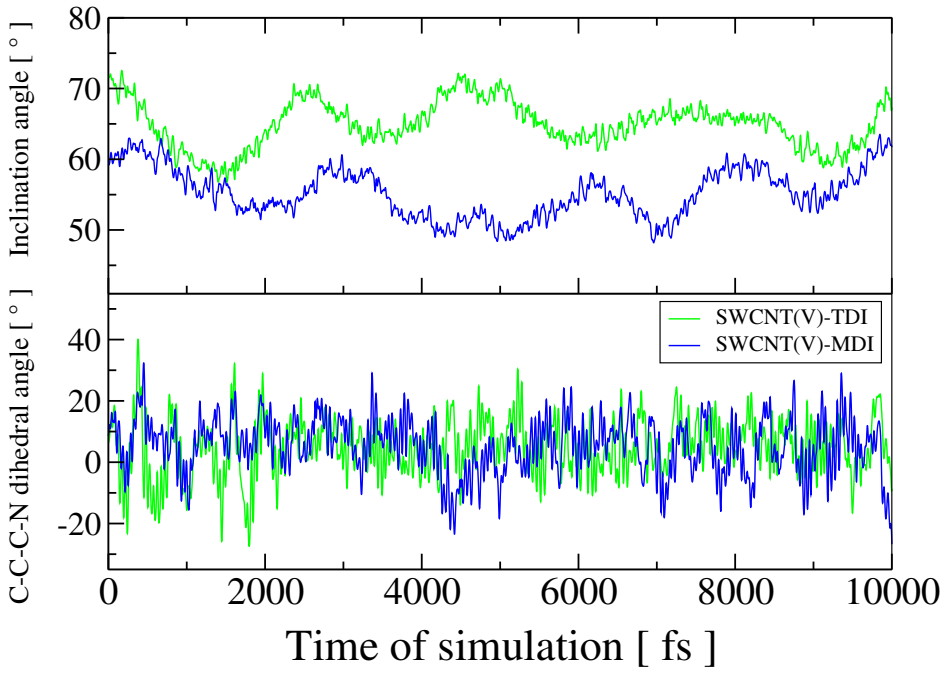

Figure 11.14: *Dynamics* of the structural parameters: inclination angle (upper panel) and rotation angle (C-C-C-N dihedral angle, lower panel), of diisocyanate molecules covalently attached to the vacancy-defective carbon nanotube. The plots for the TDI an MDI molecules are marked in green and blue colors, respectively.

Even if the values of the inclination angle in the static calculations are similar (see Table 11.2), the MD simulations show that the real behavior of the molecules is different. Due to the presence of the second phenyl ring, additional weak C-H$\cdots\pi$ interaction between the phenyl rings is possible. This intramolecular interaction stabilizes the position of the phenyl ring, which is directly connected to SWCNT, maximizing the π-contact between the aromatic rings. The formation of C-H$\cdots\pi$ hydrogen bond can be seen in snapshot "2", "3" and "4" in Figure 11.13. C-H$\cdots\pi$ hydrogen bond, which formation was confirmed during the gas-phase calculations for the MDI molecule, is extremely stable during the simulation time of 10 ps. Its formation was measured as the H$\cdots$C distance between the hydrogen atom from the C-H bond from the upper aromatic ring and the two carbon atoms from the lower aromatic ring (see Figure 11.13), located in the close vicinity to the C-H bond. The time evolution of two H$\cdots$C distances, corresponding to the formation of C-H$\cdots\pi$ hydrogen bond is shown in Figure 11.15. The red dashed line indicates the limit of the distance between the atoms, when the formation of the traditional H-bond is considered to take place. The lifetime of weak π-interactions between the MDI phenyl rings is in the range of 0.7–1.7 ps, which is significantly longer than the lifetime of C-H$\cdots\pi$ hydrogen bond formed during the MDI attachment

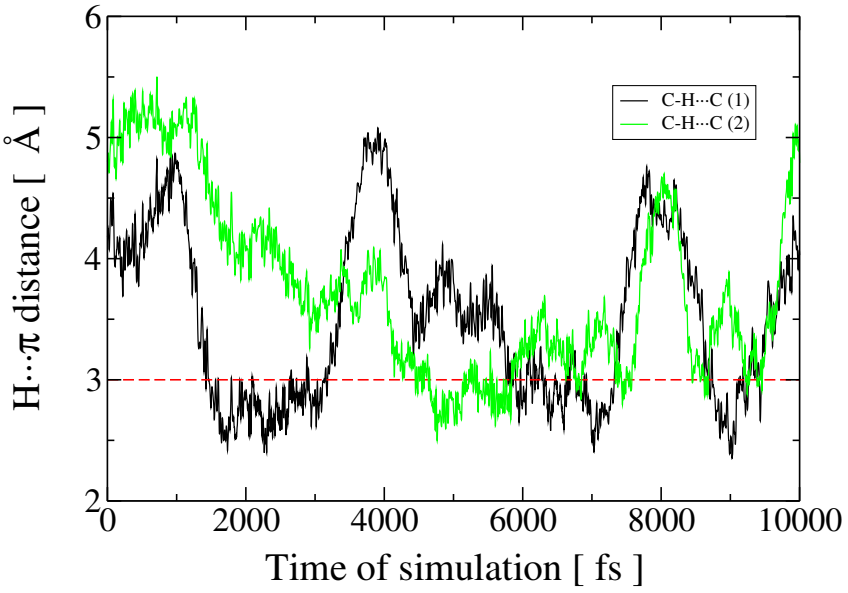

Figure 11.15: Time evolution of the H$\cdots\pi$ distance from the C-H$\cdots\pi$ hydrogen bond in the vacancy-defective SWCNT-MDI system, obtained from a CP–MD run. H$\cdots\pi$ distances correspond to the distance between the hydrogen atom from a H-bond donor and the closest carbon atoms from the second phenyl ring.

to the pristine SWCNT(10,0), shown in Figure 10.11. Moreover, C-H$\cdots\pi$ hydrogen bond is more stable and frequently formed during the MD simulation of the vacancy-defective SWCNT.

The second important structural feature of the molecules attached is the rotation angle, i.e. C-C-C-N dihedral angle, which is shown in snapshot "1" in Figure 10.7 and snapshot "2" in Figure 10.8. The rotation angle denotes the rotation of the phenyl ring, directly connected to the SWCNT, with respect to the surface. The time evolution of the C-C-C-N dihedral angle is similar for both diisocyanate molecules (see lower panel in Figure 11.14). Both molecules rotates maximally on c.a. 40° with respect to the CNT surface. Therefore, the influence of the presence of the vacancy defect has the same effect on the rotation of the molecules.

The vacancy defect on the surface of SWCNT(10,0) has a strong influence on the attachment site of the covalently bonded diisocyanate molecules. The angle of inclination is descreasing from c.a. 100°, for pristine carbon nanotube, to c.a. 52°, for the vacancy-defective SWCNT. At the same time, the rotation of the molecules is suppressed with the strong interaction with the electron density located within the vacancy defect. The intramolecular C-H$\cdots$O hydrogen bond behaves similarly as for the previously analyzed systems, steering the rotation of the molecule. Suppressed rotation of the phenyl rings of diisocyanates on vacancy-defective SWCNT indicates that the oxygen atom from the urethane bond interacts with the highly reactive defective region. The decreased angle of the rotation of the MDI molecule, with respect to the surface, enables more possible and stable formation of weak C-H$\cdots\pi$ hydrogen bonds between the phenyl rings, which additionally suppresses the movement of the molecule attached.

11.3.3 CP–MD simulations of diisocyanates covalently attached to divacancy-defective SWCNT

The selected snapshots of the structural rearrangements of diisocyanate molecules on divacancy-defective(5-8-5) SWCNT(10,0) are shown in Figure 11.16 and Figure 11.17. In comparison to the previously described, vacancy-defective system, the molecules attached to divacancy-defective carbon nanotube are less detained with more dynamical changes. Moreover, both

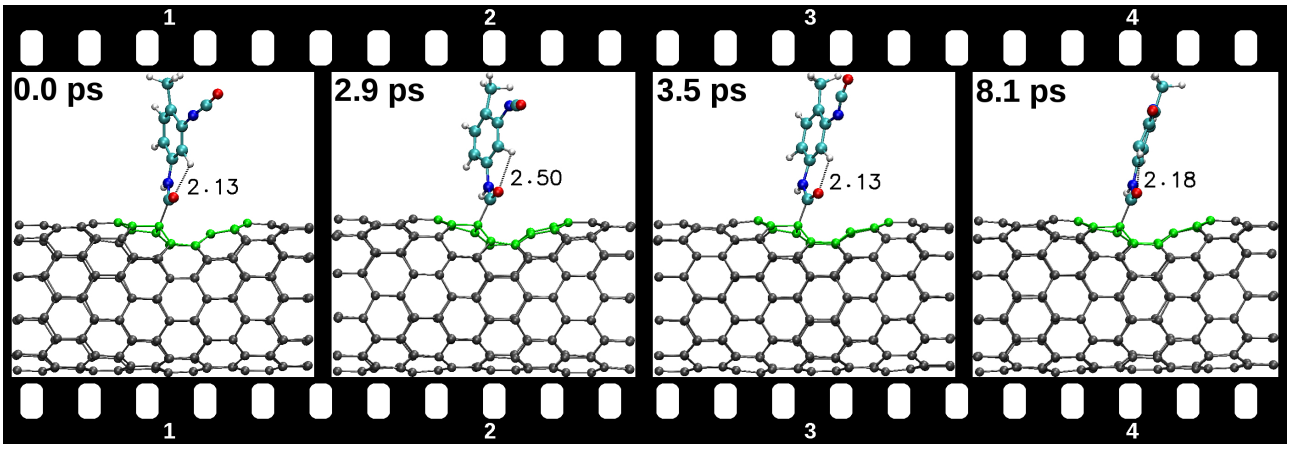

Figure 11.16: Time evolution of the TDI structural rearrangements on divacancy-defective SWCNT(10,0) after the covalent functionalization. Defective region is marked with the green color. C-H···O hydrogen bond is marked with the dashed line.

diisocyanates are attached in the position close to the molecules on pristine SWCNT, i.e. more perpendicular to the surface, than to the molecules on vacancy-defective SWCNT. The inclination angle of TDI and MDI is changing in the different way, which is depicted in the upper panel in Figure 11.18. Overall, the inclination angle of the TDI molecule is in the

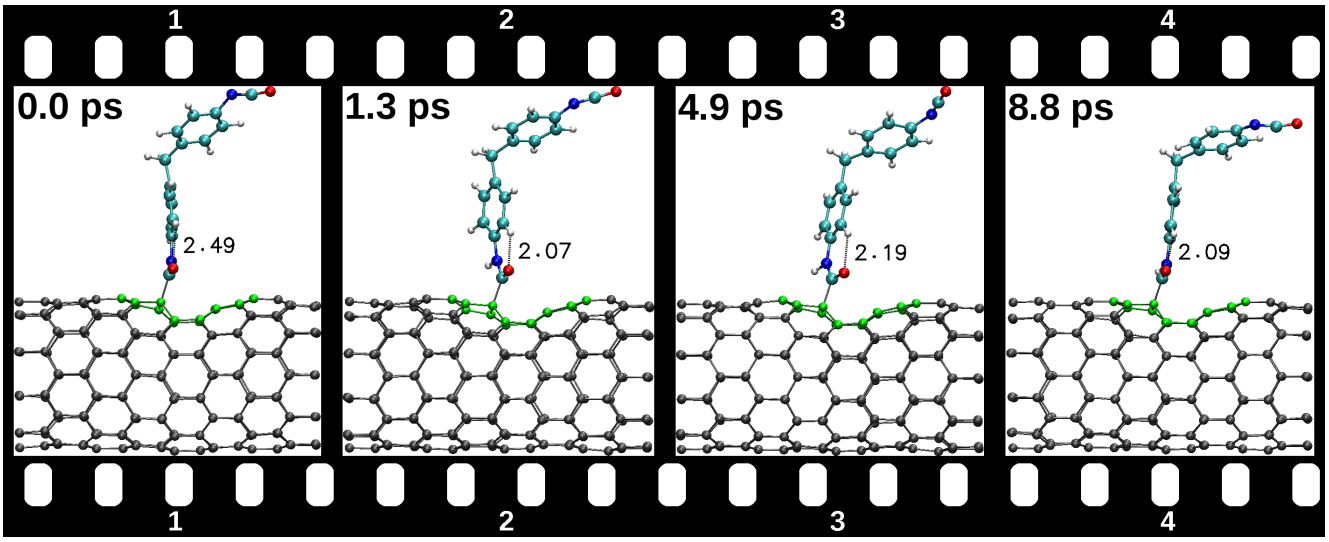

Figure 11.17: Time evolution of the MDI structural rearrangements on divacancy-defective SWCNT(10,0) after the covalent functionalization. Defective region is marked with the green color. C-H···O hydrogen bond is marked with the dashed line.

range of 63°–82°, while for the MDI molecule is in the range of 67°–89°. Higher values of the inclination angle in the case of MDI attached are connected to more significant rotation of the MDI phenyl rings. From the plots corresponding to the changes of the inclination angles of the TDI and MDI molecules (see upper panel in Figure 11.18) it can be seen that in both cases the inclination angle is gradually decreasing to some value (63° and 67° for TDI and MDI molecules, respectively) and then increasing to more constant value of c.a. 78°, which is close to the value of the C-C-C-N dihedral angle obtained due to the static calculations (see Table 11.2). Such changes are connected with the approaching of the molecule attached to the defect region and the formation of the interactions with the defect similar to the vacancy-defective carbon nanotube.

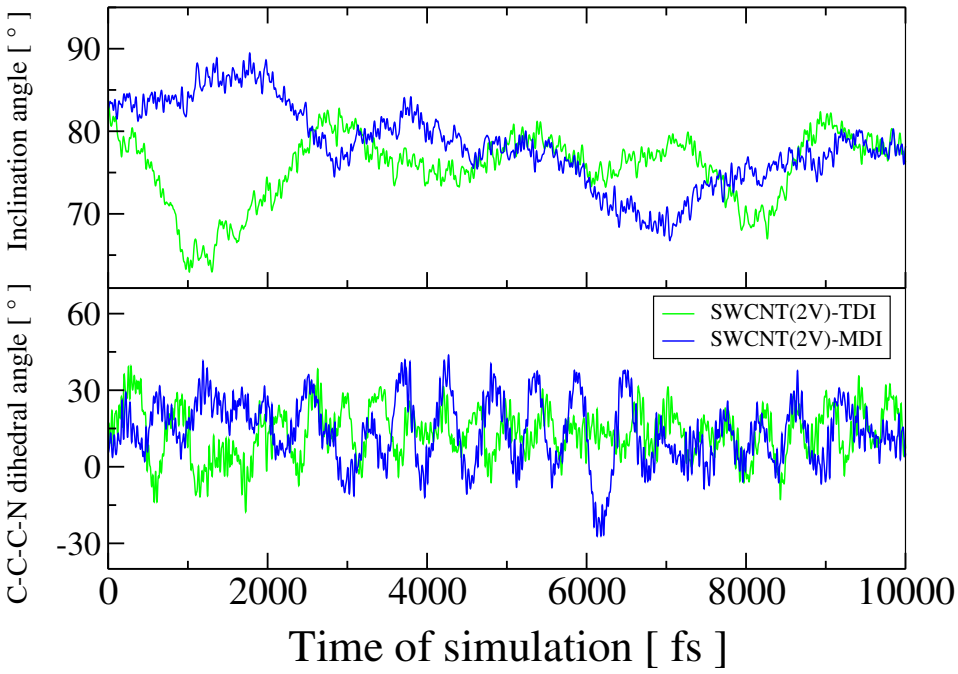

Figure 11.18: *Dynamics* of the structural parameters: inclination angle (upper panel) and rotation angle (C-C-C-N dihedral angle, lower panel), of diisocyanate molecules covalently attached to the divacancy-defective carbon nanotube. The plots for the TDI an MDI molecules are marked in green and blue colors, respectively.

As a result of different structural reorganization due to the defect formation, therefore, different distribution of the electron density within the defect (see Figure 11.3), the position of the molecule at low inclination angle, similar to the vacancy-defective system, is not stable, thus the molecules attached prefer to stay in more perpendicular position (Figure 11.16, Figure 11.17). Even if MDI is larger that TDI, in the case of the divacancy-defective system it

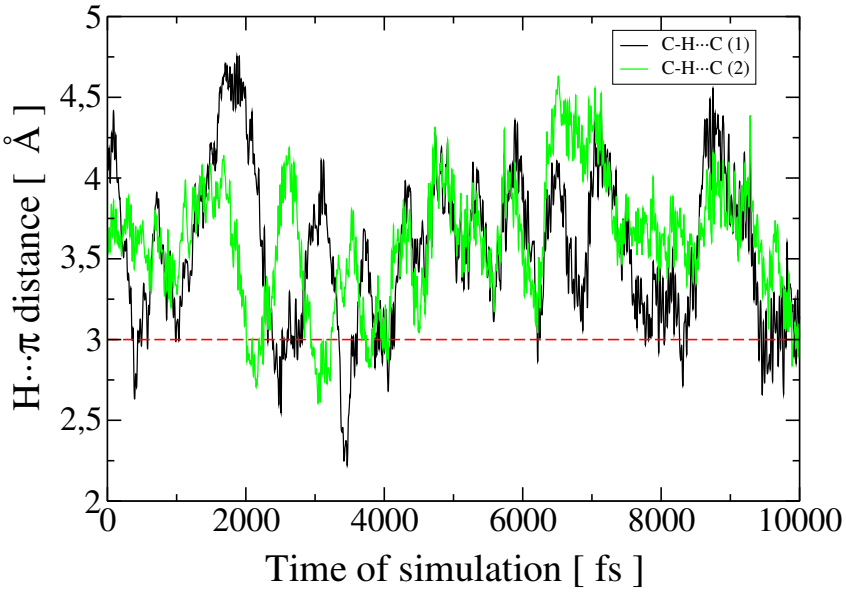

Figure 11.19: Time evolution of the H$\cdots\pi$ distance from the C-H$\cdots\pi$ hydrogen bond in the divacancy-defective SWCNT-MDI system, obtained from a CP–MD run. H$\cdots\pi$ distances correspond to the distance between the hydrogen atom from a H-bond donor and the closest carbon atoms from the second phenyl ring.

is more active than the TDI molecule. It can be confirmed by the plot of the rotation an-

gle, namely C-C-C-N dihedral angle, which is depicted in the lower panel in Figure 11.18. The MDI phenyl ring, which is directly attached to the CNT surface, rotates on c.a. 22°–49°, whereas the rotation of the TDI aromatic ring is of lower amplitude, i.e. on c.a. 30°–32°.

Higher structural *dynamics* of the MDI molecule, in comparison to the vacancy-defective system, is connected to the lack of stable C-H$\cdots\pi$ hydrogen bond between the MDI phenyl rings, which aditionally stabilizes the structure. The time evolution of the H$\cdots$C distances between the C-H hydrogen bond donor and the carbon atoms from the lower phenyl ring are depicted in Figure 11.19. There is only slight possibility for the formation of C-H$\cdots\pi$ hydrogen bond with a short lifetime of 0.2–0.4 ps. The low probability of the hydrogen bond formation can be noticed from the snapshots in Figure 11.17, where the perpendicular-like position od the first phenyl ring unable the intramolecular noncovalent stabilization. The *dynamics* of the molecules attached on divacancy-defective carbon nanotube is in between the pristine SWCNT and vacancy-defective SWCNT. It is connected with the reactivity of the defective surfaces, therefore, the structural reorganization within the defect site.

11.3.4 Defective vs. pristine covalently functionalized SWCNT with diisocyanates

In the previous sections, the description of the dynamical changes of the TDI and MDI molecules attached to different carbon nanotube surfaces were presented. The comparison of the dynamical changes of both molecules within the specific type of the CNT surface was given. To show the differences described in more transparent way, the detailed analysis of the most characteric structural parameters of the molecules attached is summarized here.

Among the characteristic features of the covalently functionalized SWCNT system by aromatic diisocyanates are:

- inclination angle, CCC_{TDI} or CCC_{MDI}, indicating the angle of the attachment of the diisocyanate molecule on SWCNT,
- rotation angle, C-C-C-N dihedral angle, corresponding to the rotation of the phenyl ring with respect to the SWCNT surface,
- intramolecular C-H$\cdots$O hydrogen bond,
- rotation angle, C-C-C-C dihedral angle, corresponding to the mutual rotation of two phenyl ring of the MDI molecule,
- C-H$\cdots\pi$ hydrogen bond between the MDI phenyl rings.

Taking into account the results reported in Section 10.3, the C-C-N-C dihedral, which denotes the deformation of the isocyanate group from the co-planarity with the phenyl ring, is not analyzed here, because there is no evidence for the noncovalent interaction with the participation of the NCO group in the case of the covalent functionalization of CNTs..

Both static DFT calculations and Car–Parrinello MD simulations have shown that the most significant difference between all systems studied is the value of the inclination angle of the molecules covalently attached to the CNT surface. The most perpendicular-like position of the molecules on the surface characterizes the pristine SWCNT-TDI and SWCNT-MDI systems. The values of the inclination angle in these systems is in the range of 82°–107° and 98°–111° for TDI and MDI attached, respectively. The time evolution of the inclination angle in the pristine-based systems in depicted with the black curve in Figure 11.20 and Figure 11.21. Due to smaller size of the TDI molecule and its more free movements, the inclination angle is changing in higher extend in the case of the SWCNT-TDI system, therefore, the amplitute of the change is higher. Moreover, the change of the inclination angle is connected to the position of the plane of the phenyl ring with respect to the nanotube axis. If the plane is parallel to the CNT axis (as in the snapshot ”2” in Figure 10.7), the inclination angle

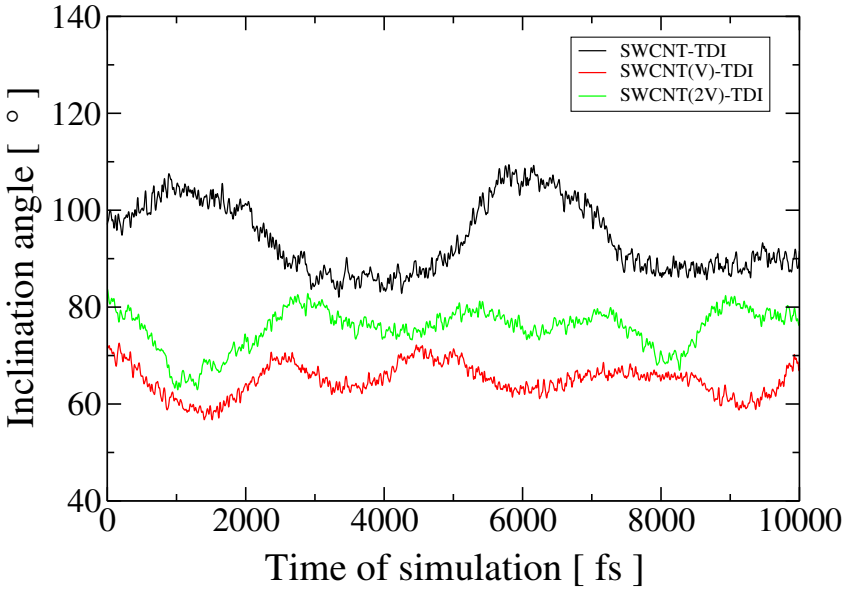

Figure 11.20: Time evolution of the CCC_{TDI} inclination angle of the TDI molecule covalently attached to the pristine (black curve), vacancy-defective (red curve) and divacancy-defective (green curve) SWCNT(10,0) surfaces obtained from a CP–MD run.

has higher values (lower inclination to the CNT surface) than in the case of the perpendicular position of the phenyl ring plane (as in the snapshot "1" in Figure 10.7).

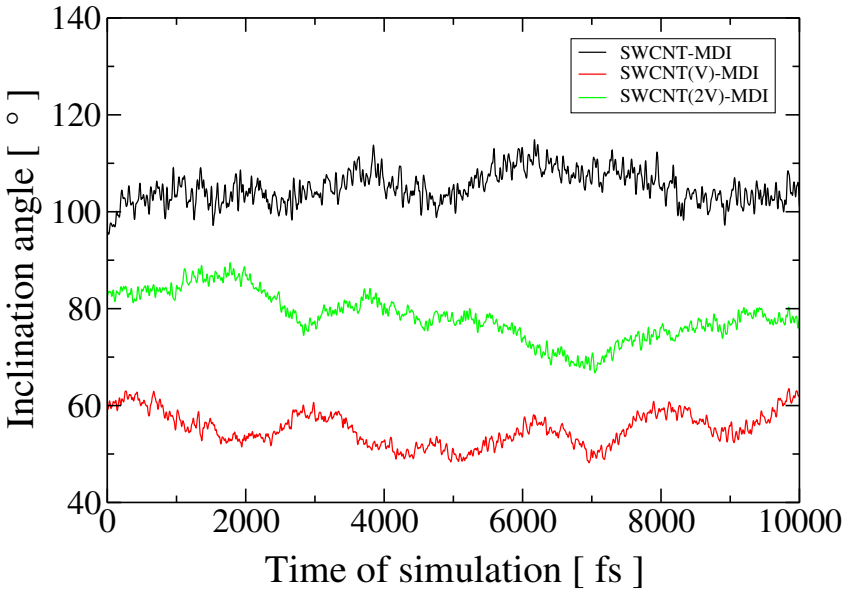

Figure 11.21: Time evolution of the CCC_{MDI} inclination angle of the MDI molecule covalently attached to the pristine (black curve), vacancy-defective (red curve) and divacancy-defective (green curve) SWCNT(10,0) surfaces obtained from a CP–MD run.

The highest change of the inclination angle is observed in the case of the vacancy-defective SWCNT surface (red curves in Figure 11.20 and Figure 11.21). The diisocyanate molecule is approaching to the CNT surface as a result of strong interaction between the oxygen atom from the urethane bond and the π-density localized around the defect region. As a result, the inclination angle changes from c.a. 100° in case of the pristine systems to c.a. 60° and c.a. 50° for the SWCNT(V)-TDI and SWCNT(V)-MDI systems. It was shown in the previously

depicted snapshots from the CP–MD run (Figure 11.12 and Figure 11.13). In the case of the divacancy(5-8-5)-defective system, the inclination angle is lower than for the pristine SWCNT, but higher than for the vacancy-defective SWCNT (green curves in Figure 11.20 and Figure 11.21). The inclination of the molecules attached depends significantly on the reactivity of the surface of the carbon nanotube: the higher reactivity of the surface, the lower value of the inclination angle (higher inclination).

The second parameter analyzed is the rotation angle specified in the present PhD thesis as the change of the C-C-C-N dihedral angle. The dynamical changes of the C-C-C-N dihedral angle of the TDI and MDI molecules, during the simulation time of 10 ps, are shown in Figure 11.22 and Figure 11.23, respectively. From the mentioned figures it can be seen that there are large differencies in the range of the rotation of the phenyl ring of the diisocyanates attached to different surfaces. The rotation angle of the TDI and MDI on the defect-free

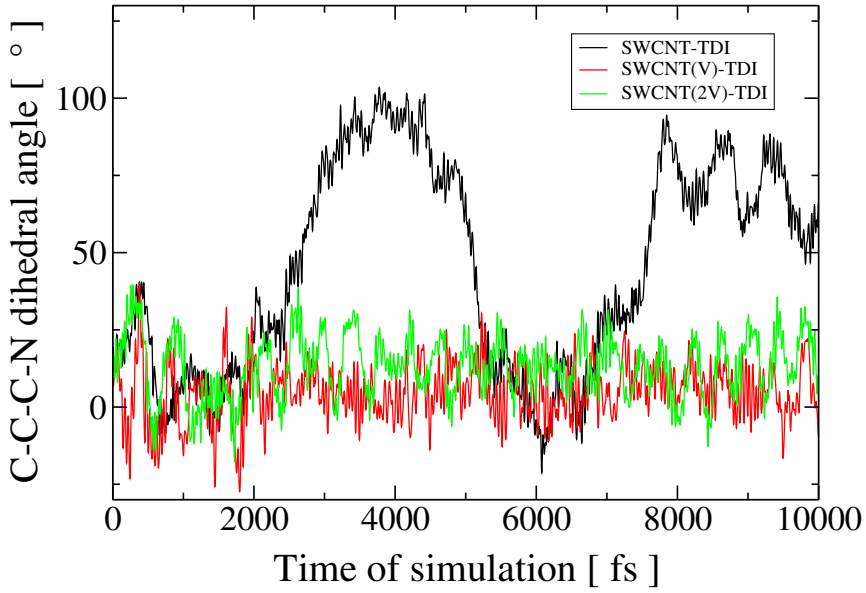

Figure 11.22: Time evolution of the C-C-C-N dihedral angle (rotation angle) of the TDI molecule covalently attached to the pristine (black curve), vacancy-defective (red curve) and divacancy-defective (green curve) SWCNT(10,0) surfaces obtained from a CP–MD run.

SWCNT(10,0) is much larger than for the defective SWCNT(10,0) systems, for example the phenyl ring of the TDI molecule rotates maximally on 102°, while the phenyl ring of the MDI molecule has two main cyclic rotations with the maximum range of 92°. For both defective CNT systems with the covalently attached diisocyanates, the suppression of the rotation of the phenyl ring is observed. The maximum angle of the rotation is c.a. 42° and 54° for vacancy- and divacancy-defective surfaces. It might be connected to more stable position of the oxygen atom from the urethane bond, which strongly interacts with the π-electron density of the vacancy/divacancy defect.

The *dynamics* of the inclination and rotation angle strondly depends on the existence of C-H$\cdots$O hydrogen bond between the oxygen atom from the urethane bond as the proton acceptor and the H atom from the phenyl ring as the proton donor. C-H$\cdots$O hydrogen bond belongs to weak NCI interactions, but in the systems analyzed it has a limited geometry, which cause that this bond exists during the whole simulation time and it is a strong one. The existence of C–H$\cdots$O H-bond was also confirmed after the DFT static calculations of all SWCNT systems functionalized by diisocyanates. The detailed analysis of the *dynamics* of this H-bond indicates that the phenyl ring, attached to the surface, directly mimics the movement of the oxygen atom. Therefore, if the movement of the O atom is suppressed,

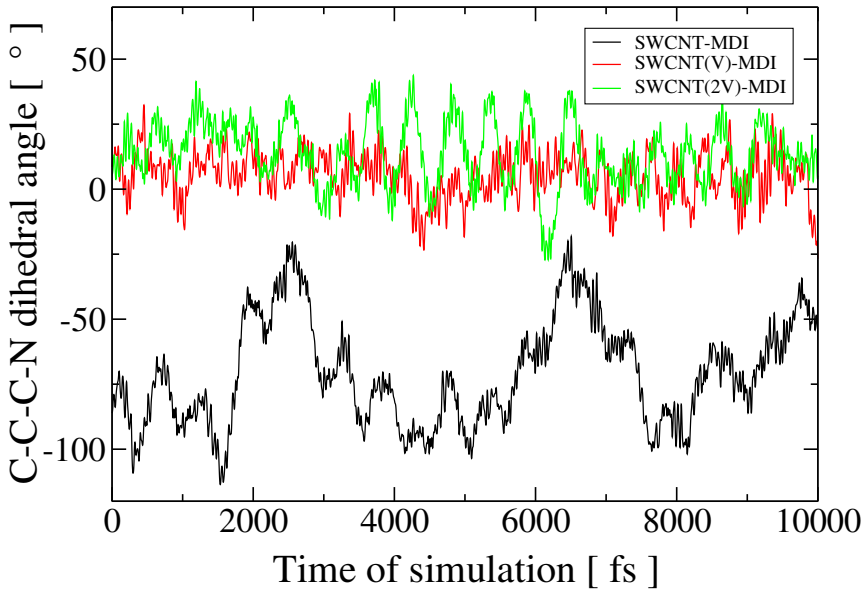

Figure 11.23: Time evolution of the C-C-C-N dihedral angle (rotation angle) of the MDI molecule covalently attached to the pristine (black curve), vacancy-defective (red curve) and divacancy-defective (green curve) SWCNT(10,0) surfaces obtained from a CP–MD run.

the whole molecule has a suppressed rotation. The average length of the H$\cdots$O distance, obtained using the radial pair distribution function, during the whole simulation time of 10 ps is 2.26 Å for all systems examined. This value is similar to those obtained from the static calculations, i.e. 2.21–2.25 Å. The full range of the H$\cdots$O distances during the MD run is 1.85–2.85 Å.

Apart from the stable C–H$\cdots$O H-bond between the C-H group from the phenyl ring and urethane bond, the formation of weak temporary C–H$\cdots$O H-bond between the H atom from the CH_3 group of the TDI molecule and the O atom from the NCO group occurs. It occurs only in the case of the attachment to pristine and vacancy-defective SWCNT(10,0), see snapshot "4" in Figure 10.7. This intramolecular hydrogen bond is weak with the average H$\cdots$O length and $\angle$(CHO) angle of 2.55 Å and 110°, respectively. Its lifetime is in the range of 0.1–0.3 ps and 0.06–0.08 ps for the pristine and vacancy-defective SWCNT(10,0), respectively.

The last structural parameter described corresponds only to the MDI molecule, which has an additional phenyl ring, which *dynamics* can be also changed as a result of the covalent attachment to the surface. The previously reported data of the CP–MD simulations of gas-phase MDI molecule (see Section 8.1.2), indicated small twists of the MDI phenyl rings of approximately 40°. It was estimated on the basis of the C-C-C-C dihedral angle between the MDI phenyl rings. After the attachment to the pristine CNT surface, the phenyl rings of the MDI molecule rotate mutually on 140° and 102° in the opposite direction during the time of the simulation of 10 ps (see black curve in Figure 11.24). The angle of rotation of the MDI on SWCNT is higher, because one phenyl ring is suppressed due to the direct attachment to the rigid surface of the carbon nanotube. In case of the attachment to the defective surface and the suppression of the phenyl ring rotation, the additional intramolecular C-H$\cdots\pi$ hydrogen bond is formed. It was described in the previous sections of this chapter. Due to the change of the inclination and rotation angle of the MDI molecule on the defective CNT surfaces, and the C-H$\cdots\pi$ hydrogen bond formation, the direction of the mutual rotation of the MDI phenyl rings is limited only to one direction with the rotation angle equal to 67°–77° and 50°–70° for the vacancy- and divacancy-defective SWCNT(10,0), respectively (see red and green plots in Figure 11.24).

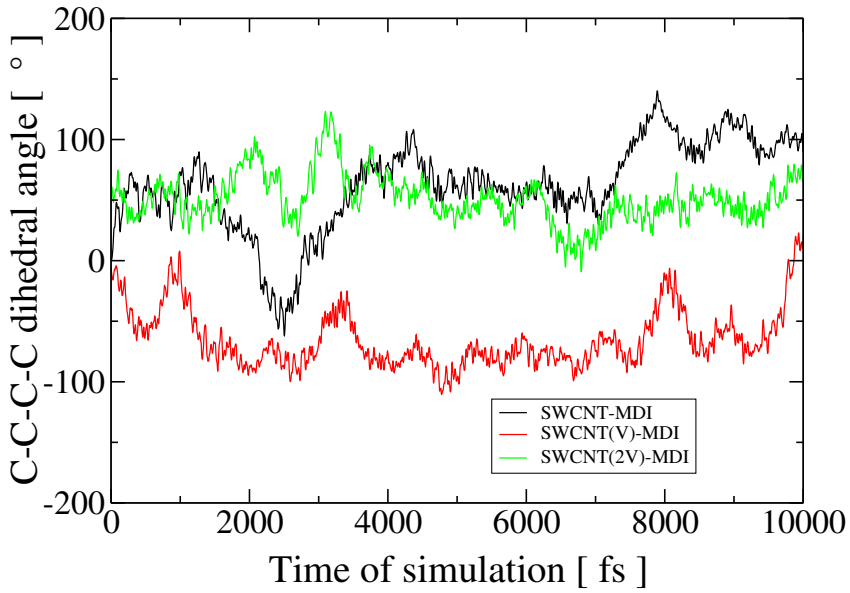

Figure 11.24: Time evolution of the C-C-C-C dihedral angle between two phenyl rings of the MDI molecule covalently attached to the pristine (black curve), vacancy-defective (red curve) and divacancy-defective (green curve) SWCNT(10,0) surfaces obtained from a CP–MD run.

The detailed analysis of the structural parameters of the covalently functionalized pristine and defective SWCNT(10,0) with aromatic diisocyanate molecules indicates that the structural properties of the molecules attached are significantly changed as a result of the formation of the defective region. The reorganization of atoms on the CNT surface with defects induces changes of the distribution of the electron density within the CNT and the existence of highly reactive regions, which interact with the molecules attached, therefore, change the overall structure of the CNT-functionalized system. Such small structural changes might possess noticeable differencies in the macroscopic properties of the material produced. Thus, the selective separation of the carbon nanotubes with the specific properties should be taken into account.

Chapter 12

Conclusions

Noncovalent interactions are of great importance in the definition of the properties of the materials and substances. It is a complicated task to imagine our life without them, because they are present everywhere. Their strength can be of different ranges, which depends on the specific type of the NCI interaction. The weakest NCI are the hardest to be analyzed in both theory and experiment. Even if they are weak, for example, van der Waals interactions, π-based interactions or hydrogen bonds, they influence the properties of the chemical compounds, especially those connected to the formation of larger clusters and aggregates. The problems in modern materials science can not be solved efficiently only on the basis of the experimental studies, which are not able to answer the question about the molecule-molecule interactions in the system.

In the present PhD thesis, the detailed analysis and description of the intramolecular and intermolecular interactions between the most frequently used aromatic diisocyanate molecules, polyethylene glycol and carbon nanotubes were given. These systems were selected as a result of the existing problem in the polyurethane synthesis connected to low dispersion of the carbon nanotubes in the polymer matrix. Firstly, the noncovalent interactions in the gas-phase molecules, used to produce polyurethane polymers, were fully described and supplemented with the Car–Parrinello molecular dynamics simulations at the finite temperature of 300 K. The most stable structures of the molecules were obtained and fully analyzed. Intramolecular C-H$\cdots\pi$ contacts between the phenyl rings of the MDI molecule were detected. Two main possibilities for the formation of strong O-H$\cdots$O hydrogen bonds in the polyethylene glycol molecules were obtained: between the terminal hydroxyl groups or between one of the hydroxyl group as H-bond donor and the etheric oxygen atom as H-bond acceptor. Moreover, the existence of C-H$\cdots$O H-bonds in the PEG molecules was reported: the strongest C-H$\cdots$O characterizes with the electron density and its Laplacian in the bond critical point of 0.0103 a.u. and 0.0388 a.u., respectively. It is formed in the PEG molecule with three repeat subunits. Additionally, the existence of the associated hydrogen bonds, which cause the deformation of the main polymer chain, was detected. The highest affinity for their formation possesses the PEG molecule with four repeat subunits. Finally, the explanation of the stabilization of the molecules and the interplay between the hydrogen–hydrogen repulsion and hydrogen bonds formation were shown.

After the understanding of the properties of the initial ingredients, the detailed analysis of the noncovalent and covalent functionalization of the single-walled carbon nanotubes with aromatic diisocyanates and polyethylene glycol was presented. On the basis of the adsorption of the TDI and MDI molecules on the surface of pristine SWCNT(6,0), the origin of the noncovalent interactions between aromatic diisocyanates and the sidewall of the carbon nanotube was discovered. The adsorption affinity of the aromatic diisocyanates was found to be originated from $\pi-\pi$ interactions, between the aromatic rings of the adsorbate and

the CNT, therefore, the typical orientation of the aromatic ring in the top or bridge positions on the surface was confirmed. Additionally, the dispersion interactions between the isocyanate groups of the molecule and the π-electron density localized on the carbon nanotube were found to stabilize the adsorption process. The energy of the adsorption of the TDI and MDI molecules on the SWCNT(6,0) was found to be of -49.21 kJ/mol and -64.74 kJ/mol, respectively, which indicates the physisorption of the molecules on the surface. The increase of the energy of adsorption is not proportional to the size of the molecule adsorbed. It depends on the strength of $\pi - \pi$ interactions between the molecule and the surface of the carbon nanotubes, which can be increased as a result of the substituent effect of the electron-withdrawing nature, which changes the distribution of the π-electron density. This effect was found to be of lower impact on the noncovalent interactions between the CNT and the MDI molecule, which has only one isocyanate group in the phenyl ring. At the same time, the TDI molecule was shown to have stronger adsorption on the SWCNT because of the enhancing of the substituent effect as the result of the *meta* position of the isocyanate groups in the aromatic ring. Due to the NCI interactions during the noncovalent functionalization of the carbon nanotubes, the electronic properties of the pristine SWCNT(6,0) are only slightly changed, what was confirmed after the analysis of the density of states of all systems analyzed. The static DFT calculations predicted the existence of weak dispersion interactions and the lack of stronger noncovalent interactions between the small polyethylene glycol molecules with two to five repeat subunits on the surface of the single-walled carbon nanotubes.

The existence of the noncovalent interactions was also analyzed during the covalent functionalization of the carbon nanotubes with one and two aromatic diisocyanates. The frequently used method to obtain the covalent attachment of diisocyanates on SWCNTs was taken into account, i.e. modification of the initially carboxylated carbon nanotubes by TDI and MDI. As a result of the calculations made, the affinity of the carboxylated carbon nanotubes to react with diisocyanates was reported. The higher binging energy corresponds to the carbon nanotube with smaller diameter, therefore, SWCNT(6,0) are more likely to be covalently functionalized by diisocyanates than SWCNT(10,0). Thus, the binding energy is inversely proportional to the diameter of the SWCNT. The formation of the covalent bond was shown to induce the change of the geometry close to the attachment of the molecule, therefore, the hybridization of the carbon atom from the SWCNT sidewall changes. This structural change influences the distribution of the electron density in close vicinity to the sp^3-hybridized carbon atom, therefore, impacts on the electronic properties of the initial carbon nanotubes and introduces the impurity states, what was confirmed during the analysis of the electronic band gap. The existence of intramolecular C-H$\cdots$O hydrogen bond, as the result of the covalent attachment of diisocyanates to the surface, was confirmed. Its stability and lifetime was also checked during the Car–Parrinello molecular dynamics simulations at finite temperature.

During the analysis of the covalent attachment of the second TDI or MDI molecule on the surface of the SWCNT(10,0), the high possibility for the formation of the sandwich-like structures of the TDI molecules was obtained. Apart from the stabilization of this mutual position of two molecules by $\pi - \pi$ interactions, the additional dispersion interactions between the isocyanates groups were detected. No evidence to form a T-shaped structure of two covalently attached TDI molecules on the CNT was reported. Such orientation of the molecules was found to be impossible because of the repulsion interactions between the C=O fragment from the isocyanate group and the π-electron density of the aromatic molecule attached. The existence of both $\pi - \pi$ interactions and C-H$\cdots\pi$ interactions between two MDI molecules covalently attached to the surface of the carbon nanotube was confirmed. These two types of π-interactions are competitive ones during the attachment of the second diisocyanate molecule on the SWCNT.

Apart from the pristine carbon nanotubes analyzed, the defective carbon nanotubes, which are highly possible to be formed during the synthesis of the carbon nanotubes, were also taken into account in the research within the present PhD thesis. To estimate the reactivity of different defective regions of the SWCNT(10,0), the carboxylation reaction was used. Among the defective SWCNTs analyzed, the most active sites were detected for the two–coordinated carbon atoms, which exist in the case of the vacancy and the adatom defects on the surface of the carbon nanotubes. The values of the binding energy for the most active sites were shown to be even 3.5–4.0 times higher than for other sites considered. As the result of the DFT calculations made, the following order of the decreasing reactivity was obtained: adatom $>$ vacancy $>$ divacancy ($2V_{5-7}$(555-777)) $>$ divacancy (2V(5-8-5)) $>$ Stone–Wales defect.

The influence of the defect formation and the carboxylation of different defective CNT regions on the structural and electronic properties of the carbon nanotubes were also estimated. The vibrational analysis of the characteristic frequencies of the carboxyl group indicated that the C=O vibrational frequency is very sensitive on the type of the defect on the surface of SWCNT(10,0). Such effect was not observed for the vibrational frequency of the hydroxyl group.

To estimate the influence of the defect existence on the sidewall of the carbon nanotubes, the Car–Parrinello molecular dynamics simulations for diisocyanates covalently attached to pristine and defective: vacancy and divacancy (5-8-5) SWCNTs, were performed and fully analyzed. Different structural patterns of the covalent attachment of the MDI and TDI molecules were observed for the carbon nanotubes with different structural reorganization. The reorganization of atoms on the CNT surface with the defects was shown to induce changes of the distribution of the electron density within the CNT and the existence of highly reactive regions, which interact with the molecules attached, changing the overall structure of the CNT-functionalized system. Such small structural changes might possess noticeable differencies in the macroscopic properties of the material produced. It was confirmed due to the CP–MD simulations and the detailed analysis of the characteristic structural parameters, which specify the structure of the system. Due to the defect formation, the attachment site of the molecules, the rotation with respect to the carbon nanotube, the structural rearrangements of the molecules were changed. Moreover, the strong interaction with the defect region was found to cause the decrease in the inclination angle of the molecule attached and to increase the possibility for the formation of the additional intramolecular hydrogen bond in the case of the MDI molecule, i.e. C-H$\cdots\pi$ one.

On the basis of the results obtained, some suggestions to increase the dispersion of the carbon nanotubes in the polymer matrix can be stated. Firstly, the type of the carbon nanotube should be carefully selected and separated from the undesirable mixtures of different carbon nanotubes. Secondly, it is better to use the stepwise procedure of the polyurethane polymer synthesis, with the CNT as a polymer filler, using the method known as *grafting from*, where the possibility to get more dispersed carbon nanotubes is higher. Finally, the PU synthesis should be dosed and controlled to achieve maximum coverage of the CNT by the monomers to increase the formation of perpendicularly-aligned polymer chains connected to the surface.

Bibliography

[1] K. Peng, Y.-J. Wan, D.-Y. Ren, Q.-W. Zeng, and L.C. Tang. Scalable preparation of multiscale carbon nanotube/glass fiber reinforcements and their application in polymer composites. *Fiber. Polym.*, 15, 6:1242, 2014.

[2] T. M. Madkour, F. M. Hagag, W. Mamdouh, and R. A. Azzam. Molecular-level modeling and experimental investigation into the high performance nature and low hysteresis of thermoplastic polyurethane/ multi-walled carbon nanotube nanocomposites. *Polymer*, 53:5788, 2012.

[3] J. Park and Y. G. Jeong. Investigation of microstructure and electric heating behavior of hybrid polymer composite films based on thermally stable polybenzimidazole and multiwalled carbon nanotube. *Polymer*, 59:102, 2015.

[4] T. K. Gupta, B. P. Singh, Satish Teotia, Varun Katyal, S. R. Dhakate, and R. B. Mathur. Designing of multiwalled carbon nanotubes reinforced polyurethane composites as electromagnetic interference shielding materials. *J. Polym. Res.*, 20:169, 2013.

[5] J. Ryszkowska. Quantitative image analysis of polyurethane/carbon nanotube composite micostructures. *Mater. Charact.*, 60:1127, 2009.

[6] E. Zawadzak, M. Bil, J. Ryszkowska, S. N. Nazhat, J. Cho, O. Bretcanu, J. A. Roether, and A. R. Boccaccini. Polyurethane foams electrophoretically coated with carbon nanotubes for tissue engineering scaffolds. *Biomed. Mater.*, 4:015008, 2009.

[7] L. B. Yan, N. Chouw, and K. Jayaraman. Effect of uv and water spraying on the mechanical properties of flax fabric reinforced polymer composites used for civil engineering applications. *Mater. Design*, 71:17, 2015.

[8] H. Im, S. C. Roh, and C. K. Kim. Characteristics of thermoplastic polyurethane composites containing surface treated multiwalled carbon nanotubes for the underwater applications. *Macromol. Res.*, 21, 6:614, 2013.

[9] J. P. Lu. Elastic properties of carbon nanotubes and nanoropes. *Phys. Rev. Lett.*, 79:1297, 1997.

[10] A. Kin-Tak Lau and D. Hui. The revolutionary creation of new advanced materials—carbon nanotube composites. *Compos. Part B-Eng.*, 33, 4:263, 2002.

[11] B. Arash, Q. Wang, and V. K. Varadan. Mechanical properties of carbon nanotube/polymer composites. *Sci. Rep.*, 4:6479, 2014.

[12] K. Yu, Y. J. Liu, Y. Liu, H. X. Peng, and J. S. Leng. Mechanical and shape recovery properties of shape memory polymer composite embedded with cup-stacked carbon nanotubes. *J. Intell. Mater. Syst. Struct.*, 25, 10:1264, 2014.

[13] L. Q. Liu, D. Tasis, M. Prato, and H. D. Wagner. Tensile mechanics of electrospun multiwalled nanotube/poly(methyl methacrylate) nanofibers. *Adv. Mater.*, 19, 9:1228, 2007.

[14] J. Wei, Y. Jia, Q. Shu, Z. Gu, K. Wang, D. Zhuang, G. Zhang, Z. Wang, J. Luo, A. Cao, and D. Wu. Double-walled carbon nanotube solar cells. *Nano Lett.*, 7,8:2317, 2007.

[15] P. G. Collins, K. Bradley, M. Ishigami, and A. Zettl. Extreme oxygen sensitivity of electronic properties of carbon nanotubes. *Science*, 287, 5459:1801, 2000.

[16] J. Kong, N. R. Franklin, C. Zhou, M. G. Chapline, S. Peng, K. Cho, and H. Dai. Nanotube molecular wires as chemical sensors. *Science*, 287, 5453:622, 2000.

[17] C. Liu, Y. Y. Fan, M. Liu, H. T. Cong, H. M. Cheng, and M. S. Dresselhaus. Hydrogen storage in single-walled carbon nanotubes at room temperature. *Science*, 286, 5442:1127, 1999.

[18] M. P. Anantram and F. Leonard. Physics of carbon nanotube electronic devices. *Rep. Prog. Phys.*, 69, 3:507, 2006.

[19] F. Buffa, G. A. Abraham, B. P. Grady, and D. Resasco. Effect of nanotube functionalization on the properties of single-walled carbon nanotube/polyurethane composites. *J. Polym. Sci. Part B: Polym. Phys.*, 45:490, 2006.

[20] K. H. Kim and W. H. Jo. Improvement of tensile properties of poly(methyl methacrylate) by dispersing multi-walled carbon nanotubes functionalized with poly(3-hexylthiophene)-graft-poly(methyl methacrylate). *Compos. Sci. Technol.*, 68, 9:2120, 2008.

[21] Ya. I. Estrin, E. R. Badamshina, A. A. Grishchuk, V. A. Lesnichaya G. S. Kulagina, Yu. A. Olkhov, A. G. Ryabenko, and S. N. Sulyanov. Properties of nanocomposites based on crosslinked elastomeric polyurethane and ultrasmall additives of single-wall carbon nanotubes. *Polym. Sci. Ser. A*, 54, 4:290, 2012.

[22] A. B. Dalton, S. Collins, E. Munoz, J. M. Razal, V. H. Ebron, J. P. Ferraris, J. N. Coleman, B. G. Kim, and R. H. Baughman. Super-tough carbon-nanotube fibres. *Nature*, 423:703, 2003.

[23] S. Pande, R. B. Mathur, B. P. Singh, and T. L. Dhami. Synthesis and characterization of multiwalled carbon nanotubes-polymethyl methacrylate composites prepared by in situ polymerization method. *Polym. Compos*, 30, 9:1312, 2009.

[24] W. Chen, X. Tao, and Y. Liu. Carbon nanotube-reinforced polyurethane composite fibers. *Compos. Sci. Technol.*, 66:3029, 2006.

[25] S.-L. Shi, L.-Z. Zhang, and J.S. Li. Electrical and dielectric properties of multiwall carbon nanotube/polyaniline composites. *J. Polym. Res.*, 16, 4:395, 2009.

[26] A. S. Ayesh. Preparation and physical characterization of SWCNTs-polycarbonate nanocomposites. *J. Polym. Res.*, 19:27, 2012.

[27] M. B. Bryning, M. F. Islam, J. M. Kikkawa, and A. G. Yodh. Very low conductivity threshold in bulk isotropic single-walled carbon nanotube–epoxy composites. *Adv. Matt.*, 17, 9:1186, 2005.

[28] M. J. Biercuk, M. C. Llaguno, M. Radosavljevic, J. K. Hyun, A. T. Johnson, and J. E. Fischer. Carbon nanotube composites for thermal management. *Appl.Phys. Lett.*, 80:2767, 2002.

[29] A. Bakour, F. Geschier, M. Baitoul, M. Mbarek, K. El-Hadj, J.-L. Duvail, S. Lefrant, E. Faulques, F. Massuyeau, and J. Wery-Venturin. Effects of single-walled carbon nanotubes on the optical and photo-conductive properties of their composite films with regio-regular poly(3-hexylthiophene). *Mater. Chem. Phys.*, 143, 3:1102, 2014.

[30] E. H. Kim, J. H. Lee, Y. G. Jung, and U. Paik. Enhancement of electro-optical properties in holographic polymer-dispersed liquid crystal films by incorporation of multiwalled carbon nanotubes into a polyurethane acrylate matrix. *Polym. Int.*, 59, 9:1289, 2010.

[31] B. Vigolo, V. Mamane, F. Valsaque, T.N.H. Le, J. Thabit, J. Ghanbaja, L. Aranda, Y. Fort, and E. McRae. Evidence of sidewall covalent functionalization of single-walled carbon nanotubes and its advantages for composite processing. *Carbon*, 47, 2:411, 2009.

[32] B. P. Singh, P. Bharadwaj, V. Choudhary, and R. B. Mathur. Enhanced microwave shielding and mechanical properties of multiwall carbon nanotubes anchored carbon fiber felt reinforced epoxy multiscale composites. *Appl. Nanosci.*, 4, 4:421, 2013.

[33] A. Fereidoon, M. G. Ahangari, and S. Saedodin. Thermal and structural behaviors of polypropylene nanocomposites reinforced with single-walled carbon nanotubes by melt processing method. *J. Macromol. Sci. Part B: Physics*, 48, 1:196, 2009.

[34] Y. Wang and X. Jing. Intrinsically conducting polymers for electromagnetic interference shielding. *Polymer. Adv. Tech.*, 16, 4:344, 2005.

[35] M. Yang, V. Koutsos, and M. Zaiser. Interactions between polymers and carbon nanotubes: A molecular dynamics study. *J. Phys. Chem. B*, 109:10009, 2005.

[36] Y. C. Jung, H. Muramatsu, T. Hayashi, J. H. Kim, Y. A. Kim, M. Endo, and M. S. Dresselhaus. Covalent attachment of aromatic diisocyanate to the sidewalls of single- and double-walled carbon nanotubes. *Eur. J. Inorg. Chem.*, page 4305, 2010.

[37] C.-H. Liu, J.-J. Li, H.-L. Zhang, B.-R. Li, and Y. Guo. Structure dependent interaction between organic dyes and carbon nanotubes. *Colloids Surf. A Physicochem. Eng. Asp.*, 313:9, 2008.

[38] D. Randall and S. Lee. *The Polyurethane Book*. Wiley-VCH, 2002.

[39] E. M. Christenson, J. M. Anderson, and A. Hittner. Biodegradation mechanism of polyurethane elastomers. *Corros. Eng. Sci. Technol.*, 42:312, 2007.

[40] O. Bayer. Das di-isocyanat-polyadditionsverfahren (polyurethane). *Angew. Chem.*, 59:257, 1947.

[41] C. S. Schollenbenger, H. Scott, and G. R. Moore. Polyurethane vc, a vivirtual cross-linked elastomer. *Rubber World*, 137:549, 1958.

[42] G. Woods. *The ICI Polyurethanes Book*. Wiley, 1990.

[43] J. Ryszkowska, M. Jurczyk-Kowalska, T. Szymborski, and K. J. Kurzydlowski. Dispersion of carbon nanotubes in polyurethane matrix. *Physica E*, 39:124, 2007.

[44] M. A. Fonseca, B. Abreu, F. A. M. M. Goncalves, A. G. M. Ferreira, R. A. S. Moreira, and M. S. A. Oliveira. Shape memory polyurethanes reinforced with carbon nanotubes. *Compos. Struct.*, 99:105, 2013.

[45] R. M. Versteegen, R. P. Sijbesma, and E. W. Meijer. [n]-polyurethanes: Synthesis and characterization. *Angew. Chem. Int. Ed. Engl.*, 38:2917, 1999.

[46] G. Rokicki and A. Piotrowska. A new route to polyurethanes from ethylene carbonate, diamines and diols. *Polymer*, 43:2927, 2002.

[47] Grand View Research. Polyurethane (PU) market analysis by product (rigid foam, flexible foam, coatings, adhesives and sealants, elastomers), by end-use (furniture and interiors, construction, electronics and appliances, automotive, footwear, packaging), and segment forecasts. *Market Research Report*, Report ID: 978-1-68038-262-4, 2017.

[48] G. Pandey and E. T. Thostenson. Carbon nanotube-based multifunctional polymer nanocomposites. *Polym. Rev.*, 52:355, 2012.

[49] M. Terrones. Science and technology of the twenty-first century: Synthesis, properties and applications of carbon nanotubes. *Annual. Rev. Mater. Sci.*, 33:419, 2003.

[50] R. Sen, B. Zhao, D. Perea, M. E. Itkis, H. Hu, J. Love, E. Bekyarova, and R. C. Haddon. Preparation of single-walled carbon nanotube reinforced polystyrene and polyurethane nanofibers and membranes by electrospinning. *Nano Lett.*, 4:459, 2003.

[51] R. Shamsi, M. Mahyari, and M. Koosha. Synthesis of CNT-polyurethane nanocomposites using ester-based polyols with different molecular structure: Mechanical, thermal, and electrical properties. *J. Appl. Polym. Sci*, DOI: 10.1002/app.44567, 2017.

[52] H.-J. Song, Z.-Z. Zhang, and X.-H. Men. Surface-modified carbon nanotubes and the effect of their addition on the tribological behavior of a polyurethane coating. *Eur. Polym. J.*, 43:4092, 2007.

[53] H. Koerner, W. D. Liu, M. Alexander, P. Mirau, H. Dowty, and R. A. Vaia. Deformation-morphology correlations in electrically conductive carbon nanotube thermoplastic polyurethane nanocomposites. *Polymer*, 46:4405, 2005.

[54] C. Zhang, J. Hu, F. Ji, Y. Fan, and Y. Liu. A combined experimental and computational study on the material properties of shape memory polyurethane. *J. Mol. Model.*, 18:1263, 2012.

[55] P. R. Supronowicz, P. M. Ajayan, K. R. Ullmann, B. P. Arulanandam, D. W. Metzger, and R. Bizios. Novel current-conducting composite substrates for exposing osteoblasts and alternating current stimulation. *J. Biomed. Mater. Res.*, 59:499, 2002.

[56] P. Slobodian, P. Riha, and P. Saha. A highly-deformable composite composed of an entangled network of electrically-conductive carbon-nanotubes embedded in elastic polyurethane. *Carbon*, 50, 10:3446, 2012.

[57] J. R. Bautista-Quijano, F. Aviles, J. V. Cauich-Rodrigues, R. Schonfelder, A. Bachmatiuk, T. Gemming, and M. H. Rummeli. Tensile piezoresistivity and disruption of percolation in singlewall and multiwall carbon nanotube/polyurethane composites. *Synth. Met.*, 185:96, 2013.

[58] J. R. Bautista-Quijano, F. Aviles, and J. V. Cauich-Rodrigues. Sensing of large strain using multiwall carbon nanotube/segmented polyurethane composites. *Appl. Polym. Sci.*, 130:375, 2013.

[59] J. Xiong, Z. Zheng, X. Qin, M. Li, H. Li, and X. Wang. The thermal and mechanical properties of a polyurethane/multi-walled carbon nanotube composite. *Carbon*, 44:2701, 2006.

[60] J. Kwon and H. Kim. Comparison of the properties of waterborne polyurethane/multiwalled carbon nanotube and acid-treated multiwalled carbon nanotube composites prepared by in situ polymerization. *J. Polym. Sci. Part A: Polym. Chem.*, 43:3973, 2005.

[61] H. Xia and M. Song. Preparation and characterization of polyurethane–carbon nanotube composites. *Soft Matter*, 1:386, 2005.

[62] M. G. Ahangari, A. Fereidoon, and M. D. Ganji. Density functional theory study of epoxy polymer chains adsorbing onto single-walled carbon nanotubes: electronic and mechanical properties. *J. Mol. Model.*, 19:3127, 2013.

[63] Y. Han and J. Elliott. Molecular dynamics simulations of the elastic properties of polymer/carbon nanotube composites. *Comput. Mater. Sci.*, 39, 2:315, 2007.

[64] E. Zaminpayma and Kavoos Mirabbaszadeh. Interaction between single-walled carbon nanotubes and polymers: A molecular dynamics simulation study with reactive force field. *Comput. Mater. Sci.*, 58:7, 2012.

[65] K. Liao and S. Li. Interfacial characteristics of a carbon nanotube-polystyrene composite system. *Appl. Phys. Lett.*, 79, 25:4225, 2001.

[66] X. Zhao, H. Yang, Y. Sheng, J. Li, and M. Sun. Molecular dynamics simulation on the effect of the distance between swcnts for short polymers diffusion among single wall carbon nanotubes. *Comput. Mater. Sci.*, 95:446, 2014.

[67] P. Kowalczyk, P. Gauden, A. P. Terzyk, S. Furmaniak, and P. J. F. Harris. Displacement of methane by coadsorbed carbon dioxide is facilitated in narrow carbon nanopores. *J. Phys. Chem. C*, 116:13640, 2012.

[68] S. J. V. Frankland, A. Caglar, D. W. Brenner, and M. Griebel. Molecular simulation of the influence of chemical cross-links on the shear strength of carbon nanotube–polymer interfaces. *J. Phys. Chem. B*, 106, 12:3046, 2002.

[69] I.-F. W. Kuo, C. J. Mundy, M. J. McGrath, J. I. Siepmann, J. VandeVondele, M. Sprik, J. Hutter, B. Chen, M. L. Klein, F. Mohamed, M. Krack, and M. Parrinello. Liquid water from first principles: investigation of different sampling approaches. *J. Phys. Chem. B*, 108:12990, 2004.

[70] T. D. Kuhne, M. Krack, F. R. Mohamed, and M. Parrinello. Efficient and accurate Car-Parrinello-like approach to Born-Oppenheimer molecular dynamics. *PRL*, 98:066401, 2007.

[71] S. A. Madbouly and J. U. Otaigbe. Recent advances in synthesis, characterization and rheological properties of polyurethanes and poss/polyurethane nanocomposites dispersions and films. *Prog. Polym. Sci.*, 34:1283, 2009.

[72] J. A. Werkmeister, R. Adhikari, J. F. White, T. A. Tebb, T. P. T. Le, H. C. Taing, R. Mayadunne, P. A. Gunatillake, S. J. Danon, and J. A. M. Ramshaw. Biodegradable and injectable cure-on-demand polyurethane scaffolds for regeneration of articular cartilage. *Acta Biomater.*, 6:3471, 2010.

[73] S. Sarkar, P. Basak, and B. Adhikari. Biodegradation of polyethylene glycol-based polyether urethanes. *Polym-Plast. Technol. Eng.*, 50:80, 2011.

[74] M. V. G. de Araujo, J. V. F. Vieira, T. A. da Silva, T. Kubota, F. M. Barboza, P. V. Farago, and S. F. Zawadzki. Innovative cross-linked polyurethane networks based on cyclodextrins and polyethylene glycols: Inclusion capacity and potential use as controlled release carrier for nifedipine. *Macromol. Symp.*, 319, 1:179, 2012.

[75] F. Mo, F. Zhou, S. Chen, H. Yang, Z. Ge, and S. Chen. Development of shape memory polyurethane based on polyethylene glycol and liquefied 4,4'-diphenylmethane diisocyanate using a bulk method for biomedical applications. *Polym. Int.*, 64:477, 2015.

[76] P. A. Kollman. Noncovalent interactions. *Acc. Chem. Res.*, 10:365, 1977.

[77] A. Lachman. A probable cause of the different colors of iodine solutions. *J. Am. Chem. Soc.*, 25:50, 1903.

[78] H. A. Bent. Structural chemistry of donor-acceptor interactions. *Chem. Rev.*, 68:587, 1968.

[79] K. Mueller-Dethlefs and P. Hobza. Noncovalent interactions: a challenge for experiment and theory. *Chem. Rev.*, 100:143, 2000.

[80] M. Nocker, S. Handschuh, C. Tautermann, and K. R. Liedl. Theoretical prediction of hydrogen bond strength for use in molecular modeling. *J. Chem. Inf. Model.*, 49:2067, 2009.

[81] A. Hirsch. The era of carbon allotropes. *Nat. Mater.*, 9:868, 2010.

[82] L. Yang, H. Y. He, and B. C. Pan. Theoretical prediction of new carbon allotropes. *J. Chem. Phys.*, 138:024502, 2013.

[83] G. R. Desiraju, P. S. Ho, L. Kloo, A. C. Legon, R. Marquardt, P. Metrangolo, P. Politzer, G. Resnati, and K. Rissanen. Definition of the halogen bond (iupac recommendations 2013). *Pure Appl. Chem.*, 85:1711, 2013.

[84] O. Hassel and J. Hvoslef. The structure of bromine 1,4-dioxanate. *Acta Chem. Scand.*, 8:873, 1954.

[85] J.-M. Dumas, H. Peurichard, and M. Gomel. Cx4...base interactions as models of weak charge-transfer interactions: Comparison with strong charge-transfer and hydrogen-bond interactions. *J. Chem. Res.(S)*, 2:54, 1978.

[86] P. Politzer, J. S. Murray, and M. C. Concha. Halogen bonding and the design of new materials: organic bromides, chlorides and perhaps even fluorides as donors. *J. Mol. Model.*, 13:643, 2007.

[87] A. R. Voth and P. S. Ho. The role of halogen bonding in inhibitor recognition and binding by protein kinases. *Curr. Top. Med. Chem.*, 7:1336, 2007.

[88] G. Cavallo, P. Metrangolo, R. Milani, T. Pilati, A. Priimagi, G. Resnati, and G. Terraneo. The halogen bond. *Chem. Rev.*, 116:2478, 2016.

[89] S. Grimme. Do special noncovalent pi-pi stacking interactions really exist? *Angew. Chem.*, 47:3430, 2008.

[90] M. O. Sinnokrot and C. D. Sherrill. High-accuracy quantum mechanical studies of $\pi - \pi$ interactions in benzene dimer. *J. Phys. Chem. A*, 110:10656, 2006.

[91] C. A. Hunter and J. K. M. Sanders. The nature of $\pi - \pi$ interactions. *J. Am. Chem. Soc.*, 112:5525, 1990.

[92] G. B. McGaughey, M. Gagne, and A. K. Rappe. π-stacking interactions. *J. Biol. Chem.*, 273:15458, 1998.

[93] S. Mecozzi, A. P. West Jr., and D. A. Dougherty. Cation– π interactions in simple aromatics: electrostatics provide a predictive tool. *J. Am. Chem. Soc.*, 118:2307, 1996.

[94] C. D. M. Churchill and S. D. Wetmore. Noncovalent interactions involving histidine: The effect of charge on pi-pi stacking and T-shaped interactions with the DNA nucleobases. *J. Phys. Chem. B*, 113:16046, 2009.

[95] D. Sriram, T. Lakshmanan, D. Loganathan, and S. Srinivasan. Crystal structure of a hydrated n-glycoprotein linkage region model and its analogue: Hydrogen bonding and pi-pi stacking driven molecular assembly. *Carbohydr. Res.*, 309:227, 1998.

[96] S. Burattini, B. W. B. W. Greenland, D. H. Merino, W. Weng, J. Seppala, H. M. Colquhoun, W. Hayes, M. E. Mackay, I. W. Hamley, and S. J. Rowan. A healable supramolecular polymer blend based on aromatic pi-pi stacking and hydrogen-bonding interactions. *J. Am. Chem. Soc.*, 132:12051, 2010.

[97] S. Burattini, B. W. Greenland, W. Hayes, M. E. Mackay, S. J. Rowan, and H. M. Colquhoun. A supramolecular polymer based on tweezer-type pi-pi stacking interactions: Molecular design for healability and enhanced toughness. *Chem. Mater.*, 23:6, 2011.

[98] J. N. Israelachvili. *Intermolecular and Surface Forces (Third edition)*. Elsevier Inc., 2011.

[99] L. Pauling. The nature of the chemical bond. application of results obtained from the quantum mechanics and from a theory of paramagnetic susceptibility to the structure of molecules. *J. Am. Chem. Soc.*, 53:1367, 1931.

[100] L. C. Pauling. *The Nature of the Chemical Bond and the Structure of Molecules and Crystals*. Cornell University Press, 1939.

[101] L. Sobczyk. *Wiązanie wodorowe*. Państwowe Wydawnictwo Naukowe, Warszawa, 1969.

[102] G. C. Pimentel and A. L. McClellan. *Ann. Rev. Phys. Chem.*, 21:347, 1971.

[103] R. Bader. A quantum theory of molecular structure and its appllcatlons. *Chem. Rev.*, 91:893, 1991.

[104] S. Scheiner. *Hydrogen Bonding*. Oxford University Press, New York, 1997.

[105] G. A. Jeffrey. *An Introduction to Hydrogen Bond*. Oxford University Press, New York, 1999.

[106] G. R. Desiraju and T. Steiner. *The Weak Hydrogen Bond:In Structural Chemistry and Biology*. Oxford University Press, New York, 1999.

[107] M. E. Alikhani, F. Fuster, and B. Silvi. What can tell the topological analysis of elf on hydrogen bonding? *Struct. Chem.*, 16:203, 2005.

[108] I. Rozas. On the nature of hydrogen bonds: an overview on computational studies and a word about patterns. *Phys. Chem. Chem. Phys.*, 9:2782, 2007.

[109] B. J. van der Veken, W. A. Herrebout, R. Szostak, D. N. Shchepkin, Z. Havlas, and P. Hobza. The nature of improper, blue-shifting hydrogen bonding verified experimentally. *J. Am. Chem. Soc.*, 123:12290, 2001.

[110] P. Hobza, V. Spirko, Z. Havlas, K. Buchhold, B. Reimann, H.-D. Barth, and B. Brutschy. Anti-hydrogen bond between chloroform and fluorobenzene. *Chem. Phys. Lett.*, 299:180, 1999.

[111] M. O. Bulanin, T. D. Kolomiitsova, V. A. Kondaurov, and S. M. Melikova. *Opt. Spectrosc. (Rus)*, 68:763, 1990.

[112] I. E. Boldeskul, I. F. Tsymbal, E. V. Ryltseva, Z. Latajka, and A. J. Barnes. Reversal of the usual ni(c-h/d) spectral shift of haloforms in some hydrogen-bonded complexes. *J. Mol. Struct.*, 436:167, 1997.

[113] K. Hermansson. Blue-shifting hydrogen bonds. *J. Phys. Chem. A*, 106:4695, 2002.

[114] S. J. Grabowski. Red- and blue-shifted hydrogen bonds: the bent rule from quantum theory of atoms in molecules perspective. *J. Phys. Chem. A*, 115:12789, 2011.

[115] S. Scheiner and T. Kar. Red- versus blue-shifting hydrogen bonds: Are there fundamental distinctions? *J. Phys. Chem. A*, 106:1784, 2002.

[116] S. M. Melikova, K. S Rutkowski, P. Rodziewicz, and A. Koll. Unusual spectroscopic properties of CF_3H dissolved in liquified Ar, N_2, CO, and CO_2,. *Chem. Phys. Lett.*, 352:301, 2002.

[117] Y. Gu, T. Kar, and S. Scheiner. Fundamental properties of the $CH\cdots O$ interaction: Is it a true hydrogen bond? *J. Am. Chem. Soc.*, 121:9411, 1999.

[118] E. Arunan, G. R. Desiraju, R. A. Klein, J. Sadlej, S. Scheiner, I. Alkorta, D. C. Clary, R. H. Crabtree, J. J. Dannenberg, P. Hobza, H. G. Kjaergaard, A. C. Legon, B. Mennucci, and D. J. Nesbitt. Definition of the hydrogen bond (IUPAC Recommendations 2011). *Pure Appl. Chem.*, 83:1637, 2011.

[119] P. Hobza and Z. Havlas. Blue-shifting hydrogen bonds. *Chem. Rev.*, 100:4253, 2000.

[120] A. Masunov, J.J. Dannenberg, and R. H. Contreras. C-H bond-shortening upon hydrogen bond formation: influence of an electric field. *J. Phys. Chem. A*, 105:4737, 2001.

[121] A. Karpfen and E. S. Kryachko. Blue-shifted a-h stretching modes and cooperative hydrogen bonding. 1. complexes of substituted formaldehyde with cyclic hydrogen fluoride and water clusters. *J. Phys. Chem. A*, 111:8177, 2007.

[122] A. C. Legon and D. J. Millen. Directional character, strength, and nature of the hydrogen bond in gas-phase dimers. *Acc. Chem. Res.*, 20:39, 1987.

[123] I. Majerz. Directionality of inter- and intramolecular OHO hydrogen bonds: DFT study followed by AIM and NBO analysis. *J. Phys. Chem. A*, 116:7992, 2012.

[124] H. Szatylowicz. Structural aspects of the intermolecular hydrogen bond strength: H-bonded complexes of aniline, phenol and pyridine derivatives. *J. Phys. Org. Chem.*, 21:897, 2008.

[125] Z. Mielke, S. Coussan, K. Mierzwicki, P. Roubin, and M. Saldyka. The complexes between ch3oh and cf4. infrared matrix isolation and theoretical studies. *J. Phys. Chem. A*, 110:4712, 2006.

[126] R. Georges, M. Freytes, D. Hurtmans, I. Kleiner, J. Vander Auwera, and M. Herman. Jet-cooled and room temperature ftir spectra of the dimer of formic acid in the gas phase. *Chem. Phys.*, 305:187, 2004.

[127] R. Linder, M. Nispel, T. Haber, and K. Kleinermanns. Gas-phase ft-ir-spectra of natural amino acids. *Chem. Phys. Lett.*, 409:260, 2005.

[128] Y. Inokuchi, Y. Kobayashi, T. Ito, and T. Ebata. Conformation of l-tyrosine studied by fluorescence-detected uv-uv and ir-uv double-resonance spectroscopy. *J. Phys. Chem. A*, 111:3209, 2007.

[129] K. Liu, M. G. Brown, J. D. Cruzan, and R. J. Saykally. Terahertz laser spectroscopy of the water pentamer: Structure and hydrogen bond rearrangement dynamics. *J. Phys. Chem. A*, 101:9011, 1997.

[130] B. B. Shirvani, J. Beheshtian, M. D. Esrali, and N. L. Hadipour. DFT study of NH3 adsorption on the (5,0), (8,0), (5,5) and (6,6) single-walled carbon nanotubes. calculated binding energies, NMR and NQR parameters. *Physica B*, 405:1455, 2010.

[131] K. Hermansson. Blue-shifting hydrogen bonds. *J. Phys. Chem. A*, 106:4695, 2002.

[132] M. Jablonski and M. Palusiak. Nature of a hydride–halogen bond. a SAPT-, QTAIM-, and NBO-based study. *J. Phys. Chem. A*, 116:2322, 2012.

[133] A. Karpfen and E. S. Kryachko. Blue-shifted hydrogen-bonded complexes. ii. ch3f...(hf)1<n<3 and ch2f2...(hf)1<n<3. *Chem. Phys.*, 310:77, 2005.

[134] K. S Rutkowski and S. M. Melikova. Vibrational spectra of oc...hcl complex in kr solutions at liquid to solid phase transition. *J. Mol. Struct.*, 511:233, 1999.

[135] S. M. Melikova, K. S Rutkowski, P. Rodziewicz, and A. Koll. Comparative studies of blue shifting and red shifting effects in fluoroform and acetylene cryogenic solutions. *J. Mol. Struct.*, 705:49, 2004.

[136] S. M. Melikova, K. S Rutkowski, P. Lipkowski, D. N. Shchepkin, and A. Koll. FTIR studies of HCl dissolved in liquid CO: Anharmonic eects in the weak OC...HCl complex. *J. Mol. Struct.*, 844:64, 2007.

[137] S. Gronert. Theoretical studies of proton transfers. 1. the potential energy surfaces of the identity reactions of the first- and second-row non-metal hydrides with their conjugate bases. *J. Am. Chem. Soc.*, 115:10258, 1993.

[138] J. M. Steed, T. A. Dixon, and W. Klemperer. Molecular beam studies of benzene dimer, hexafluorobenzene dimer, and benzene–hexafluorobenzene. *J. Chem. Phys.*, 70:4940, 1979.

[139] E. Arunan and H. S. Gutowsky. Lowj rotational spectra, internal rotation, and structures of several benzene-water dimers. *J. Chem. Phys.*, 98:4294, 1993.

[140] S. E. Wheeler and J. W. G. Bloom. Toward a more complete understanding of noncovalent interactions involving aromatic rings. *J. Phys. Chem. A*, 118:6133, 2014.

[141] M. Giese, M. Albrecht, and K. Rissanen. Experimental investigation of anion-pi interactions - applications and biochemical relevance. *Chem. Comm.*, 52:1778, 2016.

[142] S. Grimme. Semiempirical GGA-type density functional constructed with a long-range dispersion correction. *J. Comp. Chem.*, 27:1787, 2006.

[143] S. Grimme, J. Antony, S. Ehrlich, and H. Krieg. A consistent and accurate ab initio parametrization of density functional dispersion correction (dft-d) for the 94 elements h-pu. *J. Chem. Phys.*, 132:154104, 2010.

[144] A. Tkatchenko, R. A. DiStasio Jr., R. Car, and M. Scheffler. Accurate and efficient method for many-body van der Waals interactions. *PRL*, 108:236402, 2012.

[145] O. A. von Lilienfeld, I. Tavernelli, and U. Rothlisberger. Optimization of effective atom centered potentials for london dispersion forces in density functional theory. *Phys. Rev. Lett.*, 93:153004, 2004.

[146] O. A. von Lilienfeld, I. Tavernelli, U. Rothlisberger, and D. Sebastiani. Performance of optimized atom-centered potentials for weakly bonded systems using density functional theory. *Phys. Rev. B*, 71:195119, 2005.

[147] L. A. Burns, A. Vazquez-Mayagoitia, B. G. Sumpter, and C. D. Sherrill. Density-functional approaches to noncovalent interactions: a comparison of dispersion corrections (DFT-D), exchange-hole dipole moment (XDM) theory, and specialized functionals. *J. Chem. Phys.*, 134:084107, 2011.

[148] P. Jurecka, J. Cerny, P. Hobza, and D. R. Salahub. Density functional theory augmented with an empirical dispersion term. interaction energies and geometries of 80 noncovalent complexes compared with ab initio quantum mechanics calculations. *J. Comput. Chem.*, 28:555, 2007.

[149] S. Tsuzuki, T. Uchimaru, K. Matsumura, and M. MikM. Mikami. Tanabe. Effects of the higher electron correlation correction on the calculated intermolecular interaction energies of benzene and naphthalene dimers: comparison between MP2 and CCSD(T) calculations. *Chem. Phys. Lett.*, 319:547, 2000.

[150] K. E. Riley and P. Hobza. Noncovalent interactions in biochemistry. *WIREs Comput. Mol. Sci.*, 1:3, 2011.

[151] A. J. Misquitta, R. Podeszwa, B. Jeziorski, and K. Szalewicz. Intermolecular potentials based on symmetry-adapted perturbation theory with dispersion energies from time-dependent density-functional calculations. *J. Chem. Phys.*, 123:214103, 2005.

[152] R. F. W. Bader. *Atoms in Molecules, A Quantum Theory*. Oxford University Press, Oxford, 1990.

[153] S. J. Grabowski. What is the covalency of hydrogen bonding? *Chem. Rev.*, 111:2597, 2011.

[154] S. Mebs and M. A. Chilleck. Geometry versus topology: Combined aim, eli-d, and asf analysis of weak intramolecular interactions. *Chem. Phys. Lett.*, 591:1, 2014.

[155] M. Ziolkowski, S. J. Grabowski, and J. Leszczynski. Cooperativity in hydrogen-bonded interactions: Ab initio and "atoms in molecules" analyses. *J. Phys. Chem. A*, 110:6514, 2006.

[156] D. Wu and D. Jia. Theoretical analysis on the hydrogen bonding and reactivity that associated with the proton transfer reaction of carboxylic acid dimers and their monosulfur derivatives. *Int. J. Quant. Chem.*, 111:3017, 2011.

[157] S. Wojtulewski and S. J. Grabowski. Blue-shifting C–H...Y intramolecular hydrogen bonds – DFT and AIM analyses. *Chem. Phys.*, 309:183, 2005.

[158] M. Kozlowska, J. Goclon, and P. Rodziewicz. A computational study of intramolecular hydrogen bonds breaking/formation: impact on the structural flexibility of the ranitidine molecule. *J. Mol. Model.*, 21:94, 2015.

[159] U. Koch and P. L. A. Popelier. Characterization of C-H-O hydrogen bonds on the basis of the charge density. *J. Phys. Chem.*, 99:9747, 1995.

[160] T. A. Keith. AIMAll (version 10.05.04, professional). 2010.

[161] E. R. Johnson, S. Keinan, P. Mori-Sanchez, J. Contreras-Garcia, A. J. Cohen, and W. Yang. Revealing noncovalent interactions. *J. Am. Chem. Soc.*, 132:6498, 2010.

[162] J. Contreras-Garcia, E. R. Johnson, S. Keinan, R. Chaudret, J.-P. Piquemal, D. N. Beratan, and W. Yang. NCIPLOT: a program for plotting noncovalent interaction regions. *J. Chem. Theory Comput.*, 7:625, 2011.

[163] J. Contreras-Garcia, W. Yang, and E. R. Johnson. Analysis of hydrogen-bond interaction potentials from the electron density: integration of noncovalent interaction regions. *J. Phys. Chem. A*, 115:12983, 2011.

[164] M. Kozlowska, P. Rodziewicz, and A. Kaczmarek-Kedziera. Structural stability of diclofenac vs. inhibition activity from ab initio molecular dynamics simulations. comparative study with ibuprofen and ketoprofen. *Struct. Chem.*, DOI 10.1007/s11224-016-0893-8, 2017.

[165] S. Iijima. Helical microtubules of graphitic carbon. *Nature*, 354:56, 1991.

[166] W. R. Davis, R. J. Slawson, and G. R. Rigby. An unusual form of carbon. *Nature*, 171:756, 1953.

[167] J. A. E. Gibson. Early nanotubes? *Nature*, 359:369, 1992.

[168] R. T. K. Baker and P. S. Harris. *Chemistry and Physics of carbon*. Dekker Inc., New York, 1978.

[169] H. P. Boehm. Carbon from carbon monoxide disproportionation on nickel and iron catalysts: Morphological studies and possible growth mechanisms. *Carbon*, 11:583, 1973.

[170] H. P. Boehm. The first observation of carbon nanotubes. *Carbon*, 35:581, 1997.

[171] M. Monthioux and V. L. Kuznetsov. Who should be given the credit for the discovery of carbon nanotubes. *Carbon*, 44:1621, 2006.

[172] L. V. Radushkevich and V. M. Lukyanovich. On the carbon structure formed during thermal decomposition of carbon monoxide in the presence of iron (in russian). *Zh. Fizich. Khim.*, 26:88, 1952.

[173] A. Oberlin, M. Endo, and T. Koyama. Filamentous growth of carbon through benzene decomposition. *J. Crys. Growth*, 32:335, 1976.

[174] M. Endo. Grow carbon fibers in the vapor phase. *Chemtech*, 18:568, 1988.

[175] A. M. Sladkov and Y. P. Kudryavtsev. Diamond, graphite, carbyne 3/4 the allotropic forms of carbon. *Priroda (Nature)*, 58:37, 1969.

[176] H. W. Kroto, J. R. Heath, S. C. O'Brien, R. F. Curl, and R. E. Smalley. C60: Buckminsterfullerene. *Nature*, 318:162, 1985.

[177] A. V. Rode, S. T. Hyde, E. G. Gamaly, R. G. Elliman, D. R. McKenzie, and S. Bulcock. Structural analysis of a carbon foam formed by high pulse-rate laser ablation. *Appl. Phys. A*, 69:S755, 1999.

[178] P. J. F. Harris. Fullerene-related structure of commercial glassy carbons. *Philos. Mag.*, 84:3159, 2004.

[179] S. J. Tans, M. H. Devoret, H. Dai, A. Thess, R. E. Smalley, L. J. Geerligs, and C. Dekker. Individual single-wall carbon nanotubes as quantum wires. *Nature*, 386:474, 1997.

[180] X. S. Wang, Q. Q. Li, J. Xie, Z. Jin, J. Y. Wang, Y. Li, K. L. Jiang, and S. S. Fan. Fabrication of ultralong and electrically uniform single-walled carbon nanotubes on clean substrates. *Nano Lett.*, 9:3137, 2009.

[181] S. Iijima and T. Ichihashi. Single-shell carbon nanotubes of 1-nm diameter. *Nature*, 363:603, 1993.

[182] D. S. Bethune, C. H. Kiang, M. S. de Vries G. Gorman, R. Savoy, J. Vazquez, and R. Beyers. Cobalt-catalysed growth of carbon nanotubes with single-atomic-layer walls. *Nature*, 363:605, 1993.

[183] J. L. Hutchison, N. A. Kiselev, E. P. Krinichnaya, A. V. Krestinin, R. O. Loutfy, A. P. Morawsky, V. E. Muradyan, E. D. Obraztsova, J. Sloan, S. V. Terekhov, and D. N. Zakharov. Double-walled carbon nanotubes fabricated by a hydrogen arc discharge method. *Carbon*, 39:761, 2001.

[184] A. Charlier, E. McRae, R. Heyd, M. F. Charlier, and D. Moretti. Classification of double-walled carbon nanotubes. *Carbon*, 37:1779, 1999.

[185] P. J. F. Harris. *Carbon Nanotube Science. Synthesis, properties and applications*. Cambridge University Press, 2009.

[186] S. B. Fagan. TEM (Transmission Electron Microscopy) images of double, multiple and single wall carbon nanotubes (MWCN, SWCN, DWCN). *www.sbf1.sbfisica.org.br/eventos/ebee/x/*, 2007.

[187] C. T. White, D. H. Robertson, and J. W. Mintmire. Helical and rotational symmetries of nanoscale graphitic tubules. *Phys. Rev. B*, 47:5485, 1993.

[188] R. Saito, M. Fujita, G. Dresselhaus, and M. S. Dresselhaus. Electronic structure of graphene tubules based on C60. *Phys. Rev. B*, 46:1804, 1992.

[189] J. W. G. Wildöer, L. C. Venema, A. G. Rinzler, R. E. Smalley, and C. Dekker. Electronic structure of atomically resolved carbon nanotubes. *Nature*, 391:59, 1998.

[190] P. G. Collins, M. S. Arnold, and P. Avouris. Engineering carbon nanotubes and nanotube circuits using electrical breakdown. *Science*, 292:706, 2001.

[191] G. Y. Zhang, P. F. Qi, X. R. Wang, Y. Lu, X. Li, R. Tu, S. Bangsaruntip, D. Mann, L. Zhang, and H. Dai. Selective etching of metallic carbon nanotubes by gas-phase reaction. *Science*, 314:974, 2006.

[192] H. Q. Peng, N. T. Alvares, C. Kittrell, R. H. Hauge, and H. K. Schmidt. Dielectrophoresis field flow fractionation of single-walled carbon nanotubes. *J. Am. Chem. Soc.*, 128:8396, 2006.

[193] D. Chattopadhyay, I. Galeska, and F. Papadimitrakopoulos. A route for bulk separation of semiconducting from metallic single-wall carbon nanotubes. *J. Am. Chem. Soc.*, 125:3370, 2001.

[194] M. Zheng, A. Jagota, M. S. Strano, A. P. Santos, P. Barone, S. G. Chou, M. S. Dresselhaus, R. S. McLean, G. B. Onoa, G. G. Samsonidze, E. D. Semke, M. Usrey, and D. J. Walls. Structure-based carbon nanotube sorting by sequence-dependent DNA assembly. *Science*, 302:1545, 2003.

[195] C. Menard-Moyon, N. Izard, E. Doris, and C. Mioskowski. Separation of semiconducting from metallic carbon nanotubes by selective functionalization with azomethine ylides. *J. Am. Chem. Soc.*, 128:6552, 2006.

[196] H. Park, J. Zhao, and J. P. Lu. Distinct properties of single-wall carbon nanotubes with monovalent sidewall additions. *Nanotechnol.*, 16:635, 2005.

[197] C.-M. Yang, J. S. Park, K. H. An, S. C. Lim, K. Seo, B. Kim, K. A. Park, S. Han, C. Y. Park, and Y. H. Lee. Selective removal of metallic single-walled carbon nanotubes with small diameters by using nitric and sulfuric acids. *J. Phys. Chem.*, 109:19242, 2005.

[198] J. C. Charlier. Defects in carbon nanotubes. *Acc. Chem. Res.*, 35:1063, 2002.

[199] Ph. Lambin, A. Fonseca, J. P. Vigneron, J. B. Nagy, and A. A. Lucas. Structural and electronic properties of bent carbon nanotubes. *Chem. Phys. Lett.*, 245:85, 1995.

[200] K. Suenaga, H. Wakabayashi, M. Koshino, Y. Sato, K. Urita, and S. Iijima. Imaging active topological defects in carbon nanotubes. *Nat. Nanotech.*, 2:358, 2007.

[201] J. Kotakoski, A. V. Krasheninnikov, and K. Nordlund. Energetics, structure, and long-range interaction of vacancy-type defects in carbon nanotubes: Atomistic simulations. *Phys. Rev. B*, 74:245420, 2006.

[202] Friederich. Transmission electron microscope image of carbon nanotube junction. *User:OgreBot/Uploads by new users/2016 December 13 16:30*, 2016.

[203] Z. Yao, H. W. Ch. Postma, L. Balents, and C. Dekker. Carbon nanotube intramolecular junctions. *Nature*, 402:273, 1999.

[204] M. Ouyang, J. L. Huang, C. L. Cheung, and C. M. Lieber. Atomically resolved single-walled carbon nanotube intramolecular junctions. *Science*, 291:97, 2001.

[205] J. C. Charlier, T. W. Ebbesen, and Ph. Lambin. Structural and electronic properties of pentagon-heptagon pair defects in carbon nanotubes. *Phys. Rev. B*, 53:11108, 1996.

[206] L. Chico, V. H. Crespi, L. X. Benedict, S. G. Louie, and M. L. Cohen. Pure carbon nanoscale devices: Nanotube heterojunctions. *Phys. Rev. Lett.*, 76:971, 1996.

[207] R. Saito, G. Dresselhaus, and M. S. Dresselhaus. Tunneling conductance of connected carbon nanotubes. *Phys. Rev. B*, 53:2044, 1996.

[208] L. Chico, L. X. Benedict, S. G. Louie, and M. L. Cohen. Quantum conductance of carbon nanotubes with defects. *Phys. Rev. B*, 54:2600, 1996.

[209] J. Zhao, H. Park, J. Han, and J. P. Lu. Electronic properties of carbon nanotubes with covalent sidewall functionalization. *J. Phys. Chem. B*, 108:4227, 2004.

[210] R. D. Ruoff, J. Tersoff, D. C. Lorents, S. Subramoney, and B. Chan. Radial deformation of carbon nanotubes by van der waals forces. *Nature*, 364:514, 1993.

[211] H. Hiura, T. W. Ebbesen, J. Fujita, K. Tanigaki, and T. Takada. Role of sp3 defect structures in graphite and carbon nanotubes. *Nature*, 367:148, 1994.

[212] A. J. Stone and D. J. Wales. Theoretical studies of icosahedral c60 and some related species. *Chem. Phys. Lett.*, 128:501, 1986.

[213] J. Goclon, M. Kozlowska, and P. Rodziewicz. Structural, vibrational and electronic properties of defective single-walled carbon nanotubes functionalised with carboxyl groups: Theoretical studies. *ChemPhysChem*, 16 (13):2775, 2015.

[214] S. G. Louie. Electronic properties, junctions, and defects of carbon nanotubes. *Topics in Applied Physics*, 80:113, 2001.

[215] A. V. Krasheninnikov and F. Bahhart. Engineering of nanostructured carbon materials with electron or ion beams. *Nature Materials*, 6:723, 2007.

[216] H. P. Myers. *Introductory Solid State Physics*. Taylor & Francis, 1990.

[217] S. Datta. *Electronic Transport Properties in Mesoscopic Systems*. Cambridge University Press, 1995.

[218] S. Frank, P. Poncharal, Z. L. Wang, and W. A. Heer. Carbon nanotube quantum resistors. *Science*, 280:1744, 1998.

[219] H. Ajiki and T. Ando. Electronic states of carbon nanotubes. *J. Phys. Soc. Jpn.*, 62:1255, 1993.

[220] A. Bachtold, C. Strunk, J. P. Salvetat, J. M. Bonard, L. Forro, T. Nussbaumer, and C. Schoenenberger. Aharonov–bohm oscillations in carbon nanotubes. *Nature*, 397:673, 1999.

[221] U. C. Coskun, T. C. Wei, S. Vishveshwara, P. M. Goldbart, and A. Bezryadin. h/e magnetic flux modulation of the energy gap in nanotube quantum dots. *Science*, 304:1132, 2004.

[222] A. P. Ramirez, R. C. Haddon, O. Zhou, R. M. Fleming, J. Zhang, S. M. McClure, and R. E. Smalley. Magnetic susceptibility of molecular carbon: nanotubes and fullerite. *Science*, 265:84, 1994.

[223] O. Chauvet, L. Forro, W. Bacsa, D. Ugarte, B. Doudin, and W. A. de Heer. Magnetic anisotropies of aligned carbon nanotubes. *Phys. Rev. B*, 52:R6963, 1995.

[224] J. U. Lee, P. P. Gipp, and C. M. Heller. Carbon nanotube p-n junction diodes. *Appl. Phys. Lett.*, 85, 2004.

[225] S. J. Tans and A. R. M. Verschuerenand C. Dekker. Room-temperature transistor based on a single carbon nanotube. *Nature*, 393:49, 1998.

[226] V. Derycke, R. Martel, J. Appenzeller, and Ph. Avouris. Carbon nanotube inter- and intramolecular logic gates. *Nano Lett.*, 1:453, 2001.

[227] A. Modi, N. Koratkar, E. Lass, B. Q. Wei, and P. M. Ajayan. Miniaturized gas ionization sensors using carbon nanotubes. *Nature*, 424:171, 2003.

[228] R. N. Goyal, S. Chatterjee, and A. R. S. Rana. The effect of modifying an edge-plane pyrolytic graphite electrode with single-wall carbon nanotubes on its use for sensing diclofenac. *Carbon*, 48:4136, 2010.

[229] Y. Battie, O. Ducloux, P. Thobois, N. Dorval, J. S. Lauret, B. Attal-Tretout, and A. Loiseau. Gas sensors based on thick films of semi-conducting single walled carbon nanotubes. *Carbon*, 49:3544, 2011.

[230] G. Overney, W. Zhong, and D. Tomanek. Structural rigidity and low frequency vibrational modes of long carbon tubules. *Zeit. Physik D*, 27:93, 1993.

[231] R. S. Ruoff and D. C. Lorents. Mechanical and thermal properties of carbon nanotubes. *Carbon*, 33:925, 1995.

[232] J. Tersoff. Energies of fullerenes. *Phys. Rev. B*, 46:15546, 1992.

[233] A. Krishnan, E. Dujardin, T. W. Ebbesen, P. N. Yianilos, and M. M.J. Treacy. Young's modulus of single-walled nanotubes. *Phys. Rev. B*, 58, 20:14013, 1998.

[234] M. B. Nardelli, B. I. Yakobson, and J. Bernholc. Brittle and ductile behavior in carbon nanotubes. *Phys. Rev. Lett.*, 81:4656, 1998.

[235] M. M. J. Treacy, T. W. Ebbesen, and J. M. Gibson. Exceptionally high Young's modulus observed for individual carbon nanotubes. *Nature*, 381:678, 1996.

[236] F. Li, B. S. Cheng, G. Su, and M. S. Dresselhaus. Tensile strength of single-walled carbon nanotubes directly measured from their macroscopic ropes. *Appl. Phys. Lett.*, 77, 2000.

[237] J. P. Lu. Elastic properties of single and multilayered nanotubes. *J. Phys. Chem. Solids*, 58:1649, 1997.

[238] B. I. Yakobson. Mechanical relaxation and "intramolecular plasticity" in carbon nanotubes. *Appl. Phys. Lett.*, 72:918, 1998.

[239] M.F. Yu, B. S. Files, S. Arepalli, and R. S. Ruoff. Tensile loading of ropes of single wall carbon nanotubes and their mechanical properties. *Phys. Rev. Lett.*, 84:5552, 2000.

[240] J.-P. Salvetat, J.-M. Bonard, N. H. Thomson, A. J. Kulik, L. Forro, W. Benoit, and L. Zuppiroli. Mechanical properties of carbon nanotubes. *Appl. Phys. A*, 69:255, 1999.

[241] J. P. Salvetat, G. A. D. Briggs, J. M. Bonard, R. R. Bacsa, A. J. Kulik, T. Stoeckli, N. A. Burnham, and L. Forro. Elastic and shear moduli of single-walled carbon nanotube ropes. *Phys. Rev. Lett.*, 82:944, 1999.

[242] P. Poncharal, Z. L. Wang, D. Ugarte, and W. A. de Heer. Electrostatic deflections and electromechanical resonances of carbon nanotubes. *Science*, 283:1513, 1999.

[243] J. W. Jo, J. W. Jung, J. U. Lee, and W. H. Jo. Fabrication of highly conductive and transparent thin films from single-walled carbon nanotubes using a new non-ionic surfactant via spin coating. *ASC Nano*, 4:5382, 2010.

[244] C. Srinivasan. The blackest black material from carbon nanotubes. *Curr. Sci.*, 94:974, 2008.

[245] M. S. Dresselhaus, G. Dresselhaus, R. Saito, and A. Jorio. Raman spectroscopy of carbon nanotubes. *Phys. Rep.*, 409:47, 2005.

[246] R. Saito, M. Hofmann, G. Dresselhaus, A. Jorio, and M. S. Dresselhaus. Raman spectroscopy of graphene and carbon nanotubes. *Adv. Phys.*, 60:413, 2011.

[247] A. M. Rao, E. Richter, S. Bandow, B. Chase, P. C. Eklund, K. A. Williams, S. Fang, K. R. Subbaswamy, M. Menon, A. Thess, R. E. Smalley, G. Dresselhaus, and M. S. Dresselhaus. Diameter-selective raman scattering from vibrational modes in carbon nanotubes. *Science*, 275:187, 1997.

[248] F. Hennrich, R. Krupke, S. Lebedkin, K. Arnold, R. Fischer, D. Resasco, and M. Kappes. Raman spectroscopy of individual single-walled carbon nanotubes from various sources. *J. Phys. Chem. B*, 109:10567, 2005.

[249] M. Souza, A. Jorio, C. Fantini, B. R. A. Neves, M. A. Pimenta, R. Saito, A. Ismach, E. Joselevich, V. W. Brar, Ge. G. Samsonidze, G. Dresselhaus, and M. S. Dresselhaus. Single- and double-resonance Raman G-band processes in carbon nanotubes. *Phys. Rev. B*, 69:241403, 2004.

[250] M. A. Pimenta, A. Marucci, S. A. Empedocles, M. G. Bawendi, E. B. Hanlon, A. M. Rao, P. C. Eklund, R. E. Smalley, G. Dresselhaus, and M. S. Dresselhaus. Raman modes of metallic carbon nanotubes. *Phys. Rev. B*, 58:R16016, 1998.

[251] M. S. Dresselhaus, A. Jorio, M. Hofmann, G. Dresselhaus, and R. Saito. Perspectives on carbon nanotubes and graphene Raman spectroscopy. *Nano Lett.*, 10:751, 2010.

[252] J. Hone, M. Whitney, C. Piskoti, and A. Zetti. Thermal conductivity of single-walled carbon nanotubes. *Phys. Rev. B*, 59:R2514, 1999.

[253] P. Kim, L. Shi, A. Majumdar, and P. L. McEuen. Thermal transport measurements of individual multiwalled nanotubes. *Phys. Rev. Lett.*, 87:215502, 2001.

[254] S. Berber, Y. K. Kwon, and D. Tomanek. Unusually high thermal conductivity of carbon nanotubes. *Phys. Rev. Lett.*, 84:4613, 2000.

[255] T. Yamamoto, S. Watanabe, and K. Watanabe. Universal features of quantized thermal conductance of carbon nanotubes. *Phys. Rev. Lett.*, 92:075502, 2004.

[256] M. H. Nguyen, H. T. Bui, V. T. Pham, N. H. Phan, T. H. Nguyen, V. C. Nguyen, D. Q. Le, H. K. Phan, and N. M. Phan. Thermo-mechanical properties of carbon nanotubes and applications in thermal management. *Adv. Nat. Sci.: Nanosci. Nanotechnol.*, 7:025017, 2016.

[257] G. E. Begtrup, K. G. Ray, B. M. Kessler, T. D. Yuzvinsky, H. Garcia, and A. Zettl. Probing nanoscale solids at thermal extremes. *Phys. Rev. Lett.*, 99:155901, 2007.

[258] T. Guo, P. Nikolaev, A. Thess, D. T. Colbert, and R. E. Smalley. Catalytic growth of single-walled manotubes by laser vaporization. *Chem. Phys. Lett.*, 243:49, 1995.

[259] A. Thess, R. Lee, P. Nikolaev, H. Dai, P. Petit, J. Robert, C. Xu, Y. H. Lee, S. G. Kim, A. G. Rinzler, D. T. Colbert, G. E. Scuseria, D. Tomanek, J. E. Fischer, and R. E. Smalley. Crystalline ropes of metallic carbon nanotubes. *Science*, 273:483, 1996.

[260] H. J. Dai, A. G. Rinzler, P. Nikolaev, A. Thess, D. T. Colbert, and R. E. Smalley. Single-wall nanotubes produced by metal-catalyzed disproportionation of carbon monoxide. *Chem. Phys. Lett.*, 260:471, 1996.

[261] T. Koyama, M. Endo, and Y. Onuma. Carbon fibers obtained by thermal decomposition of vaporized hydrocarbon. *Jpn. J. Appl. Phys.*, 11:445, 1972.

[262] W. Z. Li, S. Xie, L. X. Qian, B. H. Chang, B. S. Zou, W. Y. Zhou, R. A. Zhao, and G. Wang. Large-scale synthesis of aligned carbon nanotubes. *Science*, 274:1701, 1996.

[263] C. P. Deck and K. Vecchio. Prediction of carbon nanotube growth success by the analysis of carbon-catalyst binary phase diagrams. *Carbon*, 44:267, 2006.

[264] A. M. Cassell, J. A. Raymakers, J. Kong, and H. Dai. Large scale CVD synthesis of single-walled carbon nanotubes. *J. Phys. Chem. B*, 103:6484, 1999.

[265] S. C. Lyu, B. C. Liu, C. J. Lee, H. K. Kang, C. W. Yang, and C. Y. Park. High-quality double-walled carbon nanotubes produced by catalytic decomposition of benzene. *Chem. Mater.*, 15:3951, 2003.

[266] E. Flahaut, R. Bacsa, A. Peigney, and C. Laurent. Gram-scale CCVD synthesis of double-walled carbon nanotubes. *Chem. Commun.*, 12:1442, 2003.

[267] D. Takagi, Y. Homma, H. Hibino, S. Suzuki, and Y. Kobayashi. Single-walled carbon nanotube growth from highly activated metal nanoparticles. *Nano Lett.*, 6:2642, 2006.

[268] S. Bhaviripudi, E. Mile, S. A. Steiner, A. T. Zare, M. S. Dresselhaus, A. M. Belcher, and J. Kong. CVD synthesis of single-walled carbon nanotubes from gold nanoparticle catalysts. *J. Am. Chem. Soc.*, 129:1516, 2007.

[269] W. W. Zhou, Z. Y. Han, J. Y. Wang, Y. Zhang, Z. Jin, X. Sun, Y. Zhang, C. Yan, and Y. Li. Copper catalyzing growth of single-walled carbon nanotubes on substrates. *Nano Lett.*, 6:2687, 2006.

[270] S. B. Sinnott, R.Andrews, D. Qian, A. M. Rao, Z. Mao, E. C. Dickey, and F. Derbyshire. Model of carbon nanotube growth through chemical vapor deposition. *Chem. Phys. Lett.*, 315:25, 1999.

[271] Y. Li, J. Liu, Y. Q. Wang, and Z. L. Wang. Preparation of monodispersed Fe-Mo nanoparticles as the catalyst for CVD synthesis of carbon nanotubes. *Chem. Mater.*, 13:1008, 2001.

[272] Y. M. Li, W. Kim, Y. G. Zhang, M. Rolandi, D. Wang, and H. Dai. Growth of single-walled carbon nanotubes from discrete catalytic nanoparticles of various sizes. *J. Phys. Chem. B*, 105:11424, 2001.

[273] C. L. Cheung, A. Kurtz, H. Park, and C. M. Lieber. Diameter-controlled synthesis of carbon nanotubes. *J. Phys. Chem. B*, 106:2429, 2002.

[274] B. O. Boskovic, V. Stolojan, R. U. A. Khan S. Haq, and S. R. Silva. Large-area synthesis of carbon nanofibres at room temperature. *Nat. Mater.*, 1:165, 2002.

[275] G. G. Tibbetts, D. W. Gorkiewicz, and R. L. Alig. A new reactor for growing carbon-fibers from liquid-phase and vapor-phase hydrocarbons (*uses ferrocene). *Carbon*, 31:809, 1993.

[276] Z. Q. Bai, H. Chen, B. Q. Li, and W. Li. Catalytic decomposition of methane over activated carbon. *J. Anal. Appl. Pyrolysis*, 73:335, 2005.

[277] Z. F. Ren, Z. P. Huang, J. W. Xu, J. H. Wang, P. Bush, M. P. Siegal, and P. N. Provencio. Synthesis of large arrays of well-aligned carbon nanotubes on glass. *Science*, 282:1105, 1998.

[278] A. Nojeh, A. Ural, R. F. Pease, and H. Dai. Electric-field-directed growth of carbon nanotubes in two dimensions. *J. Vac. Sci. Tech. B*, 22:3421, 2004.

[279] J. H. Hafner, M. J. Bronikowski, B. R. Azamian, P. Nikolaev, A. G. Rinzler, D. T. Colbert, K. A. Smith, and R. E. Smalley. Catalytic growth of single-wall carbon nanotubes from metal particles. *Chem. Phys. Lett.*, 296:195, 1998.

[280] N. R. Franklin and H. J. Dai. An enhanced chemical vapor deposition method to extensive single-walled nanotube networks with directionality. *Adv. Mater.*, 12:890, 2000.

[281] W. K. Hsu, J. P. Hare, M. Terrones, H. W. Kroto, D. R. M. Walton, and P. J. F. Harris. Condensed-phase nanotubes. *Nature*, 377:687, 1995.

[282] Y. M. Li, D. Mann, M. Rolandi, W. Kim, A. Ural, S. Hung, A. Javey, J. Cao, D. Wang, E. Yenilmez, Q. Wang, J. F. Gibbons, Y. Nishi, and H. Dai. Preferential growth of semiconducting single-walled carbon nanotubes by a plasma enhanced CVD method. *Nano Lett.*, 4:317, 2004.

[283] T. W. Ebbesen, P. M. Ajayan, H. Hiura, and K. Tanigaki. Purification of nanotubes. *Nature*, 367:519, 1994.

[284] X. H. Chen, C. S. Chen, Q. Chen, G. Zhang, and Z. Z. Chen. Non-destructive purification of multi-walled carbon nanotubes produced by catalyzed CVD. *Mater. Lett.*, 57:734, 2002.

[285] F. Ikazaki, S. Ohshima, K. Uchida, Y. Kuriki, H. Hayakawa, and M. Yumura. Chemical purification of carbon nanotubes by use of graphite intercalation compounds. *Carbon*, 32:1539, 1994.

[286] Y. J. Chen, M. L. H. Green, J. L. Griffin, J. Hammer, R. M. Lago, and S. Tsang. Purification and opening of carbon nanotubes via bromination. *Adv. Mater.*, 8:1012, 1996.

[287] R. Andrews, D. Jacques, D. Qian, and E. C. Dickey. Purification and structural annealing of multiwalled carbon nanotubes at graphitization temperatures. *Carbon*, 39:1681, 2001.

[288] S. Bandow, A. M. Rao, K. A. Williams, A. Thess, R. E. Smalley, and P. C. Eklund. Purification of single-wall carbon nanotubes by microfiltration. *J. Phys. Chem. B*, 101:8839, 1997.

[289] K. E. Hurst, A. C. Dillon, D. A. Keenan, and J. H. Lehman. Cleaning of carbon nanotubes near the pi-plasmon resonance. *Chem. Phys. Lett.*, 433:301, 2007.

[290] A. G. Rinzler, J. Liu, H. J. Dai, P. Nikolaev, C. B. Huffman, F. J. Rodriguez-Macias ans P. J. Boul, A. H. Lu, D. Heymann, D. T. Coldert, R. S. Lee, J. E. Fisher, A. M. Rao, P. C. Eklund, and R. E. Smalley. Large-scale purification of single-wall carbon nanotubes: process, product, and characterization. *Appl. Phys. A*, 67:29, 1998.

[291] J. Liu, A. G. Rinzler, H. Dai, J. H. Hafner, R. K. Bradley, P. J. Boul, A. Lu, T. Iverson, K. Shelimov, C. B. Huffman, F. Rodriguez-Macias, Y.-S. Shon, T. R. Lee, D. T. Colbert, and R. E. Smalley. Fullerene pipes. *Science*, 280:1253, 1998.

[292] H. Hu, P. Bhowmik, B. Zhao, M. Hamon, M. Itkis, and R. Haddon. Determination of the acidic sites of purified single-walled carbon nanotubes by acid-base titration. *Chem. Phys. Lett.*, 345:25, 2001.

[293] Y. Wang, H. Shan, R. H. Hauge, M. Pasquali, and R. E. Smalley. A highly selective, one-pot purification method for single-walled carbon nanotubes. *J. Phys. Chem. B*, 111:1249, 2007.

[294] Q. Zhang, J. Q. Huang, W. Z. Qian, Y. Y. Zhang, and F. Wei. The road for nanomaterials industry: A review of carbon nanotube production, post-treatment, and bulk applications for composites and energy storage. *Small*, 9:1237, 2013.

[295] A. Hirsch. Functionalization of single-walled carbon nanotubes. *Angew. Chem.*, 41:1853, 2002.

[296] S. Niyogi, M. A. Hamon, H. Hu, B. Zhao, P. Bhowmik, R. Sen, M. E. Itkis, and R. C. Haddon. Chemistry of single-walled carbon nanotubes. *Acc. Chem. Res.*, 35:1105, 2002.

[297] D. Tasis, N. Tagmatarchis, A. Bianco, and M. Prato. Chemistry of carbon nanotubes. *Chem. Rev.*, 106:1105, 2006.

[298] A. Hirsch and O. Vostowsky. Functionalization of carbon nanotubes. *Topics Current Chem.*, 245:193, 2005.

[299] N. Karousis, N. Tagmatarchis, and D. Tasis. Current progress on the chemical modification of carbon nanotubes. *Chem. Rev.*, 110:5366, 2010.

[300] L. J. Meng, C. L. Fu, and Q. H. Lu. Advanced technology for functionalization of carbon nanotubes. *Prog. Nat. Sci.*, 19:801, 2009.

[301] S. Mallakpour and S. Soltanian. Surface functionalization of carbon nanotubes: fabrication and applications. *RSC Adv.*, 6:109916, 2016.

[302] P.-X. Hou, C. Liu, and H.-M. Cheng. Purification of carbon nanotubes. *Carbon*, 46:2003, 2008.

[303] W. A. Saidi. Functionalization of single-wall zigzag carbon nanotubes by carboxyl groups: clustering effect. *J. Phys. Chem. C*, 117:9864, 2013.

[304] E. T. Mickelson, C. B. Huffman, A. G. Rinzler, R. E. Smalley, R. H. Hauge, and J. L. Margrave. Fluorination of single-wall carbon nanotubes. *Che. Phys. Lett.*, 296:188, 1998.

[305] M. J. Moghaddam, S. Taylor, M. Gao, S. Huang, L. Dai, and M. J. McCall. Highly efficient binding of dna on the sidewalls and tips of carbon nanotubes using photochemistry. *Nano Lett.*, 4:89, 2004.

[306] M. Holzinger, O. Vostrowsky, A. Hirsch, F. Hennrich, M. Kappes, R. Weiss, and F. Jellen. Sidewall functionalization of carbon nanotubes. *Angew. Chem. Int. Ed.*, 40:4002, 2001.

[307] P. J. Boul, J. Liu, E. T. Mickelson, C. B. Huffman, L. Ericson, I. W. Chiang, K. A. Smith, D. T. Colbert, R. H. Hauge, J. L. Margrave, and R. E. Smalley. Reversible sidewall functionalization of buckytubes. *Chem. Phys. Lett.*, 310:367, 1999.

[308] J. L. Bahr, J. Yang, D. V. Kosynkin, M. J. Bronikowski, R. E. Smalley, and J. M. Tour. Functionalization of carbon nanotubes by electrochemical reduction of aryl diazonium salts: A bucky paper electrode. *J. Am. Chem. Soc.*, 123:6536, 2001.

[309] K. Kim, D. Bae, J. Kim, K. Park, S. Lim, J. Kim, W. Choi, C. Park, and Y. Lee. Modification of electronic structures of a carbon nanotube by hydrogen functionalization. *Adv. Mater.*, 14:1818, 2002.

[310] G. Viswanathan, N. Chakrapani, H. Yang, B. Wei, H. Chung, K. Cho, C. Y. Ryu, and P. M. Ajayan. Single-step in situ synthesis of polymer-grafted single-wall nanotube composites. *J. Am. Chem. Soc.*, 125:9258, 2003.

[311] Z. Liu, S. M. Tabakman, Z. Chen, and H. Dai. Preparation of carbon nanotube bioconjugates for biomedical applications. *Nat. Protoc.*, 9:1372, 2009.

[312] Z. Chen, W. Thiel, and A. Hirsch. Reactivity of the convex and concave surfaces of single-walled carbon nanotubes (SWCNTs) towards addition reactions: dependence on the carbon-atom pyramidalization. *ChemPhysChem*, 4:93, 2003.

[313] W. Zhang, Z. Zhang, and Y. Zhang. The application of carbon nanotubes in target drug delivery systems for cancer therapies. *Nanoscale Res. Lett.*, 6:555, 2011.

[314] A. Garg and S. B. Sinnott. Effect of chemical functionalization on the mechanical properties of carbon nanotubes. *Chem. Phys. Lett.*, 295:273, 1998.

[315] I. V. Lara, I. Zanella, A. Gomes de Souza Filho, and S. B. Fagan. Influence of concentration and position of carboxyl groups on the electronic properties of single-walled carbon nanotubes. *Phys. Chem. Chem. Phys.*, 16:21602, 2014.

[316] I.-Y. Jeon, D. W. Chang, N. A. Kumar, and J.-B. Baek. *Carbon Nanotubes - Polymer Nanocomposites*. InTech, 2011.

[317] H.-J. Shin, S. M. Kim, S.-M. Yoon, A. Benayad, K. K. Kim, S. J. Kim, H. K. Park, J.-Y. Choi, and Y. H. Lee. Tailoring electronic structures of carbon nanotubes by solvent with electron-donating and -withdrawing groups. *J. Am. Chem. Soc.*, 130:2062, 2008.

[318] C. Ehli, G. Rahman, N. Jux, D. Balbinot, D. Guldi, F. Paolucci, M. Marcaccio, D. Paolucci, M. Melle-Franco, F. Zerbetto, S. Campidelli, and M. Prato. Interactions in single wall carbon nanotubes/pyrene/porphyrin nanohybrids. *J. Am. Chem. Soc.*, 128:11222, 2006.

[319] D. Guldi, G. Rahman, N. Jux, N. Tagmatarchis, and M. Prato. Integrating single-wall carbon nanotubes into donor-acceptor nanohybrids. *Angew. Chem. Int. Ed.*, 43:5526, 2004.

[320] J. Y. Chen and C. P. Collier. Noncovalent functionalization of single-walled carbon nanotubes with water-soluble porphyrins. *J. Phys. Chem. B*, 109:7605, 2005.

[321] R. J. Chen, Y. G. Zhan, D. W. Wang, and H. Dai. Noncovalent sidewall functionalization of single-walled carbon nanotubes for protein immobilization. *J. Am. Chem. Soc.*, 123:3838, 2001.

[322] X. Gong, J. Liu, S. Baskaran, R. Voise, and J. Young. Surfactant-assisted processing of carbon nanotube/polymer composites. *Chem. Mater.*, 12:1049, 2000.

[323] L. Vaisman, G. Marom, and H. Wagner. Dispersions of surface-modified carbon nanotubes in water-soluble and water-insoluble polymers. *Adv. Funct. Mater.*, 16:357, 2006.

[324] J. Yu, N. Grossiord, C. Koning C, and J. Loos. Controlling the dispersion of multi-wall carbon nanotubes in aqueous surfactant solution. *Carbon*, 45:618, 2007.

[325] E. Whitsitt and A. Barron. Silica coated single walled carbon nanotubes. *Nano Lett.*, 3:775, 2003.

[326] A. Star, J. F. Stoddart, D. Steuerman, M. Diehl, A. Boukai, E. W. Wong, X. Yang, S.-W. Chung, H. Choi, and J. R. Heath. Preparation and properties of polymer-wrapped single-walled carbon nanotubes. *Angew. Chem. Int. Ed.*, 40:1721, 2001.

[327] M. D. Vo and D. V. Papavassiliou. Physical adsorption of polyvinyl pyrrolidone on carbon nanotubes under shear studied with dissipative particle dynamics simulations. *Carbon*, 100:291, 2016.

[328] T. Kwon, G. Lee, H. Choi, M. S. Strano, and W. J. Kim. Highly efficient exfoliation of individual single-walled carbon nanotubes by biocompatible phenoxylated dextran. *Nanoscale*, 5:6773, 2013.

[329] M. C. Hermant, P. van der Schoot, B. Klumperman, and C. E. Koning. Probing the cooperative nature of the conductive components in polystyrene/poly(3,4-ethylenedioxythiophene): Poly(styrene sulfonate)-single-walled carbon nanotube composites. *ASC Nano*, 4:2242, 2010.

[330] A. Nish, J.-Y. Hwang, J. Doig, and R. J. Nicholas. Highly selective dispersion of single-walled carbon nanotubes using aromatic polymers. *Nat. Nanotechnol.*, 2:640, 2007.

[331] W. Z. Wang, W. F. Li, X. Y. Pan, C. M. Li, L. Li, Y. G. Mu, J. A. Rogers, and M. B. Chan-Park. Degradable conjugated polymers: Synthesis and applications in enrichment of semiconducting single-walled carbon nanotubes. *Adv. Funct. Mater.*, 21:1643, 2011.

[332] S. K. Samanta, M. Fritsch, U. Scherf, W. Gomulya, S. Z. Bisri, and M. A. Loi. Conjugated polymer-assisted dispersion of single-wall carbon nanotubes: The power of polymer wrapping. *Acc. Chem. Res.*, 47:2446, 2014.

[333] M. Zheng, A. Jagota, E. D. Semke, B. A. Diner, R. S. Mclean, S. R. Lustig, R. E. Richardson, and N. G. Tassi. Dna-assisted dispersion and separation of carbon nanotubes. *Nat. Mater.*, 2:338, 2003.

[334] Z. Guo, P. J. Sadler, and S. C. Tsang. Immobilization and visualization of dna and proteins on carbon nanotubes. *Adv. Mater.*, 10:701, 1998.

[335] F. Balavoine, P. Schultz, C. Richard, V. Mallouh, T. W. Ebbesen, and C. Mioskowski. Helical crystallization of proteins on carbon nanotubes: A first step towards the development of new biosensors. *Angew. Chem. Int. Ed.*, 38:1912, 1999.

[336] Y. Lin, L. F. Allard, and Y. P. Sun. Protein-affinity of single-walled carbon nanotubes in water. *J. Phys. Chem. B*, 108:3760, 2004.

[337] S. S. Karajanagi, A. A. Vertegel, R. S. Kane, and J. S. Dordick. Structure and function of enzymes adsorbed onto single-walled carbon nanotubes. *Langmuir*, 20:11594, 2004.

[338] L. Dong. DNA-templated synthesis of Pt nanoparticles on single-walled carbon nanotubes. *Nanotechnol.*, 20:465602, 2009.

[339] M. K. Shukla, M. Dubey, E. Zakar, R. Namburu, Z. Czyznikowska, and J. Leszczynski. Interaction of nucleic acid bases with single-walled carbon nanotube. *Chem. Phys. Lett.*, 480:269, 2009.

[340] D. Pantarotto, R. Singh, D. McCarthy, M. Erhardt, J. P. Briand, M. Prato, K. Kostarelos, and A. Bianco. Functionalized carbon nanotubes for plasmid dna gene delivery. *Angew. Chem. Int. Ed.*, 43:5242, 2004.

[341] P. C. Ma, N. Siddiqui, G. Marom, and J. K. Kim. Dispersion and functionalization of carbon nanotubes for polymer-based nanocomposites: a review. *Compos. Part A: Appl. Sci. Manuf.*, 41:1345, 2010.

[342] J. Li, P. C. MP. C. Ma. S. Chow, C. K. To, B. Z. Tang, and J. K. Kim. Ccorrelation between percolation threshold, dispersion state and aspect ratio of carbon nanotube. *Adv. Funct. Mater.*, 17:3207, 2007.

[343] H. Yu, S. Hermann, S. E. Schulz, T. Gessner, Z. Dong, and W. J. Li. Optimizing sonication parameters for dispersion of single-walled carbon nanotubes. *Chem. Phys.*, 408:11, 2012.

[344] D. L. Inglefield Jr., R. J. Bodnar, and T. E. Long. Hydrogen bond containing multiwalled carbon nanotubes in polyurethane composites. *Polym. Compos.*, 37:1425, 2016.

[345] C. Mu, L. Zhang, Y. Song, X. Chen, M. Liu, F. Wang, and X. Hu. Modification of carbon nanotubes by a novel biomimetic approach towards enhancement of the mechanical properties of polyurethane. *Polymer*, 92:231, 2016.

[346] G. Pircheraghi, T. Powell, V. S. Bonab, and I. Manas-Zloczower. Effect of carbon nanotube dispersion and network formation on thermal conductivity of thermopastic polyurethane/carbon nanotube nanocomposites. *Polym. Eng. Sci.*, 56:394, 2016.

[347] T. B. Richardson, M. A. Mosiewicki, C. Uzunpinar, N. E. Marcovich, M. I. Aranguren, F. Kilinc-Balci, R. M. Broughton Jr., and M. L. Auad. Study of nanoreinforced shape memory polymers processed by casting and extrusion. *Polym. Compos.*, 32:455, 2011.

[348] F. H. Gojny, M. H. G. Wichmann, B. Fiedler, I. A. Kinloch, W. Bauhofer, and A. H. Windle. Evaluation and identification of electrical and thermal conduction mechanisms in carbon nanotube/epoxy composites. *Polymer*, 47:2036, 2006.

[349] N. G. Sahoo, Y. C. Jung., H. J. Yoo, and J. W. Cho. Effect of functionalized carbon nanotubes on molecular interaction and properties of polyurethane composites. *Macromol. Chem. Phys.*, 207:1773, 2006.

[350] C. Wang, G. Zhou, H. Liu, J. Wu, Y. Qiu, B. L. Gu, and W. Duan. Chemical functionalization of carbon nanotubes by carboxyl groups on Stone-Wales defects: a Density Functional Theory. *J. Phys. Chem. B*, 110:10266, 2006.

[351] J. Jilili, A. Abdurahman, O. Gulseren, and U. Schwingenschlogl. Non-covalent functionalization of single wall carbon nanotubes and graphene by a conjugated polymer. *Appl. Phys. Lett.*, 105:013103, 2014.

[352] J. Goclon, M. Kozlowska, and P. Rodziewicz. Covalent functionalization of single-walled carbon nanotubes through attachment of aromatic diisocyanate molecules from first principles. *Chem. Phys. Lett.*, 619:103, 2015.

[353] K. D. Nielson, A. C. T. van Duin, J. Oxgaard, W.-Q. Deng, and W. A. Goddard III. Development of the reaxff reactive force field for describing transition metal catalyzed reactions, with application to the initial stages of the catalytic formation of carbon nanotubes. *J. Phys. Chem. A*, 109:493, 2005.

[354] T. Kar, S. Scheiner, A. K. Roy, and H. F. Bettinger. Unusual low-vibrational C=O mode of COOH can distinguish between carboxylated zigzag and armchair single-wall carbon nanotubes. *J. Chem. Phys. C*, 116:26072, 2012.

[355] C. Prisacariu. *Polyurethane Elastomers: From Morphology to Mechanical Aspects*. Springer-WienNewYork, 2011.

[356] A. Prociak, G. Rokicki, and J. Ryszkowska, editors. *Materialy Poliuretanowe (Polyurethane Materials)*. Wydawnictwo Naukowe PWN SA, 2014.

[357] M. J. Forrest. Chemical characterisation of polyurethanes. *Rapra Rev. Rep.*, 9(12):3, 1999.

[358] E. Sharmin and F. Zafar, editors. *Polyurethane: An Introduction*. InTech, 2012.

[359] M. Ionescu. *Chemistry and Technology of Polyols for Polyurethanes*. Rapra Technology Limited, 2005.

[360] G. M. Powell. *Handbook of water soluble gums and resins*. McGraw-Hill, New York, 1980.

[361] R. Duncan and J. Kopecek. Soluble synthetic polymers as potential drug carriers. *Adv. Polym. Sci.*, 57:53, 1984.

[362] S. Dreborg and E. B. Akerblom. Immunotherapy with monomethoxypolyethylene glycol modified allergens. *Crit. Rev. Ther. Drug Carrier Syst.*, 6:315, 1990.

[363] T. Yamaoka, Y. Tabata, and Y. Ikada. Distribution and tissue uptake of poly(ethylene glycol) with different molecular weights after intravenous administration in mice. *J. Pharm. Sci.*, 83:601, 1994.

[364] K. Gao. *Polyethylene glycol as an embedment for microscopy and histochemistry*. CRC Press, 1993.

[365] S. Corneillie, Ph. N. Lan, E. Schacht, M. Davies, Alex Shard, R. Green, S. Denyer, M. Wassall, H. Whitfield, and S. Choong. Polyethylene glycol-containing polyurethanes for biomedical applications. *Polym. Int.*, 46:251, 1998.

[366] M. J. Roberts, M. D. Bentley, and J. M. Harris. Chemistry for peptide and protein PEGylation. *Adv. Drug Deliv. Rev.*, 64:116, 2012.

[367] M. Popa, T. Pradell, D. Crespo, and J. M. Calderón-Moreno. Stable silver colloidal dispersions using short chain polyethylene glycol. *Colloids Surf. A: Physicochem. Eng. Asp.*, 303:184, 2007.

[368] M. F. Variava, T. L. Church, A. T. Harris, and A. I. Minett. Polyol-assisted functionalization of carbon nanotubes – a perspective. *J. Mater. Chem. A*, 1:8509, 2013.

[369] D. E. Corpet, G. Parnaud, M. Delverdier, G. Peiffer, and S. Tache. Consistent and fast inhibition of colon carcinogenesis by polyethylene glycol in mice and rats given various carcinogens. *Cancer Res.*, 60:3160, 2000.

[370] S. Parveen and S. K. Sahoo. Clinical applications of polyethylene glycol conjugated proteins and drugs. *Clin. Pharmacokinet*, 45, 10:965, 2006.

[371] A. L. Klibanov, K. Maruyama, V. P. Torchilin, and L. Huang. Amphipathic polyethyleneglycols effectively prolong the circulation time of liposomes. *FEBS Lett.*, 268, 1:235, 1990.

[372] R. Gref, Y. Minamitake, M. T. Peracchia, V. Trubetskoy, V. Torchilin, and R. Langer. Biodegradable long-circulating polymeric nanospheres. *Science*, 263, 5153:1600, 1994.

[373] W. Ding, H. Minamikawa, N. Kameta, T. Shimizu, and M. Masuda. Effects of PEGylation on the physicochemical properties and in vivo distribution of organic nanotubes. *Int. J. Nanomedicine*, 9:5811, 2014.

[374] M. Bottini, N. Rosato, and N. Bottini. PEG-modified carbon nanotubes in biomedicine: current status and challenges ahead. *Biomacromolecules*, 12:3381, 2011.

[375] A. Razzazan, F. Atyabi, B. Kazemi, and R. Dinarvand. In vivo drug delivery of gemcitabine with PEGylated single-walled carbon nanotubes. *Mater. Sci. Eng. C*, 62:614, 2016.

[376] A. Di Crescenzo, M. Aschi, and A. Fontana. Toward a better understanding of steric stabilization when using block copolymers as stabilizers of single-walled carbon nanotubes (SWCNTs) aqueous dispersions. *Macromolecules*, 45:8043, 2012.

[377] D. Ravelli, D. Merli, E. Quartarone, A. Profumo, P. Mustarelli, and M. Fagnoni. PEGylated carbon nanotubes: preparation, properties and applications. *RSC Adv.*, 3:13569, 2013.

[378] F. Mo, F. Zhou, Sh. Chen, H. Yang, Z. Ge, and Sh. Chen. Development of shape memory polyurethane based on polyethylene glycol and liquefied 4,4'-diphenylmethane diisocyanate using a bulk method for biomedical applications. *Polym. Int.*, 64:477, 2015.

[379] R. Paris, A. Marcos-Fernandez, and I. Quijada-Garrido. Synthesis and characterization of poly(ethylene glycol)-based thermo-responsive polyurethane hydrogels for controlled drug release. *Polym. Adv. Technol.*, 24:1062, 2013.

[380] L. Rao, H. Zhou, T. Li, Ch. Li, and Y. Y. Duan. Polyethylene glycol-containing polyurethane hydrogel coatings for improving the biocompatibility of neural electrodes. *Acta Biomat.*, 8:2233, 2012.

[381] G. Li, D. Li, Y. Niu, T. He, K. C. Chen, and K. Xu. Alternating block polyurethanes based on pcl and peg as potential nerve regeneration materials. *J. Biomed. Mater. Res. A*, 102, 3:685, 2014.

[382] Y. Ganji, M. Kasra, S. S. Kordestani, and M. B. Hariri. Synthesis and characterization of gold nanotube/nanowire-polyurethane composite based on castor oil and polyethylene glycol. *Mater. Sci. Eng. C Mater. Biol. Appl.*, 42:341, 2014.

[383] H. Y. Yang, X. M. Zhang, L. J. Duan, M. Y. Zhang, and G. H. Gao ang H. X. Zhang. Synthesis and characterization of fluorescent PEG–polyurethane with free carboxyl groups. *J. Polym. Res.*, 19:9973, 2012.

[384] A. Silvestri, S. Sartori, M. Boffito, C. Mattu, A. M. Di Rienzo, F. Boccafoschi, and G. Ciardelli. Biomimetic myocardial patches fabricated with poly(epsilon-caprolactone) and polyethylene glycol-based polyurethanes. *J. Biomed. Mater. Res. Part B Appl. Biomater.*, 102B, 5:1002, 2014.

[385] S.-Y. Moon, Y.-D. Park, Ch.-J. Kim, Ch. H. Won, and Y.-S. Lee. Effect of chain extenders on polyurethanes containing both poly(butylene succinate) and poly(ethylene glycol) as soft segments. *Bull. Korean Chem. Soc.*, 24, 9:1361, 2003.

[386] F. A. Girardi, G. E. Bruch, C. S. Peixoto, L. Dal Bosco, S. K. Sahoo, C. O. F. Goncalves, A. P. Santos, C. A. Furtado, C. Fantini, and D. M. Barros. Toxicity of single-wall carbon nanotubes functionalized with polyethylene glycol in zebrafish (danio rerio) embryos. *J. Appl. Toxicol.*, 37:214, 2017.

[387] H. C. Shi, H. Y. Liu, S. F. Luan, D. Shi, S. J. Yan, C. M. Liu, R. K. Y. Li, and J. H. Yin. Effect of polyethylene glycol on the antibacterial properties of polyurethane/carbon nanotube electrospun nanofibers. *RSC Adv.*, 6:19238, 2016.

[388] L. V. Karabanova, R. L. D. Whitby, V. A. Bershtein, A. V. Korobeinyk, P. N. Yakushev, O. M. Bondaruk, A. W. Lloyd, and S. V. Mikhalovsky. The role of interfacial chemistry and interactions in the dynamics of thermosetting polyurethane–multiwalled carbon nanotube composites at low filler contents. *Colloid Polym. Sci.*, 291:573, 2013.

[389] Y. C. Jung, H. J. Yoo, Y. A. Kim, J. W. Cho, and M. Endo. Electroactive shape memory performance of polyurethane composite having homogeneously dispersed and covalently crosslinked carbon nanotubes. *Carbon*, 48:1598, 2010.

[390] C. Zhao, L. Ji, H. Liu, G. Hu, S. Zhang, M. Yang, and Z. Yang. Functionalized carbon nanotubes containig isocyanate groups. *J. Solid State Chem.*, 177:4394, 2004.

[391] M. C. Lopes, H. Ribeiro, M. C. G. Santos, L. M. Seara, F. L. Q. Ferreira, R. L. Lavall, and G. G. Silva. High performance polyurethane composites with isocyanate-functionalized carbon nanotubes: Improvement in tear strength and scratch hardness. *J. Appl. Polym. Sci.*, DOI: 10.1002/APP.44394, 2017.

[392] M. Born and R. Oppenheimer. Zur quantentheorie der molekeln. *Ann. Phys.*, 389:457, 1927.

[393] L. H. Thomas. The calculation of atomic fields. *Proc. Cambridge Phil. Soc.*, 23:542, 1927.

[394] E. Fermi. Un metodo statistico per la determinazione di alcune prioprieta dell'atomo. *Rend. Accad. Naz. Lincei.*, 6:602, 1927.

[395] P. Hohenberg and W. Kohn. Inhomogeneous electron gas. *Phys. Rev.*, 136:B864, 1964.

[396] W. Kohn and L. J. Sham. Self-consistent equations including exchange and correlation effects. *Phys. Rev.*, 140:A1133, 1965.

[397] K. Burke. Perspective on density functional theory. *J. Chem. Phys.*, 136:150901, 2012.

[398] D. M. Ceperley and B. J. Alder. Ground state of the electron gas by a stochastic method. *Phys. Rev. Lett.*, 45:566, 1980.

[399] J. P. Perdew and A. Zunger. Self-interaction correction to density-functional approximations for many-electron systems. *Phys. Rev. B*, 23:5048, 1981.

[400] J. P. Perdew, K. Burke, and M. Ernzerhof. Generalized gradient approximation made simple. *Phys. Rev. Lett.*, 77:3865, 1996.

[401] S. Grimme. Accurate description of van der Waals complexes by density functional theory including empirical corrections. *J. Comput. Chem.*, 25, 12:1463, 2004.

[402] N. Troullier and J. L. Martins. Efficient pseudopotentials for plane-wave calculations. *Phys. Rev. B*, 43:1993, 1991.

[403] S. Goedecker, M. Teter, and J. Hutter. Separable dual-space gaussian pseudopotentials. *Phys. Rev. B*, 54:1703, 1996.

[404] D. Vanderbilt. Optimally smooth norm-conserving pseudopotentials. *Phys. Rev. B*, 32:8412, 1985.

[405] D. Vanderbilt. Soft self-consistent pseudopotentials in a generalized eigenvalue formalism. *Phys. Rev. B*, 41:7892, 1990.

[406] M. V. Vesolo, A. G. S. Filho, J. M. Filho, S. B. Fagan, and R. Mota. Ab initio study of covalently functionalized carbon nanotubes. *Chem. Phys. Lett.*, 430:71, 2006.

[407] C. Wang, G. Zhou, J. Wu, B. L. Gu, and W. Duan. Effects of vacancy-carboxyl pair functionalization on electronic properties of carbon nanotubes. *Appl. Phys. Lett.*, 89:173130, 2006.

[408] R. O. Jones. Density functional theory: Its origins, rise to prominence, and future. *Rev. Mod. Phys.*, 87:897, 2015.

[409] H. Y. S. Yu, S. H. L. Li, and D. G. Truhlar. Perspective: Kohn-Sham density functional theory descending a staircase. *J. Chem. Phys.*, 145:130901, 2016.

[410] R. Car and M. Parrinello. Unified approach for molecular-dynamics and density-functional theory. *Phys. Rev. Lett.*, 55:2471, 1985.

[411] Dominik Marx and Jürg Hutter. *Ab Initio Molecular Dynamics: Basic Theory and Advanced Methods*. Cambridge University Press, 2009.

[412] *CPMD, http://www.cpmd.org/, Copyright IBM Corp 1990-2008*. Copyright MPI fuer Festkoerperforschung Stuttgart 1997-2001, 2011.

[413] S. Nosé. A unified formulation of the constant temperature molecular-dynamics methods. *J. Chem. Phys.*, 81:511, 1984.

[414] W. G. Hoover. Canonical dynamics – equilibrium phase-space distributions. *Phys. Rev. A*, 31:1695, 1985.

[415] I-F. W. Kuo, C. J. Mundy, M. J. McGrath, J. I. Siepmann, J. VandeVondele, M. Sprik, J. Hutter, B. Chen, M. L. Klein, F. Mohamed, M. Krack, and M. Parrinello. Liquid water from first principles: Investigation of different sampling approaches. *J. Phys. Chem. B*, 108:12990, 2004.

[416] E. Guardia, I. Skarmoutsos, and M. Masia. Hydrogen bonding and related properties in liquid water: A car–parrinello molecular dynamics simulation study. *J. Phys. Chem. B*, 119:8926, 2015.

[417] J. Stare, J. Mavri, J. Grdadolnik, J. Zidar, Z. B. Maksic, and R. Vianello. Hydrogen bond dynamics of histamine monocation in aqueous solution: Car–parrinello molecular dynamics and vibrational spectroscopy study. *J. Phys. Chem. B*, 115:5999, 2011.

[418] R. Z. Khaliullin and T. D. Kuehne. Microscopic properties of liquid water from combined ab initio molecular dynamics and energy decomposition studies. *Phys. Chem. Chem. Phys.*, 15:15746, 2013.

[419] Y. Zheng, C. Wang, Y. Xu, W. Xu, and S. Ju. Structural properties and dynamics of thiophene in sub/supercritical carbon dioxide from Car–Parrinello molecular dynamics simulations. *J. Phys. Chem. B*, 119:8573, 2015.

[420] Z. Jiang, K. Klyukin, and V. Alexandrov. Structure, hydrolysis, and diffusion of aqueous vanadium ions from Car-Parrinello molecular dynamics. *J. Chem. Phys.*, 145:114303, 2016.

[421] R. E. Asfin, S. M. Melikova, A. V. Domanskaya, P. Rodziewicz, and K. S. Rutkowski. Degeneracy lifting effect in the FTIR spectrum of fluoroform trapped in a nitrogen matrix. an experimental and car–parrinello molecular dynamics study. *J. Phys. Chem. A*, 120:3497, 2016.

[422] C. Rovira. The description of electronic processes inside proteins from Car–Parrinello molecular dynamics: chemical transformations. *WIREs Comput. Mol. Sci.*, 3:393, 2013.

[423] http://www.cpmd.org/. Cpmd.

[424] X. Song, S. Liu, H. Yan, and Z. Gan. First-principles study on effects of mechanical deformation on outer surface reactivity of carbon nanotubes. *Physica E Low Dimens. Syst. Nanostruct.*, 41:626, 2008.

[425] T. Vo, Y. D. Wu, R. Car, and M. Robert. Structures, interactions, and ferromagnetism of fe-carbon nanotube systems. *J. Phys. Chem. C*, 112:8400, 2008.

[426] H. Yan, Z. Y. Gan, X. H. Song, Q. Lv, J. P. Xu, and S. Liu. Car–Parrinello simulation of initial growth stage of gallium nitride on carbon nanotubes. *Physica E Low Dimens. Syst. Nanostruct.*, 41:1143, 2009.

[427] P. Ravinder and V. Subramanian. Stone-wales transformation in double-walled carbon nanotubes and the role of inner tube. *J. Phys. Chem. C*, 116:16815, 2012.

[428] F. Mercuri, A. Sgamellotti, L. Valentini, I. Armentano, and J. M. Kenny. Vacancy-induced chemisorption of NO2 on carbon nanotubes: A combined theoretical and experimental study. *J. Phys. Chem. B*, 109:13175, 2005.

[429] P. Ravinder, R. Mahesh Kumar, and V. Subramanian. Studies on the encapsulation of F–in single walled nanotubes of different chiralities using density functional theory calculations and Car–Parrinello molecular dynamics simulations. *J. Phys. Chem. A*, 116:5519, 2012.

[430] J. Hutter, M.E. Tuckerman, and M. Parrinello. Integrating the car–parrinello equations. iii. techniques for ultrasoft pseudopotentials. *J. Chem. Phys.*, 102:859, 1995.

[431] S. Baroni, A. Dal Corso, S. de Gironcoli, P. Giannozzi, C. Cavazzoni, G. Ballabio, S. Scandolo, G. Chiarotti, P. Focher, A. Pasquarello, K. Laasonen, A. Trave, R. Car, N. Marzari, and A. Kokalj. *http://www.pwscf.org/*.

[432] W. Humphrey, A. Dalke, and K. Schulten. VMD – Visual Molecular Dynamics. *J. Molec. Graphics*, 14:33, 1996.

[433] T. Kar, H. F. Bettinger, and S. Scheiner. A. K. Roy. Noncovalent $\pi - \pi$ stacking and CH...π interactions of aromatics on the surface of single-wall carbon nanotubes: an MP2 study. *J. Phys. Chem. C*, 112:20070, 2008.

[434] L. M. Woods, S. C. Bădescu, and T. L. Reinecke. Adsorption of simple benzene derivatives on carbon nanotubes. *Phys. Rev. B*, 75:155415, 2007.

[435] K. Laasonen, R. Car, C. Lee, and D. Vanderbilt. Implementation of ultrasoft pseudopotentials in ab initio molecular dynamics. *Phys. Rev. B*, 43:6796, 1991.

[436] J. Goclon, M. Kozlowska, and P. Rodziewicz. Noncovalent functionalization of single-walled carbon nanotubes by aromatic diisocyanate molecules: A computational study. *Chem. Phys. Lett.*, 598:10, 2014.

[437] P. Rodziewicz and J. Goclon. Structural flexibility of 4,4 '-methylene diphenyl diisocyanate (4,4 '-mdi): evidence from first principles calculations. *J. Mol. Model.*, 20 (2):2097, 2014.

[438] R. Ansari, S. Rouhi, and S. Ajori. On the interfacial properties of polymers/functionalized single-walled carbon nanotubes. *Braz. J. Phys.*, 46:361, 2016.

[439] M. Kozlowska, J. Goclon, and P. Rodziewicz. Intramolecular hydrogen bonds in low-molecular-weight polyethylene glycol. *ChemPhysChem*, 17:1143, 2016.

[440] J. Liu, O. Bibari, P. Mailley, J. Dijon, E. Rouviere, F. Sauter-Starace, P. Caillat, F. Vinet, and G. Marchand. Stable non-covalent functionalisation of multi-walled carbon nanotubes by pyrene–polyethylene glycol through p–p stacking. *New J. Chem.*, 33:1017, 2009.

[441] L. Y. Xu and X. N. Yang. Molecular dynamics simulation of adsorption of pyrene-polyethylene glycol onto graphene. *J. Colloid Interface Sci.*, 418:66, 2014.

[442] N. Malarvizhi, B. Rajeswari, D. Prakash, and S. N. Jaisankar. Morphology and thermal properties of thermosetting polyurethane/single-walled carbon nanotube composites. *Graphene*, 3:65, 2015.

[443] Y. N. Imai, Y. Inoue, I. Nakanishi, and K. Kitaura. Amide–π interactions between formamide and benzene. *J. Comp. Chem.*, 30:2267, 2009.

[444] S. M. Bachilo, L. Balzano, J. E. Herrera, F. Pompeo, D. E. Resasco, and R. B. Weisman. Narrow (n, m)-distribution of single-walled carbon nanotubes grown using a solid supported catalyst. *J. Am. Chem. Soc.*, 125:11186, 2003.

[445] R. G. Amorim, A. FazA. Fazzio. Antonelli, F. D. Novaes, and A. J. R. da Silva. Divacancies in graphene and carbon nanotubes. *Nano Lett.*, 7:2459, 2007.

[446] A. V. Krasheninnikov and F. Banhart. Engineering of nanostructured carbon materials with electron or ion beams. *Nat. Mater.*, 6:723, 2007.